ADVANCED IMAGING OF GLIOMA

EDITED BY: Han Zhang, Yanmei Tie and Cornelia Brendle
PUBLISHED IN: Frontiers in Oncology

frontiers Research Topics

ISSN 1664-8714
ISBN 978-2-88974-199-1
DOI 10.3389/978-2-88974-199-1

About Frontiers

Frontiers is more than just an open-access publisher of scholarly articles: it is a pioneering approach to the world of academia, radically improving the way scholarly research is managed. The grand vision of Frontiers is a world where all people have an equal opportunity to seek, share and generate knowledge. Frontiers provides immediate and permanent online open access to all its publications, but this alone is not enough to realize our grand goals.

Frontiers Journal Series

The Frontiers Journal Series is a multi-tier and interdisciplinary set of open-access, online journals, promising a paradigm shift from the current review, selection and dissemination processes in academic publishing. All Frontiers journals are driven by researchers for researchers; therefore, they constitute a service to the scholarly community. At the same time, the Frontiers Journal Series operates on a revolutionary invention, the tiered publishing system, initially addressing specific communities of scholars, and gradually climbing up to broader public understanding, thus serving the interests of the lay society, too.

Dedication to Quality

Each Frontiers article is a landmark of the highest quality, thanks to genuinely collaborative interactions between authors and review editors, who include some of the world's best academicians. Research must be certified by peers before entering a stream of knowledge that may eventually reach the public - and shape society; therefore, Frontiers only applies the most rigorous and unbiased reviews.
Frontiers revolutionizes research publishing by freely delivering the most outstanding research, evaluated with no bias from both the academic and social point of view. By applying the most advanced information technologies, Frontiers is catapulting scholarly publishing into a new generation.

What are Frontiers Research Topics?

Frontiers Research Topics are very popular trademarks of the Frontiers Journals Series: they are collections of at least ten articles, all centered on a particular subject. With their unique mix of varied contributions from Original Research to Review Articles, Frontiers Research Topics unify the most influential researchers, the latest key findings and historical advances in a hot research area! Find out more on how to host your own Frontiers Research Topic or contribute to one as an author by contacting the Frontiers Editorial Office: frontiersin.org/about/contact

ADVANCED IMAGING OF GLIOMA

Topic Editors:
Han Zhang, University of North Carolina at Chapel Hill, United States
Yanmei Tie, Brigham and Women's Hospital, Harvard Medical School, United States
Cornelia Brendle, University of Tübingen, Germany

Citation: Zhang, H., Tie, Y., Brendle, C., eds. (2022). Advanced Imaging of Glioma. Lausanne: Frontiers Media SA. doi: 10.3389/978-2-88974-199-1

Table of Contents

frontiers in Oncology

ORIGINAL RESEARCH
published: 08 December 2020
doi: 10.3389/fonc.2020.593102

Non-Invasive Estimation of Glioma *IDH1* Mutation and *VEGF* Expression by Histogram Analysis of Dynamic Contrast-Enhanced MRI

Yue Hu[†], *Yue Chen*[†], *Jie Wang*, *Jin Juan Kang*, *Dan Dan Shen*[*] *and Zhong Zheng Jia*[*]

Department of Medical Imaging, Affiliated Hospital of Nantong University, Nantong, China

OPEN ACCESS

Edited by:
Han Zhang,
University of North Carolina at Chapel Hill, United States

Reviewed by:
Nuria Arias-Ramos,
Autonomous University of Madrid, Spain
Yinyan Wang,
Capital Medical University, China

***Correspondence:**
Dan Dan Shen
richie9212@163.com
Zhong Zheng Jia
jzz2397@163.com

[†]*These authors have contributed equally to this work*

Specialty section:
This article was submitted to Cancer Imaging and Image-directed Interventions, a section of the journal Frontiers in Oncology

Received: *09 August 2020*
Accepted: *30 October 2020*
Published: *08 December 2020*

Citation:
Hu Y, Chen Y, Wang J, Kang JJ, Shen DD and Jia ZZ (2020) Non-Invasive Estimation of Glioma IDH1 Mutation and VEGF Expression by Histogram Analysis of Dynamic Contrast-Enhanced MRI. Front. Oncol. 10:593102. doi: 10.3389/fonc.2020.593102

Objectives: To investigate whether glioma isocitrate dehydrogenase (*IDH*) 1 mutation and vascular endothelial growth factor (*VEGF*) expression can be estimated by histogram analysis of dynamic contrast-enhanced magnetic resonance imaging (DCE-MRI).

Methods: Chinese Glioma Genome Atlas (CGGA) database was wined for differential expression of *VEGF* in gliomas with different *IDH* genotypes. The *VEGF* expression and *IDH1* genotypes of 56 glioma samples in our hospital were assessed by immunohistochemistry. Preoperative DCE-MRI data of glioma samples were reviewed. Regions of interest (ROIs) covering tumor parenchyma were delineated. Histogram parameters of volume transfer constant (K^{trans}) and volume of extravascular extracellular space per unit volume of tissue (V_e) derived from DCE-MRI were obtained. Histogram parameters of K^{trans}, V_e and *VEGF* expression of *IDH1* mutant type ($IDH1^{mut}$) gliomas were compared with the *IDH1* wildtype ($IDH1^{wt}$) gliomas. Receiver operating characteristic (ROC) curve analysis was performed to differentiate $IDH1^{mut}$ from $IDH1^{wt}$ gliomas. The correlation coefficients were determined between histogram parameters of K^{trans}, V_e and *VEGF* expression in gliomas.

Results: In CGGA database, *VEGF* expression in IDH^{mut} gliomas was lower as compared to wildtype counterpart. The immunohistochemistry of glioma samples in our hospital also confirmed the results. Comparisons demonstrated statistically significant differences in histogram parameters of K^{trans} and V_e [mean, standard deviation (SD), 50th, 75th, 90th. and 95th percentile] between $IDH1^{mut}$ and $IDH1^{wt}$ gliomas ($P < 0.05$, respectively). ROC curve analysis revealed that 50th percentile of K^{trans} (0.019 min^{-1}) and V_e (0.039) provided the perfect combination of sensitivity and specificity in differentiating gliomas with $IDH1^{mut}$ from $IDH1^{wt}$. Irrespective of *IDH1* mutation, histogram parameters of K^{trans} and V_e were correlated with *VEGF* expression in gliomas ($P < 0.05$, respectively).

Conclusions: *VEGF* expression is significantly lower in $IDH1^{mut}$ gliomas as compared to the wildtype counterpart, and it is non-invasively predictable with histogram analysis of DCE-MRI.

Keywords: glioma, isocitrate dehydrogenase, vascular endothelial growth factor, magnetic resonance imaging, histogram

INTRODUCTION

Glioma is the most common primary intracranial tumor. According to the 2016 World Health Organization (WHO) classification criteria, mutation in the gene encoding isocitrate dehydrogenase (*IDH*) enzyme has been identified in the sub-stratification of glioma (1). Emerging evidence has shown that *IDH* mutation can convert α-ketoglutarate (α-KG) to 2-hydroxyglutaate (2-HG). Excessive 2-HG can activate prolyl hydroxylase (PHD) and then promote the degradation of hypoxia induced factor (HIF), which can weaken tumor microvascular proliferation (2, 3). Moreover, a study has reported that *IDH* mutation inhibited PI3K/Akt signaling and reduced the HIF expression level (4). Vascular endothelial growth factor (*VEGF*) regulated by HIF is one of the angiogenesis-related genes, and its over-expression correlates with poor prognoses in gliomas (5, 6). So, anti-*VEGF* therapy increases progression-free survival and improves quality of life in patients with glioma (7, 8). On account of these findings, we assumed that the expression level of *VEGF* was lower in *IDH* mutant type (IDH^{mut}) gliomas, which fitted with the indolent clinical course of IDH^{mut} gliomas. *IDH* genotypes and the expression level of *VEGF* can be detected by surgery or biopsy, but it suffers from several drawbacks such as sampling error, tumor heterogeneities, and risk of surgical complications. Therefore, it is urgent to find a non-invasive technique. The pharmacokinetic parameters derived from dynamic contrast-enhanced magnetic resonance imaging (DCE-MRI) have the ability to predict the microvascular features of glioma in a non-invasive manner (9, 10). Based on the value of DCE-MRI in gliomas and the hypothetical correlation between glioma *IDH* mutation and *VEGF* expression, we aimed to investigate whether glioma *IDH1* mutation and *VEGF* expression can be estimated by histogram analysis of DCE-MRI.

MATERIALS AND METHODS

Chinese Glioma Genome Atlas Database Analysis

The data of *VEGF* expression and *IDH* genotypes in 641 unique samples with glioma (286 samples with IDH^{mut} and 355 with *IDH* wildtype (IDH^{wt})) were available from the CGGA database. Wilcox test implemented in R language was utilized to analyze the differential expression of *VEGF* in gliomas with different *IDH* genotypes.

Glioma Samples

The inclusion criteria for case selection of this study were as follows: (1) pathologically confirmed gliomas; (2) treatment-naive before MRI examination and surgery; (3) underwent preoperative DCE-MRI. The final study population included 56 patients. All the data were retrospectively reviewed. The clinical cohort consisted of 33 males and 23 females, aged 55 ± 14 years (range, 22–75 years). This retrospective data evaluation was approved by the local institutional review board and written informed consent was obtained from each patient.

MRI

MRI was examined on a 3.0-T MR system (GE Healthcare, Milwaukee, WI, USA) with a 16-element head-neck coil. Conventional MRI were T1-weighted imaging, T2-weighted imaging, T2-weighted fluid attenuated inversion recovery (T2-Flair) imaging.

DCE-MRI was done using dynamic scan of a T1-fast field echo (T1-FFE; RF-spoiled gradient echo) sequence and setting the following parameters: repetition time (TR), 5.1 ms; echo time (TE), 1.4 ms; slice thickness, 2.8 mm; matrix, 256 × 210; field of view (FOV), 250 mm × 250 mm; axial scanning. Precontrast images with multiple flip angles 3, 6, 9, 12, and 15° were acquired for the T1 maps. Then, the contrast agent (Ommiscan, GE Healthcare, Oslo, Norway) was administered (0.1 mmol/kg of body weight) through the antecubital vein *via* a power injector at 4 ml/s, followed by a flush of 15 ml saline. A series of 1,000 images at 50 time points for 20 axial sections were acquired with a temporal resolution approximately of 7 s for each time point. Finally, the postcontrast T1-weighted imaging was conducted in the same axial geometry.

Image Analysis

A software module (OmniKinetics, GE Healthcare, China) was applied for post-processing. The volume transfer constant (K^{trans}) and volume of extravascular extracellular space per unit volume of tissue (V_e) were obtained based on the extended Tofts and Kermode pharmacokinetic model. The arterial input function was located on the superior sagittal sinus. The postcontrast T1-weighted imaging functioned as reference. When the tumor was without enhancement, the T2-Flair images were registered in the DCE images, and the registration images were taken as reference. Regions of interest (ROIs) covering tumor parenchyma were placed after consensus was reached between two experienced radiologists. The ROIs placed on the reference images can automatically transfer onto the parameters maps, and then histogram parameters of K^{trans} and V_e were generated automatically.

Pathology

All clinical glioma specimens were fixed in 4% formalin and embedded in paraffin. The paraffin blocks were cut into 5-μm sections and stained with hematoxylin and eosin (H&E).

The *IDH1* mutation was detected with a mutation-specific antibody. Staining was interpreted as positive when ≥10% of the tumor cells exhibited an intense cytoplasmic staining, whereas staining was deduced as negative when positive cells <10% (11).

Tissue blocks from each specimen were stained for VEGF rabbit anti-human polyclonal antibody (Beijing Bioss Biotechnology Co., Ltd.). All specimens were analyzed with Motic Images Advanced software (version 3.2, Motic China

Abbreviations: AUC, Area under the curve; ASL, Arterial spin labeling; CGGA, Chinese Glioma Genome Atlas; CBF, Cerebral blood flow; DCE-MRI, Dynamic contrast-enhanced magnetic resonance imaging; DSC-MRI, Dynamic susceptibility contrast-enhanced magnetic resonance imaging; *IDH*, Isocitrate dehydrogenase; K^{trans}, Volume transfer constant; ROIs, Regions of interest; ROC, Receiver operating characteristic; V_e, Volume of extravascular extracellular space per unit volume of tissue; *VEGF*, Vascular endothelial growth factor; WHO, World Health Organization.

Group Co., Ltd). A semiquantitative grading of *VEGF* expression was applied. The percentage of positive cells was calculated in five hotspots randomly selected from each section, and the percentage was scored: 1) zero point: positive cells <5%; 2) one point: positive cells 5–25%; 3) two points: positive cells 26–50%; 4) three points: positive cells 51–75%; 5) four points: positive cells 76–100%. The staining intensity was also scored: 1) zero point: no staining; 2) one point: faint yellow; 3) two points: brown-yellow; 4) three points: brown. Total score = percentage score × staining intensity score: 1) zero point: negative (−); 2) one to four points: weak positive(+); 3) five to eight points: positive (++); 4) 9–12 points: strong positive (+++).

Statistical Analysis

Statistical computations were carried out with the SPSS 22.0 (SPSS Inc, Chicago, IL, USA). Histogram parameters (mean, standard deviation (SD), 50th, 75th, 90th, and 95th percentile) of K^{trans}, V_e and *VEGF* expression of $IDH1^{mut}$ gliomas were compared with the $IDH1^{wt}$ gliomas using the Mann–Whitney U test. Receiver operating characteristic (ROC) curve analysis was plotted to differentiate $IDH1^{mut}$ from $IDH1^{wt}$ gliomas. The Spearman test was performed to calculate correlation coefficients between histogram parameters of K^{trans}, V_e and VEGF expression in gliomas. $P < 0.05$ was considered statistically significant.

RESULTS

Differential Expression of *VEGF* in Gliomas With Different *IDH* Genotypes in CGGA Database

The CGGA database analysis showed the expression level of *VEGF* was lower in IDH^{mut} gliomas (**Figure 1**).

TABLE 1 | Pathology and *IDH1* genotypes of glioma samples.

Grades	Total	$IDH1^{mut}$	$IDH1^{wt}$
G2	14	12	2
G3	3	2	1
G4	39	3	36
Total	56	17	39

G2, glioma grade II; G3, glioma grade III; G4, glioma grade IV; IDH, isocitrate dehydrogenase; $IDH1^{mut}$, IDH1 mutant type; $IDH1^{wt}$, IDH1 wildtype.

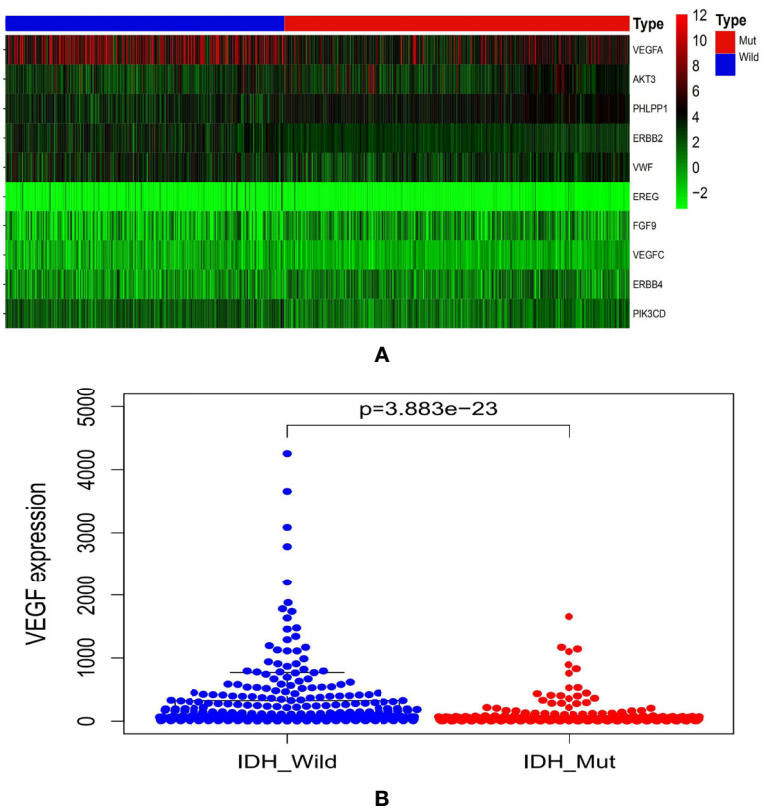

FIGURE 1 | Graphs showed the differential *VEGF* expression in gliomas with different *IDH* genotypes from CGGA database **(A, B)**. CGGA, Chinese Glioma Genome Atlas; *IDH*, isocitrate dehydrogenase; *VEGF*, vascular endothelial growth factor.

Glioma Samples' Demographics

A total of 56 patients were included. Immunohistochemistry revealed 17 patients with $IDH1^{mut}$ and 39 patients with $IDH1^{wt}$ gliomas (**Table 1**).

Comparisons of Histogram Parameters of K^{trans}, V_e and *VEGF* Expression Between $IDH1^{mut}$ and $IDH1^{wt}$ Gliomas

Comparisons demonstrated that the mean, SD, 50th, 75th, 90th, and 95th percentile of K^{trans}, V_e and *VEGF* expression were significantly lower in $IDH1^{mut}$ than $IDH1^{wt}$ gliomas ($P < 0.05$, respectively) (**Table 2** and **Figures 2**, **3**).

ROC Curve Analysis of Histogram Parameters of K^{trans} and V_e for Differentiating $IDH1^{mut}$ From $IDH1^{wt}$ Gliomas

ROC curve analysis revealed that 50th percentile of K^{trans} (0.019 min^{-1}) and V_e (0.039) provided the perfect combination of sensitivity (0.872, 0.846) and specificity (0.882, 0.824) in distinguishing $IDH1^{mut}$ with $IDH1^{w}t$ gliomas ($P < 0.05$, respectively). Area under the curve (AUC) for K^{trans} and V_e were 0.899 and 0.880 (**Table 3** and **Figure 4**).

TABLE 2 | Histogram parameters and *VEGF* expression in $IDH1^{mut}$ and $IDH1^{wt}$ glioma samples.

Parameter		$IDH1^{mut}$	$IDH1^{wt}$	*P*
$K^{trans}(min^{-1})$	Mean	0.024 ± 0.043	0.131 ± 0.144	<0.001
	SD	0.034 ± 0.052	0.154 ± 0.167	<0.001
	50th	0.013 ± 0.025	0.089 ± 0.103	<0.001
	75th	0.036 ± 0.065	0.174 ± 0.187	<0.001
	90th	0.065 ± 0.110	0.288 ± 0.297	<0.001
	95th	0.087 ± 0.143	0.393 ± 0.408	<0.001
V_e *(no units)*	Mean	0.077 ± 0.097	0.256 ± 0.185	<0.001
	SD	0.118 ± 0.101	0.212 ± 0.091	0.001
	50th	0.034 ± 0.050	0.175 ± 0.137	<0.001
	75th	0.096 ± 0.147	0.307 ± 0.194	<0.001
	90th	0.169 ± 0.224	0.451 ± 0.240	<0.001
	95th	0.225 ± 0.266	0.549 ± 0.251	<0.001
VEGF expression		1.290 ± 0.588	2.150 ± 0.670	<0.001

IDH, isocitrate dehydrogenase; $IDH1^{mut}$, IDH1 mutant type; $IDH1^{wt}$, IDH1 wildtype; K^{trans}, volume transfer constant; SD, standard deviation; V_e, volume of extravascular extracellular space per unit volume of tissue; VEGF, vascular endothelial growth factor. Data are presented as mean ± standard deviation.

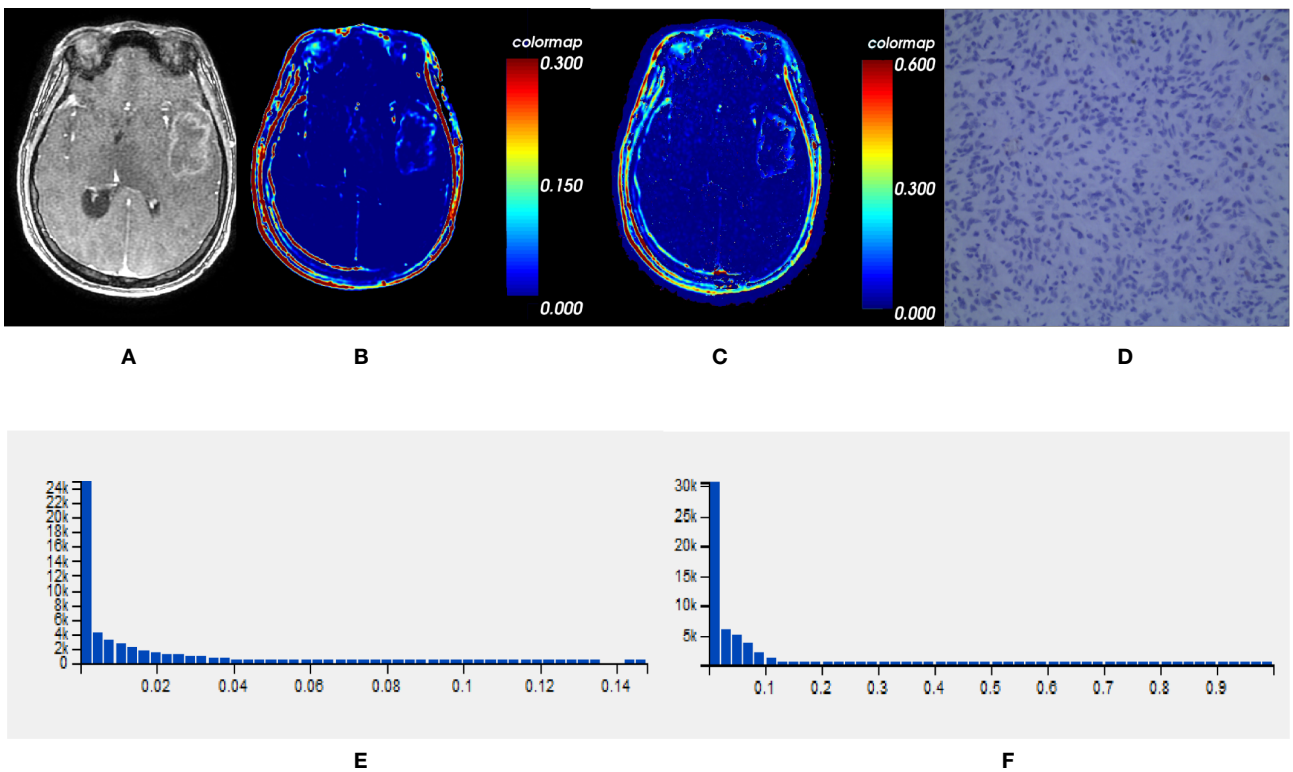

FIGURE 2 | One $IDH1^{mut}$ glioblastoma in left temporal lobe; **(A)** T1-weighted contrast map, **(B)** K^{trans} map, **(C)** V_e map, **(D)** *VEGF* sample from lesion area, **(E)** Histogram distribution of K^{trans}, **(F)** Histogram distribution of V_e. The signal intensities of K^{trans} and V_e in the lesion area were lower than those of the wildtype counterpart. In *VEGF* sample from lesion area, the staining cells and intensities were significantly fewer and lower than the wildtype counterpart. *IDH*, isocitrate dehydrogenase; $IDH1^{mut}$, *IDH1* mutant type; K^{trans}, volume transfer constant; V_e, volume of extravascular extracellular space per unit volume of tissue; *VEGF*, vascular endothelial growth factor.

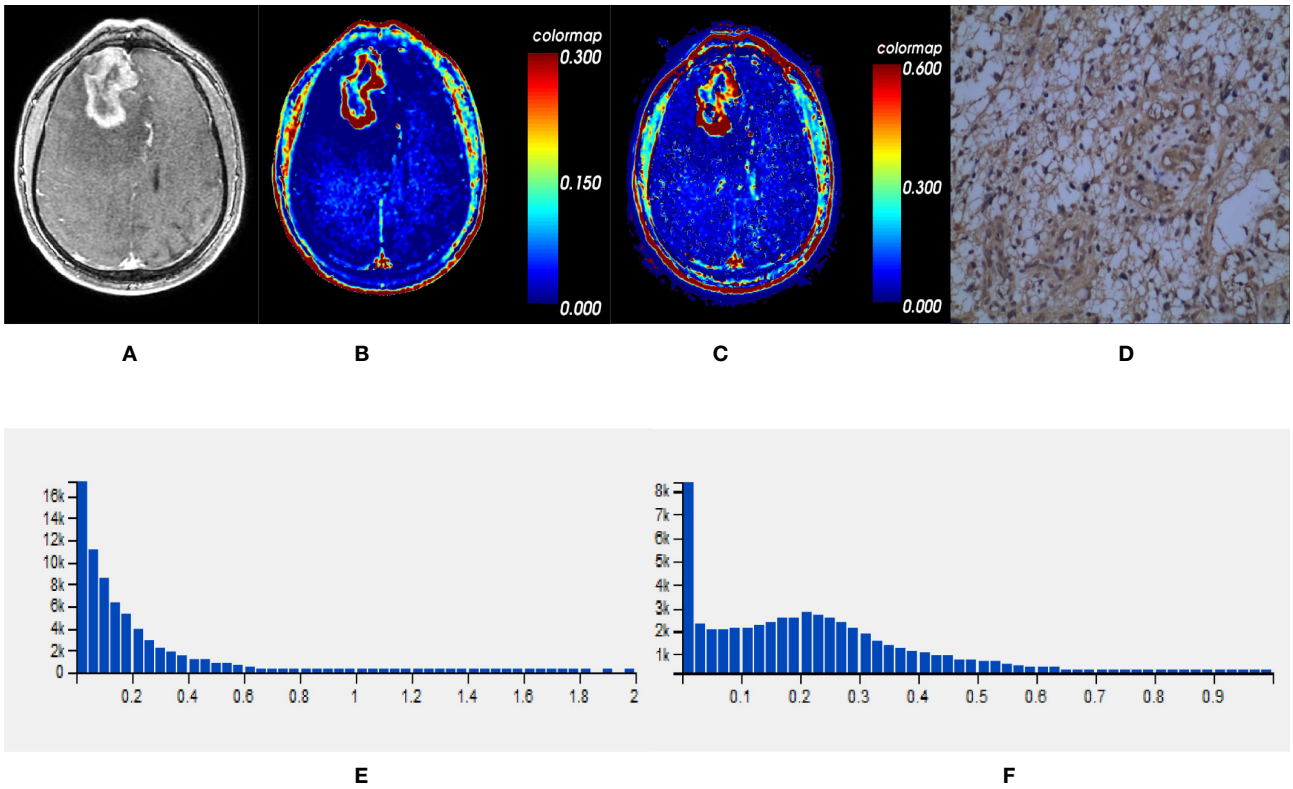

FIGURE 3 | One *IDH1*^{wt} glioblastoma in right frontal lobe; **(A)** T1-weighted contrast map, **(B)** K^{trans} map, **(C)** V_e map, **(D)** *VEGF* sample from lesion area, **(E)** Histogram distribution of K^{trans}, **(F)** Histogram distribution of V_e. The signal intensities of K^{trans} and V_e in the lesion area were higher than those of the mutant type counterpart. In *VEGF* sample from lesion area, the staining cells and intensities were significantly more and higher than those in the mutant type counterpart. *IDH*, isocitrate dehydrogenase; *IDH1*^{wt}, *IDH1* wildtype; K^{trans}, volume transfer constant; V_e, volume of extravascular extracellular space per unit volume of tissue; *VEGF*, vascular endothelial growth factor.

TABLE 3 | ROC curve analysis of histogram parameters for differentiating *IDH1*^{mut} from *IDH1*^{wt} glioma samples.

Parameter		Cut-off	Sensitivity	Specificity	AUC	*P*
K^{trans}(min^{-1})	Mean	0.035	0.872	0.824	0.882	<0.001
	SD	0.041	0.821	0.824	0.863	<0.001
	50th	0.019	0.872	0.882	0.899	<0.001
	75th	0.061	0.846	0.882	0.878	<0.001
	90th	0.076	0.872	0.824	0.862	<0.001
	95th	0.103	0.872	0.824	0.867	<0.001
V_e *(no units)*	Mean	0.095	0.897	0.765	0.858	<0.001
	SD	0.086	0.974	0.529	0.776	0.001
	50th	0.039	0.846	0.824	0.880	<0.001
	75th	0.152	0.795	0.882	0.863	<0.001
	90th	0.251	0.821	0.824	0.837	<0.001
	95th	0.242	0.923	0.706	0.833	<0.001

AUC, area under the curve; IDH, isocitrate dehydrogenase; IDH1^{mut}*, IDH1 mutant type; IDH1*^{wt}*, IDH1 wildtype;* K^{trans}*, volume transfer constant; ROC, receiver operating characteristic; SD, standard deviation;* V_e*, volume of extravascular extracellular space per unit volume of tissue.*

Correlations Between Histogram Parameters of K^{trans}, V_e and *VEGF* Expression in Gliomas

Irrespective of *IDH1* mutation, histogram parameters of K^{trans} and V_e were positively correlated with *VEGF* expression in gliomas ($P < 0.05$, respectively) (**Table 4**).

DISCUSSION

IDH mutation indicates a favorable clinical prognosis as compared to *IDH* without mutation in gliomas (12, 13). A previous study found that patients with *IDH1*^{wt} anaplastic astrocytomas even exhibited worse prognosis than those with *IDH1*^{mut} glioblastomas (14). Therefore, there are several differences between the two

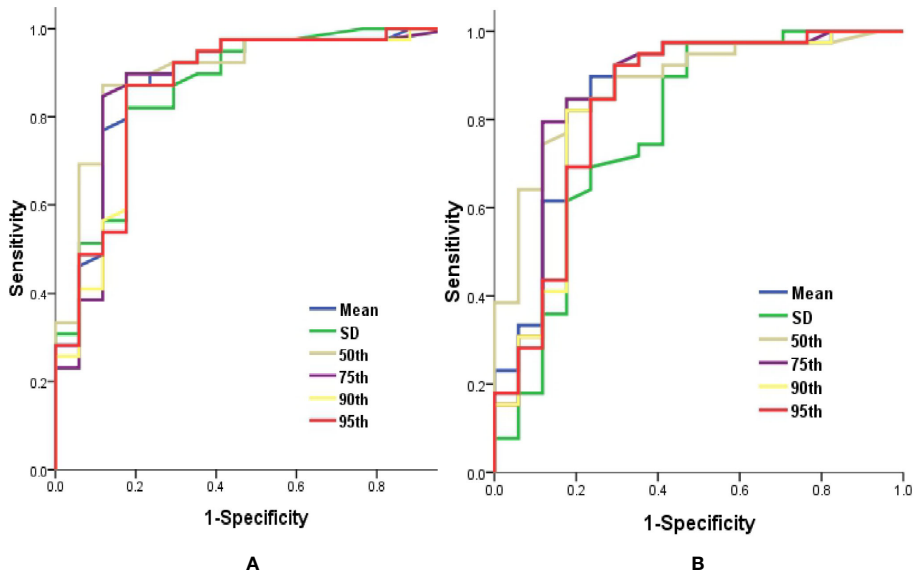

FIGURE 4 | Graphs showed ROC curves of histogram parameters of K^{trans} **(A)** and V_e **(B)** for differentiating the $IDH1^{mut}$ from $IDH1^{wt}$ gliomas. *IDH*, isocitrate dehydrogenase; $IDH1^{mut}$, *IDH1* mutant type; $IDH1^{wt}$, *IDH1* wildtype; K^{trans}, volume transfer constant; ROC, receiver operating characteristic; V_e, volume of extravascular extracellular space per unit volume of tissue.

TABLE 4 | The correlations between histogram parameters and *VEGF* expression in glioma samples.

Parameter		All gliomas		$IDH1^{mut}$ gliomas		$IDH1^{wt}$ gliomas	
		VEGF	*P*	*VEGF*	*P*	*VEGF*	*P*
$K^{trans}(min^{-1})$	Mean	r = 0.903	<0.001	r = 0.840	<0.001	r = 0.884	<0.001
	SD	r = 0.879	<0.001	r = 0.793	<0.001	r = 0.833	<0.001
	50th	r = 0.847	<0.001	r = 0.745	0.001	r = 0.813	<0.001
	75th	r = 0.893	<0.001	r = 0.834	<0.001	r = 0.878	<0.001
	90th	r = 0.909	<0.001	r = 0.840	<0.001	r = 0.898	<0.001
	95th	r = 0.911	<0.001	r = 0.847	<0.001	r = 0.898	<0.001
V_e *(no units)*	Mean	r = 0.874	<0.001	r = 0.800	<0.001	r = 0.844	<0.001
	SD	r = 0.821	<0.001	r = 0.789	<0.001	r = 0.776	<0.001
	50th	r = 0.794	<0.001	r = 0.701	0.002	r = 0.716	<0.001
	75th	r = 0.857	<0.001	r = 0.787	<0.001	r = 0.821	<0.001
	90th	r = 0.881	<0.001	r = 0.800	<0.001	r = 0.858	<0.001
	95th	r = 0.882	<0.001	r = 0.800	<0.001	r = 0.858	<0.001

IDH, isocitrate dehydrogenase; $IDH1^{mut}$, IDH1 mutant type; $IDH1^{wt}$, IDH1 wildtype; K^{trans}, volume transfer constant; SD, standard deviation; V_e, volume of extravascular extracellular space per unit volume of tissue; VEGF, vascular endothelial growth factor.

genotypes of glioma. Analysis of CGGA database and clinical practice in our hospital indicated that *VEGF* expression was significantly lower in $IDH1^{mut}$ as compared to the wildtype counterpart. Some studies demonstrated that the expression of *VEGF* was inhibited in the IDH^{mut} gliomas (15, 16). These findings supported our results indirectly.

In recent years, several MRI techniques provide insight into exploring the link between glioma *IDH* mutation and microvascular characteristics. Conventional MRI showed the frequency and degree of enhancing were lower in gliomas with *IDH* mutation (17, 18). Moreover, radiomics served as predictive markers in assessing the *IDH* mutation in gliomas (19, 20). Dynamic susceptibility contrast-enhanced magnetic resonance imaging (DSC-MRI) and arterial spin labeling (ASL) revealed that blood flow or blood volume was significantly lower in IDH^{mut} than IDH^{wt} gliomas (3, 21–23). The current results implied a discriminant function for differentiating between $IDH1^{mut}$ and $IDH1^{wt}$ gliomas was constructed using DCE-MRI. Hilario et al. and Zhang et al. found that K^{trans} was lower in gliomas with *IDH* mutation, which corroborates our results (24, 25).

Hitherto, there is no study focusing on the combined estimation of glioma *IDH1* mutation and *VEGF* expression with histogram analysis of DCE-MRI. In our study, we found that the signal intensities of lesions on K^{trans} and V_e maps were lower in $IDH1^{mut}$ than $IDH1^{wt}$ gliomas. Simultaneously, the

values of K^{trans} and V_e were significantly higher in $IDH1^{wt}$ than $IDH1^{mut}$ gliomas. Our study also demonstrated that K^{trans} and V_e were correlated with *VEGF* expression in gliomas. The conclusions clarifying K^{trans} was correlated with *VEGF* expression in gliomas were consistent with our findings (26, 27). Pang et al. published that cerebral blood flow (CBF) derived from ASL also positively correlated significantly with *VEGF* expression in gliomas (28). Although both DCE-MRI and ASL can quantitatively assess tumor perfusion, they might be not completely comparable. The ASL primarily represents the degree of microvascular capacity, while microvascular immaturity and permeability are reflected by DCE-MRI. The pivotal features of *VEGF* are to enhance microvessel leakage and stimulate mitosis of endothelial cells to develop immature vascular infrastructure for supporting tumor cells (29, 30). However, the studies conducted by Awasthi et al. and Haris et al. did not demonstrate the positive correlation between K^{trans} and *VEGF* expression in gliomas (31, 32). One reason might be that glioma samples were not exactly same. More glioblastomas were recruited in our study. The other might be that the methods used were different. The studies mentioned above chose partial areas of solid tumor as ROI, while entire tumor parenchyma was included in our study. More importantly, histogram analysis can assess the heterogeneity of tumors and improve the accuracy of diagnosis.

However, we have recognized a few limitations in the current study. First, the small sample size of glioma specimens restricts the accuracy of statistical analysis, and more samples are needed to verify the results in the future. Second, the *IDH2* mutation has not been considered due to the lack of genomic sequence analysis in our hospital. Owing to the low frequency of *IDH2* mutation in gliomas, the immunohistochemistry technique for detecting *IDH1* mutation could represent the maximum number of *IDH* mutation in gliomas (33). Nonetheless, gene sequencing should substantiate these results in following studies.

CONCLUSIONS

VEGF expression is significantly lower in $IDH1^{mut}$ gliomas as compared to that in the wildtype counterpart, and it is non-invasively predictable with histogram analysis of DCE-MRI.

DATA AVAILABILITY STATEMENT

The raw data supporting the conclusions of this article will be made available by the authors without undue reservation.

ETHICS STATEMENT

The studies involving human participants were reviewed and approved by the Ethics Committee of Affiliated Hospital of Nantong University. The patients/participants provided their written informed consent to participate in this study. Written informed consent was obtained from the individual(s) for the publication of any potentially identifiable images or data included in this article.

AUTHOR CONTRIBUTIONS

YH conceived and wrote the paper. YC processed the imaging. JW and JK analyzed the study data. DS and ZJ supervised and leaded the study. All authors contributed to the article and approved the submitted version.

FUNDING

This work is supported by the China Postdoctoral Science Foundation (2014M551641) and Jiangsu Commission of Health (H2019089).

REFERENCES

1. Louis DN, Perry A, Reifenberger G, von Deimling A, Figarella-Branger D, Cavenee WK, et al. The 2016 World Health Organization Classification of Tumors of the Central Nervous System: a summary. *Acta Neuropathol* (2016) 131:803–20. doi: 10.1007/s00401-016-1545-1
2. Koivunen P, Lee S, Duncan CG, Lopez G, Lu G, Ramkissoon S, et al. Transformation by the (R)-enantiomer of 2-hydroxyglutarate linked to EGLN activation. *Nature* (2012) 483:484–8. doi: 10.1038/nature10898
3. Kickingereder P, Sahm F, Radbruch A, Wick W, Heiland S, Deimling AV, et al. IDH mutation status is associated with a distinct hypoxia/angiogenesis transcriptome signature which is non-invasively predictable with rCBV imaging in human glioma. *Sci Rep* (2015) 5:16238. doi: 10.1038/srep16238
4. Birner P, Pusch S, Christov C, Mihaylova S, Toumangelova-Uzeir K, Natchev S, et al. Mutant IDH1 inhibits PI3K/Akt signaling in human glioma. *Cancer* (2014) 120:2440–7. doi: 10.1002/cncr.28732
5. Yuan X, Liu D, Wang Y, Li X. Significance of nuclear magnetic resonance combined with Ki-67 and VEGF detection in the diagnosis and prognosis evaluation of brain glioma. *J BUON* (2018) 23:410–5.
6. Rainer E, Wang H, Traub-Weidinger T, Widhalm G, Fueger B, Chang J, et al. The prognostic value of [^{123}I]-vascular endothelial growth factor ([^{123}I]-VEGF) in glioma. *Eur J Nucl Med Mol Imaging* (2018) 45:2396–403. doi: 10.1007/s00259-018-4088-y
7. Friedman HS, Prados MD, Wen PY, Mikkelsen T, Schiff D, Abrey LE, et al. Bevacizumab alone and in combination with irinotecan in recurrent glioblastoma. *J Clin Oncol* (2009) 27:4733–40. doi: 10.1200/JCO.2008.19.8721
8. Kreisl TN, Kim L, Moore K, Duic P, Royce C, Stroud I, et al. Phase II trial of single-agent bevacizumab followed by bevacizumab plus irinotecan at tumor progression in recurrent glioblastoma. *J Clin Oncol* (2009) 27:740–5. doi: 10.1200/JCO.2008.16.3055
9. Jia ZZ, Gu HM, Zhou XJ, Shi JL, Li MD, Zhou GF, et al. The assessment of immature microvascular density in brain gliomas with dynamic contrast-enhanced magnetic resonance imaging. *Eur J Radiol* (2015) 84:1805–9. doi: 10.1016/j.ejrad.2015.05.035
10. Jensen RL, Mumert ML, Gillespie DL, Kinney AY, Schabel MC, Salzman KL. Preoperative dynamic contrast-enhanced MRI correlates with molecular markers of hypoxia and vascularity in specific areas of intratumoral microenvironment and is predictive of patient outcome. *Neuro Oncol* (2014) 16:280–91. doi: 10.1093/neuonc/not148
11. Takano S, Tian W, Matsuda M, Yamamoto T, Ishikawa E, Kaneko MK, et al. Detection of IDH1 mutation in human gliomas: comparison of immunohistochemistry and sequencing. *Brain Tumor Pathol* (2011) 28:115–23. doi: 10.1007/s10014-011-0023-7
12. Myung JK, Cho HJ, Park CK, Kim SK, Phi JH, Park SH. IDH1 mutation of gliomas with long-term survival analysis. *Oncol Rep* (2012) 28:1639–44. doi: 10.3892/or.2012.1994

13. Houillier C, Wang X, Kaloshi G, Mokhtari K, Guillevin R, Laffaire J, et al. IDH1 or IDH2 mutations predict longer survival and response to temozolomide in low-grade gliomas. *Neurology* (2010) 75:1560–6. doi: 10.1212/WNL.0b013e3181f96282
14. Hartmann C, Hentschel B, Wick W, Capper D, Felsberg J, Simon M, et al. Patients with IDH1 wild type anaplastic astrocytomas exhibit worse prognosis than IDH1-mutated glioblastomas, and IDH1 mutation status accounts for the unfavorable prognostic effect of higher age: implications for classification of gliomas. *Acta Neuropathol* (2010) 120:707–18. doi: 10.1007/s00401-010-0781-z
15. Sun C, Zhao Y, Shi J, Zhang J, Yuan Y, Gu Y, et al. Isocitrate dehydrogenase1 mutation reduces the pericyte coverage of microvessels in astrocytic tumours. *J Neurooncol* (2019) 143:187–96. doi: 10.1007/s11060-019-03156-5
16. Polívka J, Pešta M, Pitule P, Hes O, Holubec L, Polívka J, et al. IDH1 mutation is associated with lower expression of VEGF but not microvessel formation in glioblastoma multiforme. *Oncotarget* (2018) 9:16462–76. doi: 10.18632/oncotarget.24536
17. Qi S, Yu L, Li H, Ou Y, Qiu X, Ding Y, et al. Isocitrate dehydrogenase mutation is associated with tumor location and magnetic resonance imaging characteristics in astrocytic neoplasms. *Oncol Lett* (2014) 7:1895–902. doi: 10.3892/ol.2014.2013
18. Ding H, Huang Y, Li Z, Li S, Chen Q, Xie C, et al. Prediction of IDH Status Through MRI Features and Enlightened Reflection on the Delineation of Target Volume in Low-Grade Gliomas. *Technol Cancer Res Treat* (2019) 18:1533033819877167. doi: 10.1177/1533033819877167
19. Kim M, Jung SY, Park JE, Jo Y, Park SY, Nam SJ, et al. Diffusion- and perfusion-weighted MRI radiomics model may predict isocitrate dehydrogenase (IDH) mutation and tumor aggressiveness in diffuse lower grade glioma. *Eur Radiol* (2020) 30:2142–51. doi: 10.1007/s00330-019-06548-3
20. Tan Y, Zhang ST, Wei JW, Dong D, Wang XC, Yang GQ, et al. A radiomics nomogram may improve the prediction of IDH genotype for astrocytoma before surgery. *Eur Radiol* (2019) 29:3325–37. doi: 10.1007/s00330-019-06056-4
21. Xing Z, Zhang H, She D, Lin Y, Zhou X, Zeng Z, et al. IDH genotypes differentiation in glioblastomas using DWI and DSC-PWI in the enhancing and peri-enhancing region. *Acta Radiol* (2019) 60:1663–72. doi: 10.1177/0284185119842288
22. Xing Z, Yang X, She D, Lin Y, Zhang Y, Cao D. Noninvasive Assessment of IDH Mutational Status in World Health Organization Grade II and III Astrocytomas Using DWI and DSC-PWI Combined with Conventional MR Imaging. *AJNR Am J Neuroradiol* (2017) 38:1138–44. doi: 10.3174/ajnr.A5171
23. Brendle C, Hempel JM, Schittenhelm J, Skardelly M, Tabatabai G, Bender B, et al. Glioma Grading and Determination of IDH Mutation Status and ATRX loss by DCE and ASL Perfusion. *Clin Neuroradiol* (2018) 28:421–8. doi: 10.1007/s00062-017-0590-z
24. Hilario A, Hernandez-Lain A, Sepulveda JM, Lagares A, Perez-Nuñez A, Ramos A. Perfusion MRI grading diffuse gliomas: Impact of permeability parameters on molecular biomarkers and survival. *Neurocirugia (Astur)* (2019) 30:11–8. doi: 10.1016/j.neucir.2018.06.004
25. Zhang HW, Lyu GW, He WJ, Lei Y, Lin F, Wang MZ, et al. DSC and DCE Histogram Analyses of Glioma Biomarkers, Including IDH, MGMT, and TERT, on Differentiation and Survival. *Acad Radiol* (2020) S1076–6332(19):30624–5. doi: 10.1016/j.acra.2019.12.010
26. Di N, Cheng W, Jiang X, Liu X, Zhou J, Xie Q, et al. Can dynamic contrast-enhanced MRI evaluate VEGF expression in brain glioma? An MRI-guided stereotactic biopsy study. *J Neuroradiol* (2019) 46:186–92. doi: 10.1016/j.neurad.2018.04.008
27. Di N, Yao C, Cheng W, Ren Y, Qu J, Wang B, et al. Correlation of dynamic contrast-enhanced MRI derived volume transfer constant with histological angiogenic markers in high-grade gliomas. *J Med Imaging Radiat Oncol* (2018) 62:1954–6. doi: 10.1111/1754-9485.12701
28. Pang H, Dang X, Ren Y, Zhuang D, Qiu T, Chen H, et al. 3D-ASL Perfusion Correlates With VEGF Expression and Overall Survival in Glioma Patients: Comparison of Quantitative Perfusion and Pathology on Accurate Spatial Location-Matched Basis. *J Magn Reson Imaging* (2019) 50:209–20. doi: 10.1002/jmri.26562
29. Ferrara N, Adamis AP. Ten years of anti-vascular endothelial growth factor therapy. *Nat Rev Drug Discov* (2016) 15:385–403. doi: 10.1038/nrd.2015.17
30. Carmeliet P, Jain RK. Angiogenesis in cancer and other diseases. *Nature* (2016) 407:249–57. doi: 10.1038/35025220
31. Awasthi R, Rathore RK, Soni P, Sahoo P, Awasthi A, Husain N, et al. Discriminant analysis to classify glioma grading using dynamic contrast-enhanced MRI and immunohistochemical markers. *Neuroradiology* (2012) 54:205–13. doi: 10.1007/s00234-011-0874-y
32. Haris M, Husain N, Singh A, Husain M, Srivastava S, Srivastava C, et al. Dynamic contrast-enhanced derived cerebral blood volume correlates better with leak correction than with no correction for vascular endothelial growth factor, microvascular density, and grading of astrocytoma. *J Comput Assist Tomogr* (2012) 32:955–65. doi: 10.1097/RCT.0b013e31816200d1
33. Hartmann C, Meyer J, Balss J, Capper D, Mueller W, Christians A, et al. Type and frequency of IDH1 and IDH2 mutations are related to astrocytic and oligodendroglial differentiation and age: a study of 1,010 diffuse gliomas. *Acta Neuropathol* (2009) 118:469–74. doi: 10.1007/s00401-009-0561-9

Conflict of Interest: The authors declare that the research was conducted in the absence of any commercial or financial relationships that could be construed as a potential conflict of interest.

frontiers in Oncology

ORIGINAL RESEARCH
published: 23 February 2021
doi: 10.3389/fonc.2020.625474

Scale-Free Analysis of Intraoperative ECoG During Awake Craniotomy for Glioma

Diana Cristina Ghinda[1,2,3†], Ben Lambert[4†], Junfeng Lu[2], Ning Jiang[4], Eve Tsai[1], Adam Sachs[1], Jin-Song Wu[2] and Georg Northoff[3*]*

[1] Department of Neurosurgery, The Ottawa Hospital, University of Ottawa, Ottawa Hospital Research Institute, Ottawa, ON, Canada, [2] Glioma Surgery Division, Department of Neurosurgery, Huashan Hospital, Shanghai Medical College, Fudan University, Shanghai, China, [3] Mind, Brain Imaging and Neuroethics, Institute of Mental Health Research, University of Ottawa, Ottawa, ON, Canada, [4] Faculty of Engineering, Department of Systems Design Engineering, University of Waterloo, Waterloo, ON, Canada

OPEN ACCESS

Edited by:
Yanmei Tie,
Brigham and Women's Hospital and Harvard Medical School, United States

Reviewed by:
Jiang Tao,
Capital Medical University, China
Adomas Bunevicius,
University of Virginia, United States

***Correspondence:**
Georg Northoff
georg.northoff@theroyal.ca
Jin-Song Wu
wjsongc@126.com

[†]These authors share first authorship

Specialty section:
This article was submitted to Cancer Imaging and Image-directed Interventions, a section of the journal Frontiers in Oncology

Received: *03 November 2020*
Accepted: *31 December 2020*
Published: *23 February 2021*

Citation:
Ghinda DC, Lambert B, Lu J, Jiang N, Tsai E, Sachs A, Wu J-S and Northoff G (2021) Scale-Free Analysis of Intraoperative ECoG During Awake Craniotomy for Glioma. Front. Oncol. 10:625474. doi: 10.3389/fonc.2020.625474

Background: Electrocorticography (ECoG) has been utilized in many epilepsy cases however, the use of this technique for evaluating electrophysiological changes within tumoral zones is spare. Nonetheless, epileptic activities seem to arise from the neocortex surrounding the gliomas suggesting a link between epileptogenesis and glioma cell infiltration in the peritumoral area. The purpose of this study was to implement novel scale-free measures to assess how cortical physiology is altered by the presence of an invasive brain tumor.

Methods: Twelve patients undergoing an awake craniotomy for resection of a supratentorial glioma were included. ECoG data over the main tumor and the exposed surroundings was acquired intra-operatively just prior to tumor resection. Six of the patients presented with seizures and had data acquired both in the awake and anesthetic state. The corresponding anatomical location of each electrode in relation to the macroscopically-detectable tumor was recorded using the neuronavigation system based on structural anatomical images obtained pre-operatively. The electrodes were classified into tumoral, healthy or peritumoral based on the macroscopically detectable tumoral tissue from the pre-operative structural MRI.

Results: The electrodes overlying the tumoral tissue revealed higher power law exponent (PLE) values across tumoral area compared to the surrounding tissues. The difference between the awake and anesthetic states was significant in the tumoral and healthy tissue ($p < 0.05$) but not in the peritumoral tissue. The absence of a significant PLE reduction in the peritumoral tissue from the anesthetic to the awake state could be considered as an index of the presence or absence of infiltration of tumor cells into the peritumoral tissue.

Conclusions: The current study portrays for the first time distinct power law exponent features in the tumoral tissue, which could provide a potential novel electrophysiological marker in the future. The distinct features seen in the peritumoral tissue of gliomas seem to indicate the area where both the onset of epileptiform activity and the tumor infiltration take place.

Keywords: glioma, electrocorticography, brain tumor, awake craniotomy, glioma-related epilepsy, scale-free measures

INTRODUCTION

Although the main presenting symptom of low-grade gliomas are seizures, the pathophysiological mechanisms and related structural-functional abnormalities underlying the epileptogenesis in patients with these tumors remain unclear (1–3).

The recording of electrical changes in the brain by electrodes placed directly on the cerebral cortex, electrocorticography (ECoG), has previously been used for delineation of tumors when the non-invasive imaging techniques were not yet available. Similarly, the electroencephalogram (EEG) had localizing value in cases of brain tumor and epilepsy and the occurrence of delta waves was thought to be a better guide than areas of electrical silence (4). Subcortical tumors have also been localized by the presence of slow wave activity over the tumor while the epileptogenic focus could be determined by focal spontaneous spiking, induction of seizures by electrical stimulation and occurrence of long-lasting after-discharges (5). The use of ECoG for cerebral tumors revealed distinct changes in the setting of infiltrative tumors (6), for instance slow delta-waves were found in the surrounding edema (7). The origin of these slow waves was assumed to be related to intracranial hypertension however, another study analyzing the morphological and pathophysiological features of the peritumoral area concluded that those changes result from direct influence of the tumor on brain parenchyma, rather than from peritumoral edema or intracranial hypertension (8). As such, historically, ECoG was not only of scientific interest but was also of great practical value for neurosurgery.

Besides delineating the eloquent areas that need to be preserved during the surgical resection, ECoG use for assessment of electrophysiological changes occurring in the setting of glioma is currently a relatively non-explored domain. It is postulated that the peritumoral neocortex around gliomas represents a pivotal structure both for the genesis of glioma related epilepsy (GRE) and for infiltration by glioma cells, which has significant implications in terms of the treatment recommended to the patients and their oncological prognosis (3, 9–12). In a systematic review performed on this subject, using medical subject headings and text words related to ECoG, epilepsy and gliomas in MEDLINE (OVID interface, 1946 onward), EMBASE (OVID interface, 1947 onward), and the Cochrane Central Register of Controlled Trials, we found only nine articles using EEG or ECoG for assessment of glioma-related electrophysiological changes (**Figure 1**). In this paper, we

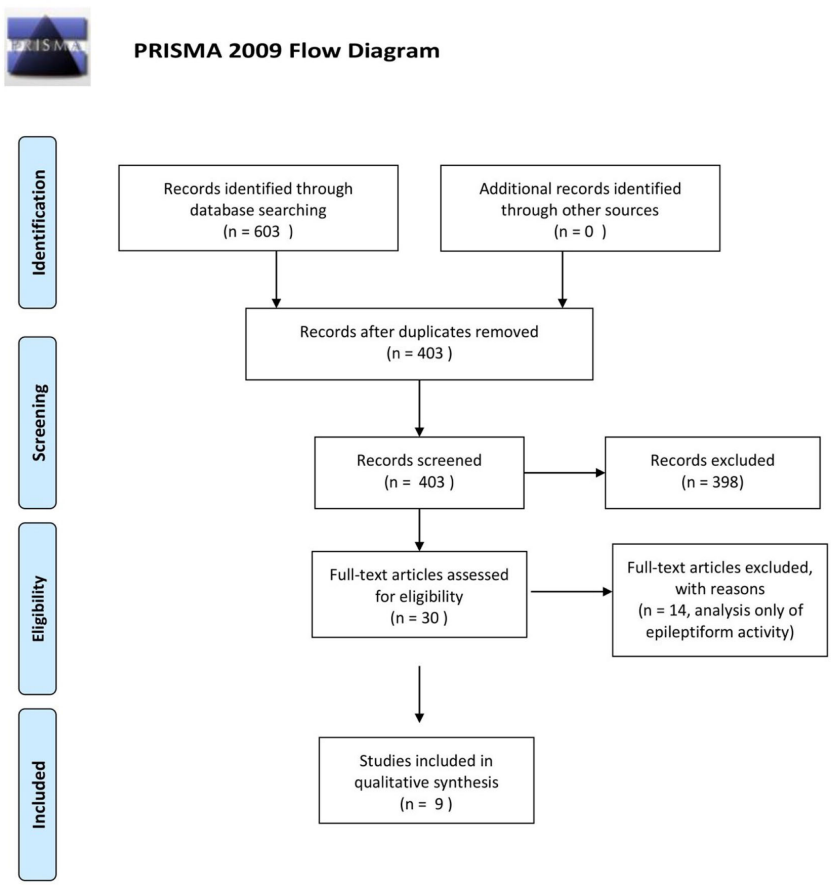

FIGURE 1 | PRISMA flow diagram.

outline a novel *in vivo* electrophysiological investigation of tumoral tissue in patients undergoing awake craniotomy for tumor resection. Subsequently, we discuss our findings in the context of the available literature.

METHODS

Subjects and Recordings

Twelve patients with a newly diagnosed intracranial glioma, out of which six presenting with multiple seizures, were enrolled after providing informed consent. Patients were eligible for inclusion if they were aged ≥18 years, presented with a supratentorial lesion suggestive of a glioma, and had an indication for surgery as confirmed by an experienced neurosurgery team (J-S.W., J.L.). Of the patients sequentially admitted for treatment, we excluded patients not eligible for awake surgery, patients with other brain pathologies and those who had undergone previous cranial irradiation or chemotherapy and/or for whom electrophysiological recordings could not be obtained.

The patients' demographics including the presenting symptoms are presented in **Table 1**. All patients underwent awake craniotomy for tumor resection. A monitored anesthesia care approach was adopted for all patients as per previous publications (13). After the anesthesiologists administered premedication by infusing midazolam (0.02–0.03 mg/kg) and 5 mg of tropisetron, intravenous lines, a central venous catheter, an arterial line, and a urethral catheter were inserted. The supraorbital, supratrochlear, zygomaticotemporal, auriculotemporal, greater occipital, and lesser occipital nerves were blocked bilaterally using a mixture of lidocaine (0.67%) and ropivacaine (0.5%). Once the patient was brought into moderate sedation with boluses of intravenous propofol, the head was fixed into its fitted position using a custom-designed high-field MRI-safe head holder (DORO Radiolucent Headrest System, Pro Med Instruments GmbH, Freiburg, Germany), which was integrated with an intraoperative MR imaging system (IMRIS^{TM}). Once the scalp was prepared and draped, remifentanil (0.01–0.03 lg/kg/min) or dexmedetomidine (0.1–0.7 lg/kg/h) were administered for analgesia. To minimize brain swelling, mannitol (1 g/kg) was infused intravenously before the dura opening. Because of the minimal draping used, no laryngeal mask airway or endotracheal tubing was applied.

The ECoG grid was placed over the exposed brain surface as indicated by the needs of the patient. ECoG signals were recorded with a 20, 32 or 48-channel grid of 4.0 mm diameter electrodes with 2.3mm exposure (Ad-tech, Germany) connected to a BP amplifier (Brain Product, Germany). The reference electrode was placed on the contralateral earlobe to avoid any potential increase in coherence due to the reference electrode location.

5 min of recording in the awake state were acquired prior to the tumor resection. For the six patients presenting with seizures, the ECoG signal was also acquired in the anesthetic state. The signals were sampled at 1,000 Hz with a hardware filter between 0.01 and 1,000 Hz. The ECoG electrodes for each patient were classified in TT (tumoral tissue), HT (macroscopically healthy-tissue) and PT (peritumoral tissue) according to the radiological defined boundaries as per the conventional structural MRI.

ECoG Localization Method *via* Intra-Operative Photography

An intra-operative picture was taken after the electrode grid was placed over the exposed brain. Intra-operative location of each electrode were recorded with the neuro-navigation system (Medtronic, Inc., Minneapolis, MN, USA). Image guided localization of the electrode location were performed as soon as possible after the craniotomy was completed in order to minimize potential brain shift. The electrode location was recorded using the intra-operative Medtronic neuronavigation system (**Figure 2**). The accuracy of the neuronavigation approach used is well established and represents the standard method for image-guided resection of brain tumors (14, 15). The electrodes were classified as overlying the tumoral, peritumoral or macroscopically healthy tissue. This was performed for each patient according to the radiological defined boundaries as per the conventional structural MRI: FLAIR for non-enhancing diffuse low-grade gliomas and the T1 MPRAGE with contrast for contrast enhancing tumors (16) (**Figures 2** and **S2**). The peritumoral tissue was defined as an area within a two cm margin from tumor borders according to the RANO criteria (16). All MR brain images were acquired one or two days preoperatively in the diagnostic room of an iMRI-integrated neurosurgical suite using

TABLE 1 | Patient's demographics and clinical data.

Patient #	Age, gender	AED prior to admission	Tumor Location	WHO Grade	IDH 1 status	Presenting Symptoms
1	50, F	None	Frontal	III	Wild-type	Focal aware seizure, non-motor onset-sensory
2	40, M	Oxycarbazepine	Frontal & insular	III	Wild-type	Focal aware seizure, motor onset-epileptic spasm
3	39, M	VPA	Temporal & insular	IV	Wild-type	Focal aware seizure, non-motor onset-autonomic
4	34, M	VPA	Fronto-temporal	II	Mutant	Generalized seizure, motor – tonic-clonic
5	29, F	VPA	Parietal	II	Mutant	Generalized seizure, motor – tonic-clonic
6	35, F	None	Frontal	II	Mutant	Generalized seizure, motor – tonic-clonic
7	52, F	None	Frontal	IV	Wild-type	Contralateral weakness
8	49, F	None	Frontal	II	Mutant	Incidental
9	42, M	None	Frontal	II	Mutant	Incidental
10	48, M	None	Frontal	II	Mutant	Contralateral sensory changes
11	33, F	None	Frontal	II	Mutant	Headaches
12	41, F	None	Frontal & parietal	II	Mutant	Headaches

AED, anti-epileptic drugs; IDH, Isocitrate Dehydrogenase; WHO, World Health Organisation; VPA, Valproic Acid.

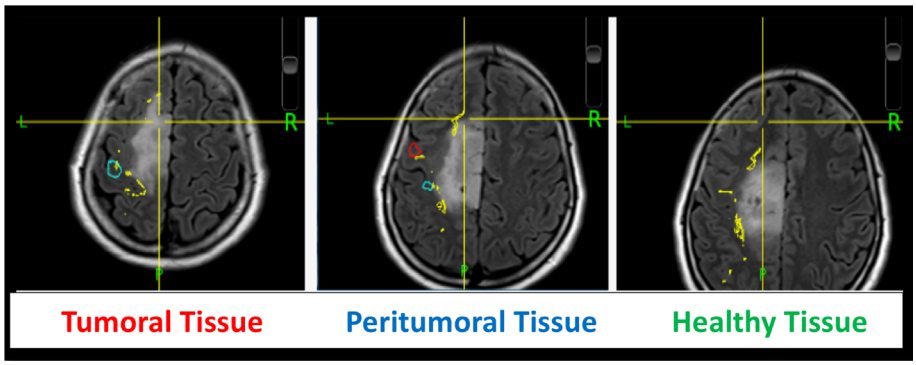

FIGURE 2 | ECoG localization method *via* intra-operative neuronavigation.

a 3T Siemens MRI scanner (Siemens MAGNETOM Verio 3.0 T, Germany) with a standard 32-channel head coil. The cortical surface was segmented from the pre-operative MRI using the Analysis of Functional NeuroImages software (http://afni.nimh.nih.gov/afni). Intra-operative photograph was superposed on the segmented cortical surface in order to confirm the electrode location in respect to the tumor with the help of visible sulcal patterns on the cortical surface obtained from the pre-op MRI (**Figure 3**). A total of 351 ECoG channels from 12 subjects were recorded for this study. The total channels per tissue type were as follows: 112 macroscopically healthy, 106 peritumoral, and 133 tumoral electrodes.

ECoG Signal Analysis

ECoG signals were manually inspected for quality using EEGLAB for full-length data visualization. Data for electrodes, or channels, were deemed to be of untrustworthy quality if obvious artifacts were present in at least ¼ of the full length of channel data. The entire set of data for these bad channels was removed from further analysis. We calculated the power law exponent (PLE) using an in-house MATLAB script as per previous publications (17–21) using an uninterrupted 5 minutes resting-state signal. Coarse-graining spectral analysis (CGSA) (22) was applied to the uninterrupted 5 min resting-state data to separate harmonic activity from the non-harmonic or scale-free activity of interest. The power spectral density of the uninterrupted 5 min resting-state data was then calculated using Welch's averaged, modified periodogram method of spectral estimation (23) with 50% windowed segment overlap, eight window segments, and a Hamming window type. Subsequently, power spectrums of each channel were then averaged for each tissue type and this averaged spectrum was log-log transformed according to previous studies (19, 24, 25). A notch filter was applied in software to the 45–55 Hz band to eliminate mains electricity noise, and for PLE-fitting continuity a linear interpolation replaced the spectrum across this bandwidth. MATLAB's fit function was then used to fit a linear polynomial curve to the log-log spectrum, and the slope of this line was extracted as the PLE value. One PLE value was extracted for each tissue type, i.e., tumoral, peritumoral and respectively tumoral, and all PLEs were compared using a paired T-test. A p value < 0.05 was considered statistically significant.

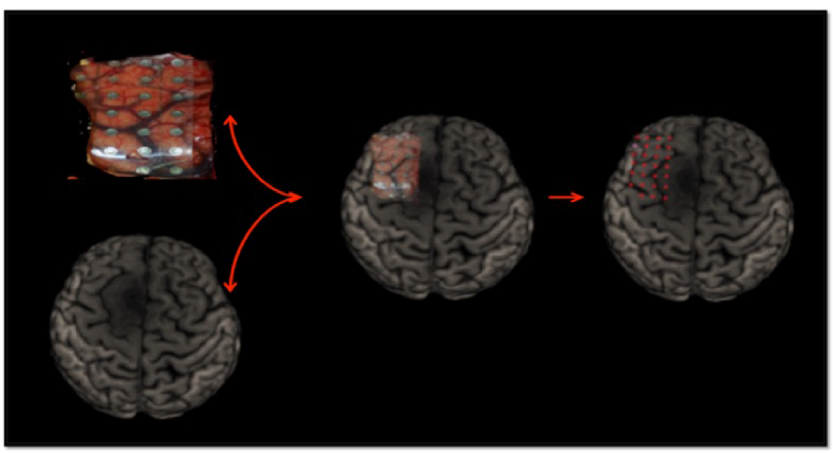

FIGURE 3 | ECoG localization method *via* intra-operative photograph merged with the cortical surface segmented from the pre-operative MRI.

RESULTS

When assessing scale-free measures, we noticed that the electrodes over the tumoral tissue were found to have a higher PLE value than the electrodes over the macroscopically healthy tissue for the twelve patients (**Figure 4**). Furthermore, the peritumoral tissue displayed significantly higher values than the macroscopically normal tissue ($p = 0.02$), which we hypothesized is due to the different nature of that tissue. The difference between PT and TT did not reach statistical significance ($p = 0.10$). The higher PLE values observed in the peritumoral tissue was in concordance with the observed lack of reaction to anesthesia in the peritumoral tissue (**Figure 5**), which we hypothesized that it is related to a different tissue type which maintains the already high PLE values. This can entail that the peritumoral tissue displays a higher level of entropy than the surrounding tissue. When comparing the PLE results according to the presenting symptoms (respectively with or without seizures) or according to previous antiepileptic drug use, no significant differences were observed (**Figures S3–S5**).

For the six patients presenting with multiple seizures for which ECoG recordings were obtained in the two anesthetic states (i.e., awake and anesthesia), we observed that the electrodes overlying the peritumoral tissue displayed smaller changes between the anesthesia and awake state than the changes observed across the adjacent tissues, respectively over the TT and macroscopically HT (**Figure 5**). Furthermore, we observed distinct features of the PT's power spectrum when comparing with the power spectrum of the HT and TT as showed in the individual results (**Figure 6**). For instance, patient #1 displayed a higher power spectrum of the peritumoral tissue in the lower frequencies in respect to the healthy and tumoral tissue. Nonetheless, the peritumoral tissue shows the opposite pattern in the higher frequencies of the power spectrum; the patient had a WHO Grade III tumor. Patients #2 and #3 showed a different pattern where the power spectrum of the peritumoral tissue was similar to that of the tumoral tissue; those patients had a grade III and, respectively, grade IV tumor. The three patients with a WHO grade II tumor showed an intermediate PT power spectrum (patient #5) and respectively a higher peritumoral power spectrum than the other tissues (patient # 4 and # 6). The same power spectrum pattern remained in the anesthetic state. Further genetic analysis would be required to assess whether there is any correlation between the tissue infiltration and the different electrophysiological features.

In addition, given that the glial tumor can displace otherwise healthy non-glioma neural tissue and that this mass effect can cause electrophysiological changes in the intraoperative ECoG, we performed a subgroup analysis according to the presence of mass effect. Two subjects included in this study presented with intracranial mass effect, as identified on the preoperative MRI. The PLE of these subjects (sample size = 61, $\mu = 3.218$, $\sigma^2 = 0.179$) was not found to be different from the PLE of the subjects presenting without a mass effect (sample size = 290, $\mu = 3.306$, $\sigma^2 = 0.486$, $P = 0.231$). Based on these results, the intracranial mass effect was not considered to influence the PLE in this study. It should be noted however, that only two subjects presented with glioma-related mass effect. Also, given the limited time available for intra-operative recordings during the awake procedures, we, unfortunately, could not perform post-resection ECoG recordings.

Furthermore, the distance between tumor and the brain surface is also important and to further explore this factor we looked at the influence of the cortical/subcortical tumor location. To study the effect that glioma's proximity to the cortex has on the PLE results, we compared the PLE of patients with gliomas predominantly involving the cortical surface with the PLE of patients having a more extensive subcortical involvement. The PLE of patients with predominant cortical involvement (sample size = 233, $\mu = 3.238$, $\sigma^2 = 0.540$) was lower than the PLE of patients with both cortical and subcortical glioma (sample size = 118, $\mu = 3.416$, $\sigma^2 = 0.207$, $P = 0.0067$, $\alpha = 0.0167$). The PLE of

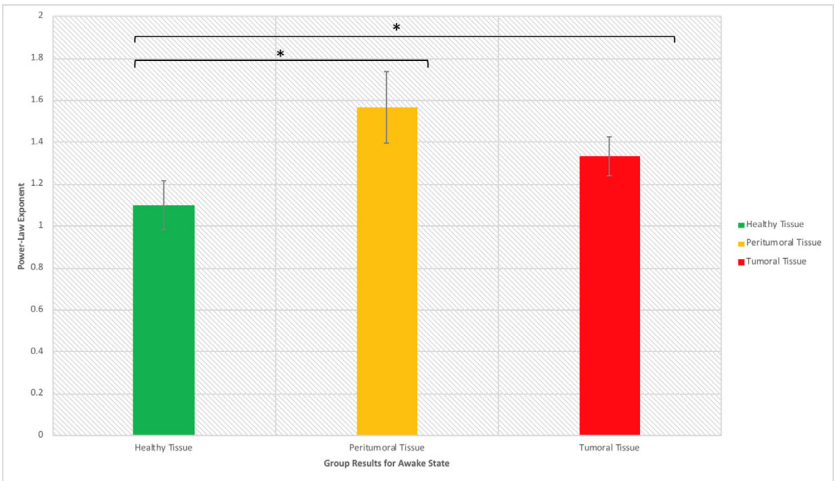

FIGURE 4 | Power law exponent in the awake resting-state activity for distinguishing healthy, peritumoral and tumoral tissue (*significant at $p < 0.05$).

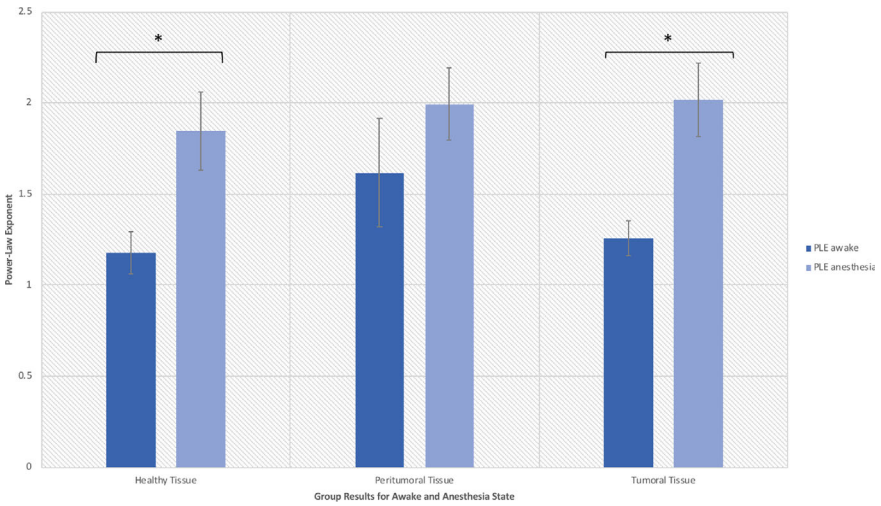

FIGURE 5 | Power law exponent results in the anesthetic and awake states (*significant at $p < 0.05$).

patients with both cortical and subcortical glioma was less variant than the PLE of patients with only cortical glioma. This suggests that further analysis should focus on studying the subcortical glioma involvement, and a continuous representation of glioma depth from the cortical surface could be incorporated in the future to study the effect that glioma depth has on the PLE of the surrounding neural tissue.

Lastly, the importance of the glioma's molecular and histological characteristics cannot be overemphasized given the known strong correlation with clinical outcomes. Although we have a small sample of subjects, in order to study the effect that this mechanism could have on the PLE results, all channels for each subject were labeled as low-grade (grade II) or high-grade (grade III & IV) which coincided with an IDH-mutant and respectively an IDH wild-type status. The PLE of low-grade glioma-associated channels (sample size = 236, $\mu = 3.266$, $\sigma^2 = 0.505$) was not found to be different from the PLE of high-grade associated channels (sample size = 115, $\mu = 3.348$, $\sigma^2 = 0.318$, $P = 0.248$). From this analysis, it was concluded that there was not enough evidence to suggest that an unbalanced representation of glioma graded tissue in this study would bias the PLE results presented.

In summary, ECoG recordings performed prior to glioma resection allowed us to investigate scale-free related changes in the resting state activity of tumor tissue and its reactivity to anesthesia. We observed an increased PLE in the anesthetic state for all types of tissues (with a larger extent within the tumoral tissue) and additionally, a different behavior of the PT when comparing PLE in the two anesthetic states (smaller PLE changes than in the adjacent tissues). We thus noticed a lack of reaction to anesthesia in the peritumoral tissue and hypothesized that it is related to a different tissue type which maintain the already high PLE values.

DISCUSSION

Extrapolating our group's previous work in functional MRI, for the first time to our knowledge, the analysis of the signal from ECoG electrodes in this study concentrated on power law exponent. Power laws have been reported in many distinct scientific, geographical and social phenomena and have been associated with long memory behavior, self-similarity and fractal structures (26). Power law was initially utilized to characterize the distribution of wealth in a society being known as the Pareto principle, where a small percentage of the population has a large proportion of wealth. Similarly, our investigation of the cortical electrophysiological changes occurring in the setting of twelve patients undergoing craniotomy for resection of glioma revealed distinct electrophysiological features across the tumoral area compared to the surrounding tissues, namely a higher PLE value over the tumoral tissue than for the surrounding areas. The tumoral tissue PLE difference between the two anesthetic states resembled to the one observed in macroscopically healthy tissue which could imply a functionally independent state of the tumoral tissue. This has been previously suggested in recent articles, which demonstrated that gliomas develop functional multicellular network structures where tumor cells "communicate and cooperate with each other in a complex but ordered manner that is by itself reminiscent of a functional organ" (27, 28). Therefore, as a correlate, the tumor could be seen like the tall trees that continue to grow using more resources from the ecosystem on the expense of smaller trees (29), for instance surrounding cells, that do not have access anymore to the scarce resources.

Furthermore, the tumor's surrounding tissue showed specific features. A universal definition of the peritumoral area in glioma is lacking and its complex features are not yet elucidated (30, 31). Nonetheless, current guidelines recommend the radiation therapy target volume to be delineated on the surgical cavity with the

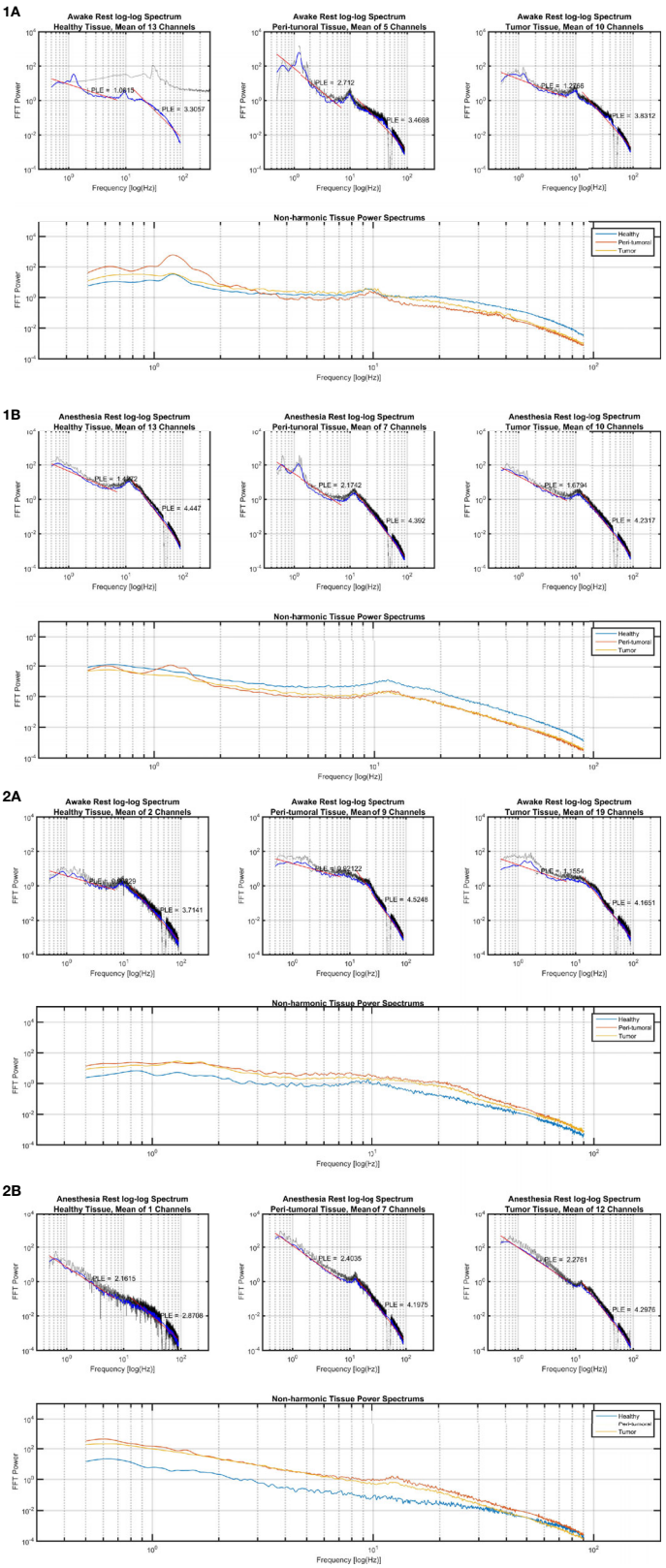

FIGURE 6 | Continued

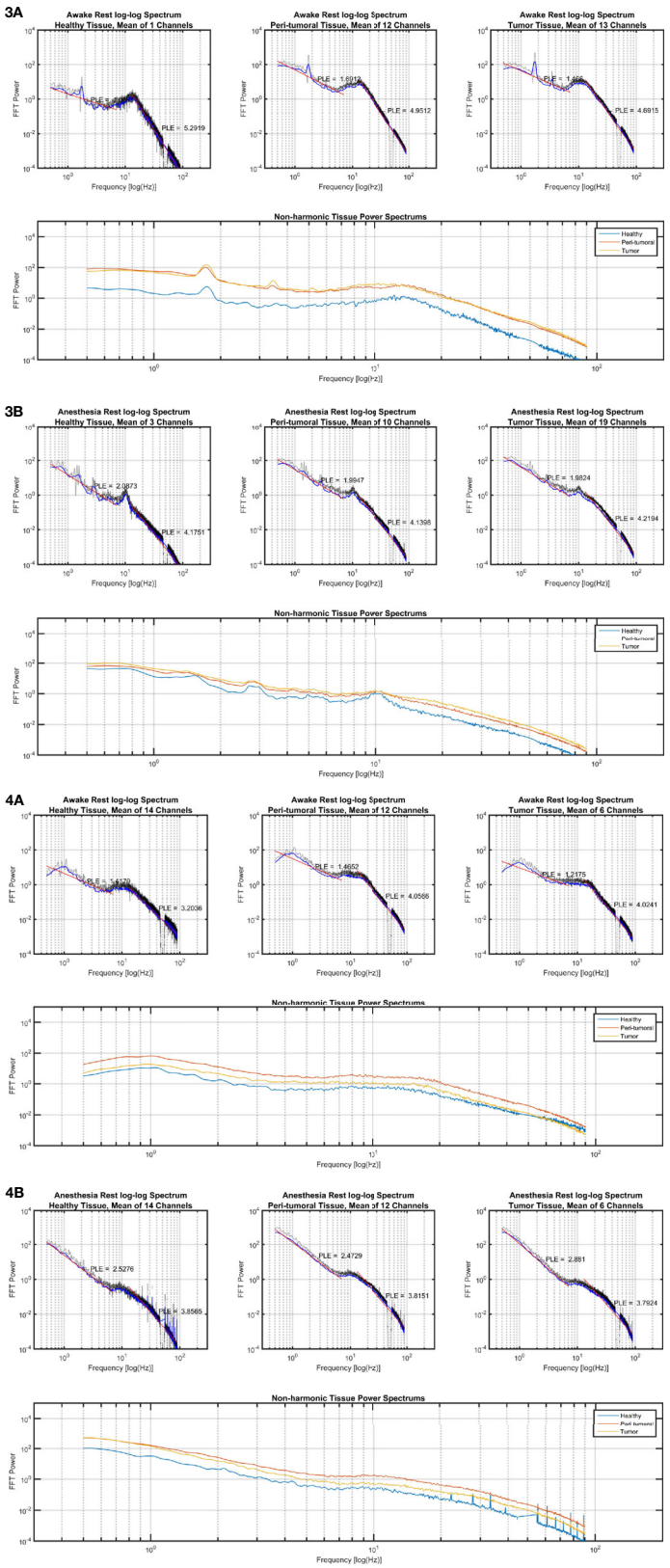

FIGURE 6 | Power law exponent results in individual cases. **(1A)** Subject 1 in awake state, **(1B)** Subject 1 in anesthetic state; **(2A)** Subject 2 in awake state, **(2B)** Subject 2 in anesthetic state; **(3A)** Subject 3 in awake state, **(3B)** Subject 3 in anesthetic state; **(4A)** Subject 4 in awake state, **(4B)** Subject 4 in anesthetic state.

addition of a 20-mm margin, which represents the most common site of recurrence (30–32). Gliomas are well known to infiltrate the brain tissue well beyond the radiological boundaries of the tumor (33, 34) and thus, our HT electrodes should be perceived as macroscopically healthy tissue. For instance, in **Figures 5** and **6**, the PT tissue displays an intermediate feature between the TT or macroscopically HT-electrodes as well as a smaller PLE change when investigating the difference between the two anesthetic states. We suspect that these features are related to tumor cell infiltration. Further studies with prolonged recordings and combined genetic analysis could test our hypothesis. Also, the loss of PLE change in the PT between the awake and anesthesia states in patients presenting with seizures could suggest a distinctive state of the peritumoral area. As such, PT could represent an interlaid area between the brain and the functional tumor with specific characteristics favoring the generation and propagation of seizures. Being characterized as an interface between the tumoral and healthy brain, the peritumoral tissue could thus represent an area requiring a higher energy expenditure as it represents the invasion front of tumor cells into the neighboring tissue (33). Hatcher et al. recently reported spontaneous episodes of cortical spreading depolarization that arose frequently from the peritumoral region (35). This depolarizing phenomenon occurs in the setting of a variety of pathological states and represents a spreading loss of ion homeostasis, altered vascular response while in healthy tissue an increased electrical activity is coupled with the release of vasodilatory factors such as nitric oxide to increase local blood flow to meet increased energy expenditure (36). Although in GBM, the peritumoral tissue was found to contain cancer stem cells, Cubillos et al. reported that the concentration of taurine, an amino acid that may have a protective effect or be involved in cell proliferation, was found to be higher in the peritumoral tissue of gliomas (37). The large histological and molecular heterogeneity of gliomas highlights the need for a better understanding of the underlying biomolecular characterization and biochemical reorganization occurring in this important region. This could give more insights in terms of the resulting electrophysiological changes recorded over these regions in order to allow the development of personalized therapies.

The origins and mechanisms of GRE are multifactorial (3) and the current evidence suggests that there is a link between epileptogenesis and glioma cell infiltration in the peritumoral area since epileptic activities seem to arise from the neocortex surrounding the gliomas (31–33). Also, glioma cell infiltration seems to promote growth and recurrence of tumors at sites around their core (34, 35). In a recent study performed by Pallud et al., it was demonstrated that in slices of human tissue, the peritumoral neocortex infiltrated by glioma cells generates spontaneous interictal discharges that depend on both glutamatergic and GABAergic signaling (36). This link may explain both the anti-epileptic effects of oncological treatments (38, 39) and the increase in seizure frequency as tumors progress (9, 40, 41). Early operative intervention and gross-total resection contributes strongly to seizure freedom and improving quality-of-life (1, 42, 43). Emerging evidence advocates an aggressive and early surgical approach and suggests that the opportune time to perform epilepsy surgery may be when the patient is already undergoing oncosurgery in the same area (10). As such, proper seizure diagnosis and therapy requires accurate identification and management of the infiltrated peritumoral tissue.

Electrocorticography plays an important role in the localization of epileptogenic foci and evaluation of the effects of microsurgical procedures intraoperatively. An accurate estimation of the epileptogenic cortex and its removal requires the estimation of spatial spread of ECoG. Recent studies estimating the spatial spread of ECoG suggested that although brains' signals capture different features of the neural network, ECoG records a local signal (diameter of ∼3 mm) confirming the precision required for its use in determining the epileptogenic focus (44). Furthermore, Berger et al. previously proposed that electrocorticography-guided epilepsy surgery for pediatric patients with brain tumors is highly effective (45). Given that some patient populations cannot participate during awake craniotomies (for example with severe neurological deficits), several investigators have utilized high-gamma ECoG changes during language and motor tasks to localize eloquent cortex and have reported good concordance with cortical stimulation mapping (46–50). High gamma activity (HGA) between 80 and 140 Hz on electrocorticography is assumed to reflect localized cortical processing, whereas the cortico-cortical evoked potential (CCEP) can reflect bidirectional responses evoked by monophasic pulse stimuli to the language cortices when there is no patient cooperation. The use of "passive" mapping was thus proposed by combining HGA mapping and CCEP recording without active tasks during conscious resections of brain tumors (51). In terms of localizing the ECoG electrodes in relation to the tumor, an approach using solely the intra-operative photography might be prone to errors given that areas invaded by the tumor might not be clearly delineated and the sulcal patterns may not be easily segmented. However, as the neuronavigation is used clinically to decide the extent of resection, we confirmed the electrode locations using the neuronavigation probe thus reducing the risk of error in electrode localization. Furthermore, the ECoG recording was performed as soon as the craniotomy was completed in order to minimize the effect of the brain shift.

In tumoral epilepsy surgery, the first aim is to maximize the extent of tumor resection while minimizing postsurgical morbidity, in order to increase the median survival as well as to preserve the quality of life (52). Gross-total resection of tumors is also a critical factor in achieving seizure freedom (40) in infiltrating tumors such as gliomas, where these lesions migrate along white matter tracts. A significantly higher resection volume was associated with a higher chance of favorable seizure outcome in multiple studies, especially in long-term epilepsy-associated with glial tumors (53). Extraoperative mapping by strips/grids is often not sufficient in tumoral surgery, since in essence, it allows the study of the cortex but cannot map subcortical pathways (52). Although, recent research demonstrated that awake craniotomy can be performed safely without ECoG, even in patients with preoperative intractable epilepsy (54), some studies showed that when

complete ECoG-guided resection is performed there is a greater likelihood of long-term seizure freedom (55). Awake functional mapping allows surgeons to maximize tumor resection while minimizing neurological deficits, thus improving patient's survival and quality of life (56, 57). This approach has allowed an improvement of both oncologic and neurological outcomes however, many patients do not reach the complete postsurgical control of seizures. Therefore, the use of more precise preoperative evaluation and adequate surgical techniques is desirable for those patients. Recently, Ius et al. outlined the importance of the EOR on postoperative seizure outcome as the EOR was independent of the molecular class of the tumor (58). Similarly, Xu et al. showed that an EOR threshold of more than 80% was associated with a long-term seizure freedom (59). In a larger multicenter investigation, Still and colleagues demonstrated that for patients with a supratentorial DLGG, postoperative seizure control was more likely to occur when the EOR was ≥ 91% and/or when the residual tumor volume was ≤ 19 cc (60). Our findings of progressive PLE changes from the tumor core could be used to further delineate the electrophysiological changes induced by the tumor (**Figure S6**). However, these preliminary findings need to be first correlated with genetic/histological data. Future prospective studies integrating direct electrical stimulation and ECoG could refine the supramarginal resection technique when functionally possible. A multidisciplinary approach including epileptologists for a comprehensive assessment and accurate localization of the epileptogenic focus are primordial for a better understanding of the potential clinical applications of our findings. The correlation of the intra-operative electrophysiologic changes with clinical markers and outcome measures is an important aspect that should be explored in the future with well-designed prospective studies.

The concept of individualized surgery for managing glial tumors is based on the goal of achieving a maximal tumor resection and seizure freedom without inducing new neurological deficits (61–64). We already dispose of ample information in terms of the clinical and biological behavior of gliomas. Nonetheless, the persistent challenge remains integrating the information obtained from various analyses in a way that provides a comprehensive view of the alterations underlying the interplay between epileptogenesis and oncology. Scale-free measures such as PLE are ubiquitously present in many scientific topics and this research represents the first confirmation of its relevance to the tumoral tissue. Further research including in-vivo neural recording could help improve our insight into latent sources of PLE changes.

CONCLUSION

In summary, we present for the first time distinct power law exponent features in the tumoral and peritumoral tissue of gliomas that seems to represent a critical structure both for the onset and propagation of epileptiform activity and for infiltration by glioma cells. Although neuro-oncology and epilepsy surgery have traditionally been separate disciplines, we postulate that the analysis of the mechanisms underlying the tumor related epilepsy might equally yield significant insight into tumorigenesis. We expect that the contributions made from a multidisciplinary approach to unravel the complex pathways underlying the clinical features of gliomas related epilepsy will lead to meaningful progress for the patients affected by these devastating tumors.

DATA AVAILABILITY STATEMENT

The raw data supporting the conclusions of this article will be made available by the authors, without undue reservation.

ETHICS STATEMENT

The studies involving human participants were reviewed and approved by the Huashan Hospital ethics board (approval nos. KY201209 and KY2015-168). The patients/participants provided their written informed consent to participate in this study.

AUTHOR CONTRIBUTIONS

Conception and design: GN, J-SW, JL, and DG. Acquisition of data: DG, JL, and J-SW. Analysis and interpretation of data: BL, DG, J-SW, NJ, JL, GN, ET, and AS. Drafting the article: DG. Critically revising the article: J-SW, DG, NJ, ET, AS, and GN. Reviewed submitted version of manuscript: all authors. Approved the final version of the manuscript on behalf of all authors: GN. Statistical analysis: BL, DG, and JL. Administrative/technical/material support: J-SW and GN. Study supervision: J-SW and GN. All authors contributed to the article and approved the submitted version.

FUNDING

This study was supported by The National Key Technology R&D Program of China (grant no. 2014BAI04B05 [J-SW]), and Shanghai Shenkang Hospital Development Center (grant no. SHDC12018114 [J-SW]).

ACKNOWLEDGMENTS

We thank Prof. Dong-Xiao Zhuang for assistance with manuscript revision, Dr. Zhang Jie and Dr. Zhengda Yu for data collection, Dr. Zhong Yang for iMRI acquisition, Jian-Bing Shi for technical support in navigational procedures, and Geng Xu for help with the electrophysiological data collection.

SUPPLEMENTARY MATERIAL

The Supplementary Material for this article can be found online at: https://www.frontiersin.org/articles/10.3389/fonc.2020.625474/full#supplementary-material

REFERENCES

1. Pallud J, Audureau E, Blonski M, Sanai N, Bauchet L, Fontaine D, et al. Epileptic seizures in diffuse low-grade gliomas in adults. *Brain* (2014) 137(2):449–62. doi: 10.1093/brain/awt345
2. Pallud J, Capelle L, Huberfeld G. TUMORS AND TUMORAL EPILEPSY Tumoral epileptogenicity: How does it happen? *Epilepsia* (2013) 54:30–4. doi: 10.1111/epi.12440
3. De Groot M, Reijneveld JC, Aronica E, Heimans JJ. Epilepsy in patients with a brain tumour: focal epilepsy requires focused treatment. *Brain* (2012) 135 (4):1002–16. doi: 10.1093/brain/awr310
4. Van Der Horst L. Electroencephalography and its significance in biopsychology and clinical diagnosis. *Psychiatr Neurologische Bl Amsterdam* (1947) 50:17–42.
5. Marshall C, Earl WA. Electrocorticography. *Bull Johns Hopkins Hosp* (1949) 85:344–59.
6. Ectors L, Achslogh J. Corticography. *Rev Neurol* (1950) 82:465–86.
7. Jung R, Riechert T, Heines KD. Technique and evaluation of operative electrocorticography and registration of subcortical potentials. *Nervenarzt* (1951) 22:433–6.
8. Hossmann KA, Wechsler W, Wilmes F. Experimental peritumorous edema. Morphological and pathophysiological observations. *Acta Neuropathol* (1979) 45:195–203. doi: 10.1007/BF00702671
9. Englot DJ, Berger MS, Barbaro NM, Chang EF. Extent of Surgical Resection Predicts Seizure. *Neurosurgery* (2012) 70:11–3. doi: 10.1227/NEU.0b013e31823c3a30
10. Huberfeld G, Vecht CJ. Seizures and gliomas [mdash] towards a single therapeutic approach. *Nat Rev Neurol* (2016) 12:204–16. doi: 10.1038/nrneurol.2016.26
11. Cowie CJA, Cunningham MO. Peritumoral epilepsy: Relating form and function for surgical success. *Epilepsy Behav* (2014) 38:53–61. doi: 10.1016/j.yebeh.2014.05.009
12. Shamji MF, Fric-Shamji EC, Benoit BG. Brain tumors and epilepsy: Pathophysiology of peritumoral changes. *Neurosurg Rev* (2009) 32:274–84. doi: 10.1007/s10143-009-0191-7
13. Ghinda D, Zhang N, Lu J, Yao C, Yuan S, Wu J-S. Contribution of combined intraoperative electrophysiological investigation with 3-T intraoperative MRI for awake cerebral glioma surgery: comprehensive review of the clinical implications and radiological outcomes. *Neurosurg Focus* (2016) 40:E14. doi: 10.3171/2015.12.FOCUS15572
14. Barone DG, Lawrie TA, Hart MG. Image guided surgery for the resection of brain tumours. *Cochrane Database Syst Rev* (2014) 1:CD009685. doi: 10.1002/14651858.CD009685.pub2
15. Jenkinson MD, Barone DG, Bryant A, Vale L, Bulbeck H, Lawrie TA, et al. Intraoperative imaging technology to maximise extent of resection for glioma. *Cochrane Database Syst Rev* (2018) 1:CD012788. doi: 10.1002/14651858.CD012788.pub2
16. Ellingson BM, Wen PY, Cloughesy TF. Modified Criteria for Radiographic Response Assessment in Glioblastoma Clinical Trials. *Neurotherapeutics* (2017) 14:307–20. doi: 10.1007/s13311-016-0507-6
17. Wolff A, Gomez-Pilar J, Nakao T, Northoff G. Interindividual neural differences in moral decision-making are mediated by alpha power and delta/theta phase coherence. *Sci Rep* (2019) 9:4432. doi: 10.1038/s41598-019-40743-y
18. Wolff A, Di Giovanni DA, Gómez-Pilar J, Nakao T, Huang Z, Longtin A, et al. The temporal signature of self: Temporal measures of resting-state EEG predict self-consciousness. *Hum Brain Mapp* (2019) 40:789–803. doi: 10.1002/hbm.24412
19. Huang Z, Wang Z, Zhang J, Dai R, Wu J, Li Y, et al. Altered temporal variance and neural synchronization of spontaneous brain activity in anesthesia. *Hum Brain Mapp* (2014) 35:5368–78. doi: 10.1002/hbm.22556
20. He BJ. Scale-free properties of the functional magnetic resonance imaging signal during rest and task. *J Neurosci* (2011) 31:13786–95. doi: 10.1523/JNEUROSCI.2111-11.2011
21. He BJ. Scale-free brain activity: Past, present, and future. *Trends Cognit Sci* (2014) 18:480–7. doi: 10.1016/j.tics.2014.04.003
22. Yamamoto Y, Hughson RL. Coarse-graining spectral analysis: new method for studying heart rate variability. *J Appl Physiol* (1991) 71:1143–50. doi: 10.1152/jappl.1991.71.3.1143
23. Welch P. The use of fast Fourier transform for the estimation of power spectra: a method based on time averaging over short, modified periodograms. *IEEE Trans Audio Electroacoust* (1967) 15:70–3. doi: 10.1109/TAU.1967.1161901
24. Bullmore E, Sporns O. Complex brain networks: graph theoretical analysis of structural and functional systems. *Nat Rev Neurosci* (2009) 10:186–98. doi: 10.1038/nrn2575
25. He BJ, Zempel JM, Snyder AZ, Raichle ME. The temporal structures and functional significance of scale-free brain activity. *Neuron* (2010) 66(3):353–69. doi: 10.1016/j.neuron.2010.04.020
26. Tenreiro Machado JA, Pinto CMA, Lopes AM. Power Law and Entropy Analysis of Catastrophic Phenomena. *Math Probl Eng* (2013) 2013:1–10. doi: 10.1155/2013/562320
27. Osswald M, Jung E, Sahm F, Solecki G, Venkataramani V, Blaes J, et al. Brain tumour cells interconnect to a functional and resistant network. *Nature* (2015) 528:93–8. doi: 10.1038/nature16071
28. Osswald M, Solecki G, Wick W, Winkler F. A malignant cellular network in gliomas: Potential clinical implications. *Neuro Oncol* (2016) 18:479–85. doi: 10.1093/neuonc/now014
29. Scanlon TM, Caylor KK, Levin SA, Rodriguez-Iturbe I. Positive feedbacks promote power-law clustering of Kalahari vegetation. *Nature* (2007) 449:209–12. doi: 10.1038/nature06060
30. Leao DJ, Craig PG, Godoy LF, Leite CC, Policeni B. Response Assessment in Neuro-Oncology Criteria for Gliomas: Practical Approach Using Conventional and Advanced Techniques. *Am J Neuroradiol* (2020) 41:10–20. doi: 10.3174/ajnr.A6358
31. Ghinda DC, Yang Y, Wu S, Lu J, Su L, Damiani S, et al. Personalized Multimodal Demarcation of Peritumoral Tissue in Glioma. *JCO Precis Oncol* (2020) 4:1128–40. doi: 10.1200/PO.20.00115
32. Cabrera AR, Kirkpatrick JP, Fiveash JB, Shih HA, Koay EJ, Lutz S, et al. Radiation therapy for glioblastoma: Executive summary of an American Society for Radiation Oncology Evidence-Based Clinical Practice Guideline. *Pract Radiat Oncol* (2016) 6(4):217–25. doi: 10.1016/j.prro.2016.03.007
33. D'Alessio A, Proietti G, Sica G, Scicchitano BM. Pathological and Molecular Features of Glioblastoma and Its Peritumoral Tissue. *Cancers (Basel)* (2019) 11:469. doi: 10.3390/cancers11040469
34. Lemée J-M, Clavreul A, Menei P. Intratumoral heterogeneity in glioblastoma: don't forget the peritumoral brain zone. *Neuro Oncol* (2015) 17:1322–32. doi: 10.1093/neuonc/nov119
35. Hatcher A, Yu K, Meyer J, Aiba I, Deneen B, Noebels JL. Pathogenesis of peritumoral hyperexcitability in an immunocompetent CRISPR-based glioblastoma model. *J Clin Invest* (2020) 130:2286–300. doi: 10.1172/JCI133316
36. Kramer DR, Fujii T, Ohiorhenuan I, Liu CY. Cortical spreading depolarization: Pathophysiology, implications, and future directions. *J Clin Neurosci* (2016) 24:22–7. doi: 10.1016/j.jocn.2015.08.004
37. Cubillos S, Obregón F, Vargas MF, Salazar LA, Lima L. Taurine concentration in human gliomas and meningiomas: Tumoral, peritumoral, and extratumoral tissue. *Adv Exp Med Biol.* (2005) 583:419–22. doi: 10.1007/978-0-387-33504-9_47
38. Koekkoek JAF, Kerkhof M, Dirven L, Heimans JJ, Reijneveld JC, Taphoorn MJB. Seizure outcome after radiotherapy and chemotherapy in low-grade glioma patients: A systematic review. *Neuro Oncol* (2015) 17:924–34. doi: 10.1093/neuonc/nov032
39. Koekkoek JAF, Dirven L, Heimans JJ, Postma TJ, Vos MJ, Reijneveld JC, et al. Seizure reduction is a prognostic marker in low-grade glioma patients treated with temozolomide. *J Neurooncol* (2015) 126:347–54. doi: 10.1007/s11060-015-1975-y
40. Englot DJ, Berger MS, Barbaro NM, Chang EF, Francisco S. Predictors of seizure freedom after resection of supratentorial low-grade gliomas. A review. *J Neurosurg* (2011) 115:240–4. doi: 10.3171/2011.3.JNS1153
41. Chang EF, Potts MB, Keles GE, Lamborn KR, Chang SM, Barbaro NM, et al. Seizure characteristics and control following resection in 332 patients with low-grade gliomas. *J Neurosurg* (2008) 108:227–35. doi: 10.3171/JNS/2008/108/2/0227
42. Van Breemen MSM, Wilms EB, Vecht CJ. Review Epilepsy in patients with brain tumours: epidemiology, mechanisms, and management. *Lancet Neurol* (2007) 6(5):421–30. doi: 10.1016/S1474-4422(07)70103-5
43. Rudà R, Bello L, Duffau H, Soffietti R. Seizures in low-grade gliomas: natural history, pathogenesis, and outcome after treatments. *NeuroOncol* (2012) 14 (4):iv55–64. doi: 10.1093/neuonc/nos199

44. Dubey A, Ray S. Cortical Electrocorticogram (ECoG) Is a Local Signal. *J Neurosci* (2019) 39:4299–311. doi: 10.1523/JNEUROSCI.2917-18.2019
45. Berger MS, Ghatan S, Haglund MM, Dobbins J, Ojemann GA. Low-grade gliomas associated with intractable epilepsy: seizure outcome utilizing electrocorticography during tumor resection. *J Neurosurg* (1993) 79:62–9. doi: 10.3171/jns.1993.79.1.0062
46. Sinai A, Bowers CW, Crainiceanu CM, Boatman D, Gordon B, Lesser RP, et al. Electrocorticographic high gamma activity versus electrical cortical stimulation mapping of naming. *Brain* (2005) 128:1556–70. doi: 10.1093/brain/awh491
47. Qiu B, Ou S, Song T, Hu J, You L, Wang Y, et al. Intraoperative electrocorticography-guided microsurgical management for patients with onset of supratentorial neoplasms manifesting as epilepsy: a review of 65 cases. *Epileptic Disord* (2014) 16:175–84. doi: 10.1684/epd.2014.0662
48. Qian T, Member S, Wu W, Member S, Zhou W, Gao S, et al. ECoG based cortical function mapping using general linear model. *Annual International Conference of the IEEE Engineering in Medicine and Biology Society* (2011), 2347–50. doi: 10.1109/IEMBS.2011.6090656
49. Miller KJ, Weaver KE, Ojemann JG. Direct electrophysiological measurement of human default network areas. *Proc Natl Acad Sci U S A* (2009) 106:12174–7. doi: 10.1073/pnas.0902071106
50. Genetti M, Grouiller F, Vulliemoz S, Spinelli L, Seeck M, Michel CM, et al. Noninvasive language mapping in patients with epilepsy or brain tumors. *Neurosurgery* (2013) 72:555–65. doi: 10.1227/NEU.0b013e318282cdad
51. Tamura Y, Ogawa H, Kapeller C, Prueckl R, Takeuchi F, Anei R, et al. Passive language mapping combining real-time oscillation analysis with cortico-cortical evoked potentials for awake craniotomy. *J Neurosurg* (2016) 125:1580–8. doi: 10.3171/2015.4.JNS15193
52. Duffau H. Brain mapping in tumors: Intraoperative or extraoperative? *Epilepsia* (2013) 54:79–83. doi: 10.1111/epi.12449
53. Roessler K, Hofmann A, Sommer B, Grummich P, Coras R, Kasper BS, et al. Resective surgery for medically refractory epilepsy using intraoperative MRI and functional neuronavigation: The Erlangen experience of 415 patients. *Neurosurg Focus* (2016) 40(3):E15. doi: 10.3171/2015.12.FOCUS15554
54. Boetto J, Bertram L, Moulinie G, Herbet G, Moritz-Gasser S, Duffau H. Low Rate of Intraoperative Seizures During Awake Craniotomy in a Prospective Cohort with 374 Supratentorial Brain Lesions: Electrocorticography Is Not Mandatory. *World Neurosurg* (2015) 84:1838–44. doi: 10.1016/j.wneu.2015.07.075
55. Fallah A, Weil AG, Sur S, Miller I, Jayakar P, Morrison G, et al. Epilepsy surgery related to pediatric brain tumors: Miami Children's Hospital experience. *J Neurosurg Pediatr* (2015) 16:675–80. doi: 10.3171/2015.4.PEDS14476
56. Zigiotto L, Annicchiarico L, Corsini F, Vitali L, Falchi R, Dalpiaz C, et al. Effects of supra-total resection in neurocognitive and oncological outcome of high-grade gliomas comparing asleep and awake surgery. *J Neurooncol* (2020) 148:97–108. doi: 10.1007/s11060-020-03494-9
57. Duffau H, Taillandier L. New concepts in the management of diffuse low-grade glioma: Proposal of a multistage and individualized therapeutic approach. *Neuro Oncol* (2015) 17:332–42. doi: 10.1093/neuonc/nou153
58. Ius T, Pauletto G, Tomasino B, Maieron M, Budai R, Isola M, et al. Predictors of postoperative seizure outcome in low grade glioma: From volumetric analysis to molecular stratification. *Cancers (Basel)* (2020) 12(2):397. doi: 10.3390/cancers12020397
59. Xu DS, Awad AW, Mehalechko C, Wilson JR, Ashby LS, Coons SW, et al. An extent of resection threshold for seizure freedom in patients with low-grade gliomas. *J Neurosurg* (2018) 128(4):1084–90. doi: 10.3171/2016.12.JNS161682
60. Still MEH, Roux A, Huberfeld G, Bauchet L, Baron M-H, Fontaine D, et al. Extent of Resection and Residual Tumor Thresholds for Postoperative Total Seizure Freedom in Epileptic Adult Patients Harboring a Supratentorial Diffuse Low-Grade Glioma. *Neurosurgery* (2019) 85:E332–40. doi: 10.1093/neuros/nyy481
61. Robles SG, Gatignol P, Lehericy S, Duffau H. Long-term brain plasticity allowing a multistage surgical approach to World Health Organization Grade II gliomas in eloquent areas: Report of 2 cases. *J Neurosurg* (2008) 109:615–24. doi: 10.3171/JNS/2008/109/10/0615
62. Duffau H. Resecting diffuse low-grade gliomas to the boundaries of brain functions: a new concept in surgical neuro-oncology. *J Neurosurg Sci* (2015) 59:361–71.
63. Mandonnet E, Duffau H. Understanding entangled cerebral networks: a prerequisite for restoring brain function with brain-computer interfaces. *Front Syst Neurosci* (2014) 8:82. doi: 10.3389/fnsys.2014.00082
64. Duffau H. The challenge to remove diffuse low-grade gliomas while preserving brain functions. *Acta Neurochir (Wien)* (2012) 154:569–74. doi: 10.1007/s00701-012-1275-7

Conflict of Interest: The authors declare that the research was conducted in the absence of any commercial or financial relationships that could be construed as a potential conflict of interest.

frontiers in Oncology

ORIGINAL RESEARCH
published: 26 February 2021
doi: 10.3389/fonc.2021.617179

The Functional Reorganization of Language Network Modules in Glioma Patients: New Insights From Resting State fMRI Study

Lu Jin[1], Chuzhong Li[2], Yazhuo Zhang[2], Taoyang Yuan[2], Jianyou Ying[2], Zhentao Zuo[3] and Songbai Gui[1]**

[1] Department of Neurosurgery, Beijing Tiantan Hospital, Capital Medical University, Beijing, China, [2] Beijing Neurosurgical Institute, Capital Medical University, Beijing, China, [3] State Key Laboratory of Brain and Cognitive Science, Institute of Biophysics, Chinese Academy of Sciences, Beijing, China

OPEN ACCESS

Edited by:
Yanmei Tie,
Brigham and Women's Hospital and Harvard Medical School, United States

Reviewed by:
Andrei Holodny,
Memorial Sloan Kettering Cancer Center, United States
Marco Riva,
University of Milan, Italy
Lei Jin,
Fudan University, China

***Correspondence:**
Zhentao Zuo
ztzuo@bcslab.ibp.ac.cn
Songbai Gui
guisongbai@yeah.net

Specialty section:
This article was submitted to Cancer Imaging and Image-directed Interventions, a section of the journal Frontiers in Oncology

Received: 14 October 2020
Accepted: 12 January 2021
Published: 26 February 2021

Citation:
Jin L, Li C, Zhang Y, Yuan T, Ying J, Zuo Z and Gui S (2021) The Functional Reorganization of Language Network Modules in Glioma Patients: New Insights From Resting State fMRI Study. Front. Oncol. 11:617179. doi: 10.3389/fonc.2021.617179

Background: Prior investigations of language functions have focused on the response profiles of particular brain regions. However, the specialized and static view of language processing does not explain numerous observations of functional recovery following brain surgery. To investigate the dynamic alterations of functional connectivity (FC) within language network (LN) in glioma patients, we explored a new flexible model based on the neuroscientific hypothesis of core-periphery organization in LN.

Methods: Group-level LN mapping was determined from 109 glioma patients and forty-two healthy controls (HCs) using independent component analysis (ICA). FC and mean network connectivity (mNC: l/rFCw, FCb, and FCg) were compared between patients and HCs. Correlations between mNC and tumor volume (TV) were calculated.

Results: We identified ten separate LN modules from ICA. Compared to HCs, glioma patients showed a significant reduction in language network functional connectivity (LNFC), with a distinct pattern modulated by tumor position. Left hemisphere gliomas had a broader impact on FC than right hemisphere gliomas, with more reduced edges away from tumor sites (p=0.011). mNC analysis revealed a significant reduction in all indicators of FC except for lFCw in right hemisphere gliomas. These alterations were associated with TV in a double correlative relationship depending on the tumor position across hemispheres.

Conclusion: Our findings emphasize the importance of considering the modulatory effects of core-periphery mechanisms from a network perspective. Preoperative evaluation of changes in LN caused by gliomas could provide the surgeon a reference to optimize resection while maintaining functional balance.

Keywords: language network, mean functional network connectivity, glioma, surgery, reorganization

INTRODUCTION

Traditionally, the posterior part of the left superior temporal gyrus (Wernicke's area) and the rostral part of the left inferior frontal cortices (Broca's area) have been associated with language comprehension and production and are classically designated as "eloquent" areas (1, 2). However, recent studies have revealed that additionally bilateral temporal, parietal, prefrontal, and putamen regions (3) and even the cerebellum (4) are involved in language processing, reflecting a large-scale network engaging in language comprehension and production distributed at both the cortical and subcortical levels. Within this distributed language processing system, the left hemisphere frontotemporal subnetwork is widely assumed to underpin language comprehension in the key combinatorial language domains of grammatical computations and semantic operations (5), while the right hemisphere subnetwork contributes to linguistic working memory capacity (6, 7). Together, these findings indicate that the language system is best considered a core-periphery model regulated by a domain-general and domain-specific subnetwork (8), an approach that has been proven to be constructive in understanding the functional architecture of language (9).

As the language network strikes a balance between integration and segregation among functionally specialized brain regions, we hypothesized that distinct structural damage would lead to different maladaptation and reorganization of inter versus intra-hemisphere connectivity due to their distinct roles in the network. Compared with task-based fMRI, resting-state fMRI obviates task compliance from patients, allows the parallel assessment of functional networks. Abnormal communications within brain functional network has been reported in series of brain lesion studies using resting-state fMRI functional connectivity (10, 11), however, the degree to which lesion topography (sizes, locations) accounts for the variability of functional connectivity across different modules is mostly unknown.

Thus, we subdivided the language-related regions into four subsystems, the left frontal module, the left temporal module, and their contralateral homologues (12). Then, we performed ICA to identify LN maps at rest in the presence of structural brain damage caused by gliomas located in the four subsystems, and compared FC and mNC among LN modules between glioma patients and demographically matched HCs. Finally, the possible correlations between TV and mNC patterns in glioma patients were assessed.

MATERIALS AND METHODS

Participants

112 glioma patients were recruited from our Department of Neurosurgery, and forty-two demographically matched HCs were included in this study. These patients were selected from a pool of database collected between December 2016 – November 2017. The patient selection flowchart can be seen in **Supplementary Figure S1**. All participants met the following criteria (1): Patients with a glioma affecting one of the language subsystem areas; (2) No symptoms of motor impairment; (3) Right hand according to the Edinburgh Inventory (13); (4) No history of brain surgery and psychiatric illness. Corresponding to the glioma locations in the four subsystems of language-related areas, we categorized the patients into four subgroups, the left frontal glioma subgroup (LFG), left temporal glioma subgroup (LTG), right frontal glioma subgroup (RFG), and right temporal glioma subgroup (RTG), to study the effect of lesion topography on language network functional connectivity (LNFC). This study was approved by the ethics committee of Beijing Tiantan Hospital, and written informed consent was obtained from all participants.

All participants were assessed by an experienced surgeon (J.Y.Y.) to identify the general psychological status on the day of MRI. Specifically, we assessed cognitive capability by the Mini Mental State Examination (MMSE), and motor and mental statuses were assessed with the Karnofsky Performance Scale (KPS) (14), Beck Depression Inventory (BDI) (15).

Imaging Protocols

We acquired whole-brain fMRI data on a Siemens Prisma 3.0 Tesla scanner (Siemens Healthineers, Erlangen, Germany) with a 20-channel head coil. During the scanning, subjects were asked to relax and close their eyes. Three types of images were collected: (i) High-resolution 3D T1-weighted images; (ii) Resting-state fMR images; and (iii) T2-weighted images. The 3D T1-weighted sagittal images were acquired with a magnetism-prepared rapid acquired with gradient echo (MPRAGE) sequence: 192 slices, acquisition time = 7.4 min; acquisition matrix = 256 x 256, slice thickness/gap = 1/0 mm, TI/TR/TE = 900/2300/2.3 ms, flip angle = 8 deg, and field of view (FOV) = 256 x 256 mm^2. The rs-fMRI data were acquired using an echo-planar image sequence: 30 axial slices, acquisition matrix = 64 x 64, slice thickness/gap = 5/0.5 mm, repetition time = 2,000 ms, echo time = 30 ms, and FOV = 192 x 192 mm^2. The T2 images were acquired with a turbo-spin echo (TSE) sequence along the axial plane (33 axial slices; matrix size = 448 x 406, slice thickness/gap = 3/0.9 mm, repetition time = 5,000 ms, echo time = 105 ms, flip angle = 150 deg, and FOV = 220 x 199 mm^2).

Lesion Mapping

To define the lesion feature of each patient anatomically, we first coregistered and resliced the T2 images to the native space of the averaged 3D images with the trilinear interpolation method in SPM12 (SPM12; Wellcome Department of Imaging Neuroscience, University College London, UK). Then, the images were normalized to the Montreal Neurological Institute (MNI) template with a spatial resolution of 1 × 1 × 1 mm. The resulting images were manually traced by a senior neurosurgeon (L.J.) with MRIcron software (http://people.cas.sc.edu/rorden/mricron.html). A volume of interest (VOI) was created for each patient. Delineation of the affected volume was based on the same criterion for all glioma patients: the entire hyperintense portion of the coregistered 3D T2-weighted images. A

neurologist (T.Y.Y.) reviewed all segmentations a second time, paying special attention to the borders of the lesions and the degree of white matter disease. Then, we used the MATLAB script get_totals provided by Ridgway (www.cs.ucl.ac.uk/staff/g.ridgway/vbm/get_totals.m.) to obtain the tumor volume (TV) of every patient. Finally, patients' tumor masks of the four subgroups were separately stacked together to construct overlapping tumor images, which are displayed in **Figure 1**.

Image Preprocessing

Preprocessing was conducted using the DPABI toolbox (http://rfmri.org/dpabi). The first 10 volumes were discarded to allow for saturation effects and magnetization equilibrium. Then, the remaining images were slice-timing corrected, motion corrected, aligned with the anatomical scan, normalized to the MNI space, resampled to 3.0 mm^3, and spatially smoothed with a 4-mm FWHM Gaussian kernel. The linear trend was removed for the time series of each voxel, and several nuisance signals, including Friston's 24 head motion parameter, white matter and cerebrospinal fluid signals, were regressed out. Notably, we did not regress out the global signal because this procedure remains controversial. Finally, temporal bandpass filtering (0.01–0.08 Hz) was applied to the time courses. Of the 112 patients, three were excluded for excessive head motion (exclusion criteria: 3.0 mm and 3.0 degrees in maximum head motion). Finally, 109 glioma patients and 42 HCs were included, and the demographic data and clinical features of all participants are summarized in **Table 1**. Statistical analyses were conducted using SPSS (IBM, CA, USA), with the alpha level set at $p < 0.05$ for all tests.

Group ICA

We performed ICA using GIFT software (http://icatb.sourceforge.net/, version 1.3b) for MATLAB on all subjects. Thirty independent components (ICs) were created as a group-wide spatial map of the resting-state networks.

LN Analysis

The IC showing the largest and most significant spatial correlation with the LN in the resting-state networks (RSNs) template (http://findlab.stanford.edu/functional_ROIs.htm) was selected by the software as the target network to study. Then, we obtained the mask of the LN consisting of eight separated cerebral clusters obtained at a threshold of T > 5.0 and two cerebellar clusters at a threshold of T > 3.0. This map was intended to identify the peak voxel coordinates of the LN for seed placement in the seed-based FC analysis. The LN maps identified by group-level ICA were shown in **Figure 2** and included the bilateral inferior frontal gyri (bi-IFG), bilateral middle frontal gyri (bi-MFG), bilateral superior temporal gyri (bi-STG), medial cingulate cortices (anterior, posterior), and bilateral cerebellar cortices.

FC Analysis

A 6 mm spherical region of interest (ROI) was placed at the peak voxel of each LN cluster in the MNI template space. The LN

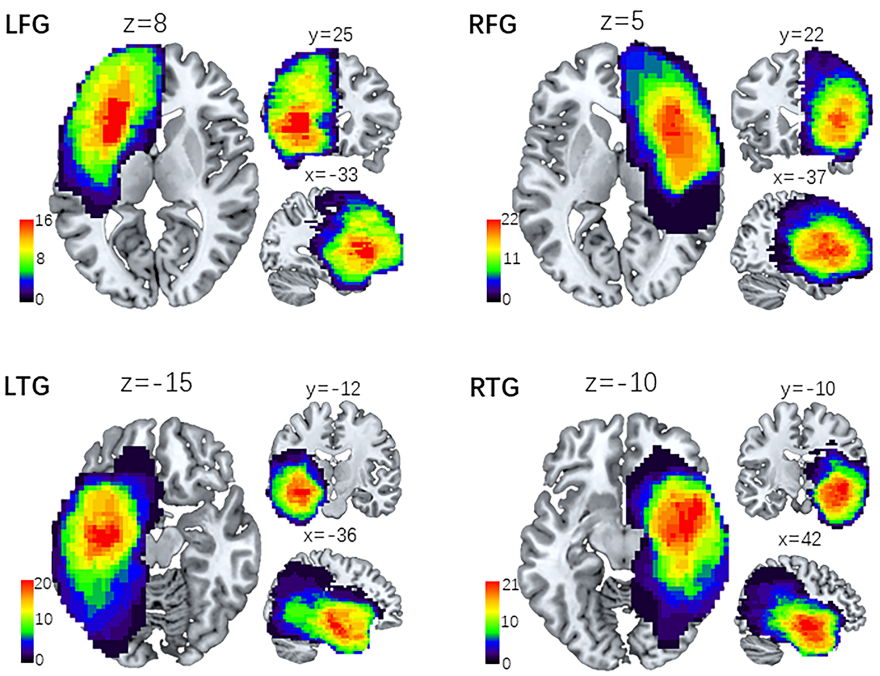

FIGURE 1 | Lesion overlap maps of four subgroups of patients. Lesion distributive density maps are obtained by stacking together the manually traced tumor volume of interest (VOI). Then, the four groups of lesion maps are overlapped onto the MNI template separately. The coordinates (x, y, z) represent three dimensional positions on the standard template, and the color bar indicates the number of VOI in a given voxel. LFG, left frontal glioma; LTG, left temporal glioma; RFG, right frontal glioma; RTG, right temporal glioma.

TABLE 1 | Sample demographic and clinical characteristics.

Variable	LFG(27)	LTG(26)	RFG(29)	RTG(27)	HC(42)	F/χ^2	*P*
Age (mean ± SD, y)	45.04 ± 12.82	42.35 ± 11.53	40.76 ± 12.68	43.44 ± 13.93	39.55 ± 9.96	0.842	0.501[a]
Gender (M/F)	15/12	10/16	15/14	18/9	24/18	4.524	0.340[b]
Education (mean ± SD, y)	11.37 ± 3.58	13.12 ± 3.99	12.61 ± 3.78	11.93 ± 4.70	13.71 ± 3.79	1.776	0.137[a]
Tumor volume (mean ± SD, cm^3)	106.6 ± 64.60	85.58 ± 44.69	110.7 ± 67.60	98.16 ± 66.77	–	0.866	0.461[a]
MMSE (mean ± SD)	28.11 ± 1.78	27.00 ± 3.62	27.41 ± 2.73	28.11 ± 2.61	29.48 ± 1.11	5.345	0.0005[a]
Language score	8.89 ± 0.32	8.35 ± 1.16	8.62 ± 0.62	8.56 ± 0.80	8.83 ± 0.49	2.75	0.03[a]
BDI (mean ± SD)	3.82 ± 4.23	2.77 ± 4.07	4.57 ± 4.93	4.11 ± 4.36	2.50 ± 3.60	1.452	0.220[a]
KPS (mean ± SD)	82.59 ± 11.30	85.77 ± 8.09	81.38 ± 11.25	81.84 ± 14.86	100.0 ± 0.00	23.98	<0.0001[a]
Pathological types							
Low-grade glioma	15	13	15	12	–		
Anaplastic astrocytoma/oligodendroglioma	7	8	5	4	–	5.66	0.462[b]
Glioblastoma	5	5	9	11	–		
Pathological grades							
Low-grade glioma(WHO I/II)	15	13	15	12	–	0.692	0.875[b]
High-grade glioma(WHO III/IV)	12	13	14	15	–		

BDI, Beck depression inventory; F, female; HC, healthy control; KPS, Karnofsky performance scale; LFG, left frontal glioma; LTG, left temporal glioma; M, male; MMSE, Mini mental state examination; NA, not applicable; RFG, right frontal glioma; RTG, right temporal glioma; SD =standard deviation; TV, tumor volume; [a]p-value obtained using one-way ANOVA; [b]p-value obtained using Pearson's chi-square test.

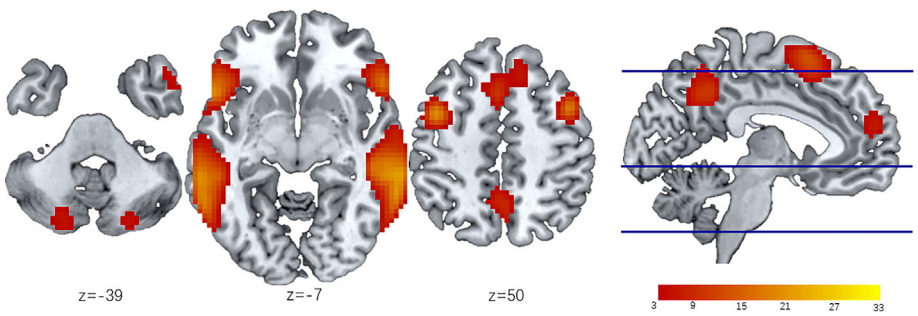

FIGURE 2 | LN identified by ICA of all participants. The LN is extracted from 30 independent components obtained from Independent component analysis (ICA). Then the group level LN map is overlap onto the MNI template to create resting state spatial map of all participants (n=109). Eight separated cerebral clusters are obtained at a threshold of T > 5.0 and two cerebellar clusters are obtained at a threshold of T > 3.0. The z-coordinates represent axial positions on the standard space, and the color bar indicates the T value of LN modules. ICA, independent component analysis; LN, language network.

ROIs and their MNI coordinates are delineated in **Table 2**. Mean signals extracted from the nodes were correlated with each other using Pearson's correlation coefficient (r), resulting in a total of forty-five connectivity measurements (edges). These correlation coefficients were then converted to Z-scores using Fisher's transformation. An independent two-sample t test was performed to compare all edge values in each patient subgroup with those in HCs. A threshold of one-tailed false discovery rate (FDR)-corrected $p < 0.05$ was applied to correct for multiple comparisons. These significantly reduced edges were classified as two different types: reduced edges connected with nodes within tumor located subsystems, which indicated connections directedly affected by tumor infiltration, and reduced edges connected between nodes in non-neoplastic modules, which suggested connections undirectedly disturbed by gliomas. Furthermore, the chi-square test was performed to analyze differences in the numbers of the two different edges between left and right hemisphere gliomas (LFG, LTG vs. RFG, RTG). $p < 0.05$ was considered statistically significant.

NC Analysis

We selected homotopic ROIs (the same location on opposite hemispheres), including the bi-IFG, bi-MFG, and bi-STG, to balance the seed regions to obtain mNC representing ipsi/contralesional intrahemispheric and interhemispheric connectivity. The mNC values among the ROIs within the left and right hemispheres (intra/within-hemisphere, l/rFCw), among the ROIs between the left and right hemispheres (inter/between-hemisphere, FCb), and among all ROIs of the LN (global, FCg) were calculated by reducing each subject's FC correlation matrix into a single variable, separately. NC analysis results were entered into one-way ANOVA. Finally, correlations between TV and mNC (l/rFCw, FCb, and FCg) were assessed by using Pearson coefficients.

TABLE 2 | List of the language network modules.

LN modules	Module size (in voxels)	Peak MNI Coordinates			T score peak level
		X	Y	Z	
lIFG	218	-51	21	-9	10.93
lSTG	955	-57	-57	12	16.27
lMFG	136	-45	3	48	11.30
rIFG	127	54	24	-6	8.26
rSTG	1,149	60	-51	12	19.82
rMFG	104	45	9	45	9.86
l/rSFG	109	-3	12	57	7.85
l/rPC	133	0	-57	39	8.39
lCPL	92	-21	-78	-39	3.47
rCPL	43	21	-81	-42	3.17

The language network modules identified by ICA. The MNI coordinates of peak voxels are listed in the table. ICA, independent component analysis; LN, language network; lIFG, left inferior frontal gyrus; lSTG, left superior temporal gyrus; lMFG, left middle frontal gyrus; l/rSFG, left/right superior frontal gyrus; l/rPC, left/right precuneus; lCPL, left cerebellum posterior lobe; MNI, Montreal Neurological Institute. rIFG, right inferior frontal gyrus; rSTG, right superior temporal gyrus; rMFG, right middle frontal gyrus; rCPL, right cerebellum posterior lobe.

Data Availability

Anonymized data and data analysis pipeline will be shared by request from any qualified investigator.

RESULTS

Demographic Data

109 glioma patients and forty-two demographically matched HCs were studied (**Table 1**): LFG (15 males/12 females, mean age 45.04 ± 12.82 years); LTG (10 males/16 females, mean age 42.35 ± 11.53 years); RFG (15 males/14 females, mean age 40.76 ± 12.68 years); RTG (18 males/9 females, mean age 43.44 ± 13.93 years); and HCs (24 males/18 females, mean age 39.55 ± 9.96 years). There were no significant differences among the five groups in age [F (4, 146) = 0.84; p =0.50], the distribution of sex (χ^2 = 4.52; p =0.34), or level of education [F (4, 146) = 1.77; p = 0.14]. Although language scores derived from MMSE sections demonstrated a significant difference among patient groups and HCs [F (4, 146) = 2.75; p =0.03], no remarkable difference was found among the four patient groups [F (3, 105) = 1.77; p = 0.09]. And the pathological types and grades of glioma also showed no difference (χ^2 = 5.66, p =0.462; χ^2 = 0.692, p =0.875).

Reduced FC Patterns in Glioma Patients

In glioma patients, we found significantly reduced FC of LN in comparison with HCs. **Figure 3** shows the distribution of FC edges with a significant reduction for the four subgroups (detailed results of the T values can be seen in the **Supplementary material, Table S1**). More importantly, we found that the left hemisphere lesions (LFG, LTG) caused much more severe disturbance to the whole-brain LN topology than the right hemisphere lesions (RFG, RTG) by comparing the numbers of reduced edges connected with nodes within tumor located subsystems (directly affected by gliomas) with edges connected between nodes in non-neoplastic modules (undirectedly disturbed by gliomas) (χ^2 = 6.399, p=0.011, **Supplementary Results, Table S2**).

Reduced NC at the Hemisphere Level

Having demonstrated the single-edge FC decrease in the LN in all subgroups, we further studied alterations in FC at the hemisphere level. One-way ANOVA was separately performed for mNC (l/rFCw, FCb, and FCg) among the four subgroups of patients and HCs (**Figure 4**). Specifically, in terms of FCb and FCg, Tukey's test for multiple comparisons suggested significant differences between the HC and all four tumor subgroups (FCb: LFG p=0.003, LTG p=0.001, RFG p<0.001, RTG p<0.001, **Figure 4C**; FCg: LFG p=0.005, LTG p<0.001, RFG p=0.014, RTG p<0.001, **Figure 4D**). Interestingly, *post hoc* analysis confirmed that patients with left hemisphere lesions exhibited a simultaneous decrease in bilateral FCw (l/rFCw) compared with HCs (LFG: lFCw p=0.011, rFCw p=0.014; LTG: lFCw p=0.002, rFCw p=0.002, **Figures 4A, B**), while patients with right hemisphere lesions only exhibited a significant difference in ipsilesional FCw (rFCw) (RFG: lFCw p=0.760, rFCw p<0.001; RTG: lFCw p=0.200, rFCw p=0.007, **Figures 4A, B**). There was no difference in any aspect of mNC among the four subgroups of patients.

In addition, we did not find a remarkable difference between lFCw and rFCw in HCs using the paired t test [t(41)=0.893, p=0.377, **Supplementary Results, Figure S2**], indicating that the strength of LNFC between the left and right hemispheres is almost equivalent under normal circumstances. Based on this result, we then explored whether there is a difference in ipsilesional versus contralesional FC (ipsi-FCw, con-FCw) using repeated measures ANOVA with FCw as a within-subject factor and group as a between-subject factor. We found a main effect of FCw [F(1,109)=4.98, p=0.028], indicating that ipsilesional FC (mean=0.35) decreased, on average, much more significantly than contralesional FC (mean=0.41) for all glioma patients. Second, when considering the l/rFCw of each subgroup separately, there was a significant difference only in the RFG subgroup (paired t test: LFG p=0.564; LTG p=0.743; RFG p=0.018; RTG p=0.396; **Supplementary Results, Figure S3**)

Association of LNFC With Glioma Topography

Next, we investigated the extent to which lesion topography explained the decrease in FC within LN in glioma patients. For the four subgroups of patients, we separately tested the relationship between brain lesions and mNC (l/rFCw, FCb, and FCg) using a univariate correlation with TV. For left hemisphere lesions (LFG, LTG), TV was negatively correlated with ipsilesional (lFCw: LFG, R_{27}=-0.479, p=0.012; LTG, R_{26}=-0.606, p=0.001, **Figures 5A, B**), interhemispheric (FCb: LFG, R_{27}=-0.510, p=0.007; LTG, R_{26}=-0.479, p=0.013, **Figures 5E, F**), and global (FCg: LFG, R_{27}=-0.482, p=0.011; LTG, R_{26}=-0.424, p=0.031, **Figures 5E, F**) FC but not with contralesional FC (rFCw: LFG, R_{27}=-0.183, p=0.360; LTG, R_{26}=-0.206, p=0.314, **Figures 5A, B**). However, in regard to the RFG and RTG subgroups, there were no remarkable negative correlations between TV and the four types of

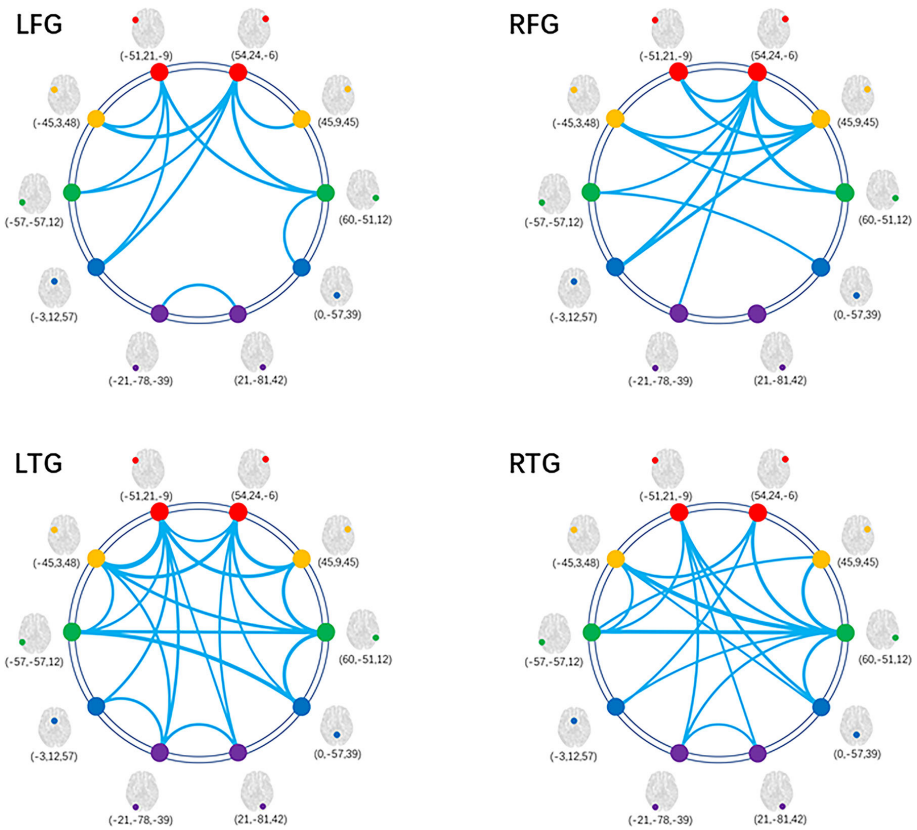

FIGURE 3 | Decreased FC within LN for patient subgroups compared with HCs. Graphical presentation of the decreased FC within LN by comparing the four subgroups of patients with HCs separately. The thickness of lines is proportional to the absolute value of between-group T (one-tailed t test, FDR-corrected $p < 0.05$). FC, functional connectivity; HC, healthy control; LN, language network; LFG, left frontal glioma; LTG, left temporal glioma; RFG, right frontal glioma; RTG, right temporal glioma.

mNC. Interestingly, we found that TV was positively correlated with contralesional intrahemispheric FC (lFCw: RFG, R29 = 0.499, p=0.006; RTG, R27 = 0.448, p=0.019; **Figures 5C, D**). These contradictory results may suggest that tumors located in different language-related areas can reorganize the LN in different manners following the development of gliomas. And the strengths of reorganized mNC can be predicted by lesion volumes, but the prediction was not improved by adding information about lesion topography (pathology, grades). More details can be seen in the Supplementary material (**Supplementary Results, Table S3**).

DISCUSSION

In this study, we identified robust changes in LN synchrony (measured with rs-fMRI) in the setting of gliomas regardless of the specific functional-defined language areas that the tumor was involved with. However, the reduced pattern in LNFC following glioma development was modulated by tumor position. Gliomas in the left hemisphere had a broader impact on LN than gliomas in the right hemisphere, usually with weak connections between nodes located in non-neoplastic modules. Compared with HCs, mNC (l/rFCw, FCb, and FCg) showed a significant reduction in glioma patients (except for lFCw in the right hemisphere glioma subgroups [RFG, RTG]). In addition, mNC has a different correlative relationship with TV depending on the tumor position across hemispheres. These results agree with the proposal that language processing is the product of dynamic interactions among domain-specific and domain-general brain regions (16, 17); therefore, lesions in different eloquent areas have different impacts on the LN.

It is important to note that although the gliomas of the four subgroups led to a similarly widespread decrease in LNFC, their functional profiles varied considerably. In lesion-functional topography studies, one of the key methods often used to determine the importance of an area in network communication is to examine how much the network properties change if a given area is damaged (18). Core regions, also known as lesion hubs under disease status, have the greatest contribution to the functional network and are highly indispensable in the healthy network systems. Damage to these areas can have a fatally widespread effect on the transmission of information throughout the system (19, 20). Our study found that left frontotemporal subsystem

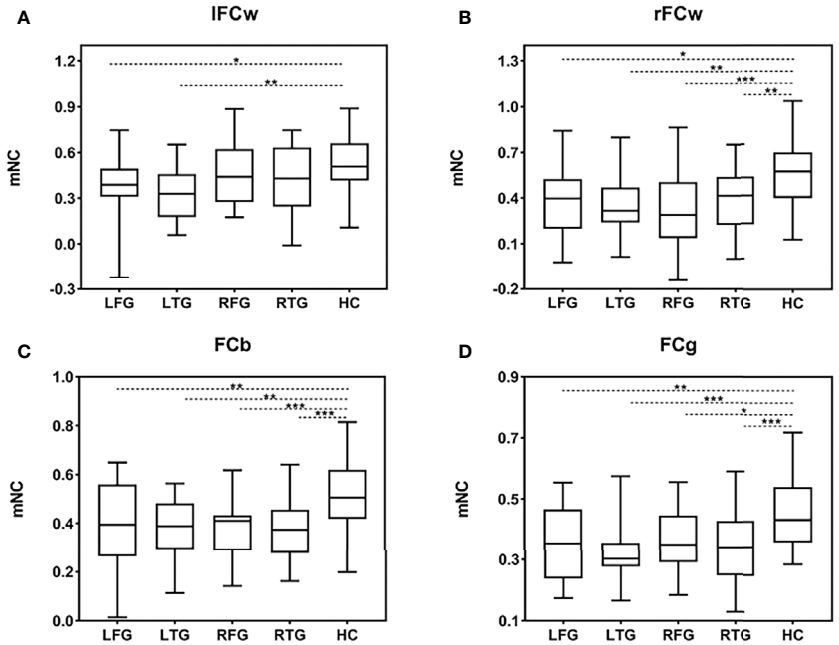

FIGURE 4 | mNC differences among the four subgroups of patients and HCs. **(A–D)** Group differences in mNC (l/rFCw, FCb, and FCg) among the four subgroups of patients and HCs. Significant mNC differences are observed between the four subgroups of patients and HCs except for lFCw in the groups of RFG and RTG. Post hoc analysis shows that there is no difference in any aspect of mNC among the four subgroups of patients. Error bars represent one standard error of the mean (SEM). (*$p < 0.05$; **$p < 0.01$; ***$p < 0.001$). FCb, inter/between-hemisphere functional connectivity; FCg, global functional connectivity; HC, healthy control; LFG, left frontal glioma; LTG, left temporal glioma; lFCw, left intra/within-hemisphere functional connectivity; mNC, mean network connectivity; rFCw, right intra/within-hemisphere functional connectivity; RFG, right frontal glioma; RTG, right temporal glioma.

gliomas strongly affected global LN communication, with the overwhelming majority of reduced edges away from the lesion sites, indicating that the transmission of information among remote modules in LN has been significantly disturbed. However, for right frontotemporal subsystem gliomas, most of the affected edges were connected with lesion sites, highlighting that disturbance to the right frontotemporal subsystems induced limited impacts on the whole network topology. With voxel-based lesion symptom mapping in mind, our study supports the hypothesis that both left frontal and temporal subsystems are the "core" regions of the LN; on the other hand, right frontal and temporal subsystems are the "periphery" regions (16, 17, 21).

From a core-periphery linguistic point of view, inter- and intrahemispheric FC was studied to identify specific alterations in mNC in the presence of gliomas. We found that the LFG and LTG subgroups demonstrated a consistent pattern in which mNC (l/rFCw, FCb, and FCg) decreased significantly in comparison with HCs. Moreover, decreased mNC between the two subgroups suggested no significant differences among the four types of mNC. By contrast, patients with right hemispheric gliomas (RFG, RTG) did not exhibit a remarkable decrease in mNC in the left frontotemporal subnetwork (lFCw) compared with HCs. Thus, our subsequent hemisphere level studies suggested that the LN was implemented in the model of left-dominant organization, damage to which has a very large disturbance on the LN, not only in communication among the left frontotemporal subnetwork but also in the structurally intact right frontotemporal subnetwork that participates in language processing (22). Furthermore, given the different alterations of left frontotemporal subnetwork, lFCw may be considered a sensitive indicator for distinguishing the extent of LNFC reorganization in the context of gliomas before surgery.

Most previous studies have revealed that the left frontotemporal network is crucial and specialized for language functions (23, 24). Comprehension and repetition deficits are associated with left frontotemporal brain damage, and lesion-deficit studies have revealed that lesion volume and the fractional anisotropy (FA) value of subcortical tissue are significantly correlated with the severity of impairment in language behavior (25, 26). Furthermore, the right hemisphere contributes to linguistic processing and working memory, which are needed for normal speech comprehension dynamically (27). Pathologies on the right temporal and frontal cortex tend to have a selective effect on language performance (e.g., cognitive control, working memory, executive function) (7, 28). However, our combined bilateral glioma study confirmed that right hemisphere structural damage only diminished subnetwork level connections among the periphery (rFCw) rather than core modules (lFCw). Thus, some aspects of key language functions may still be preserved in right hemisphere glioma patients; however, their language systems could be less synchronized, diminishing their ability to adapt dynamically to language processing demands (29).

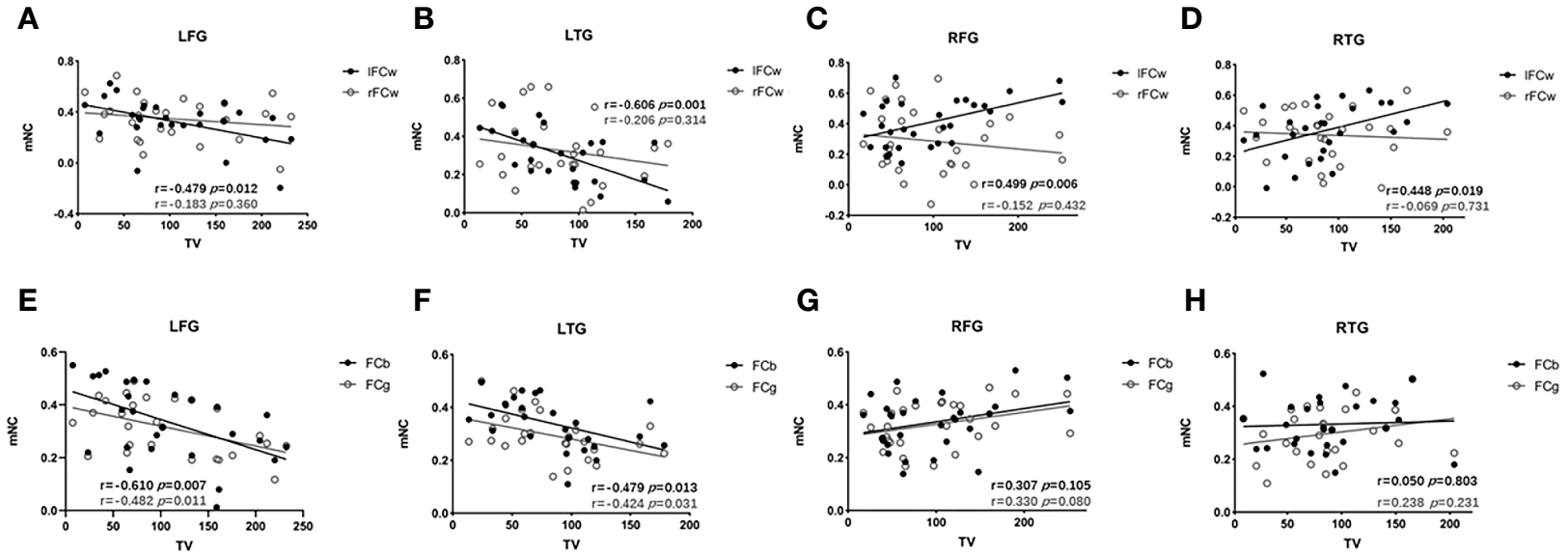

FIGURE 5 | Associations between mNC and TV. Associations between mNC (l/rFCw, FCb, and FCg) and lesion volume. For LFG and LTG, TV is negatively correlated with ipsilesional (lFCw: LFG, R_{27}=-0.479, p=0.012; LTG, R_{26}=-0.606, p=0.001, **A, B**), interhemispheric (FCb: LFG, R_{27}=-0.510, p=0.007; LTG, R_{26}=-0.479, p=0.013, **E, F**), and global (FCg: LFG, R_{27}=-0.482, p=0.011; LTG, R_{26}=-0.424, p=0.031, **(E, F)**; while, for the RFG and RTG, positive correlations are found between lFCw and TV (lFCw: RFG, R_{29} = 0.499, p=0.006; RTG, R_{27} = 0.448, p=0.019; **(C, D)** and there are no remarkable negative correlations between TV and the other types of mNC (rFCw: RFG, R29 = -0.152, p=0.432, RTG, R27 = -0.069, p=0.731, C, D; FCb: RFG, R29 = 0.307, p=0.105, RTG, R27 = 0.050, p=0.803; FCg: RFG, R29 = 0.330, p=0.080, RTG, R27 = 0.238, p=0.231, **G, H**). FCb, inter/between-hemisphere functional connectivity; FCg, global functional connectivity; lFCw, left intra/within-hemisphere functional connectivity; LFG, left frontal glioma; LTG, left temporal glioma; mNC, mean network connectivity; rFCw, right intra/within-hemisphere functional connectivity; RFG, right frontal glioma; RTG, right temporal glioma; TV, tumor volume.

The neurological mechanism underlying FC reduction between LN modules following glioma remains unclear. A possible explanation is the neurovascular uncoupling (NVU) –the abnormal tumor neo-vasculature may arouse disturbances over neuronal metabolism and neurotransmitter, which would affect the consistency and synchrony of neural functional activities at the whole brain level (30–32). In line with this notion, our findings additionally highlighted that the disturbances of connectivity with LN were associated with pathological topographies, especially lesion volumes and sites. For left hemisphere lesions (LFG, LTG), mNC, including ipsilesional intrahemispheric (lFCw), interhemispheric (FCb), and global (FCg) FC, was negatively correlated with TV. However, for right hemisphere lesions (RFG, RTG), there were no negative correlations between TV and the four types of mNC. Notably, although right hemispheric gliomas did not exhibit a significant decrease in contralesional intrahemispheric FC (lFCw) compared with HCs, a positive correlation was demonstrated between TV and lFCw. These interesting results suggest that disrupted communication among modules of LN is a central feature of left hemisphere lesions. Conversely, for right hemisphere lesions, it was likely to exist a dynamic functional compensation among LN core modules associated with tumor progression, which reflect the reconfiguration mechanism of core-periphery subsystems to regions most capable of meeting linguistic operations.

Our study found that the human language system retains functional organization under a hierarchical network framework, the processing of which depends on bilateral frontotemporal language areas. Language deficits can arise not only from a pure disruption in functionally specialized cores but also from a disturbance of communication among the functionally interconnected remote modules within LN (33). As demonstrated by numerous functional imaging studies, language disorders are well predicted both by lesion topography and FC: the former's primary principle is that specific language functions dominate in specific regions of the brain, and the latter is based on the theory that high-level cognitive function is embedded with the connections among a large-scale functional network. Importantly, in addition to lesion-behavior and FC-behavior mapping, our study provides a more fundamental association between lesion topography and LNFC on the basis of cognitive functional studies. Given recent evidence for network data to provide prognostic markers (34–36), particularly in relation to postsurgical language outcomes, it is therefore anticipated that a combination of core-periphery connectome models with brain lesion topography will further our understanding of associated language dysfunctions and the likelihood of recovery following an operation—a crucial factor in facilitating surgical strategies and improving the care of glioma patients.

CONCLUSIONS

Our findings emphasize the importance of considering the modulatory effects of core-periphery mechanisms when considering language reconfiguration for glioma patients from a network perspective. Lesion-behavior and FC-behavior models are important predictors for language dysfunction. The correlative relationship of these two factors suggests that a much broader approach is needed to evaluate language functional reorganization following glioma development. Recent evidence indicates that language recovery after surgery in glioma patients is linked to the organization patterns of the presurgical language system (37). Therefore, our findings of LN core-periphery organizational forms may provide the surgeon a reference to optimize resection of gliomas while maintaining a functional balance as well as a unique opportunity to further our understanding of the language system.

DATA AVAILABILITY STATEMENT

The raw data supporting the conclusions of this article will be made available by the authors, without undue reservation.

ETHICS STATEMENT

The studies involving human participants were reviewed and approved by the Ethics Committee of Beijing Tiantan Hospital. The patients/participants provided their written informed consent to participate in this study.

AUTHOR CONTRIBUTIONS

LJ: design and conceptualized study, analyzed the data, and drafted the manuscript for intellectual content. CL: design and conceptualized study. YZ: design and conceptualized study. TY: major role in the acquisition of data. JY: major role in the acquisition of data. ZZ: interpreted the data and revised the manuscript for intellectual content. SG: interpreted the data and revised the manuscript for intellectual content. All authors contributed to the article and approved the submitted version.

FUNDING

Our study is funded by Beijing Municipal Science & Technology Commission (Grant No. Z171100000117002), Beijing Municipal Science & Technology Commission (Grant No. Z191100006619087), and National Natural Science Foundation of China (Nos. 61872020).

SUPPLEMENTARY MATERIAL

The Supplementary Material for this article can be found online at: https://www.frontiersin.org/articles/10.3389/fonc.2021.617179/full#supplementary-material

REFERENCES

1. Dronkers NF, Wilkins DP, Van Valin RD, Redfern BB, Jaeger JJ. Lesion analysis of the brain areas involved in language comprehension. *Cognition* (2004) 92:145–77. doi: 10.1016/j.cognition.2003.11.002
2. Just MA, Carpenter PA, Keller TA, Eddy WF, Thulborn KR. Brain activation modulated by sentence comprehension. *Science (New York N Y)* (1996) 274:114–6. doi: 10.1126/science.274.5284.114
3. Duffau H. The huge plastic potential of adult brain and the role of connectomics: new insights provided by serial mappings in glioma surgery. *Cortex J Devoted Study Nerv Syst Behav* (2014) 58:325–37. doi: 10.1016/j.cortex.2013.08.005
4. Cho NS, Peck KK, Zhang Z, Holodny AI. Paradoxical Activation in the Cerebellum During Language fMRI in Patients with Brain Tumors: Possible Explanations Based on Neurovascular Uncoupling and Functional Reorganization. *Cerebellum (Lond Engl)* (2018) 17:286–93. doi: 10.1007/s12311-017-0902-5
5. Campbell KL, Tyler LK. Language-related domain-specific and domain-general systems in the human brain. *Curr Opin Behav Sci* (2018) 21:132–7. doi: 10.1016/j.cobeha.2018.04.008
6. Sollmann N, Tanigawa N, Ringel F, Zimmer C, Meyer B, Krieg SM. Language and its right-hemispheric distribution in healthy brains: an investigation by repetitive transcranial magnetic stimulation. *NeuroImage Null* (2014) 70:185–95. doi: 10.1016/j.neuroimage.2014.09.002
7. Gajardo-Vidal A, Lorca-Puls DL, Hope TMH, Parker Jones O, Seghier ML, Prejawa S, et al. How right hemisphere damage after stroke can impair speech comprehension. *Brain: J Neurol* (2018) 141:3389–404. doi: 10.1093/brain/awy270
8. Hagoort P. The core and beyond in the language-ready brain. *Neurosci Biobehav Rev* (2017) 81:194–204. doi: 10.1016/j.neubiorev.2017.01.048
9. Fedorenko E, Behr MK, Kanwisher N. Functional specificity for high-level linguistic processing in the human brain. *Proc Natl Acad Sci U S A* (2011) 108:16428–33. doi: 10.1073/pnas.1112937108
10. Zhang N, Xia M, Qiu T, Wang X, Lin CP, Guo Q, et al. Reorganization of cerebro-cerebellar circuit in patients with left hemispheric gliomas involving language network: A combined structural and resting-state functional MRI study. *Hum Brain Mapp* (2018) 39:4802–19. doi: 10.1002/hbm.24324
11. Briganti C, Sestieri C, Mattei PA, Esposito R, Galzio RJ, Tartaro A, et al. Reorganization of functional connectivity of the language network in patients with brain gliomas. *AJNR Am J Neuroradiol* (2012) 33:1983–90. doi: 10.3174/ajnr.A3064
12. He X, Bassett DS, Chaitanya G, Sperling MR, Kozlowski L, Tracy JI. Disrupted dynamic network reconfiguration of the language system in temporal lobe epilepsy. *Brain: J Neurol* (2018) 141:1375–89. doi: 10.1093/brain/awy042
13. Oldfield RC. The assessment and analysis of handedness: the Edinburgh inventory. *Neuropsychologia* (1971) 9:97–113. doi: 10.1016/0028-3932(71)90067-4
14. Clancey JK. Karnofsky performance scale. *J Neurosci Nurs J Am Assoc Neurosci Nurses* (1995) 27:220.
15. Reiland SA. Beck Depression Inventory. In: V Zeigler-Hill, TK Shackelford, editors. *Encyclopedia of Personality and Individual Differences*. Cham: Springer International Publishing (2017). p. 1–3. doi: 10.1007/978-3-319-28099-8_6-1
16. Rodd JM, Johnsrude IS, Davis MH. The role of domain-general frontal systems in language comprehension: evidence from dual-task interference and semantic ambiguity. *Brain Lang* (2010) 115:182–8. doi: 10.1016/j.bandl.2010.07.005
17. Klimovich-Gray A, Bozic M. Domain-general and domain-specific computations in single word processing. *NeuroImage Undefined* (2019) 202:116112. doi: 10.1016/j.neuroimage.2019.116112
18. Gratton C, Nomura EM, Pérez F, D'Esposito M. Focal brain lesions to critical locations cause widespread disruption of the modular organization of the brain. *J Cogn Neurosci* (2012) 24:1275–85. doi: 10.1162/jocn_a_00222
19. Honey CJ, Sporns O. Dynamical consequences of lesions in cortical networks. *Hum Brain Mapp* (2008) 29:802–9. doi: 10.1002/hbm.20579
20. Aerts H, Fias W, Caeyenberghs K, Marinazzo D. Brain networks under attack: robustness properties and the impact of lesions. *Brain J Neurol* (2016) 139:3063–83. doi: 10.1093/brain/aww194
21. Kiran S, Thompson CK. Neuroplasticity of Language Networks in Aphasia: Advances, Updates, and Future Challenges. *Front Neurol* (2019) 10:295. doi: 10.3389/fneur.2019.00295
22. Hickok G, Poeppel D. The cortical organization of speech processing. *Nat Rev Neurosci* (2007) 8:393–402. doi: 10.1038/nrn2113
23. Yang M, Li Y, Li J, Yao D, Liao W, Chen H. Beyond the Arcuate Fasciculus: Damage to Ventral and Dorsal Language Pathways in Aphasia. *Brain Topogr* (2017) 30:249–56. doi: 10.1007/s10548-016-0503-5
24. Rosso C, Vargas P, Valabregue R, Arbizu C, Henry-Amar F, Leger A, et al. Aphasia severity in chronic stroke patients: a combined disconnection in the dorsal and ventral language pathways. *Neurorehabil Neural Repair* (2015) 29:287–95. doi: 10.1177/1545968314543926
25. Han Z, Ma Y, Gong G, He Y, Caramazza A, Bi Y. White matter structural connectivity underlying semantic processing: evidence from brain damaged patients. *Brain: J Neurol* (2013) 136:2952–65. doi: 10.1093/brain/awt205
26. Kümmerer D, Hartwigsen G, Kellmeyer P, Glauche V, Mader I, Klöppel S, et al. Damage to ventral and dorsal language pathways in acute aphasia. *Brain: J Neurol* (2013) 136:619–29. doi: 10.1093/brain/aws354
27. Yang X, Zhang X, Yang Y, Lin N. How context features modulate the involvement of the working memory system during discourse comprehension. *Neuropsychologia* (2018) 111:36–44. doi: 10.1016/j.neuropsychologia.2018.01.010
28. Dietrich S, Hertrich I, Seibold VC, Rolke B. Discourse management during speech perception: A functional magnetic resonance imaging (fMRI) study. *NeuroImage* (2019) 202:116047. doi: 10.1016/j.neuroimage.2019.116047
29. Fedorenko E, Thompson-Schill SL. Reworking the language network. *Trends Cogn Sci* (2014) 18:120–6. doi: 10.1016/j.tics.2013.12.006
30. Fraga de Abreu VH, Peck KK, Petrovich-Brennan NM, Woo KM, Holodny AI. Brain Tumors: The Influence of Tumor Type and Routine MR Imaging Characteristics at BOLD Functional MR Imaging in the Primary Motor Gyrus. *Radiology* (2016) 281:876–83. doi: 10.1148/radiol.2016151951
31. Hou BL, Bradbury M, Peck KK, Petrovich NM, Gutin PH, Holodny AI. Effect of brain tumor neovasculature defined by rCBV on BOLD fMRI activation volume in the primary motor cortex. *NeuroImage* (2006) 32:489–97. doi: 10.1016/j.neuroimage.2006.04.188
32. Holodny AI, Schulder M, Liu WC, Wolko J, Maldjian JA, Kalnin AJ. The effect of brain tumors on BOLD functional MR imaging activation in the adjacent motor cortex: implications for image-guided neurosurgery. *AJNR Am J Neuroradiol* (2000) 21:1415–22.
33. Abel S, Weiller C, Huber W, Willmes K, Specht K. Therapy-induced brain reorganization patterns in aphasia. *Brain: J Neurol* (2015) 138:1097–112. doi: 10.1093/brain/awv022
34. Geranmayeh F, Leech R, Wise RJS. Network dysfunction predicts speech production after left hemisphere stroke. *Neurology* (2016) 86:1296–305. doi: 10.1212/WNL.0000000000002537
35. Siegel JS, Ramsey LE, Snyder AZ, Metcalf NV, Chacko RV, Weinberger K, et al. Disruptions of network connectivity predict impairment in multiple behavioral domains after stroke. *Proc Natl Acad Sci U S A* (2016) 113:E4367–76. doi: 10.1073/pnas.1521083113
36. Herbet G, Maheu M, Costi E, Lafargue G, Duffau H. Mapping neuroplastic potential in brain-damaged patients. *Brain: J Neurol* (2016) 139:829–44. doi: 10.1093/brain/awv394
37. Kristo G, Raemaekers M, Rutten GJ, de Gelder B, Ramsey NF. Inter-hemispheric language functional reorganization in low-grade glioma patients after tumour surgery. *Cortex J Devoted Study Nerv Syst Behav* (2015) 64:235–48. doi: 10.1016/j.cortex.2014.11.002

Conflict of Interest: The authors declare that the research was conducted in the absence of any commercial or financial relationships that could be construed as a potential conflict of interest.

frontiers in Oncology

BRIEF RESEARCH REPORT
published: 22 March 2021
doi: 10.3389/fonc.2021.651137

Quantitative Multicomponent T2 Relaxation Showed Greater Sensitivity Than Flair Imaging to Detect Subtle Alterations at the Periphery of Lower Grade Gliomas

Pietro Bontempi[1]*, *Umberto Rozzanigo*[2], *Dante Amelio*[1], *Daniele Scartoni*[1], *Maurizio Amichetti*[1] and *Paolo Farace*[1]

[1] Proton Therapy Unit, Hospital of Trento, Azienda Provinciale per i Servizi Sanitari (APSS), Trento, Italy, [2] Radiology Department, Hospital of Trento, Azienda Provinciale per i Servizi Sanitari (APSS), Trento, Italy

OPEN ACCESS

Edited by:
Cornelia Brendle,
Tübingen University Hospital,
Germany

Reviewed by:
Alexander Lloyd MacKay,
University of British Columbia, Canada
Yajun Ma,
University of California, San Diego,
United States

***Correspondence:**
Pietro Bontempi
pietro.bontempi@univr.it

Specialty section:
This article was submitted to Cancer Imaging and Image-directed Interventions, a section of the journal Frontiers in Oncology

Received: 08 January 2021
Accepted: 02 March 2021
Published: 22 March 2021

Citation:
Bontempi P, Rozzanigo U, Amelio D, Scartoni D, Amichetti M and Farace P (2021) Quantitative Multicomponent T2 Relaxation Showed Greater Sensitivity Than Flair Imaging to Detect Subtle Alterations at the Periphery of Lower Grade Gliomas. Front. Oncol. 11:651137. doi: 10.3389/fonc.2021.651137

Purpose: To demonstrate that quantitative multicomponent T2 relaxation can be more sensitive than conventional FLAIR imaging for detecting cerebral tissue abnormalities.

Methods: Six patients affected by lower-grade non-enhancing gliomas underwent T2 relaxation and FLAIR imaging before a radiation treatment by proton therapy (PT) and were examined at follow-up. The T2 decay signal obtained by a thirty-two-echo sequence was decomposed into three main components, attributing to each component a different T2 range: water trapped in the lipid bilayer membrane of myelin, intra/extracellular water and cerebrospinal fluid. The T2 quantitative map of the intra/extracellular water was compared with FLAIR images.

Results: Before PT, in five patients a mismatch was observed between the intra/extracellular water T2 map and FLAIR images, with peri-tumoral areas of high T2 that typically extended outside the area of abnormal FLAIR hyper-intensity. Such mismatch regions evolved into two different types of patterns. The first type, observed in three patients, was a reduced extension of the abnormal regions on T2 map with respect to FLAIR images (T2 decrease pattern). The second type, observed in two patients, was the appearance of new areas of abnormal hyper-intensity on FLAIR images matching the anomalous T2 map extension (FLAIR increase pattern), that was considered as asymptomatic radiation induced damage.

Conclusion: Our preliminarily results suggest that quantitative T2 mapping of the intra/extracellular water component was more sensitive than conventional FLAIR imaging to subtle cerebral tissue abnormalities, deserving to be further investigated in future clinical studies.

Keywords: magnetic resonance imaging, radiotherapy, glioma, multicomponent T2 analysis, myelin water imaging, relaxometry

INTRODUCTION

Non-invasive characterization of brain water can provide valuable insights for a better understanding of pathologic conditions affecting the central nervous system (CNS). Previous studies have used T2 relaxometry to investigate brain water (1), as the T2 distribution for normal brain *in vivo* can be represented by multiple components, corresponding to water in different compartments (2). A short T2 component (T2 around time = 10–50 ms) has been associated with water trapped between myelin bilayers, an intermediate component (T2 around 60–100 ms) has been linked to intra/extracellular water and a long T2 component has been associated with cerebrospinal fluid (CSF).

T2 relaxometry is at the basis of myelin water imaging (MWI) for the quantification of myelin component (3–5). Well-studied applications have been developed to investigate demyelinating diseases in the CNS, such as multiple sclerosis and neuromyelitis optica (6). However, to our knowledge only an attempt to apply multicomponent T2 relaxometry for the investigation of brain tumors has been performed so far (7).

In a prospective study that enrolled patients who received proton irradiation to the CNS, we investigated the potential of multicomponent T2 relaxometry in radiation oncology. Herein, we describe the method for acquisition and analysis of multicomponent T2 relaxometry and the first data obtained on a sample of six lower grade glioma patients. The data accidentally showed that decomposing T2 can be more sensitive than conventional FLAIR imaging for detecting subtle tissue alterations in the peri-tumoral region.

MATERIALS AND METHODS

Subjects

Patients were recruited from an ongoing institutional review board approved study on the application of MWI in radiotherapy. Written informed consent was obtained for all participants. Six patients affected by lower grade glioma WHO grades II–III were selected. All the lesions had no or marginal enhancement on post-contrast imaging. Patients characteristics, dose prescriptions and time between surgery and treatment are listed in **Supplementary Table S1**. All the patients were irradiated by fractionated proton therapy (PT), uniformly delivered on the clinical target volume (CTV). FLAIR images were manually segmented to identify gross tumor volume (GTV) on pre-PT by two expertized radiation oncologists (DA and DS), using the contouring tools of the treatment planning system. For brainstem gliomas (patients #1 and #6, see **Supplementary Table S1**) the CTV was the GTV plus a 10 mm safety margin in cranial-caudal direction and a 5 mm safety margin in latero-lateral direction to account for typical anatomical spread (8). The safety margins were manually corrected taking into account anatomical barriers. For cerebral gliomas (patients #2–5, see **Supplementary Table S1**) the CTV was the composite of the FLAIR GTV, the T1-enhancing disease at pre-PT and the surgical cavity plus a 1.5 cm expansion beyond that (9).

MR Acquisitions

Images were acquired with a 1.5T MR scanner (Philips Ingenia system, Philips Medical Systems, Best, The Netherlands). A 16-channel head coil was utilized, routinely used for brain examinations. MWI was obtained using a multicomponent T2 relaxation technique by a 3D GraSE (10) multi-echo sequence with the following parameters: TR = 1,000 ms, 32 equally spaced echoes ranging from 10 to 320 ms, EPI factor = 5, FOV = 210 × 184 mm^2, acquisition matrix = 128 × 126 reconstructed to 256x256, 18 contiguous slices 5mm thickness reconstructed to 36 slices 2.5 mm thickness. MWI scans were acquired before PT (pre-PT), at the end of PT (end-PT) and in some cases (see *Results* section) at follow-up. All the patient underwent diagnostic MRI examination before PT and at follow-up, including conventional 3D FLAIR, which was acquired also at the end of PT. FLAIR parameters were TE = 95 ms, TR = 6,000 ms, inversion time = 1,740 ms, contiguous slice thickness = 1.2 mm and pixel size = 0.5 × 0.5 mm^2 for patient #1 and TE = 150 ms, TR = 4,800 ms, inversion time = 1,660 ms, contiguous slice thickness = 1.15 mm and pixel size = 1.0 × 1.0 mm^2 for the other patients.

For all patients, MWI and FLAIR pre-PT images were acquired at the beginning of the PT treatment and MWI and FLAIR end-PT images were acquired within one month after treatment. Follow-up diagnostic MR examinations were acquired more than three months after treatment for patients #1–5 and around fifty days after treatment for patient # 6. MWI was also acquired at follow-up for patients #2 and #3 (see below results).

MWI Post Processing

Multi-echo images were processed on a dedicated workstation by FSL, created by the Analysis Group, FMRIB, Oxford, UK (11), by MatLab (MATLAB®, The MathWorks.inc, Natick, MA, USA) and by MERA (12). MERA is a free tool for multi-exponential relaxation analysis, which fits data with a distribution of decaying exponential functions. In the MERA tool (version 2.04) two-hundred logarithmically-spaced time constants, ranging from 1 to 3,000 ms, and a minimum curvature regularization were set. The analysis included fitting the refocusing flip angle (13) as implemented in MERA. Each volume of the multi-echo MRI data was smoothed by a 3D Gaussian kernel (standard deviation equal to 1.5). Multi-echo data were then processed by MERA to identify in each voxel three T2 component from the obtained T2 spectrum. The T2 component below 40 ms was labeled as myelin water (2), the T2 component between 40 and 250 ms was labeled as intra-extracellular water (IEw) and above 250 ms was considered as cerebrospinal fluid/free water. The above 40–250 ms range has been chosen to exclude the myelin water component, but possibly to include tissue alterations (14), hence avoiding the exclusion of potentially informative regions. According to this labeling six 3D maps were extracted, three maps for the weighted average T2 of each compartment and three maps for the relative amplitude of the signal intensity in each compartment. However, the estimated T2 time of the myelin water component is not reliable as only a few echoes go into determining its value. Likewise, the estimated T2 time for

CSF is also not accurate, given that the longest measured echo time is only 320 ms. In **Supplementary Figure S1** exemplary images acquired on a healthy volunteer in the implementation phase are shown. In the following sections a specific focus is reported on the analysis of the quantitative IEw T2 map.

Image Analysis

FLAIR images and IEw T2 maps were aligned by means of FLIRT tools of FSL (15). FLIRT was set with 6 degrees of freedom (i.e. rotations and translations are allowed), trilinear interpolation and using the correlation ratio as the cost function.

The volume of hyper-intensity was manually outlined on FLAIR images on both pre-PT (where it was defined as being the GTV) and end-PT.

On both pre-PT and end-PT data, the volume of hyper-intense IEw T2 inside the CTV was automatically segmented by selecting the voxels with T2 higher than a threshold value. This threshold value was chosen on pre-PT data by the normalized distribution of T2 values, at the intersection between the T2 distribution of the voxels inside the GTV and the T2 distribution obtained on the voxels outside the same GTV. The same threshold value was applied to segment end-PT IEw T2 maps.

A quantitative comparison was performed on both pre- and end-PT between the segmented volumes on T2 maps and the corresponding volumes on FLAIR imaging.

The evolution of the lesion and of the surrounding tissue was visually assessed at pre-PT, at end-PT and at follow-up on the acquired IEw T2 maps and on conventional multi-parameter MRI.

Finally, a quantitative analysis was performed on an identified region of interest (ROI), assessing the corresponding T2 distribution of the ROI at different time points.

RESULTS

Quantitative volume analysis is reported in **Supplementary Table S2**, where the values of the segmented volumes are reported together with the CTV values. The volume of hyper-intense IEw T2 inside the CTV was segmented by selecting only the voxels with T2 higher than around 88 ms, i.e. the intersection on pre-PT data between the T2 distributions of the voxels inside and outside the GTV (see **Supplementary Figure S2**). The quantitative analysis showed a mismatch at pre-PT examination, i.e. the volume of hyper-intensity in IEw T2 maps exceeded the GTV volume identified on pre-PT FLAIR images. Both the segmented IEw T2 volumes and FLAIR hyper-intensities were greater on pre-PT than on end-PT except for patient #3, where they increased, and for patient #4, where the FLAIR segmented volumes did not change.

Qualitative visual analysis confirmed that for all the patients except patient #4 a spatial mismatch was observed before PT between the IEw T2 quantitative map and FLAIR images, with an area of high T2 that typically extended outside the area identified by abnormal FLAIR hyper-intensity. Only marginal differences were observed in patient #4, with no clear mismatch (not shown). At end-PT, the observed mismatch tends to decrease, by two different evolution patterns.

A reduced extension of the exceeding mismatch region (T2 decrease pattern) was observed for two patients, respectively #1 and #5 (shown in **Figure 1**). Such T2 decrease was confirmed on FLAIR images at follow-up (data not shown).

For three patients (#2, #3 and #6) new areas of abnormal hyper-intensity on FLAIR images were observed in the mismatch regions identified before PT (FLAIR increase pattern, which were diagnosed as asymptomatic radiation induced damage at last follow-up examination). Images showing the mismatch on patient #3 and #6 are reported in **Figure 2**. For patient #3 there was a further increase of the hyper-intense area at follow-up (data not shown). For patient #2, the IEw alteration in the mismatch area identified on pre-PT first partially decreased at end-PT and later increased at follow-up, when it was associated with large FLAIR hyper-intensity (**Figure 3**).

A ROI analysis was performed to investigate the characteristics of the T2 distribution that enabled the IEw T2 map to visualize abnormalities not evident with FLAIR imaging (**Figure 4**). For each patient, a mismatch ROI was manually delineated, corresponding to the region where the spatial mismatch was observed before PT between the IEw T2 quantitative map and FLAIR images, as shown in **Figures 1–3**. Patient #4 was excluded from the ROI analysis as for this patient it was difficult to identify a mismatch ROI. For comparison, a contralateral ROI on healthy tissue was also manually delineated in the same patients (see **Figures 1–3**). Whereas the T2 distribution only slightly changed at different time points in the healthy ROIs, it markedly changed in the mismatch ROIs and in a different way among the patients (**Figure 4**). In details, for all the five patients at pre-PT the T2 distribution in the mismatch ROIs showed a shift of the maximum toward higher T2 values and a positive skew of the T2 distribution. Thereafter, at end-PT for patients #1 and #5 it resulted similar to the T2 distribution of the healthy contralateral ROI. These findings were consistent with the observed T2 decrease pattern. On the opposite, at end-PT for patients #3 and #6 there was a further shift and/or a further positive skew of the T2 distribution. These latter findings were consistent with the FLAIR increase pattern observed for these patients. For patient #2 the observed T2 distributions were consistent with a FLAIR increase pattern at follow-up after a temporary T2 decrease at end-PT.

Visual inspection of IEw T2 maps put into evidence a very small decrease in the contralateral healthy tissue after therapy (see **Figures 1B** and **3**). These variations were diffuse in the whole brain, outside the CTV that received full treatment dose. These small changes of few milliseconds were emphasized by the chosen colored map, but they were negligible compared to the changes occurring in the mismatch ROIs, as above clarified in **Figure 4**.

Finally, it was more difficult to clearly identify tissue alterations in the other maps (myelin water maps are exemplarily shown in **Supplementary Figure S3**).

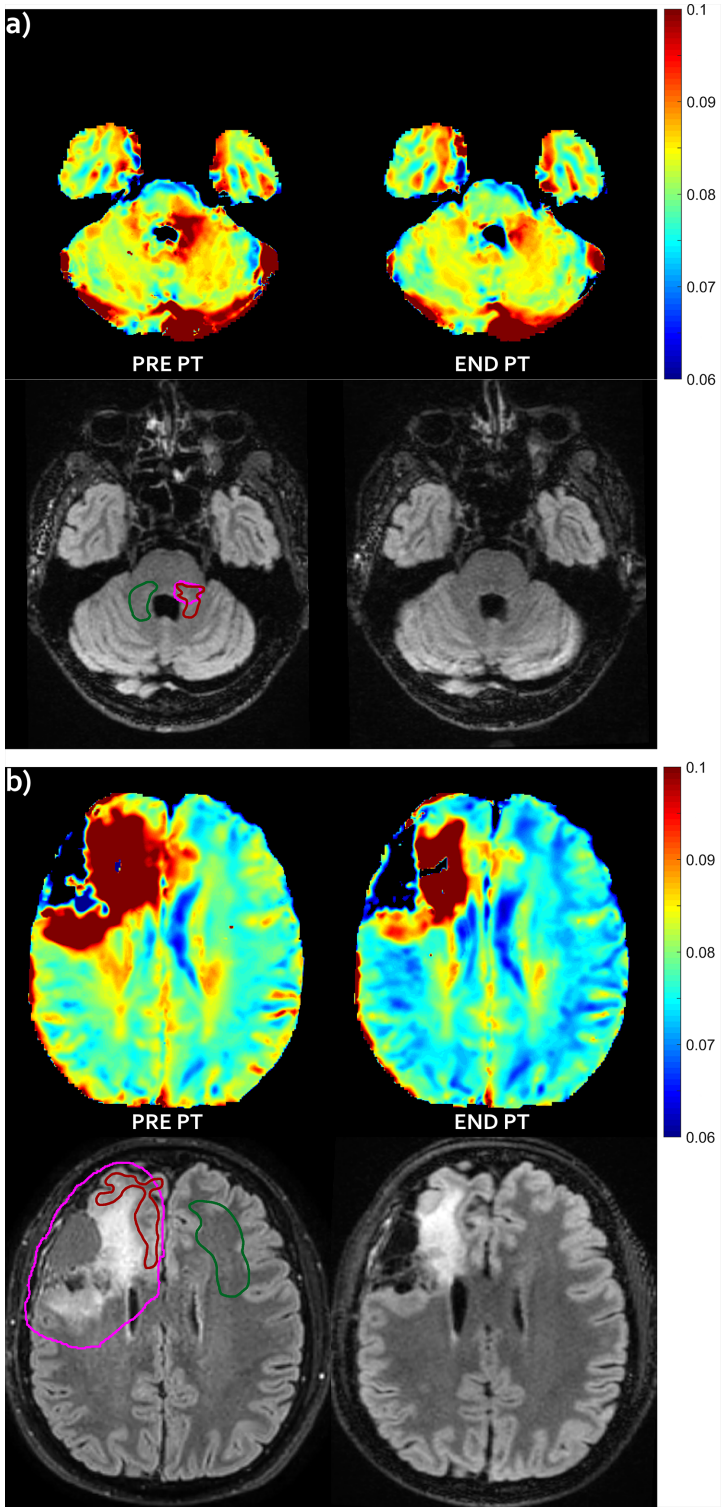

FIGURE 1 | T2 decrease pattern—Evolution pattern observed in patient #1 **(A)** and #5 **(B)**. The mismatch, i.e. abnormal T2 area that extended outside the hyperintense FLAIR area before proton irradiation (left) markedly reduced at the end of the radiation treatment (right), with no appearance of successive FLAIR hyperintensity in this region (not shown). For patient #1, no FLAIR abnormality was visible in panel **(A)**, but it was visible at a different slice level (not shown). T2 intra/extracellular water maps (top) and FLAIR images (bottom) are shown. Colored bar is shown in seconds. On pre-PT FLAIR image the contours of the CTV (violet line), of the mismatch ROI (red line) and of the contralateral healthy ROI (green line) are shown.

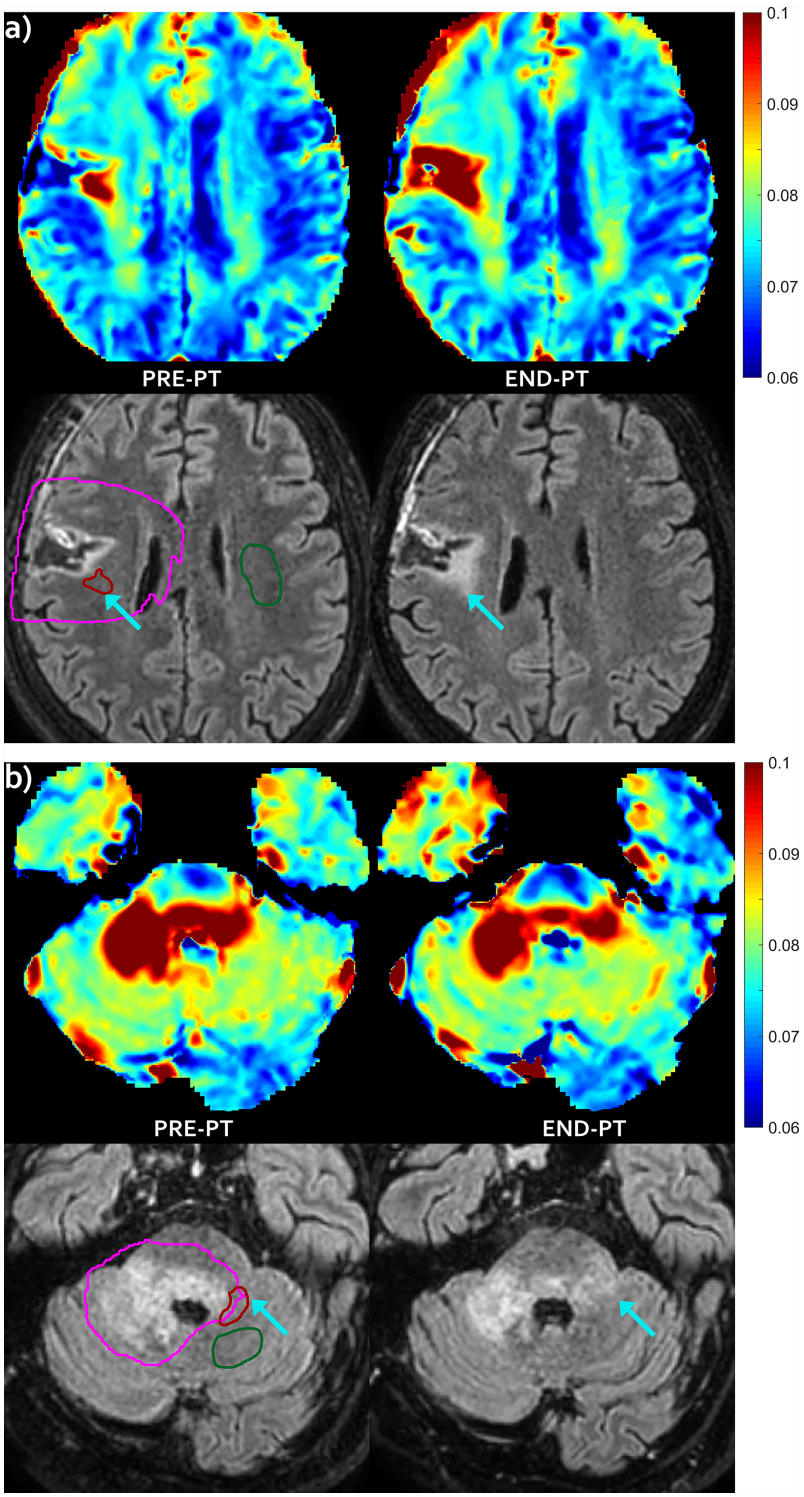

FIGURE 2 | FLAIR increase pattern—Evolution pattern observed in patient #3 **(A)** and in patient #6 **(B)** as highlighted by the arrows. The mismatch, i.e. the abnormal T2 area that extended outside hyper-intense FLAIR area before proton irradiation (left) evolved into a new area of FLAIR hyper-intensity at end-PT (right), that was diagnosed as radiation induced damage. T2 intra/extracellular water maps (top) and FLAIR images (bottom) are shown. Colored bar is shown in seconds. On pre-PT FLAIR image the contours of the CTV (violet line), of the mismatch ROI (red line) and of the contralateral healthy ROI (green line) are shown.

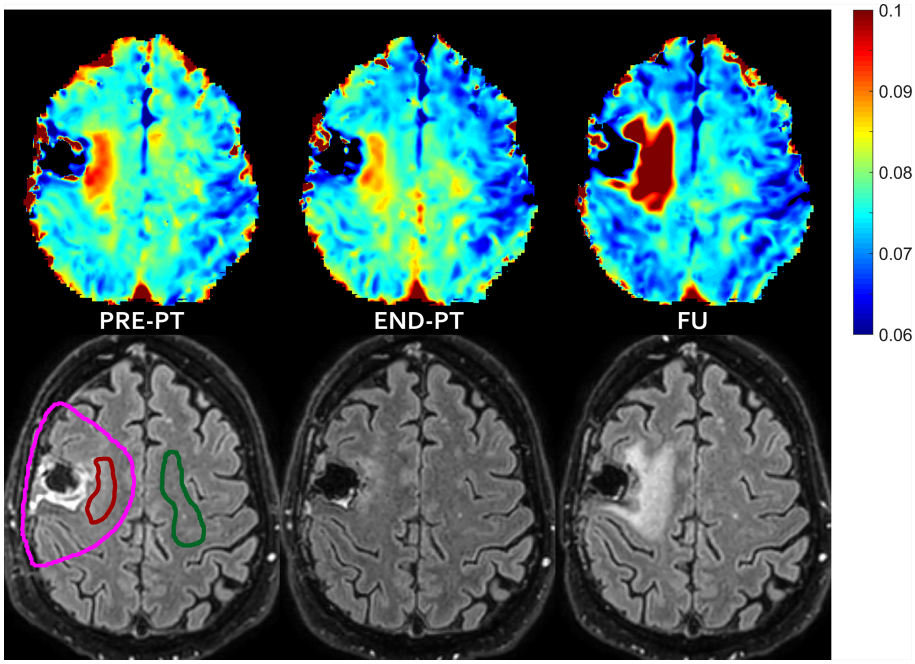

FIGURE 3 | FLAIR increase pattern after temporary T2 decrease—In patient #2 the mismatch, i.e. the abnormal T2 area that extended outside hyper-intense FLAIR area before proton irradiation (left) evolved into new area of FLAIR hyper-intensity diagnosed as radiation induced damage at follow-up (right), with some partial temporary recovery at the end of the radiation treatment (middle). T2 intra/extracellular water maps (top) and FLAIR images (bottom) are shown. Colored bar is shown in seconds. On pre-PT FLAIR image the contours of the CTV (violet line), of the mismatch ROI (red line) and of the contralateral healthy ROI (green line) are shown.

DISCUSSION

Multicomponent T2 relaxation is one of the MRI methods, generically named by MWI (16–18), developed to investigate demyelinating diseases in the CNS. MWI by T2 relaxation typically provides three main components. While the typical focus of MWI is on the short component arising from water trapped in the lipid bilayer membrane of myelin, our analysis focused instead on the intra/extracellular IEw component and, particularly, on its quantitative map of T2 relaxation times. Indeed, IEw T2 maps describe both the axonal and neural cells and, in our data, showed clear signal alterations.

In this study, we applied for the first time this technique to investigate irradiated brain tumor patients. To our knowledge, only a case report (19) previously described MWI changes after irradiation, by investigating the myelin water fraction without reporting IEw T2 mapping. In that study myelin water maps, which showed some alteration in the white matter, were investigated more than twenty months after radiotherapy, when marked changes were also visible on conventional imaging. Robust and accurate myelin water or myelin lipid imaging might be useful in the early assessment of radiation induced response or in other brain tumor assessment. However, our data did not show any clear alteration of myelin water on visual assessment and thus the analysis was focused on the IEw component.

In particular, a mismatch between IEw T2 maps and FLAIR images was observed in some ROIs of five over six glioma patients, with areas of high T2 that typically extended outside the area identified by abnormal FLAIR hyper-intensity.

In FLAIR imaging, both the myelin water and the fluid component are attenuated, the first due to long echo times with respect to the typical decay time of water trapped in the lipid bilayer, and the latter by an inversion recovery pulse. IEw T2 maps, calculated as the weighted average T2 of the intra/extracellular water, describe a similar compartment and can be somehow considered as a quantitative FLAIR imaging. Due to their quantitative information, IEw T2 maps resulted in a higher sensitivity compared to conventional FLAIR imaging for detecting subtle tissue abnormalities. In fact, the analysis in the mismatch ROIs showed clear differences in the T2 distribution with respect to the healthy tissue at pre-PT. Such differences became even greater for patient #2 at follow-up and for patients #3 and #6 at end-PT. Correspondingly, the mismatch regions resulted clearly hyper-intense also on FLAIR imaging only for patient #2 at follow-up and for patients #3 and #6 at end-PT.

The sequence used in this study is representative of most of the multi-echo sequences used for white matter myelin water studies in the literature and it has been demonstrated to be in agreement with histological measures of myelin content. Since some of the acquisition time is used to sample more echo times instead of the k-space, the improved T2 resolution is obtained at the price of a worse spatial resolution. In this view, it can be considered complementary rather than alternative to FLAIR imaging, which is characterized by poorer T2 resolution (only qualitative) and much better spatial resolution.

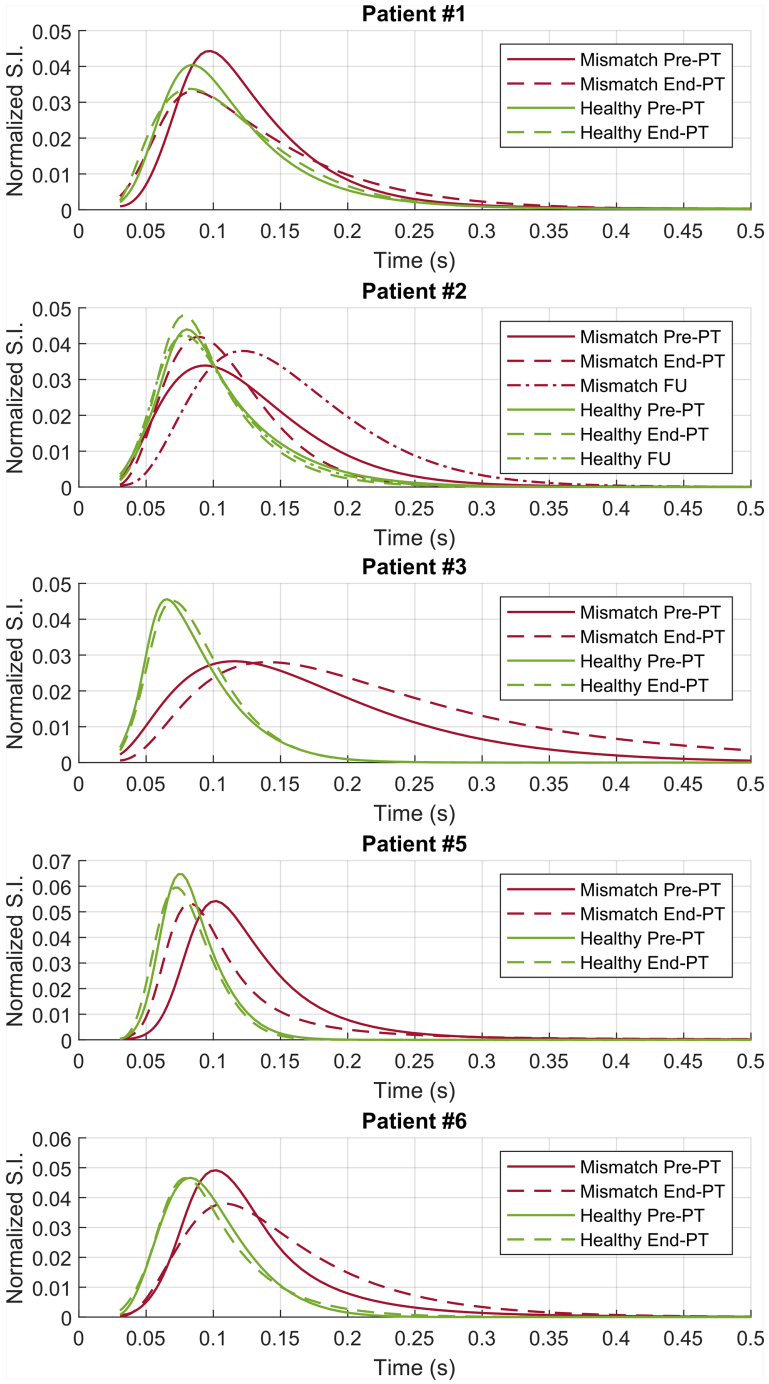

FIGURE 4 | ROI analysis—T2 distributions on the contralateral healthy (green lines) and on the mismatch (red lines) ROIs for patients #1–3 and #5–6. Pre-PT (continuous lines) and end-PT (dashed lines) T2 distributions are shown. For patient #2 also the follow-up T2 distributions (dotted lines) are shown.

Moreover, conventional T2-FLAIR sequence provides the information of both T2 relaxation and proton density of the IEw component, but this study only focused on the T2 relaxation of the IEw component. Indeed, the obtained proton fraction maps were not particularly informative as the subtle alterations, clearly visible on the T2 map, were not visible in the proton fraction map (data not shown). An additional map could be obtained by multiplication of T2 relaxation and the corresponding proton fraction of the IEw. However, this last map does not seem to add too much and it would miss the quantitative information available in the corresponding T2 map.

Since our sampling of the T2 decay curve stopped at a TE of 320 ms, the analysis of longer T2 components was inaccurate.

Besides that, using discrete tissue models with a fixed number of components may work quite well in defined systems, such as normal white matter, but for tissue alterations it might be inappropriate, if the model is incorrect. In a previous study (7), T2 components greater than 250 ms were found in a oligodendroglioma and the last TE time of 1,120 ms allowed to measure T2 times of several hundred milliseconds in a glioblastoma. That study by Laule et al. (7) focused on the marked alteration visible on T2-weighted imaging. Accordingly, we also observed some tumor area hyper-intense on FLAIR imaging (data not shown) with a T2 component that was assigned to be a fluid component in our model. However, the focus of the present study was on normal appearing brain regions on T2-weighted FLAIR imaging and, particularly, on the mismatch area identified by IEw T2 mapping. In these regions, the fluid water compartment with high T2 was almost negligible. As evidenced in the T2 distributions obtained by the ROI analysis, the mismatch regions were described by a water compartment whose T2 was in the range of 40–500 ms. The corresponding peak values were approximately in the range 70–140 ms. The echo sampling we used allowed an accurate measurement around those peaks to detect subtle alterations, as small as around 20 ms.

Further and deeper investigations are required to properly assess the specificity of the alteration additionally detected by IEw T2 mapping. MWI is not a well-established widespread used technique and it has to be considered as an experimental method still under development. Visual inspection of IEw T2 maps showed in some cases a diffuse but very small decrease outside the region that received full treatment dose. The ROI analysis demonstrated that these changes in the healthy tissue were negligible compared to the greater changes occurring in the mismatch regions.

The regions characterized by a mismatch between FLAIR and IEw T2 followed two different evolution patterns at follow-up. In the FLAIR increase pattern, tissue alteration might be ascribed to predisposition to tissue damage, which was finally diagnosed as asymptomatic radiation induced damage. Due to initial disease, these areas could have been more sensitive to the radiation insult and might be predictive of the corresponding sequelae.

The T2 decrease seems more difficult to be specified, as the observed mismatch might be due to evolving post-surgical sequelae or oedema but tumor infiltration cannot be excluded a priori. Lower grade gliomas are heterogeneous neoplasms with infiltrative behaviour along white matter tracts and surgical treatment poses special challenge for the neurosurgeon since, due to their diffusely infiltrative growth pattern, intraoperative identification of the exact tumor border is frequently not possible with certainty (20). Lower grade gliomas do not undergo significant gadolinium enhancement and the FLAIR sequences have been shown to precisely demonstrate the margins with increased reproducibility and sensitivity relative to T2 weighted imaging (21). However, morphological MRI tends to underestimate the extent of lower grade gliomas and previous studies using multiple biopsies have identified tumor cells outside the radiological border on FLAIR or T2 weighted sequences (22). In this perspective, the IEw T2 quantitative technique described in our study might be used in pre-operative imaging and correlated with biopsy results.

In conclusion, the contrast obtained in FLAIR imaging is based on the attenuation of the myelin water, due to long echo-times, and of fluid by inversion recovery. A similar attenuation was expected in T2 relaxation when considering only the intra/extracellular water component, thus T2 mapping of the intra/extracellular component can be considered as equivalent to a quantitative FLAIR. In our preliminarily study, T2 mapping of the intra/extracellular component in lower grade gliomas showed a mismatch with FLAIR imaging, with areas of high T2 that typically extended outside the area identified by abnormal FLAIR hyper-intensity. Such mismatch was due to an increased sensitivity of quantitative T2 mapping to detect subtle cerebral tissue abnormalities and deserves to be further investigated in future clinical studies.

DATA AVAILABILITY STATEMENT

The original contributions presented in the study are included in the article/**Supplementary Materials**, further inquiries can be directed to the corresponding author.

ETHICS STATEMENT

The studies involving human participants were reviewed and approved by ethics committee for clinical research of Azienda Provinciale per i Servizi Sanitari (APSS, Trento, Italy). The patients/participants provided their written informed consent to participate in this study.

AUTHOR CONTRIBUTIONS

PF and PB contributed to conception and design of the study. PB performed MRI acquisitions and data analysis. PF supported data analysis and data interpretation. UR supported radiological data interpretation. DA, DS, and MA provided patients for the study and supported clinical data interpretation. PF wrote the first draft of the manuscript. PB and UR wrote sections of the manuscript. All authors contributed to the article and approved the submitted version.

FUNDING

PB was supported by a grant founded by the Fondazione CARITRO—via Calepina 1, 38122 Trento, Italy.

SUPPLEMENTARY MATERIAL

The Supplementary Material for this article can be found online at: https://www.frontiersin.org/articles/10.3389/fonc.2021.651137/full#supplementary-material

REFERENCES

1. Does MD. Inferring brain tissue composition and microstructure via MR relaxometry. *Neuroimage* (2018) 182:136–48. doi: 10.1016/j.neuroimage.2017.12.087
2. MacKay AL, Laule C. Magnetic Resonance of Myelin Water: An in vivo Marker for Myelin. *Brain Plast* (2016) 2(1):71–91. doi: 10.3233/BPL-160033
3. Lee J, Hyun JW, Lee J, Choi EJ, Shin HG, Min K, et al. So You Want to Image Myelin Using MRI: An Overview and Practical Guide for Myelin Water Imaging. *J Magn Reson Imaging* (2020) 53(2):360–73. doi: 10.1002/jmri.27059
4. Heath F, Hurley SA, Johansen-Berg H, Sampaio-Baptista C. Advances in noninvasive myelin imaging. *Dev Neurobiol* (2018) 78(2):136–51. doi: 10.1002/dneu.22552
5. Laule C, Vavasour IM, Kolind SH, Li DK, Traboulsee TL, Moore GR, et al. Magnetic resonance imaging of myelin. *Neurotherapeutics* (2007) 4(3):460–84. doi: 10.1016/j.nurt.2007.05.004
6. Alonso-Ortiz E, Levesque IR, Pike GB. MRI-based myelin water imaging: A technical review. *Magn Reson Med* (2015) 73(1):70–81. doi: 10.1002/mrm.25198
7. Laule C, Bjarnason TA, Vavasour IM, Traboulsee AL, Wayne Moore GR, Li DKB, et al. Characterization of brain tumours with spin-spin relaxation: pilot case study reveals unique T2 distribution profiles of glioblastoma, oligodendroglioma and meningioma. *J Neurol* (2017) 264(11):2205–14. doi: 10.1007/s00415-017-8609-6
8. Combs SE, Steck I, Schulz-Ertner D, Welzel T, Kulozik AE, Behnisch W, et al. Long-term outcome of high-precision radiotherapy in patients with brain stem gliomas: results from a difficult-to-treat patient population using fractionated stereotactic radiotherapy. *Radiother Oncol* (2009) 91(1):60–6. doi: 10.1016/j.radonc.2009.02.012
9. Shih HA, Sherman JC, Nachtigall LB, Colvin MK, Fullerton BC, Daartz J, et al. Proton therapy for low-grade gliomas: Results from a prospective trial. *Cancer* (2015) 121(10):1712–9. doi: 10.1002/cncr.29237
10. Ljungberg E, Vavasour I, Tam R, Yoo Y, Rauscher A, Li DKB, et al. Rapid myelin water imaging in human cervical spinal cord. *Magn Reson Med* (2017) 78(4):1482–7. doi: 10.1002/mrm.26551
11. Smith SM, Jenkinson M, Woolrich MW, Beckmann CF, Behrens TE, Johansen-Berg H, et al. Advances in functional and structural MR image analysis and implementation as FSL. *Neuroimage* (2004) 23 Suppl 1:S208–19. doi: 10.1016/j.neuroimage.2004.07.051
12. *MERA - Multi Exponential Relaxation Analysis toolbox for MATLAB*. Available at: https://github.com/markdoes/MERA.
13. Prasloski T, Mädler B, Xiang QS, MacKay A, Jones C. Applications of stimulated echo correction to multicomponent T2 analysis. *Magn Reson Med* (2012) 67(6):1803–14. doi: 10.1002/mrm.23157
14. Stewart WA, MacKay AL, Whittall KP, Moore GR, Paty DW. Spin-spin relaxation in experimental allergic encephalomyelitis. Analysis of CPMG data using a non-linear least squares method and linear inverse theory. *Magn Reson Med* (1993) 29(6):767–75. doi: 10.1002/mrm.1910290608
15. Jenkinson M, Beckmann CF, Behrens TE, Woolrich MW, Smith SM. FSL. *Neuroimage* (2012) 62(2):782–90. doi: 10.1016/j.neuroimage.2011.09.015
16. Dvorak AV, Wiggermann V, Gilbert G, Vavasour IM, MacMillan EL, Barlow L, et al. Multi-spin echo T(2) relaxation imaging with compressed sensing (METRICS) for rapid myelin water imaging. *Magn Reson Med* (2020) 84(3):1264–79. doi: 10.1002/mrm.28199
17. Lee J, Lee D, Choi JY, Shin D, Shin HG, Lee J. Artificial neural network for myelin water imaging. *Magn Reson Med* (2020) 83(5):1875–83. doi: 10.1002/mrm.28038
18. Wu Z, Bilgic B, He H, Tong Q, Sun Y, Du Y, et al. Wave-CAIPI ViSTa: highly accelerated whole-brain direct myelin water imaging with zero-padding reconstruction. *Magn Reson Med* (2018) 80(3):1061–73. doi: 10.1002/mrm.27108
19. Wiggermann V, Lapointe E, Litvin L, Graf C, Hernández-Torres E, McKenzie M, et al. Longitudinal advanced MRI case report of white matter radiation necrosis. *Ann Clin Transl Neurol* (2018) 6(2):379–85. doi: 10.1002/acn3.704
20. Mert A, Kiesel B, Wöhrer A, Martínez-Moreno M, Minchev G, Furtner J, et al. Introduction of a standardized multimodality image protocol for navigation-guided surgery of suspected low-grade gliomas. *Neurosurg Focus* (2015) 38(1):E4. doi: 10.3171/2014.10.FOCUS14597
21. Connor SE, Gunny R, Hampton T, O'gorman R. Magnetic resonance image registration and subtraction in the assessment of minor changes in low grade glioma volume. *Eur Radiol* (2004) 14(11):2061–6. doi: 10.1007/s00330-004-2391-4
22. Zetterling M, Roodakker KR, Berntsson SG, Edqvist PH, Latini F, Landtblom AM, et al. Extension of diffuse low-grade gliomas beyond radiological borders as shown by the coregistration of histopathological and magnetic resonance imaging data. *J Neurosurg* (2016) 125(5):1155–66. doi: 10.3171/2015.10.JNS15583

Conflict of Interest: The authors declare that the research was conducted in the absence of any commercial or financial relationships that could be construed as a potential conflict of interest.

frontiers in Oncology

ORIGINAL RESEARCH
published: 14 April 2021
doi: 10.3389/fonc.2021.636672

Radiomic Analysis to Predict Outcome in Recurrent Glioblastoma Based on Multi-Center MR Imaging From the Prospective DIRECTOR Trial

*Alex Vils[1], Marta Bogowicz[1], Stephanie Tanadini-Lang[1], Diem Vuong[1], Natalia Saltybaeva[1], Johannes Kraft[1], Hans-Georg Wirsching[2], Dorothee Gramatzki[2], Wolfgang Wick[3], Elisabeth Rushing[4], Guido Reifenberger[5], Matthias Guckenberger[1], Michael Weller[2] and Nicolaus Andratschke[1]**

[1] Department of Radiation Oncology, University Hospital Zurich, Zurich, Switzerland, [2] Department of Neurology, University Hospital Zurich, Zurich, Switzerland, [3] Neurology Clinic, University Heidelberg Medical School, Heidelberg, Germany, [4] Department of Neuropathology, University Hospital Zurich, Zurich, Switzerland, [5] Department of Neuropathology, Heinrich Heine University Düsseldorf, Düsseldorf, Germany

OPEN ACCESS

Edited by:
Han Zhang,
University of North Carolina at Chapel Hill, United States

Reviewed by:
Zhongxiang Ding,
Zhejiang University, China
Martin Kocher,
University of Cologne, Germany

***Correspondence:**
Nicolaus Andratschke
nicolaus.andratschke@usz.ch

Specialty section:
This article was submitted to Cancer Imaging and Image-directed Interventions, a section of the journal Frontiers in Oncology

Received: 01 December 2020
Accepted: 17 March 2021
Published: 14 April 2021

Citation:
Vils A, Bogowicz M, Tanadini-Lang S, Vuong D, Saltybaeva N, Kraft J, Wirsching H-G, Gramatzki D, Wick W, Rushing E, Reifenberger G, Guckenberger M, Weller M and Andratschke N (2021) Radiomic Analysis to Predict Outcome in Recurrent Glioblastoma Based on Multi-Center MR Imaging From the Prospective DIRECTOR Trial. Front. Oncol. 11:636672. doi: 10.3389/fonc.2021.636672

Background: Based on promising results from radiomic approaches to predict O^6-*methylguanine DNA methyltransferase promoter methylation status* (*MGMT* status) and clinical outcome in patients with newly diagnosed glioblastoma, the current study aimed to evaluate radiomics in recurrent glioblastoma patients.

Methods: Pre-treatment MR-imaging data of 69 patients enrolled into the DIRECTOR trial in recurrent glioblastoma served as a training cohort, and 49 independent patients formed an external validation cohort. Contrast-enhancing tumor and peritumoral volumes were segmented on MR images. 180 radiomic features were extracted after application of two MR intensity normalization techniques: fixed number of bins and linear rescaling. Radiomic feature selection was performed *via* principal component analysis, and multivariable models were trained to predict *MGMT* status, progression-free survival from first salvage therapy, referred to herein as PFS_2, and overall survival (OS). The prognostic power of models was quantified with concordance index (CI) for survival data and area under receiver operating characteristic curve (AUC) for the *MGMT* status.

Results: We established and validated a radiomic model to predict *MGMT* status using linear intensity interpolation and considering features extracted from gadolinium-enhanced T1-weighted MRI (training AUC = 0.670, validation AUC = 0.673). Additionally, models predicting PFS_2 and OS were found for the training cohort but were not confirmed in our validation cohort.

Conclusions: A radiomic model for prediction of *MGMT* promoter methylation status from tumor texture features in patients with recurrent glioblastoma was successfully

established, providing a non-invasive approach to anticipate patient's response to chemotherapy if biopsy cannot be performed. The radiomic approach to predict PFS_2 and OS failed.

Keywords: radiomics, recurrent glioblastoma, *MGMT* status, DIRECTOR trial, linear intensity interpolation

INTRODUCTION

Glioblastoma is the most commonly occurring and aggressive malignant brain tumor in adults (1) and is classified by the World Health Organization as astrocytoma grade 4 (2). Patients enrolled in clinical trials show a dismal outcome with a median overall survival (OS) of 14.6 to 16.8 months and a 2 year survival rate of 27.2 to 33.9% (3–5). For newly diagnosed glioblastoma, the standard of care consists of gross total tumor resection when feasible followed by involved field radiotherapy as well as concomitant and sequential chemotherapy with the alkylating agent temozolomide. In contrast, for recurrent disease, optimal salvage therapy has not been defined with data lacking on predictive factors and superiority of the various treatment options (6). Glioblastoma is a heterogeneous tumor entity with various prognostic and predictive factors, including clinical (patient age, Karnofsky performance status) and molecular characteristics (O^6-methylguanine DNA methyltransferase promoter methylation status, *MGMT* status) (7, 8) affecting survival and treatment response. *MGMT* status is a well-established biomarker for newly diagnosed and recurrent glioblastoma and is predictive for both overall survival and treatment response to temozolomide (9). In a systematic review, temozolomide was found effective in recurrent glioblastoma (10) and possibly superior to nitriosurea-based chemotherapy (11, 12). The hypothesis of dose-dense or metronomic application being superior to the conventional schedule could not be confirmed in later randomized trials (9, 11). Yet, the DIRECTOR trial could establish the predictive role of *MGMT* status for response to temozolomide (9). Furthermore, the field of radiomics has introduced a large number of non-invasive medical imaging characteristics to describe specific phenotypic differences of tumors. Accordingly, several quantitative radiomic approaches have shown their potential to predict *MGMT* status and clinical outcome in patients with newly diagnosed glioblastoma (13–16). However, there are no reliable data on the value of quantitative radiomics for recurrent glioblastoma. This study was designed to evaluate the association of clinical outcome (progression-free survival, PFS_2, and OS) and molecular characteristics (*MGMT* status) with radiomic features from tumoral and peritumoral tissue on gadolinium-enhanced T1-weighted MR images in glioblastoma patients at first progression.

Abbreviations: AUC, area under receiver operating characteristic curve; CI, concordance index; *MGMT* status, O6-methylguanine DNA methyltransferase promoter methylation status; OS, overall survival; PFS_2, progression free survival; VOI, volume of interest.

MATERIALS AND METHODS

Patient Population

MR imaging data of the DIRECTOR trial (9), a prospective randomized multicenter trial that compared two dose-intensified temozolomide regimens in recurrent glioblastoma either with or without repeat surgery, were retrospectively analyzed and represented the training cohort (N = 105). The DIRECTOR trial showed a similar outcome in both study arms. Furthermore, imaging data were examined from an independent validation cohort (N = 49) at the University Hospital of Zurich enrolled by the same inclusion criteria as in the DIRECTOR trial (**Table S1**). All patients underwent prior treatment with standard of care for newly diagnosed glioblastoma (gross total resection if feasible followed by involved field radiotherapy and concomitant and sequential temozolomide chemotherapy) and were monitored for disease status by MRI in 8-week-cycles. DIRECTOR patients were excluded by the following criteria: unavailable pre- and post-contrast T1-weighted MR imaging data at recurrence prior to second surgery (N = 30), slice thickness of imaging data larger than 6.6 mm (N = 1), tumor volume at recurrence smaller than 0.2 ml (N = 4), newly diagnosed tumor located in the spinal cord (N = 1). Finally, 69 patients remained in the training cohort. Patient and imaging characteristics are summarized in **Table 1** and inclusion and exclusion criteria in **Table S1**. PFS_2 (in contrast to the time of diagnosis to first progression, PFS_1) and OS as clinical and *MGMT* status as epigenetic characteristic(s) were available. PFS_2 was defined as the duration from the date of first progression until further progression. OS was defined as the duration from the date of the first progression to the date of tumor-related death. According to available literature, *MGMT* status rarely changes in the course of disease (17); therefore, *MGMT* status was determined by tissue analysis either from newly diagnosed or recurrent tumor. In the training cohort at the time of data analysis (April 17, 2015), tumor progression was documented in 65 patients and tumor related death in 61 patients out of all 69 patients. All patients gave written informed consent, and the study was approved by the local ethics committees and designated authorities (KEK-ZH-Nr. 20140540, KEK-ZH-Nr. 2009-0135/1, KEK-ZH-Nr. 2015-0437).

Image Acquisition and Segmentation

MRI data, acquired by either 1, 1.5, or 3 T systems, according to the protocols at each institution, were available. Technical data are shown in **Table 1**. The segmentation of the tumor volume was performed manually by medical doctors (AV, JK) on gadolinium contrast-enhanced T1-weighted MRIs using MIM VISTA (Version 6.7.9., MIM software Inc., Cleaveland, USA) and audited by a senior radiation oncologist with 10 years of

TABLE 1 | Clinical characteristics of studied patient cohorts (training and validation) and imaging protocol details.

Characteristic		Training cohort N = 69	Validation cohort N = 49
Age at diagnosis	Median (y)	58	53
	Range (y)	37–77	38–77
Sex	Female	26 (38%)	12 (24%)
	Male	43 (62%)	37 (76%)
MGMT status	Methylated	28 (41%)	17 (52%)
	Unmethylated	41 (59%)	16 (48%)
	No data	0	16
Median survival	PFS_2 (mo, range)	2.7 (0–63)	3.7 (1–31)
	OS (mo, range)	11.3 (2–63)	13.4 (2–84)
KPS at first progression	90-100	37 (54%)	29 (59.2%)
	70-80	23 (33%)	17 (34.7%)
	<70	9 (13%)	3 (6.1%)
Steroids at first progression	Yes	20 (35%)	12 (24.5%)
	No	38 (65%)	37 (75.5%)
	No data	11	0
Second surgery	Yes	42 (61%)	20 (41%)
	No	27 (39%)	29 (59%)
Median VOI	Tumoral (ml, range)	11.7 (0.23–121.3)	5.0 (0.39–48.9)
	Peritumoral (ml, range)	75.2 (7.35–204.5)	53.0 (22.2–203.8)
MR Scanner	GE Medical Systems	N = 6	N = 17
	Discovery MR750	0	2 (4.1%)
	Signa Excite	0	5 (10.2%)
	Signa HDxt	6 (8.7%)	10 (20.4%)
	Philips Healthcare	N = 24	N = 22
	Ingenia	0	12 (24.5%)
	Achieva	3 (4.4%)	4 (8.2%)
	Intera	21 (30.4%)	6 (12.2%)
	Siemens	N = 39	N = 10
	Aera	1 (1.4%)	0
	Avanto	6 (8.7%)	0
	Numaris 3D	1 (1.4%)	0
	Skyra	4 (5.8%)	8 (16.4%)
	Sonata	9 (13%)	1 (2%)
	Symphony	5 (7.3%)	0
	TrioTim	5 (7.3%)	0
	Verio	6 (8.7%)	1 (2%)
	No data	2 (2.9%)	0
Magnetic field strength	1.0 T	1 (1.4%)	0
	1.5 T	39 (63.8%)	25 (51%)
	3.0 T	24 (34.8%)	24 (49%)
Image parameters	Slice thickness (mm, range)	0.44–6.6	0.7–5.3
	In-plane resolution (mm, range)	0.36–1.20	0.38–0.99

MGMT status, O^6-methylguanine-DNA methyltransferase promoter methylation status; PFS_2, progression-free survival; OS, overall survival; KPS, Karnofsky performance status; VOI, volume of interest.

experience after board certification (NA). Tumor volume of interest (VOI) included contrast-enhancing and cystic or necrotic areas. The resection cavity from first surgery was excluded if no sign of contrast enhancement was present. If blood residuals were seen along the border of the resection cavity, we subtracted hyperintense pre-contrast T1 volume from the post-contrast T1 volume. Segmentation of the peritumoral VOI was performed semi-automatically using an in-house developed MIM workflow. An isotropic 15-mm rim around the tumor volume was then generated. Non-brain tissue such as resection cavities, ventricle, subarachnoid space, and cranial bone were excluded manually by authors AV and JK and checked by author NA. Both tumor and peritumoral volumes of post-contrast T1-weighted images were considered for radiomic feature extraction (**Figure 1**).

Image Postprocessing and Radiomic Feature Extraction

Prior to radiomic feature extraction, images were resized to cubic voxel size of 1 mm for shape analysis and to cubic voxel size of 3 mm for intensity and texture analysis using trilinear interpolation. The training cohort consisted of multicenter data with variable imaging protocols, thus prior to radiomic feature extraction, intensity normalization was performed. Currently, there are no consensus guidelines regarding a standard MRI intensity normalization technique for radiomic feature calculation. Therefore, we investigated two methods and compared prognostic power of MRI-based radiomics after use of these two normalized techniques (**Figure 1**). In the first normalization approach, the entire range of intensities was divided into a series of 32 bins (fixed bin number normalization). In the second approach, a linear intensity interpolation was used with two fixed tissues of reference: white matter of the contralateral brain tissue and vitreous body of one eye (Function showing the relation of the original to the transformed intensities, **Figure S1**). Additionally, texture features were extracted using fixed bin size of 50. Bin size was adjusted in the second method, so that the number of bins was similar to the number analyzed with the first method. Large variations in the number of bins between the methods would result in differential sensitivity to noise and the values of both normalization techniques would then not be comparable. Feature extraction and statistical analysis were done for both techniques.

Radiomic feature extraction was performed with the in-house developed software Z-Rad (18) written in Python programming language (v 2.7, Python Software Foundation, Delaware, USA). This software was benchmarked in the Image Biomarker Standardization Initiative (19) and allocates three-dimensional image analysis including all four feature extraction methods: shape, intensity, texture, and wavelet transformation. For our analysis, a total number of 180 features (shape N = 24, intensity N = 19, and texture N = 137, full list represented in the **Table S2**) per tumoral and peritumoral volume per patient were calculated. Intensity and texture analyses were performed, as mentioned, using 32 bins or linear rescaling with bin size of 50. All wavelet features were excluded due to the small volumes of the analyzed regions (**Figure 1**).

Statistical Analysis

The methods applied were developed by our group and recently published (20). Briefly, this statistical method reduces feature space and correlates independent radiomic features with clinical endpoints to find prognostic or predictive biomarkers. The statistical analysis was performed in R (Version 3.5.3, The R Foundation, Vienna, Austria) (21). For both intensity

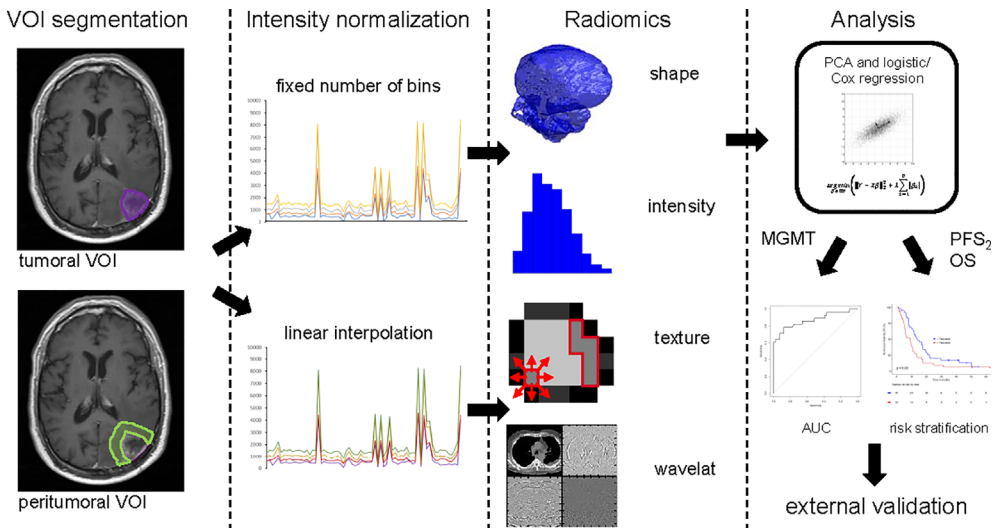

FIGURE 1 | Image postprocessing and radiomics workflow. VOI Segmentation: Tumor contour (violet) and peritumoral area (light green) are shown on MRI imaging data. Intensity normalization: Either with fixed numbers of bins or linear interpolation. Radiomics: Features of three groups' shape, intensity and texture were extracted with in-house developed software. Analysis: The statistical process of radiomic feature selection and risk stratification is shown up to validation on an external cohort. VOI, volume of interest; PCA, principal component analysis; *MGMT* status, O6-Methylguanin-DNA-Methyltransferase promoter methylation status; PFS_2, progression free survival; OS, overall survival.

normalization techniques and both volumes, tumoral and peritumoral, the statistical analysis was done separately. In total, per endpoint four models were trained using two intensity normalization techniques and two volumes of interest. To account for inter-features, correlation radiomic features were scaled and subsequently grouped according to the principal component analysis. The optimal number of retained principal components was determined using the Horn method (22). Each feature was assigned to the retained principal component to which the contribution was the greatest. Each of these principal components represented one group of correlated features (**Figure 1**).

Prediction of *MGMT* Promoter Methylation Status

Univariate logistic regression analysis was used to identify correlated radiomic features ($p < 0.05$) for *MGMT* status for both tumoral and peritumoral volumes. Only the most prognostic and significant ($p < 0.05$) feature per principal component feature group was included in further analysis. Feature prognostic value was quantified by area under receiver operating characteristic curve (AUC). The preselected features were enrolled in the multivariable logistic regression analysis, and the Akaike information criterion in the backward selection of variables was used to build the multivariable model. All results were verified in the independent external validation cohort. Additionally, an internal 5-fold-cross validation was performed (**Figure 1**).

Radiomics Prognostic Value of PFS_2 and OS

Similar statistical methods were used to predict PFS_2 and OS. Again, we analyzed tumoral and peritumoral volumes. Univariable Cox regression analysis was used to select the most prognostic feature (concordance index, CI) representing each principal component feature group. Only one feature per group was included in the multivariable analysis. Again, we used the Akaike information criterion in the backward selection of variables to build the final model, and all results were verified in an external validation cohort. Further, an internal 5-fold-cross validation was performed. Both training and validation cohorts were split into two prognostic groups based on the optimal threshold to generate survival curves and compared using log-rank test ($p < 0.05$). The threshold was defined as the median prediction value in the training cohort calculated from the final model using the prediction function in R (**Figure 1**).

Image Quality

Variations in image quality between different cohorts may also be critical for radiomic features and modeling. These variations may be identified by visual inspection of individual MRI datasets. However, such an approach is laborious, not sensitive to subtle variations between MR images (23) and subjective due to high inter-rater variability (24). In this work, the image quality of two cohorts was investigated by the semi-automatic approach using open-source tool MRQy. This tool is based on the HistoQC Python framework (25) and allows for automatic foreground detection for any MR image and extraction of imaging-specific metadata and quality measures. The major components of the MRQy tool and all the measures extracted by MRQy were described by Sadri et al. (26). We divided all investigated metrics in four groups: a) resolution-related features, extracted from the image metadata; b) acquisition-related features

including repetition time and echo time; c) foreground-related measures including mean values, range and signal-to-noise ratio; d) artifacts-related metrics. The difference in the variance of the extracted measures between training and validation cohorts was tested for significance using Kruskal–Wallis test; p-values below 0.05 were considered statistically significant.

RESULTS

Analyzed Volumes

In the MRI data of the training cohort, median volume of the tumoral VOI was 11.7 ml (range: 0.23–121.32 ml) and median volume of the peritumoral VOI was 75.2 ml (range: 7.35–204.53 ml, **Table 1**). In the validation cohort, median volume of the tumoral and peritumoral VOI was 5.0 ml (range: 0.39–48.89 ml) and 53.0 ml (range: 22.19–203.8 ml, **Table 1**), respectively.

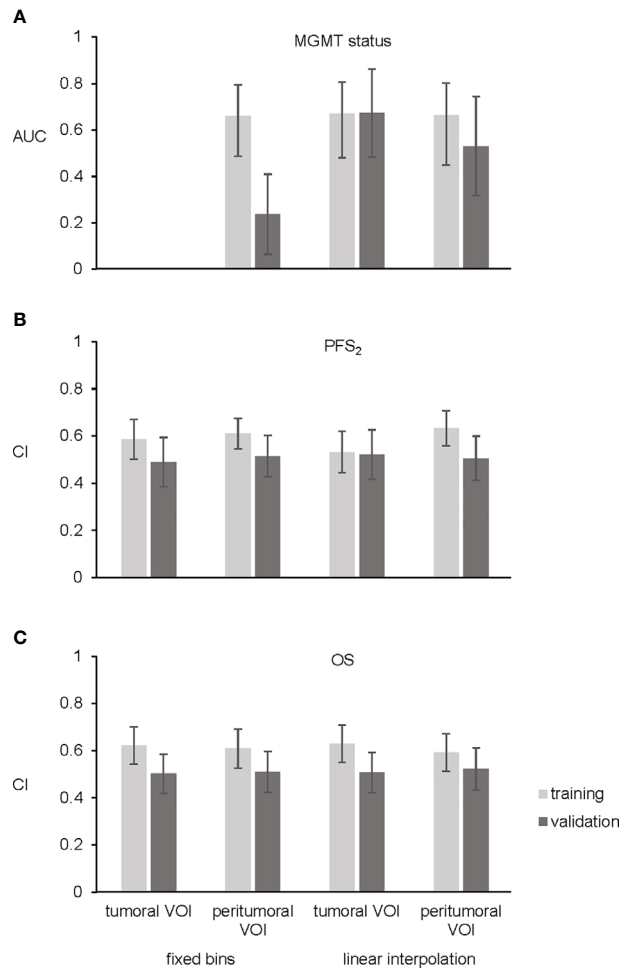

FIGURE 2 | Bar plots. **(A)** Shows area under receiver operating characteristic curve (AUC) of the three final models for *MGMT* status. No significant features were found for prediction of *MGMT* status using tumoral VOI and fixed number of bins. **(B)** Four final models for PFS_2 showing concordance index (CI). **(C)** CI of the four final OS models. Training cohort in light gray and validation cohort in dark gray. Error bars representing 95% confidence interval.

Feature Selection

In the training cohort, the principal component analysis resulted in seven groups of correlated radiomic features for the tumoral VOI (range group size: 15 to 47) and six groups for the peritumoral VOI (range group size: 11 to 62), considering only the images normalized with fixed number of 32 bins. In the linear interpolated images with 50 bin size, six groups for the tumoral VOI (range group size: 23 to 51) and six groups for the peritumoral VOI (range group size: 18 to 49) were built using the principal component analysis.

Prediction of *MGMT* Promoter Methylation Status

In the images normalized with fixed number of bins, there was no correlation between radiomic features extracted from the tumoral VOI and *MGMT* status. However, one independent and significant radiomic feature was identified in the peritumoral VOI. The final model (feature: Neighborhood Gray Tone Difference Matrix busyness; AUC 0.660, 95% confidence interval 0.528–0.793, **Figure 2A**) was not validated in the validation cohort (5-fold-cross validation in **Table S3**).

In the images normalized with linear interpolation, three uncorrelated radiomic features from the tumoral VOI and three uncorrelated radiomic features from the peritumoral VOI correlated with *MGMT* status. Upon backward selection of variables, one feature (Neighborhood Gray Level Dependence Matrix low dependence emphasis) in the tumoral VOI and one feature (coefficient of variation) in the peritumoral VOI remained significant. The final model of the tumoral VOI predicting *MGMT* status achieved an AUC of 0.670 (95% CI: 0.5341–0.8056, **Figure 2A** and **Table 2**) and was successfully validated in an independent cohort (AUC 0.673, 95% confidence interval 0.4837–0.8618, **Figure 2A**, 5-fold-cross validation in **Table S3**). In contrast, the peritumoral VOI model showing an AUC of 0.663 (95% CI: 0.5225–0.8024, **Figure 2A**, 5-fold-cross validation in **Table S3**) was not validated.

Prediction of PFS_2 and OS

For analysis of radiomics to predict PFS_2 and OS, MRI data of tumoral and peritumoral VOI were analyzed after intensity normalization using either fixed number of bins or linear interpolation.

PFS_2 Prediction

Multivariable Cox regression in images normalized with fixed number of bins and considering backward selection of variables

TABLE 2 | Details of the final model for MGMT status prediction.

VOI	feature	coefficient	p-value
tumoral	intercept	–2.46	0.018
tumoral	Neighborhood Gray Level Dependence Matrix low dependence emphasis	5.77	0.036

resulted in two significant radiomic features (Gray Level Size Zone Matrix zone size entropy, Gray Level Size Zone Matrix large zone low gray level emphasis) in the tumoral VOI and two (kurtosis, enhancing tumor volume 70%) in the peritumoral VOI. These analyses resulted in two radiomic models with a CI of 0.585 in the tumoral and a CI of 0.61 in the peritumoral VOI. The multivariable Cox model for both tumoral and peritumoral VOI was not validated (**Figure 2B**, 5-fold-cross validation in **Table S3**). In the training cohort, stratification into two risk groups was significant in the peritumoral VOI ($p = 0.02$) but not in the tumoral VOI for PFS_2.

After analyzing data normalized with linear interpolation with multivariable Cox regression based on backward selection of variables, two uncorrelated radiomic features (Gray Level Run Length Matrix long runs emphasis; Gray Level Run Length Matrix run length variance) in the tumoral VOI and two (kurtosis; Grey Level Size Zone Matrix large zone low gray level emphasis) in the peritumoral VOI predicting PFS_2 remained. These analyses predicting PFS_2 resulted in two models with a CI of 0.532 in the tumoral VOI and CI of 0.633 in the peritumoral VOI. However, both final models could not be validated in the external validation cohort (**Figure 2B**, 5-fold-cross validation in **Table S3**). In contrast to the images with fixed numbers of bins, the stratification in the training cohort into two risk groups was not significant for tumoral and peritumoral VOI.

OS Prediction

In the normalized imaging data with fixed number of bins, two radiomic features (enhancing tumor volume 30%, enhancing tumor volume 40%) for the tumoral VOI and one (enhancing tumor volume 30%) for the peritumoral VOI were entered into the multivariable Cox regression for OS prediction. These analyses resulted in two models with a CI of 0.621 in the tumoral VOI and a CI of 0.609 in the peritumoral VOI. The multivariable Cox model for both, tumoral and peritumoral VOI could not be validated in the external validation cohort (**Figure 2C**, 5-fold-cross validation in **Table S3**). Stratification into two risk groups was not significant.

Multivariable Cox regression of images normalized with linear interpolation led to one radiomic feature (histogram energy) in the tumoral VOI and one (minor axis) in the peritumoral VOI. These analyses resulted in two models with a CI of 0.629 in the tumoral VOI and a CI of 0.592 in the peritumoral VOI, respectively. Both final models could not be validated in the external validation cohort (**Figure 2C**, 5-fold-cross validation in **Table S3**), and stratification into two risk groups was not significant.

Image Quality

The results of the Kruskal–Wallis test are depicted in **Figure S2**; the investigated metrics and respective p-values are shown in **Table S4**. The test demonstrated a significant difference in variance between cohorts in terms of acquisition protocols: both variances in repetition time and echo time in the training cohort are significantly larger from those in the validation one, p-values of 0.027 and 0.005 for repetition time and echo time, respectively. In the MRI data of our training cohort, slice thickness varied from 0.44 to 6.6 mm (median, 1 mm) and in-plane resolution varied from 0.36 to 1.2 mm, whereas in the validation cohort slice thickness varied from 0.7 to 5.3 mm (median, 1.5 mm) and in-plane resolution from 0.38 to 0.99 mm. Only the variance of y voxel dimension was significantly larger in the training cohort. Additionally, variance of the entropy focus criterion, which describes motion artifacts, was significantly larger ($p = 0.013$) in the training cohort. Unexpectedly, despite the fact that about 71% of the validation cohort was collected in a single institution, substantial variation in the image quality was observed, which corresponds to the variation observed (**Figure S2**) in the multicenter data collection (training cohort).

DISCUSSION

In this study, we performed a radiomic analysis on gadolinium contrast enhanced T1-weighted MR images from patients with recurrent glioblastoma after alkylating chemotherapy. In terms of analyzed volume of interest, two volumes, tumoral and peritumoral, were included. Data for the training cohort are based on the prospective randomized DIRECTOR trial, which showed similar outcome in both arms (9). Validation data were obtained from a matched in-house recurrent glioblastoma patient cohort (27, 28).

The proposed radiomic model reliably predicted *MGMT* status from MRI contrast enhancing tumor regions after intensity normalization with linear interpolation in an independent cohort. This result has been reported previously in a radiomic analysis only from patients with newly diagnosed gliomas prior to standardized treatment (16, 29–33). In contrast, our models for *MGMT* prediction failed for intensity normalization with fixed bins or radiomic data from the peritumoral region. This finding highlights the importance of intensity normalization in quantitative MR analysis. Two models predicting PFS_2 and OS, respectively, were trained. However, neither of these models could be validated in the independent external patient cohort, and differences in models' performances were not statistically significant. Despite the ability to build prognostic models for outcome in the DIRECTOR cohort, the model ultimately failed in an external cohort, emphasizing the need for independent validation of model results for generalized applicability as mandated by the TRIPOD statement (34).

The key strengths of our study are the heterogeneity of the imaging data with regard to scanner models and image acquisition protocols in our training cohort collected during a prospective multicenter study (9) as well as the normalization methods. We hypothesized that finding a model in such a heterogeneous data pool would improve validation success in an independent cohort. However, variation is not only restricted to patients treated in different centers but also extends to different MRI acquisition protocols within one center, see **Figure S2** (*e.g.* different scanners, magnetic field strength, MRI slice thickness, or in plane resolution). Therefore, we performed voxel size resampling to a common resolution of 3 mm. The advantage of this method is the comparability of images, which is commonly used in radiomic research (19). On the other hand, much information from the

images with originally small cubic voxel sizes is lost. In addition, artificial data is introduced for images with originally large vox sizes. Whereas voxel size interpolation is standard in radiomic analysis, intensity normalization is often omitted (35, 36). We tested two different intensity normalization techniques to standardize grayscale MRI data to reduce interpatient and interstudy variability of the images. The simpler methods, fixed number of bins normalization, causes loss of information about absolute range of observed intensities. Using this method, none of the models could be validated. The second linear intensity interpolation is more labor intensive, as it requires segmentation of two additional structures. However, this method has the advantage of preserving information about absolute intensity range within the tumor. Importantly, this method allowed for successful validation of the *MGMT* status model, improving comparability between cohorts, while preserving information about tumor biology. The PFS_2 and OS models, however, could not be validated. This might be explained by much higher complexity of the endpoint and non-standardized treatment. On the technical side, the results might be further improved with application of bias field correction (37). Although the method applied for feature selection results in a restrictive and small number of features, as it has been shown to be superior to alternative approaches: recent findings show the method used here delivers the best models in comparison to maximum relevance minimum redundancy, mutual information and least absolute shrinkage and selection operator (LASSO) methods (38).

Model building, validation and reporting should be performed according to the TRIPOD statement which distinguishes different levels corresponding to the model validation process (34). Most studies using radiomic approaches in glioblastoma correspond to type 1b, 2a, or 2b analyses, where the model is trained and only validated on the data from the same or similar origin (see reviews by Park and colleagues) (39). When relying only on internal validation data, such models risk of overfitting and may provide an optimistic estimate of prediction performance. In addition, for a model to be used as a broadly applicable decision-making tool, external validation is mandatory. Park and colleagues reported that 63 out of 77 radiomic studies lack external validation (81.8%) (39). To overcome this limitation, we aimed to perform a TRIPOD statement type 3 model development using an independent curated patient cohort for validation. So far, only few studies have reported their model results based on this validation type (30, 40, 41). In the final model evaluation on an external dataset, we were not able to validate our models for PFS_2 and OS, but for *MGMT* prediction. Therefore, we consider our results as reliable and robust and conclude that the use of TRIPOD level 3 should be a prerequisite for a model's applicability in routine clinical use.

A possible explanation for the failure to validate the models for outcome prediction may be due to biological aspects of glioblastoma progression and alterations due to treatment. Draaisma and colleagues (42) showed that tumor biology differs at the genetic level from first presentation to recurrence, suggesting alterations in tumor biology over the course of disease. The primary treatment (*e.g.* different amounts of scaring tissue, resection cavities due to surgery) may also influence the presentation of recurrent tumor on MR images. Additionally, tumor volume at recurrence is often very small, thus yielding less tumor information for calculations (*e.g.* wavelet transformation features) compared to MRIs obtained at initial diagnosis. Furthermore, reproducibility of the contours is limited due to an unclear distinction between cystic or necrotic areas and resection cavities. Contouring could be improved, however, by comparison to MRI after first resection. Another limitation of our model is the small sample size available for this analysis, thus indicating the need of further investigations in a larger cohort. Finally, incorporating additional sequences such as T2-weighted and FLAIR gaining complementary radiomic information may improve prediction.

Even though the current results are promising, the vast majority of the studies in the growing field of quantitative radiomics have analyzed newly diagnosed glioblastomas. Only a few radiomic approaches have been published on glioblastomas at recurrence (15, 43, 44). Since our study focuses on recurrent glioblastoma, we provide additional models for predictive and diagnostic criteria for patients with a poor prognosis. This finding may represent a small but significant step towards highlighting the clinical relevance of radiomic approaches for newly diagnosed glioblastoma.

In conclusion, our model predicts *MGMT* promoter methylation status based on tumor texture features on gadolinium-enhanced T1-weighted MRI in patients with recurrent glioblastoma treated with alkylating chemotherapy. Therefore, our model provides a non-invasive approach to predict patient response to chemotherapy. However, the radiomic approach to predict PSF_2 and OS remained unsuccessful for patients with recurrent glioblastoma.

DATA AVAILABILITY STATEMENT

The datasets presented in this article are not readily available because patient individual data has been taken from a prospective trial which would need consent of all involved study PI if data sharing upon request is initiated. Requests to access the datasets should be directed to nicolaus.andratschke@usz.ch.

ETHICS STATEMENT

The studies involving human participants were reviewed and approved by the local ethics committees and designated authorities (KEK-ZH-Nr. 20140540, KEK-ZH-Nr. 2009-0135/1, KEK-ZH-Nr. 2015-0437). The patients/participants provided their written informed consent to participate in this study.

AUTHOR CONTRIBUTIONS

Study concept and design: AV, MB, ST-L, MG, NA. Collection and provision of patient data: H-GW, DG, GR, ER, WW, MW. Performance of data processing and analysis: AV, MB, ST-L, DV, NS, JK, H-GW, DG, NA. Data interpretation and postprocessing: AV, MB, ST-L, NA. Writing the manuscript: AV, MB, NS, NA.

Revision of the manuscript for important intellectual content: AV, MB, ST-L, DV, NS, JK, H-GW, DG, WW, ER, GR, MG, MW, NA. All authors contributed to the article and approved the submitted version.

FUNDING

The research project has been partially funded by the Clinical Research Priority Program "Artificial Intelligence in Oncological Imaging" of the University of Zurich. The research project was partially funded by SPHN IMAGINE.

ACKNOWLEDGMENTS

The authors acknowledge all colleagues, patients, and caregivers that contributed to the DIRECTOR study or the Canton of Zurich Registry study.

SUPPLEMENTARY MATERIAL

The Supplementary Material for this article can be found online at: https://www.frontiersin.org/articles/10.3389/fonc.2021.636672/full#supplementary-material

REFERENCES

1. Ostrom QT, Cioffi G, Gittleman H, Patil N, Waite K, Kruchko C, et al. CBTRUS Statistical Report: Primary Brain and Other Central Nervous System Tumors Diagnosed in the United States in 2012–2016. *Neuro-Oncol* (2019) 21 (Supplement_5):v1–v100. doi: 10.1093/neuonc/noz150
2. Louis DN, Ohgaki H, Wiestler OD, Cavenee WK, Burger PC, Jouvet A, et al. The 2007 WHO classification of tumours of the central nervous system. *Acta Neuropathol* (2007) 114(2):97–109. doi: 10.1007/s00401-007-0243-4
3. Gilbert MR, Dignam JJ, Armstrong TS, Wefel JS, Blumenthal DT, Vogelbaum MA, et al. A randomized trial of bevacizumab for newly diagnosed glioblastoma. *N Engl J Med* (2014) 370(8):699–708. doi: 10.1056/NEJMoa1308573
4. Chinot OL, Wick W, Mason W, Henriksson R, Saran F, Nishikawa R, et al. Bevacizumab plus radiotherapy-temozolomide for newly diagnosed glioblastoma. *N Engl J Med* (2014) 370(8):709–22. doi: 10.1056/NEJMoa1308345
5. Stupp R, Hegi ME, Mason WP, van den Bent MJ, Taphoorn MJB, Janzer RC, et al. Effects of radiotherapy with concomitant and adjuvant temozolomide versus radiotherapy alone on survival in glioblastoma in a randomised phase III study: 5-year analysis of the EORTC-NCIC trial. *Lancet Oncol* (2009) 10 (5):459–66. doi: 10.1016/S1470-2045(09)70025-7
6. Weller M, van den Bent M, Tonn JC, Stupp R, Preusser M, Cohen-Jonathan-Moyal E, et al. European Association for Neuro-Oncology (EANO) guideline on the diagnosis and treatment of adult astrocytic and oligodendroglial gliomas. *Lancet Oncol* (2017) 18(6):e315–e29. doi: 10.1016/S1470-2045(17)30194-8
7. Sasmita AO, Wong YP, Ling APK. Biomarkers and therapeutic advances in glioblastoma multiforme. *Asia Pac J Clin Oncol* (2018) 14(1):40–51. doi: 10.1111/ajco.12756
8. McNamara MG, Sahebjam S, Mason WP. Emerging biomarkers in glioblastoma. *Cancers (Basel)* (2013) 5(3):1103–19. doi: 10.3390/cancers5031103
9. Weller M, Tabatabai G, Kästner B, Felsberg J, Steinbach JP, Wick A, et al. MGMT Promoter Methylation Is a Strong Prognostic Biomarker for Benefit from Dose-Intensified Temozolomide Rechallenge in Progressive Glioblastoma: The DIRECTOR Trial. *Clin Cancer Res* (2015) 21(9):2057–64. doi: 10.1158/1078-0432.CCR-14-2737
10. Chen C, Xu T, Lu Y, Chen J, Wu S. The efficacy of temozolomide for recurrent glioblastoma multiforme. *Eur J Neurol* (2013) 20(2):223–30. doi: 10.1111/j.1468-1331.2012.03778.x
11. Brada M, Stenning S, Gabe R, Thompson LC, Levy D, Rampling R, et al. Temozolomide versus procarbazine, lomustine, and vincristine in recurrent high-grade glioma. *J Clin Oncol* (2010) 28(30):4601–8. doi: 10.1200/jco.2009.27.1932
12. Yung WK, Albright RE, Olson J, Fredericks R, Fink K, Prados MD, et al. A phase II study of temozolomide vs. procarbazine in patients with glioblastoma multiforme at first relapse. *Br J Cancer* (2000) 83(5):588–93. doi: 10.1054/bjoc.2000.1316
13. Kickingereder P, Burth S, Wick A, Götz M, Eidel O, Schlemmer H-P, et al. Radiomic Profiling of Glioblastoma: Identifying an Imaging Predictor of Patient Survival with Improved Performance over Established Clinical and Radiologic Risk Models. *Radiology* (2016) 280(3):880–9. doi: 10.1148/radiol.2016160845
14. Kickingereder P, Neuberger U, Bonekamp D, Piechotta PL, Götz M, Wick A, et al. Radiomic subtyping improves disease stratification beyond key molecular, clinical, and standard imaging characteristics in patients with glioblastoma. *Neuro-Oncol* (2018) 20(6):848–57. doi: 10.1093/neuonc/nox188
15. Kickingereder P, Götz M, Muschelli J, Wick A, Neuberger U, Shinohara RT, et al. Large-scale Radiomic Profiling of Recurrent Glioblastoma Identifies an Imaging Predictor for Stratifying Anti-Angiogenic Treatment Response. *Clin Cancer Res* (2016) 22(23):5765–71. doi: 10.1158/1078-0432.CCR-16-0702
16. Sasaki T, Kinoshita M, Fujita K, Fukai J, Hayashi N, Uematsu Y, et al. Radiomics and MGMT promoter methylation for prognostication of newly diagnosed glioblastoma. *Sci Rep* (2019) 9(1):14435. doi: 10.1038/s41598-019-50849-y
17. Felsberg J, Thon N, Eigenbrod S, Hentschel B, Sabel MC, Westphal M, et al. Promoter methylation and expression of MGMT and the DNA mismatch repair genes MLH1, MSH2, MSH6 and PMS2 in paired primary and recurrent glioblastomas. *Int J Cancer* (2011) 129(3):659–70. doi: 10.1002/ijc.26083
18. USZ Medical Physics. (2020). Available at: https://medical-physics-usz.github.io/.
19. Zwanenburg A, Vallières M, Abdalah MA, Aerts HJWL, Andrearczyk V, Apte A, et al. The Image Biomarker Standardization Initiative: Standardized Quantitative Radiomics for High-Throughput Image-based Phenotyping. *Radiology* (2020) 295(2):328–38. doi: 10.1148/radiol.2020191145
20. Bogowicz M, Riesterer O, Ikenberg K, Stieb S, Moch H, Studer G, et al. Computed tomography radiomics predicts HPV status and local tumor control after definitive radiochemotherapy in head and neck squamous cell carcinoma. *Int J Radiat Oncol Biol Phys* (2017) 99(4):921–8. doi: 10.1016/j.ijrobp.2017.06.002
21. R: The R Project for Statistical Computing. (2019). Available at: https://www.r-project.org/.
22. Horn JL. A rationale and test for the number of factors in factor analysis. *Psychometrika* (1965) 30:179–85. doi: 10.1007/BF02289447
23. Gardner EA, Ellis JH, Hyde RJ, Aisen AM, Quint DJ, Carson PL. Detection of degradation of magnetic resonance (MR) images: Comparison of an automated MR image-quality analysis system with trained human observers. *Acad Radiol* (1995) 2(4):277–81. doi: 10.1016/S1076-6332(05)80184-9
24. Esteban O, Birman D, Schaer M, Koyejo OO, Poldrack RA, Gorgolewski KJ. MRIQC: Advancing the automatic prediction of image quality in MRI from unseen sites. *PloS One* (2017) 12(9):e0184661. doi: 10.1371/journal.pone.0184661
25. Janowczyk A, Zuo R, Gilmore H, Feldman M, Madabhushi A. HistoQC: An Open-Source Quality Control Tool for Digital Pathology Slides. *JCO Clin Cancer Inform* (2019) 3:1–7. doi: 10.1200/CCI.18.00157
26. Sadri AR, Janowczyk A, Zou R, Verma R. MRQy: An Open-Source Tool for Quality Control of MR Imaging Data. *Med Phys* (2020) 47(12):6029–38. doi: 10.1002/mp.14593
27. Gramatzki D, Dehler S, Rushing EJ, Zaugg K, Hofer S, Yonekawa Y, et al. Glioblastoma in the Canton of Zurich, Switzerland revisited: 2005 to 2009. *Cancer* (2016) 122(14):2206–15. doi: 10.1002/cncr.30023
28. Gramatzki D, Roth P, Rushing EJ, Weller J, Andratschke N, Hofer S, et al. Bevacizumab may improve quality of life, but not overall survival in

glioblastoma: an epidemiological study. *Ann Oncol* (2018) 29(6):1431–6. doi: 10.1093/annonc/mdy106
29. Wei J, Yang G, Hao X, Gu D, Tan Y, Wang X, et al. A multi-sequence and habitat-based MRI radiomics signature for preoperative prediction of MGMT promoter methylation in astrocytomas with prognostic implication. *Eur Radiol* (2019) 29(2):877–88. doi: 10.1007/s00330-018-5575-z
30. Li Z-C, Bai H, Sun Q, Li Q, Liu L, Zou Y, et al. Multiregional radiomics features from multiparametric MRI for prediction of MGMT methylation status in glioblastoma multiforme: A multicentre study. *Eur Radiol* (2018) 28 (9):3640–50. doi: 10.1007/s00330-017-5302-1
31. Beig N, Bera K, Prasanna P, Antunes J, Correa R, Singh S, et al. Radiogenomic-Based Survival Risk Stratification of Tumor Habitat on Gd-T1w MRI Is Associated with Biological Processes in Glioblastoma. *Clin Cancer Res* (2020) 26(8):1866–76. doi: 10.1158/1078-0432.CCR-19-2556
32. Qian J, Herman MG, Brinkmann DH, Laack NN, Kemp BJ, Hunt CH, et al. Prediction of MGMT Status for Glioblastoma Patients Using Radiomics Feature Extraction from 18F-DOPA-PET Imaging. *Int J Radiat Oncol Biol Phys* (2020) 108(5):1339–46. doi: 10.1016/j.ijrobp.2020.06.073
33. Kickingereder P, Isensee F, Tursunova I, Petersen J, Neuberger U, Bonekamp D, et al. Automated quantitative tumour response assessment of MRI in neuro-oncology with artificial neural networks: a multicentre, retrospective study. *Lancet Oncol* (2019) 20(5):728–40. doi: 10.1016/S1470-2045(19)30098-1
34. Collins GS, Reitsma JB, Altman DG, Moons KGM. Transparent reporting of a multivariable prediction model for individual prognosis or diagnosis (TRIPOD): the TRIPOD statement. *Br J Cancer* (2015) 112(2):251–9. doi: 10.1038/bjc.2014.639
35. Cattell R, Chen S, Huang C. Robustness of radiomic features in magnetic resonance imaging: review and a phantom study. *Vis Comput Ind BioMed Art* (2019) 2(1):19. doi: 10.1186/s42492-019-0025-6
36. Carré A, Klausner G, Edjlali M, Lerousseau M, Briend-Diop J, Sun R, et al. Standardization of brain MR images across machines and protocols: bridging the gap for MRI-based radiomics. *Sci Rep* (2020) 10(1):12340. doi: 10.1038/s41598-020-69298-z
37. Moradmand H, Aghamiri SMR, Ghaderi R. Impact of image preprocessing methods on reproducibility of radiomic features in multimodal magnetic resonance imaging in glioblastoma. *J Appl Clin Med Phys* (2020) 21(1):179–90. doi: 10.1002/acm2.12795
38. Bogowicz M, Riesterer O, Stark LS, Studer G, Unkelbach J, Guckenberger M, et al. Comparison of PET and CT radiomics for prediction of local tumor control in head and neck squamous cell carcinoma. *Acta Oncol (Stockholm Sweden)* (2017) 56(11):1531–6. doi: 10.1080/0284186x.2017.1346382
39. Park JE, Kim D, Kim HS, Park SY, Kim JY, Cho SJ, et al. Quality of science and reporting of radiomics in oncologic studies: room for improvement according to radiomics quality score and TRIPOD statement. *Eur Radiol* (2020) 30 (1):523–36. doi: 10.1007/s00330-019-06360-z
40. Cui Y, Tha KK, Terasaka S, Yamaguchi S, Wang J, Kudo K, et al. Prognostic imaging biomarkers in glioblastoma: development and independent validation on the basis of multiregion and quantitative analysis of MR images. *Radiology* (2016) 278(2):546–53. doi: 10.1148/radiol.2015150358
41. Lao J, Chen Y, Li Z-C, Li Q, Zhang J, Liu J, et al. A Deep Learning-Based Radiomics Model for Prediction of Survival in Glioblastoma Multiforme. *Sci Rep* (2017) 7(1):10353. doi: 10.1038/s41598-017-10649-8
42. Draaisma K, Chatzipli A, Taphoorn M, Kerkhof M, Weyerbrock A, Sanson M, et al. Molecular Evolution of IDH Wild-Type Glioblastomas Treated With Standard of Care Affects Survival and Design of Precision Medicine Trials: A Report From the EORTC 1542 Study. *J Clin Oncol* (2020) 38(1):81–99. doi: 10.1200/JCO.19.00367
43. Akbari H, Rathore S, Bakas S, Nasrallah MP, Shukla G, Mamourian E, et al. Histopathology-validated machine learning radiographic biomarker for noninvasive discrimination between true progression and pseudo-progression in glioblastoma. *Cancer* (2020) 126(11):2625–36. doi: 10.1002/cncr.32790
44. Grossmann P, Narayan V, Chang K, Rahman R, Abrey L, Reardon DA, et al. Quantitative imaging biomarkers for risk stratification of patients with recurrent glioblastoma treated with bevacizumab. *Neuro-Oncol* (2017) 19 (12):1688–97. doi: 10.1093/neuonc/nox092

Conflict of Interest: The authors declare that the research was conducted in the absence of any commercial or financial relationships that could be construed as a potential conflict of interest.

frontiers in Oncology

ORIGINAL RESEARCH
published: 27 April 2021
doi: 10.3389/fonc.2021.645316

TERT-Promoter Mutational Status in Glioblastoma – Is There an Association With Amino Acid Uptake on Dynamic ^{18}F-FET PET?

*Marcus Unterrainer[1,2,3], Viktoria Ruf[4], Katharina von Rohr[2], Bogdana Suchorska[3,5], Lena Maria Mittlmeier[2], Leonie Beyer[2], Matthias Brendel[2], Vera Wenter[2], Wolfgang G. Kunz[1], Peter Bartenstein[2,3], Jochen Herms[4], Maximilian Niyazi[3,6], Jörg C. Tonn[3,5] and Nathalie Lisa Albert[2,3]**

[1] Department of Radiology, University Hospital, LMU Munich, Munich, Germany, [2] Department of Nuclear Medicine, University Hospital, LMU Munich, Munich, Germany, [3] German Cancer Consortium (DKTK), Partner Site Munich and German Cancer Research Center (DKFZ), Heidelberg, Germany, [4] Department of Neuropathology and Prion Research, LMU Munich, Munich, Germany, [5] Department of Neurosurgery, University Hospital, LMU Munich, Munich, Germany, [6] Department of Radiation Oncology, University Hospital, LMU Munich, Munich, Germany

OPEN ACCESS

Edited by:
Han Zhang,
University of North Carolina at Chapel Hill, United States

Reviewed by:
Orazio Schillaci,
University of Rome Tor Vergata, Italy
Philipp Lohmann,
Julich-Forschungszentrum, Helmholtz-Verband Deutscher Forschungszentren (HZ), Germany

***Correspondence:**
Nathalie Lisa Albert
nathalie.albert@med.uni-muenchen.de

Specialty section:
This article was submitted to Cancer Imaging and Image-directed Interventions, a section of the journal Frontiers in Oncology

Received: 22 December 2020
Accepted: 26 March 2021
Published: 27 April 2021

Citation:
Unterrainer M, Ruf V, von Rohr K, Suchorska B, Mittlmeier LM, Beyer L, Brendel M, Wenter V, Kunz WG, Bartenstein P, Herms J, Niyazi M, Tonn JC and Albert NL (2021) TERT-Promoter Mutational Status in Glioblastoma – Is There an Association With Amino Acid Uptake Characteristics on Dynamic ^{18}F-FET PET? Front. Oncol. 11:645316. doi: 10.3389/fonc.2021.645316

Objective: The mutation of the 'telomerase reverse transcriptase gene promoter' (TERTp) has been identified as an important factor for individual prognostication and tumorigenesis and will be implemented in upcoming glioma classifications. Uptake characteristics on dynamic ^{18}F-FET PET have been shown to serve as additional imaging biomarker for prognosis. However, data on the correlation of TERTp-mutational status and amino acid uptake on dynamic ^{18}F-FET PET are missing. Therefore, we aimed to analyze whether static and dynamic ^{18}F-FET PET parameters are associated with the TERTp-mutational status in de-novo *IDH*-wildtype glioblastoma and whether a TERTp-mutation can be predicted by dynamic ^{18}F-FET PET.

Methods: Patients with de-novo *IDH*-wildtype glioblastoma, WHO grade IV, available TERTp-mutational status and dynamic ^{18}F-FET PET scan prior to any therapy were included. Here, established clinical parameters maximal and mean tumor-to-background-ratios (TBR_{max}/TBR_{mean}), the biological-tumor-volume (BTV) and minimal-time-to-peak (TTP_{min}) on dynamic PET were analyzed and correlated with the TERTp-mutational status.

Results: One hundred *IDH*-wildtype glioblastoma patients were evaluated; 85/100 of the analyzed tumors showed a TERTp-mutation (C228T or C250T), 15/100 were classified as TERTp-wildtype. None of the static PET parameters was associated with the TERTp-mutational status (median TBR_{max} 3.41 vs. 3.32 (p=0.362), TBR_{mean} 2.09 vs. 2.02 (p=0.349) and BTV 26.1 vs. 22.4 ml (p=0.377)). Also, the dynamic PET parameter TTP_{min} did not differ in both groups (12.5 vs. 12.5 min, p=0.411). Within the TERTp-mutant subgroups (i.e., C228T (n=23) & C250T (n=62)), the median TBR_{max} (3.33 vs. 3.69, p=0.095), TBR_{mean} (2.08 vs. 2.09, p=0.352), BTV (25.4 vs. 30.0 ml, p=0.130) and TTP_{min} (12.5 vs. 12.5 min, p=0.190) were comparable, too.

Conclusion: Uptake characteristics on dynamic ^{18}F-FET PET are not associated with the TERTp-mutational status in glioblastoma However, as both, dynamic ^{18}F-FET PET parameters as well as the TERTp-mutation status are well-known prognostic biomarkers, future studies should investigate the complementary and independent prognostic value of both factors in order to further stratify patients into risk groups.

Keywords: amino acid PET, molecular genetics, glioblastoma, TERT (telomerase reverse transcriptase), FET PET

INTRODUCTION

According to the updated 2016 WHO classification of brain tumors, the molecular genetic profile plays a major role for the glioma characterization and highly affects the further clinical management and treatment strategies (1, 2). Beyond the current molecular genetic stratification using the isocitrate dehydrogenase (*IDH*)-mutational status and 1p/19q-codeletion, additional molecular genetic markers are increasingly identified and gradually gain access into clinical routine. In particular, mutations of the telomerase reverse transcriptase gene promoter (TERTp) were identified as important factor within the tumorigenesis and individual prognostication (3, 4), with inferior outcome in combination with an *IDH*-wildtype status (5, 6), which will be implemented in upcoming glioma classifications.

As recommended by the Response assessment in Neurooncology (RANO) working group in their clinical guidelines (7–9), molecular imaging using positron-emission-tomography (PET) with radiolabeled amino acids such as O-(2-^{18}F-fluoroethyl)-L-tyrosine (^{18}F-FET) is increasingly used for the comprehensive evaluation and characterization of brain neoplasms beyond morphological standard imaging with MRI, e. g. for treatment planning (10–13), but also for noninvasive tumor characterization at initial diagnosis (14–20). Recent studies indicated that the *IDH*-mutational status is highly associated with ^{18}F-FET PET uptake in brain tumors, especially with the 'minimal time to peak' (TTP_{min}) on dynamic ^{18}F-FET PET, and has thus a high diagnostic power for the identification of *IDH*-wildtype gliomas (21). With regard to TERTp, no study has hitherto evaluated the association of amino acid uptake on PET and the TERTp-mutational status. Hence, we aimed to assess whether the uptake characteristics on static and dynamic ^{18}F-FET PET are likewise associated with the TERTp-mutation status in a homogeneous group of de-novo, *IDH*-wildtype glioblastoma and whether PET can predict the TERTp-mutation status.

METHODS AND MATERIALS

Patients

Patients with histologically confirmed, newly diagnosed *IDH*-wildtype glioblastoma WHO grade IV with available molecular genetic analyses of the TERT-promoter mutation status as well as a dynamic ^{18}F-FET PET scan prior to stereotactic biopsy or surgical resection were identified. All patients have given written informed consent prior to the PET examination as part of the clinical routine. Ethical approval of the retrospective study protocol was given by the institutional review board of the LMU.

Histological Confirmation, Tumor Grading and Molecular Genetic Analysis

Stereotactic biopsy procedures and microsurgical resections were performed at the Department of Neurosurgery, LMU Munich, Germany. As part of the clinical routine, histopathological and molecular genetic evaluations were performed at the Institute of Neuropathology, LMU Munich, Germany, and were initially classified according to the 2007 WHO classification of brain tumors (22) and were re-classified according to the updated 2016 WHO classification (1). The *IDH*-mutation status and TERT-promoter methylation were analyzed in clinical routine according to standard protocols (23–25). For further specification regarding the histopathological workup see also (26, 27).

^{18}F-FET PET Image Acquisition and Data Analysis

^{18}F-FET PET scans were performed at the Department of Nuclear Medicine, LMU. Data of the dynamic ^{18}F-FET PET scans were acquired using an ECAT Exact HR+ scanner (Siemens). After a 15-min transmission scan with a ^{68}Ge rotating rod source, approximately 180 MBq of ^{18}F-FET were injected. Dynamic emission recording was accomplished after tracer injection up to 40 min post injection in 3-D mode consisting of 16 frames (7 x 10 s; 3 x 30 s; 1 x 2 min; 3 x 5 min; 2 x 10 min). Two-dimensional filtered back-projection, reconstruction algorithms using a 5 mm Hann Filter were used for image reconstruction and corrected for photon attenuation and model-based scatter. The mean background activity (BG) was assessed using 6 large crescent-shaped regions of interests (ROI) in the frontal lobe of the healthy contralateral hemisphere fused to a volume of interest (VOI), in which the mean BG was derived (28). The biological tumor volume (BTV) was estimated by a semiautomatic threshold-based delineation of a volume of interest (VOI) using a standardized uptake value (SUV) threshold of 1.6 x BG, as previously described as optimal threshold (29). The maximal SUV (SUV_{max}) and mean SUV (SUV_{mean}) as derived within the BTV were then divided by the BG resulting in mean and maximal tumor-to-background ratio (TBR_{mean}/TBR_{max}). Data on dynamic PET was evaluated using the software PET Display Dynamic implemented in the Hermes workstation: in early summation images (10-30 min p.i.), a 90%

isocontour region of interest was created to extract the time-activity-curves (TACs) on a slice-by-slice manner. Then, the time to peak (TTP) was assessed on each slice of the tumor and the shortest TTP in at least 2 consecutive slices was defined as minimal TTP (TTP_{min}), see also (30, 31).

Statistics

SPSS for Windows (version 23.0; SPSS, Chicago, IL) was used for statistical analyses. Descriptive statistics are displayed as median (range). Normal distribution was assessed using the Shapiro-Wilk-test. The unpaired Wilcoxon-test was used for independent and not-normally distributed continuous parameters. Receiver operating curves (ROC) analyses were used to assess the diagnostic power of continuous parameters, the 'Area under the curve' (AUC) served as quantitative measure for the diagnostic power. Statistical significance was defined as a two-tailed p-value <0.05.

RESULTS

Patients

One-hundred patients with de-novo, *IDH*-wildtype glioblastoma, WHO grade IV were included (62/100 (62.0%) male, 38/100 (38.0%) female). The median age was 62.0 (range, 30.1-82.7) years. Tissue samples for histological and molecular genetic analyses were obtained by stereotactic biopsy in 74/100 (74.0%) and by surgical resection in 26/100 (26.0%) cases. Overall, 15/100 (15%) did not comprise a TERTp-mutation and were classified as TERTp-wildtype. Of the remaining 85/100 (85%) patients with TERTp-mutation, 62/85 (72.9%) showed a C228T-mutation and 23/85 (27.1%) showed a C250T-mutation.

Overall ^{18}F-FET-Uptake Characteristics

All included gliomas were ^{18}F-FET-positive providing a median TBR_{max} of 3.37 (2.06-7.07), a median TBR_{mean} of 2.06 (range, 1.70-2.92) and a median BTV of 25.8 (range, 3.8-133.3) ml. In the dynamic analysis, median TTP_{min} was 12.5 (range, 3.0-35.0) minutes with a small proportion of late $TTP_{min} \geq 25$ minutes in 13/100 (13.0%) cases only.

^{18}F-FET-Uptake Characteristics Comparing TERTp-Mutant and TERTp-Wildtype Glioblastomas and Predictability of TERTp Mutational Status

Comparing glioblastomas with TERTp-mutation (n=85) and those without (n=15) revealed no statistically significant difference in terms of median TBR_{max} (3.41 (range, 2.06-7.07) vs. 3.32 (range, 2.32-4.67), p=0.362), TBR_{mean} (2.09 (range, 1.70-2.92) vs. 2.02 (range, 1.79-2.56), p=0.349) and BTV (26.1 (range, 3.8-133.3) ml vs. 22.4 (range, 3.9-75.7) ml, p=0.377). Not only the evaluated static PET parameters, but also the dynamic parameter TTP_{min} did not differ between those two groups (12.5 (range, 3.0-35.0) min vs. 12.5 (range, 7.5-25.0) min, p=0.411). By consequence, the ROC-analysis to assess the diagnostic power of ^{18}F-FET PET for the prediction of the TERTp mutational status did not reveal reliable thresholds for the differentiation between TERTp-mutant and TERTp-wildtype glioblastomas. Analyzing the static parameters TBR_{max}, TBR_{mean} and BTV, the AUC ranged between 0.572 and 0.576 only. Also, for the dynamic parameter TTP_{min} the AUC reached only 0.562 at a best cut-off at 7.5 min. Further specifications can be found in **Table 1** and **Table 2**. Patient examples can be found on **Figure 1**.

^{18}F-FET-Uptake Characteristics Comparing TERT-Mutation Subtypes (C228T vs. C250T)

Comparing the two subtypes of TERT-promoter mutation C228T (n=62) & C250T (n=23), there was also no statistically significant difference in terms of median TBR_{max} (3.33 (range, 2.06-5.51) vs. 3.69 (range, 2.37-7.07), p=0.095), TBR_{mean} (2.08 (range, 1.70-2.56) vs. 2.09 (range, 1.79-2.92), p=0.352) or BTV (25.4 (range, 3.8-133.3) ml vs. 30.0 (range, 5.7-102.1) ml, p=0.130). On dynamic PET analyses, the median TTP_{min} was also statistically comparable between those two mutation subtypes (12.5 (range, 7.5-35.0) min vs. 12.5 (range, 3.0-35.0) min, p=0.190). For further specifications, please see **Table 3**.

DISCUSSION

This is the first study evaluating the association of amino acid uptake by means of ^{18}F-FET PET and the TERTp-mutational status in glioma patients. As the TERTp-mutational status has shown additional prognostic value in *IDH*-wildtype gliomas/glioblastomas (5, 6, 32, 33), a non-invasive tool for the prediction of a TERTp-mutation would be helpful for the

TABLE 2 | Diagnostic power of ^{18}F-FET PET for detection TERTp mutation.

Parameter	Best cut-off value	Area under the curve	Level of significance
TBR_{max}	3.60	0.574	p=0.323
TBR_{mean}	2.21	0.576	p=0.297
BTV	24.1 ml	0.572	p=0.359
TTP_{min}	7.5 min	0.562	p=0.391

TABLE 1 | Influence of TERT-mutation on ^{18}F-FET-uptake characteristics [median (range)].

	Overall (n=100)	TERT-mutation (n=85)	TERT-wildtype (n=15)	Level of significance
TBR_{max}	3.37 (2.06-7.07)	3.41 (2.06-7.07)	3.32 (2.32-4.67)	p=0.362
TBR_{mean}	2.06 (1.70-2.92)	2.09 (1.70-2.92)	2.02 (1.79-2.56)	p=0.349
BTV	25.8 (3.8-133.3) ml	26.1 (3.8-133.3) ml	22.4 (3.9-75.7) ml	p=0.377
TTP_{min}	12.5 (3.0-35.0) min	12.5 (3.0-35.0) min	12.5 (7.5-25.0) min	p=0.411

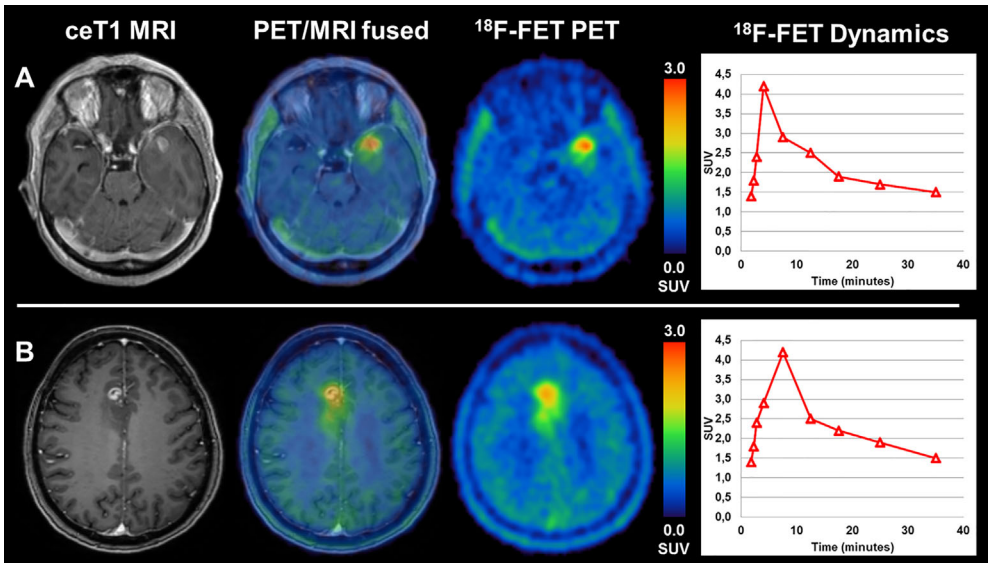

FIGURE 1 | **(A)** a patient with TERTp-mutant glioblastoma (TBR_{max} 4,1; TBR_{mean} 2,3; BTV 15,4 ml, TTP_{min} 5 $_{min}$) shows comparable, only slightly diverging imaging features as **(B)**, a patient with TERTp-wildtype glioblastoma (TBR_{max} 2,9; TBR_{mean} 1,9; BTV 12,3 ml, TTP_{min} 10 $_{min}$).

TABLE 3 | Influence of TERT-mutation subtypes on ^{18}F-FET-uptake characteristics [median (range)].

	TERT-mutation overall (n = 85)	C228T (n = 62)	C250T (n = 23)	Level of significance
TBR_{max}	3.41 (2.06-7.07)	3.33 (2.06-5.51)	3.69 (2.37-7.07)	p=0.095
TBR_{mean}	2.09 (1.70-2.92)	2.08 (1.70-2.56)	2.09 (1.79-2.92)	p=0.352
BTV	26.1 (3.8-133.3) ml	25.4 (3.8-133.3) ml	30.0 (5.7-102.1) ml	p=0.130
TTP_{min}	12.5 (3.0-35.0) min	12.5 (7.5-35.0) min	12.5 (3.0-35.0) min	p=0.190

clinical management of glioma patients. In our large cohort with homogeneous histological and molecular genetic profile (i.e. WHO grade IV glioblastoma, *IDH*-wildtype only), we observed a high proportion of patients with TERTp mutation of 85%, which is in line with the proportion of patients with TERTp mutation in the current literature (4). Moreover, within the group of TERTp mutant glioblastomas, the C228T-mutation was present more frequently (72.9%) than the C250T-mutation (27.1%), which is also in line with the distribution within *IDH*-wildtype glioblastomas as described in the current literature (6, 34).

Comparing the TERTp-mutational status with the static PET parameters in terms of uptake intensity (TBR_{max} and TBR_{mean}) and tumor extent (BTV), we observed a high overlap between TERTp-mutant and TERTp-wildtype tumors so that no cutoff could be found to differentiate between those groups. Moreover, TTP_{min} on dynamic PET was also indifferent between TERTp-mutant and TERTp-wildtype glioblastomas. Taken together, both groups presented with comparable imaging findings and could not be distinguished on ^{18}F-FET PET. This leads to the assumption that dynamic ^{18}F-FET PET cannot predict the TERTp-mutational status in *IDH*-wildtype glioblastoma. Taking a closer look at the *IDH*-mutational status, however, recent studies indicated that the *IDH*-mutational status can be identified non-invasively by dynamic ^{18}F-FET PET with a relatively high diagnostic accuracy. In particular, the prognostically poor *IDH*-wildtype status can be predicted by a short TTP_{min} on dynamic ^{18}F-FET PET (21).

When analyzing the TERTp-mutation subtypes (i.e. C228T & C250T), expectedly, no difference in terms of uptake-intensity (TBR_{max} & TBR_{mean}) and tumor extent (i.e. BTV) on PET could be observed; also, TTP_{min} on dynamic PET was indifferent between C228T & C250T mutations. This finding, however, is not surprising, as these two mutations of hot spot promoter regions (C228T and C250T) are basically responsible for the same molecular mechanism (32, 33).

In general, one could speculate that the pathophysiological changes that are accompanied with TERTp mutations and their influence on cell regulation might also affect the cellular metabolism in terms of amino acid metabolism. Moreover, one could argue that both static and dynamic ^{18}F-FET PET parameters were described to be of prognostic value in the further disease course of glioma patients; as the same is true for TERTp mutations, a certain intercorrelation does not seem unlikely. On a molecular level, the TERT as a catalytic subunit of the telomerase enzyme complex is critically involved in telomere maintenance and lengthening. Abnormal upregulation and activity of TERT as a consequence of TERTp-mutations are considered one of the mechanisms of cellular immortality in cancer cells during division, particularly in gliomas (35–37). With regard to PET imaging, the activity and/or expression of the large neutral amino

acid transporter (LAT) at the tumor cells and at the brain capillary endothelial cells (38) is considered a key factor responsible for the intracellular uptake of amino acids in gliomas (39). The very exact mechanisms and the histopathological or even molecular genetic correlate resulting in diverging uptake dynamics of ^{18}F-FET are not fully clarified yet and may be influenced by further factors such as vascularization. Our study findings suggest that the presence or, vice versa, the absence of TERTp-mutation in glioblastoma and the accompanying features on a cellular basis, although prognostically relevant, do neither result in an altered level of amino acid metabolism nor in changes of uptake dynamics on ^{18}F-FET PET.

Notably, there is an occurrence of TERTp-mutations in different tumor types as well, also in molecular subgroups with superior prognosis compared to *IDH*-wildtype gliomas, e. g. in *IDH*-mutant gliomas. Interestingly, among *IDH*-mutant gliomas, *IDH*-mutant gliomas with TERTp-mutation comprise a superior clinical outcome compared to *IDH*-mutant glioma without TERTp-mutation, also with emphasis on the particular histological features (5). Therefore, the presence of TERTp-mutations in brain tumors per se is not necessarily linked to a more aggressive course in general. Particularly, in the group of oligodendroglial tumors (i.e. gliomas with both *IDH*-mutation and 1p/19q-codeletion), basically every tumor presents with TERTp-mutation. This molecular genetic subgroup is associated with favorable outcome compared to e.g. *IDH*-wildtype gliomas (32, 40), despite a basically general presence of TERTp mutations. These phenomena also warrant further investigation of PET-based imaging characteristics in the subgroup of *IDH*-mutant gliomas. First preliminary data using radiomic features on MRI could show certain moderate diagnostic power for the detection of TERTp mutations particularly in low-grade/*IDH*-mutant gliomas (41, 42).

Moreover, a vast body of literature exists dealing with radiomics, deep learning and machine learning with special emphasis on (^{18}F-FET) PET and hybrid imaging in neuro-oncology (43–49), not just for the differentiation of treatment-related changes from real progression (44, 50, 51), but also for the predication of prognostically relevant mutations such as the *IDH*-mutation (52). Hence, it needs to be evaluated, if further PET-based analyses with the extraction of radiomic features may add value to the conventional image analysis in order to non-invasively identify the TERTp-mutational status. Interestingly, the predictability of key mutations using standard and advanced PET quantification also seems to vary depending on the used radioligands (53–57).

Particularly, as dynamic ^{18}F-FET PET was previously reported to show a high prognostic value in gliomas in addition to the clinically most important molecular genetic biomarkers according to the 2016 WHO classification [*IDH*-mutation and 1p/19q-codeletion status (14, 26)], it would be interesting to evaluate whether the additional prognostic value of PET remains even after further subgroup stratification according to the TERTp mutation status. In order to test this hypothesis, further studies with a larger number of patients (particularly in the relatively small TERTp-wildtype subgroup) are needed to perform multivariate analyses.

Limitations arise from the retrospective study design. Moreover, as mentioned above, the absolute number of tumors without TERTp mutations is relatively low (i.e. n=15 vs. n=85), however, this proportion is in line with the previously reported distribution of TERTp mutations in glioblastoma. In the current manuscript, only filtered-back projection (FBP) reconstructions were used due to the applied scanner; quantification of PET parameters could potentially be diverging using other reconstruction algorithms such as ordered subset expectation maximization (OSEM).

CONCLUSION

The prognostically relevant TERTp-mutational status in *IDH*-wildtype glioblastoma is not associated with uptake characteristics on dynamic ^{18}F-FET PET. As both, dynamic ^{18}F-FET PET parameters as well as the TERTp-mutation status are well-known prognostic biomarkers, but show no association in our analysis, it seems highly interesting to evaluate in larger studies if both factors are independent predictors of patients' survival and can thereby further stratify patients into risk groups.

DATA AVAILABILITY STATEMENT

The raw data supporting the conclusions of this article will be made available by the authors upon reasonable request.

ETHICS STATEMENT

The studies involving human participants were reviewed and approved by Ethics committee, LMU Munich. Written informed consent for participation was not required for this study in accordance with the national legislation and the institutional requirements.

AUTHOR CONTRIBUTIONS

Conceptualization, MU and NA. Methodology, MU, VR, KR, BS, LM, LB, MB, VW, and WK. Formal analysis, MU, VR, KR, and NA. Resources, all authors. Writing—original draft preparation, MU and NA. Writing—review and editing, all authors. Visualization, MU and NA. Supervision, NA, MN, JH, JT, and PB. Project administration, MU and NA. All authors contributed to the article and approved the submitted version.

ACKNOWLEDGMENTS

Parts of this paper originate from the doctoral thesis of KR. This work was supported by the Collaborative Research Centre SFB-824 of the Deutsche Forschungsgemeinschaft (DFG) and by the Else Kröner-Fresenius-Stiftung.

REFERENCES

1. Louis DN, Perry A, Reifenberger G, Von Deimling A, Figarella-Branger D, Cavenee WK, et al. The 2016 World Health Organization classification of tumors of the central nervous system: a summary. *Acta Neuropathol* (2016) 131:803–20. doi: 10.1007/s00401-016-1545-1
2. Weller M, van den Bent M, Tonn JC, Stupp R, Preusser M, Cohen-Jonathan-Moyal E, et al. European Association for Neuro-Oncology (EANO) Guideline on the Diagnosis and Treatment of Adult Astrocytic and Oligodendroglial Gliomas. *Lancet Oncol* (2017) 18:e315–29. doi: 10.1016/S1470-2045(17)30194-8
3. Nonoguchi N, Ohta T, Oh J-E, Kim Y-H, Kleihues P, Ohgaki H. TERT Promoter Mutations in Primary and Secondary Glioblastomas. *Acta Neuropathol* (2013) 126:931–7. doi: 10.1007/s00401-013-1163-0
4. Simon M, Hosen I, Gousias K, Rachakonda S, Heidenreich B, Gessi M, et al. TERT Promoter Mutations: a Novel Independent Prognostic Factor in Primary Glioblastomas. *Neuro-oncology* (2014) 17:45–52. doi: 10.1093/neuonc/nou158
5. Eckel-Passow JE, Lachance DH, Molinaro AM, Walsh KM, Decker PA, Sicotte H, et al. Glioma Groups Based on 1p/19q, IDH, and TERT Promoter Mutations in Tumors. *New Engl J Med* (2015) 372:2499–508. doi: 10.1056/NEJMoa1407279
6. Labussière M, Boisselier B, Mokhtari K, Di Stefano A-L, Rahimian A, Rossetto M, et al. Combined Analysis of TERT, EGFR, and IDH Status Defines Distinct Prognostic Glioblastoma Classes. *Neurology* (2014) 83:1200–6. doi: 10.1212/WNL.0000000000000814
7. Albert NL, Weller M, Suchorska B, Galldiks N, Soffietti R, Kim MM, et al. Response Assessment in Neuro-Oncology Working Group and European Association for Neuro-Oncology Recommendations for the Clinical use of PET Imaging in Gliomas. *Neuro-oncology* 2016:now058. doi: 10.1093/neuonc/now058
8. Galldiks N, Langen K-J, Albert NL, Chamberlain M, Soffietti R, Kim MM, et al. PET Imaging in Patients With Brain Metastasis—Report of the RANO/PET Group. *Neuro-oncology* (2019). doi: 10.1093/neuonc/noz003
9. Law I, Albert NL, Arbizu J, Boellaard R, Drzezga A, Galldiks N, et al. Joint EANM/EANO/RANO Practice Guidelines/SNMMI Procedure Standards For Imaging Of Gliomas Using PET With Radiolabelled Amino Acids and [18 F] FDG: Version 1.0. *Eur J Nucl Med Mol Imaging* (2019) 46:540–57. doi: 10.1007/s00259-018-4207-9
10. Niyazi M, Geisler J, Siefert A, Schwarz SB, Ganswindt U, Garny S, et al. FET-PET for Malignant Glioma Treatment Planning. *Radiother Oncol* (2011) 99:44–8. doi: 10.1016/j.radonc.2011.03.001
11. Piroth MD, Pinkawa M, Holy R, Stoffels G, Demirel C, Attieh C, et al. Integrated-Boost IMRT or 3-D-CRT Using FET-PET Based Auto-Contoured Target Volume Delineation for Glioblastoma Multiforme–a Dosimetric Comparison. *Radiat Oncol* (2009) 4:57. doi: 10.1186/1748-717X-4-57
12. Fleischmann DF, Unterrainer M, Schön R, Corradini S, Maihöfer C, Bartenstein P, et al. Margin Reduction in Radiotherapy for Glioblastoma Through 18F-Fluoroethyltyrosine PET?–A Recurrence Pattern Analysis. *Radiother Oncol* (2020) 145:49–55. doi: 10.1016/j.radonc.2019.12.005
13. Unterrainer M, Eze C, Ilhan H, Marschner S, Roengvoraphoj O, Schmidt-Hegemann N, et al. Recent Advances of PET Imaging in Clinical Radiation Oncology. *Radiat Oncol* (2020) 15:1–15. doi: 10.1186/s13014-020-01519-1
14. Bauer EK, Stoffels G, Blau T, Reifenberger G, Felsberg J, Werner JM, et al. Prediction of Survival in Patients With IDH-Wildtype Astrocytic Gliomas Using Dynamic O-(2-[18F]-Fluoroethyl)-l-Tyrosine PET. *Eur J Nucl Med Mol Imaging* (2020) 47:1486–95. doi: 10.1007/s00259-020-04695-0
15. Ceccon G, Lazaridis L, Stoffels G, Rapp M, Weber M, Blau T, et al. Use of FET PET in Glioblastoma Patients Undergoing Neurooncological Treatment Including Tumour-Treating Fields: Initial Experience. *Eur J Nucl Med Mol Imaging* (2018) 45:1626–35. doi: 10.1007/s00259-018-3992-5
16. Galldiks N, Dunkl V, Ceccon G, Tscherpel C, Stoffels G, Law I, et al. Early Treatment Response Evaluation Using FET PET Compared to MRI in Glioblastoma Patients at First Progression Treated With Bevacizumab Plus Lomustine. *Eur J Nucl Med Mol Imaging* (2018) 45:2377–86. doi: 10.1007/s00259-018-4082-4
17. Galldiks N, Unterrainer M, Judov N, Stoffels G, Rapp M, Lohmann P, et al. Photopenic Defects on O-(2-[18F]-fluoroethyl)-L-Tyrosine PET: Clinical Relevance in Glioma Patients. *Neuro-oncology* (2019) 21:1331–8. doi: 10.1093/neuonc/noz083
18. Romagna A, Unterrainer M, Schmid-Tannwald C, Brendel M, Tonn J-C, Nachbichler SB, et al. Suspected Recurrence of Brain Metastases After Focused High Dose Radiotherapy: can [18 F] FET-PET Overcome Diagnostic Uncertainties? *Radiat Oncol* (2016) 11:139. doi: 10.1186/s13014-016-0713-8
19. Unterrainer M, Schweisthal F, Suchorska B, Wenter V, Schmid-Tannwald C, Fendler WP, et al. Serial 18F-FET PET Imaging of Primarily 18F-FET–Negative Glioma: Does it Make Sense? *J Nucl Med* (2016) 57:1177–82. doi: 10.2967/jnumed.115.171033
20. Verger A, Stoffels G, Bauer EK, Lohmann P, Blau T, Fink GR, et al. Static and Dynamic 18F–FET PET for the Characterization of Gliomas Defined by IDH and 1p/19q Status. *Eur J Nucl Med Mol Imaging* (2018) 45:443–51. doi: 10.1007/s00259-017-3846-6
21. Vettermann F, Suchorska B, Unterrainer M, Nelwan D, Forbrig R, Ruf V, et al. Non-Invasive Prediction of IDH-Wildtype Genotype in Gliomas Using Dynamic 18 F-FET PET. *Eur J Nucl Med Mol Imaging* (2019) 46:2581–9. doi: 10.1007/s00259-019-04477-3
22. Louis DN, Ohgaki H, Wiestler OD, Cavenee WK, Burger PC, Jouvet A, et al. The 2007 WHO Classification of Tumours of the Central Nervous System. *Acta Neuropathol* (2007) 114:97–109. doi: 10.1007/s00401-007-0243-4
23. Thon N, Eigenbrod S, Kreth S, Lutz J, Tonn JC, Kretzschmar H, et al. IDH1 Mutations in Grade II Astrocytomas are Associated With Unfavorable Progression-Free Survival and Prolonged Postrecurrence Survival. *Cancer* (2012) 118:452–60. doi: 10.1002/cncr.26298
24. Thon N, Eigenbrod S, Grasbon-Frodl EM, Ruiter M, Mehrkens JH, Kreth S, et al. Novel Molecular Stereotactic Biopsy Procedures Reveal Intratumoral Homogeneity of Loss of Heterozygosity of 1p/19q and TP53 Mutations in World Health Organization Grade II Gliomas. *J Neuropathol Exp Neurol* (2009) 68:1219–28. doi: 10.1097/NEN.0b013e3181bee1f1
25. Biczok A, Kraus T, Suchorska B, Terpolilli NA, Thorsteinsdottir J, Giese A, et al. TERT Promoter Mutation is Associated With Worse Prognosis in WHO Grade II and III Meningiomas. *J Neuro-oncol* (2018) 139:671–8. doi: 10.1007/s11060-018-2912-7
26. Suchorska B, Giese A, Biczok A, Unterrainer M, Weller M, Drexler M, et al. Identification of Time-to-Peak on Dynamic 18F-FET-PET as a Prognostic Marker Specifically in IDH1/2 Mutant Diffuse Astrocytoma. *Neuro-Oncology* (2017). doi: 10.1093/neuonc/nox153
27. Jansen NL, Suchorska B, Wenter V, Eigenbrod S, Schmid-Tannwald C, Zwergal A, et al. Dynamic 18F-FET PET in Newly Diagnosed Astrocytic Low-Grade Glioma Identifies High-Risk Patients. *J Nucl Med* (2014) 55:198–203. doi: 10.2967/jnumed.113.122333
28. Unterrainer M, Vettermann F, Brendel M, Holzgreve A, Lifschitz M, Zähringer M, et al. Towards Standardization of 18 F-FET PET Imaging: do we Need a Consistent Method of Background Activity Assessment? *EJNMMI Res* (2017) 7:48. doi: 10.1186/s13550-017-0295-y
29. Pauleit D, Floeth F, Hamacher K, Riemenschneider MJ, Reifenberger G, Muller HW, et al. O-(2-[18F]fluoroethyl)-L-Tyrosine PET Combined with MRI Improves the Diagnostic Assessment of Cerebral Gliomas. *Brain* (2005) 128:678–87. doi: 10.1093/brain/awh399
30. Jansen NL, Suchorska B, Wenter V, Schmid-Tannwald C, Todica A, Eigenbrod S, et al. Prognostic Significance of Dynamic 18F-FET PET in Newly Diagnosed Astrocytic High-Grade Glioma. *J Nucl Med* (2015) 56:9–15. doi: 10.2967/jnumed.114.144675
31. Jansen NL, Graute V, Armbruster L, Suchorska B, Lutz J, Eigenbrod S, et al. MRI-Suspected Low-Grade Glioma: is There a Need to Perform Dynamic FET PET? *Eur J Nucl Med Mol Imaging* (2012) 39:1021–9. doi: 10.1007/s00259-012-2109-9
32. Labussiere M, Di Stefano A, Gleize V, Boisselier B, Giry M, Mangesius S, et al. TERT Promoter Mutations in Gliomas, Genetic Associations and Clinico-Pathological Correlations. *Br J Cancer* (2014) 111:2024–32. doi: 10.1038/bjc.2014.538
33. Patel B, Taiwo R, Kim AH, Dunn GP. TERT, a Promoter of CNS Malignancies. *Neuro-Oncol Adv* (2020) 2:vdaa025. doi: 10.1093/noajnl/vdaa025
34. Lee Y, Koh J, Kim S-I, Won JK, Park C-K, Choi SH, et al. The Frequency and Prognostic Effect of TERT Promoter Mutation in Diffuse Gliomas. *Acta Neuropathol Commun* (2017) 5:62. doi: 10.1186/s40478-017-0465-1
35. Horn S, Figl A, Rachakonda PS, Fischer C, Sucker A, Gast A, et al. TERT Promoter Mutations in Familial and Sporadic Melanoma. *Science* (2013) 339:959–61. doi: 10.1126/science.1230062

36. Huang FW, Hodis E, Xu MJ, Kryukov GV, Chin L, Garraway LA. Highly Recurrent TERT Promoter Mutations in Human Melanoma. *Science* (2013) 339:957–9. doi: 10.1126/science.1229259
37. Vinagre J, Almeida A, Pópulo H, Batista R, Lyra J, Pinto V, et al. Frequency of TERT Promoter Mutations in Human Cancers. *Nat Commun* (2013) 4:1–6. doi: 10.1038/ncomms3185
38. Boado RJ, Li JY, Nagaya M, Zhang C, Pardridge WM. Selective Expression of the Large Neutral Amino Acid Transporter at the Blood–Brain Barrier. *Proc Natl Acad Sci U S A* (1999) 96:12079–84. doi: 10.1073/pnas.96.21.12079
39. Habermeier A, Graf J, Sandhöfer BF, Boissel JP, Roesch F, Closs E. System l Amino Acid Transporter LAT1 Accumulates O-(2-fluoroethyl)-l-Tyrosine (FET). *Amino Acids* (2015) 47:335–44. doi: 10.1007/s00726-014-1863-3
40. Wesseling P, van den Bent M, Perry A. Oligodendroglioma: Pathology, Molecular Mechanisms and Markers. *Acta Neuropathol* (2015) 129:809–27. doi: 10.1007/s00401-015-1424-1
41. Arita H, Kinoshita M, Kawaguchi A, Takahashi M, Narita Y, Terakawa Y, et al. Lesion Location Implemented Magnetic Resonance Imaging Radiomics for Predicting IDH and TERT Promoter Mutations in grade II/III Gliomas. *Sci Rep* (2018) 8:1–10. doi: 10.1038/s41598-018-30273-4
42. Ivanidze J, Lum M, Pisapia D, Magge R, Ramakrishna R, Kovanlikaya I, et al. MRI Features Associated with TERT Promoter Mutation Status in Glioblastoma. *J Neuroimaging* (2019) 29:357–63. doi: 10.1111/jon.12596
43. Gutsche R, Scheins J, Kocher M, Bousabarah K, Fink GR, Shah NJ, et al. Evaluation of FET PET Radiomics Feature Repeatability in Glioma Patients. *Cancers* (2021) 13:647. doi: 10.3390/cancers13040647
44. Kebir S, Schmidt T, Weber M, Lazaridis L, Galldiks N, Langen K-J, et al. A Preliminary Study on Machine Learning-Based Evaluation of Static and Dynamic FET-PET for the Detection of Pseudoprogression in Patients with IDH-Wildtype Glioblastoma. *Cancers* (2020) 12:3080. doi: 10.3390/cancers12113080
45. Li XT, Huang RY. Standardization of Imaging Methods for Machine Learning in Neuro-Oncology. *Neuro-oncol Adv* (2020) 2:iv49–55. doi: 10.1093/noajnl/vdaa054
46. Lohmann P, Galldiks N, Kocher M, Heinzel A, Filss CP, Stegmayr C, et al. Radiomics in Neuro-Oncology: Basics, Workflow, and Applications. *Methods* (2021) 188:112–21. doi: 10.1016/j.ymeth.2020.06.003
47. Lohmann P, Kocher M, Ruge MI, Visser-Vandewalle V, Shah NJ, Fink GR, et al. PET/MRI Radiomics in Patients With Brain Metastases. *Front Neurol* (2020) 11. doi: 10.3389/fneur.2020.00001
48. Lohmann P, Meißner A-K, Kocher M, Bauer EK, Werner J-M, Fink GR, et al. Feature-Based PET/MRI Radiomics in Patients With Brain Tumors. *Neuro-Oncol Adv* (2021) 2:iv15–21. doi: 10.1093/noajnl/vdaa118
49. Wiestler B, Menze B. Deep Learning for Medical Image Analysis: a Brief Introduction. *Neuro-Oncol Adv* (2020) 2:iv35–41. doi: 10.1093/noajnl/vdaa092
50. Lohmann P, Elahmadawy MA, Gutsche R, Werner J-M, Bauer EK, Ceccon G, et al. FET PET Radiomics for Differentiating Pseudoprogression from Early Tumor Progression in Glioma Patients Post-Chemoradiation. *Cancers* (2020) 12:3835. doi: 10.3390/cancers12123835
51. Lohmann P, Kocher M, Ceccon G, Bauer EK, Stoffels G, Viswanathan S, et al. Combined FET PET/MRI Radiomics Differentiates Radiation Injury From Recurrent Brain Metastasis. *NeuroImage: Clin* (2018) 20:537–42. doi: 10.1016/j.nicl.2018.08.024
52. Lohmann P, Lerche C, Bauer EK, Steger J, Stoffels G, Blau T, et al. Predicting IDH Genotype in Gliomas Using FET PET Radiomics. *Sci Rep* (2018) 8:13328. doi: 10.1038/s41598-018-31806-7
53. Bumes E, Wirtz F-P, Fellner C, Grosse J, Hellwig D, Oefner PJ, et al. Non-Invasive Prediction of IDH Mutation in Patients with Glioma WHO II/III/IV Based on F-18-FET PET-Guided In Vivo 1H-Magnetic Resonance Spectroscopy and Machine Learning. *Cancers* (2020) 12:3406. doi: 10.3390/cancers12113406
54. Cimini A, Chiaravalloti A, Ricci M, Villani V, Vanni G, Schillaci O. MGMT Promoter Methylation and IDH1 Mutations Do Not Affect [18F]FDOPA Uptake in Primary Brain Tumors. *Int J Mol Sci* (2020) 21:7598. doi: 10.3390/ijms21207598
55. Li L, Mu W, Wang Y, Liu Z, Liu Z, Wang Y, et al. A Non-Invasive Radiomic Method Using 18F-FDG PET Predicts Isocitrate Dehydrogenase Genotype and Prognosis in Patients With Glioma. *Front Oncol* (2019) 9. doi: 10.3389/fonc.2019.01183
56. Matsui Y, Maruyama T, Nitta M, Saito T, Tsuzuki S, Tamura M, et al. Prediction of Lower-Grade Glioma Molecular Subtypes Using Deep Learning. *J Neuro-Oncol* (2020) 146:321–7. doi: 10.1007/s11060-019-03376-9
57. Zhou W, Zhou Z, Wen J, Xie F, Zhu Y, Zhang Z, et al. A Nomogram Modeling 11C-MET PET/CT and Clinical Features in Glioma Helps Predict IDH Mutation. *Front Oncol* (2020) 10. doi: 10.3389/fonc.2020.01200

Conflict of Interest: NA is a member of the Neuroimaging Committee of the EANM.

The remaining authors declare that the research was conducted in the absence of any commercial or financial relationships that could be construed as a potential conflict of interest.

frontiers in Oncology

ORIGINAL RESEARCH
published: 29 April 2021
doi: 10.3389/fonc.2021.645162

^{18}F-Trifluoromethylated D-Cysteine as a Promising New PET Tracer for Glioma Imaging: Comparative Analysis With MRI and Histopathology in Orthotopic C6 Models

Hui Ma[1,2†], Jing Zhao[1†], Shaoyu Liu[2,3], Dingxiang Xie[1], Zhanwen Zhang[2,4], Dahong Nie[2,5], Fuhua Wen[2], Zhiyun Yang[1] and Ganghua Tang[2,6*]*

[1] Department of Radiology, The First Affiliated Hospital, Sun Yat-sen University, Guangzhou, China, [2] Department of Nuclear Medicine, Guangdong Engineering Research Center for Translational Application of Medical Radiopharmaceuticals, The First Affiliated Hospital, Sun Yat-sen University, Guangzhou, China, [3] Department of Nuclear Medicine, The First Affiliated Hospital of Guangzhou Medical University, Guangzhou, China, [4] Department of Nuclear Medicine, The Sixth Affiliated Hospital, Sun Yat-sen University, Guangzhou, China, [5] Department of Radiation Oncology, The First Affiliated Hospital, Sun Yat-sen University, Guangzhou, China, [6] Nanfang PET Center, Department of Nuclear Medicine, Nanfang Hospital, Southern Medical University, Guangzhou, China

OPEN ACCESS

Edited by:
Cornelia Brendle, Tübingen University Hospital, Germany

Reviewed by:
Tadashi Watabe, Osaka University, Japan
Shushi Nagamori, Jikei University School of Medicine, Japan

***Correspondence:**
Shaoyu Liu
liushy69@mail.sysu.edu.cn
Ganghua Tang
tangghua@mail.sysu.edu.cn

[†]These authors have contributed equally to this work and share first authorship

Specialty section:
This article was submitted to Cancer Imaging and Image-directed Interventions, a section of the journal Frontiers in Oncology

Received: 22 December 2020
Accepted: 15 February 2021
Published: 29 April 2021

Citation:
Ma H, Zhao J, Liu S, Xie D, Zhang Z, Nie D, Wen F, Yang Z and Tang G (2021) ^{18}F-Trifluoromethylated D-Cysteine as a Promising New PET Tracer for Glioma Imaging: Comparative Analysis With MRI and Histopathology in Orthotopic C6 Models. Front. Oncol. 11:645162. doi: 10.3389/fonc.2021.645162

Comparing MRI and histopathology, this study aims to comprehensively explore the potential application of ^{18}F-trifluoromethylated D-cysteine (*S*-[^{18}F]CF_3-D-CYS) in evaluating glioma by using orthotopic C6 glioma models. Sprague–Dawley (SD) rats (n = 9) were implanted with C6 glioma cells. Tumor growth was monitored every week by multiparameter MRI [including dynamic contrast-enhanced MRI (DCE-MRI)], [^{18}F]FDG, *S*-[^{18}F]CF_3-D-CYS, and [^{18}F]FDOPA PET imaging. Repeated scans of the same rat with the two or three [^{18}F]-labeled radiotracers were investigated. Initial regions of interest were manually delineated on T_2WI and set on the same level of PET images, and tumor-to-normal brain uptake ratios (TNRs) were calculated to semiquantitatively assess the tracer accumulation in the tumor. The tumor volume in PET and histopathology was calculated. HE and Ki67 immunohistochemical staining were further performed. The correlations between the uptake of *S*-[^{18}F]CF_3-D-CYS and Ki67 were analyzed. Dynamic *S*-[^{18}F]CF_3-D-CYS PET imaging showed tumor uptake rapidly reached a peak, maintained plateau during 10–30 min after injection, then decreased slowly. Compared with [^{18}F]FDG and [^{18}F]FDOPA PET imaging, *S*-[^{18}F]CF_3-D-CYS PET demonstrated the highest TNRs ($P < 0.05$). There were no significant differences in the tumor volume measured on *S*-[^{18}F]CF_3-D-CYS PET or HE specimen. Furthermore, our results showed that the uptake of *S*-[^{18}F]CF_3-D-CYS was significantly positively correlated with tumor Ki67, and the poor accumulated *S*-[^{18}F]CF_3-D-CYS was consistent with tumor hemorrhage. There was no significant correlation between the *S*-[^{18}F]CF_3-D-CYS uptakes and the

K^{trans} values derived from DCE-MRI. In comparison with MRI and histopathology, *S*-[^{18}F]CF_3-D-CYS PET performs well in the diagnosis and evaluation of glioma. *S*-[^{18}F]CF_3-D-CYS PET may serve as a valuable tool in the clinical management of gliomas.

Keywords: glioma, PET imaging, MRI, PET tracers, amino acid

INTRODUCTION

Gliomas are the most common primary intracranial tumor with high mortality and poor prognosis. The high tumor heterogeneity and invasiveness present a considerable obstacle to the treatment of glioma, which was the reason for causing tumor recurrence and treatment resistance (1). Thus, seeking a non-invasive modality to the full extent of depicting the tumor invasion and demonstrating the tumor heterogeneity is proficient for glioma diagnosis and treatment design. MRI has been routinely and wildly used to evaluate gliomas. However, the conventional and advanced MRI sequences are still not good enough to identify the tumor boundary and to provide all needed pathophysiological information of gliomas (2, 3). Beyond the MRI, PET provides additional insights into the pathophysiology of gliomas (4, 5).

[^{18}F]FDG is the most commonly used PET tracer in the clinic, and it has been widely used to evaluate a variety of cancers, including gliomas. However, the high uptakes of [^{18}F]FDG in both tumor and normal gray matter bring a strong challenge for the diagnosis of gliomas and tumor boundary delineation. Currently, amino acid (AA) tracers have been used predominantly for glioma imaging and exhibit lower uptake in a normal brain tissue, which is better suitable for the delineation of tumor extent and treatment planning than [^{18}F]FDG (6). This would be explained by the fact that, compared with the normal tissue, the AA transporters such as LAT-1 (belonging to system L) are overexpressed in gliomas (7, 8). Among all types of amino acid tracers, *S*-[^{11}C]methyl-L-methionine ([^{11}C]-MET) is preferred in clinical use (9, 10). Some investigations have demonstrated that [^{11}C]-MET had a higher sensitivity and a lower specificity, which varied between 75 and 100%. Unfortunately, [^{11}C]-MET is not an ideal tumor tracer since inflammatory processes are also known to show increased [^{11}C]-MET uptake, and the short half-life of the radionuclide ^{11}C (20.38 min) further limits the extensive clinical application of [^{11}C]-MET (11). In addition, 6-[^{18}F]fluoro-L-3,4-dihydroxyphenylalanine ([^{18}F]FDOPA, a classic dopamine neurotransmitter imaging agent) has recently been used for evaluating glioma and demonstrated promising results in predicting low-grade glioma prognosis and in diagnosing recurrent glioma (12, 13). However, it cannot be ignored that the high uptake in basal ganglia of [^{18}F]FDOPA may have an impact on the delineation of glioma boundary. Besides, the longer half-lives (109.7 min) and similar transport mechanism to [^{11}C]-MET make O-(2-[^{18}F]fluoroethyl)-L-tyrosine ([^{18}F]-FET, a tyrosine analog radiolabeled PET tracer) more suitable for clinical use (14). However, the slow renal elimination and some false negatives in diagnosing gliomas make [^{18}F]-FET flawed (15). Thus, novel PET tracers for good imaging of gliomas are still in demand.

Taking the advantage of ^{18}F with a relatively long half-life time (109.7 min) into consideration, our group has developed a pair of novel ^{18}F-labeled AA PET tracers (^{18}F-trifluoromethylated D- and L-cysteines) (16). They were designed as "structure-mimetic" amino acid tracers via replacement of methyl group with the ^{18}F-trifluoromethyl group according to a structure-based bioisosterism strategy. Based on a series of cellular and biological evaluations, our preliminary results suggested that ^{18}F-trifluoromethylated D-cysteine (*S*-[^{18}F]CF_3-D-CYS) was a promising PET tracer for evaluating gliomas. In addition, *S*-[^{18}F]CF_3-D-CYS is an analog of *S*-[^{11}C]methyl-L-cysteine, in which its low uptake by the brain tissue has been reported and was able to detect recurrent glioma (17). Hence, in this study, we plan to further evaluate the ability of *S*-[^{18}F]CF_3-D-CYS PET imaging in the diagnosis of glioma compared to [^{18}F]FDG and [^{18}F]FDOPA PET with reference to MRI and histopathology through orthotropic C6 glioma models.

MATERIALS AND METHODS

Study Design

This study has complied with the recommendations of the Guidance for the Care and Use of Laboratory Animals of the Ministry of Science and Technology of the People's Republic of China. Our experiments were approved by the Institutional Animal Care and Use Committee (IACUC), Sun Yat-sen University (Permit Number SYSU-IACUC-2019-000057).

The male Sprague–Dawley (SD) rats ($n = 9$) were stereotactically injected with C6 glioma cells for the establishment of orthotropic C6 glioma models. Multiparameter MRI including conventional MRI and DCE-MRI and [^{18}F]FDG PET imaging was performed on the 7th, 14th, and 21st days after the operation. Subsequently, *S*-[^{18}F]CF_3-D-CYS and [^{18}F]FDOPA PET imaging was performed in the succeeding days. Experimental procedures are shown in **Figure 1**. After imaging acquisition, tumor-bearing rat models were sacrificed for pathological examinations including hematoxylin–eosin staining (HE) and Ki67 immunohistochemical staining. During the whole experimental procedures, if the rats were dead (glioma-bearing rats were vulnerable to death), they were immediately subjected to pathological examinations.

Cell Culture and Animal Models

C6 glioma cells were purchased from the Cell Bank of the Chinese Academy of Sciences in Shanghai. Cells were cultivated in culture medium composed of 90% Dulbecco's modified Eagle's

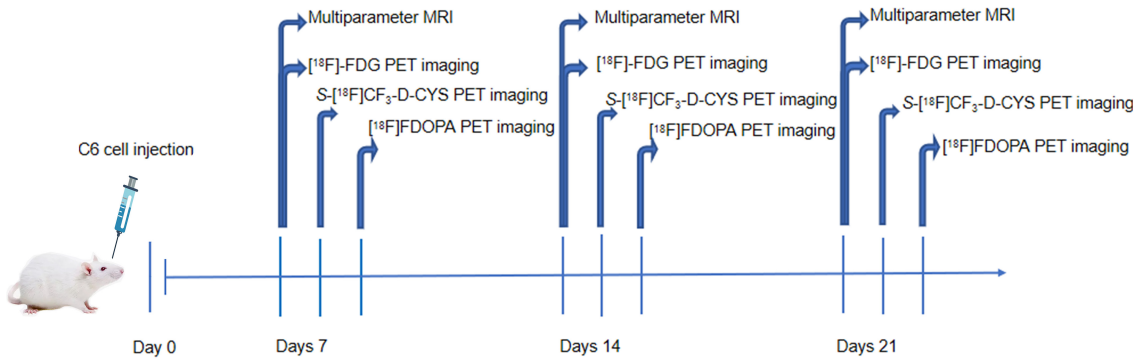

FIGURE 1 | The outline of this study.

medium (GIBCO) and 10% fetal bovine serum (GIBCO) in a cell incubator with a humidified atmosphere of 5% CO_2 and 95% air at 37°C. Cells were harvested or passaged with trypsinization when they reached over 90% confluence in the logarithmic growth phase.

To establish orthotropic C6 glioma models, about 1×10^6 C6 cells in 10 μL of phosphate-buffered saline (PBS) was injected into the right hemisphere (the right caudate nucleus in more specific terms) of each male SD rat (6–8-weeks old, 200–250 g in weight) through a small-animal stereotactic instrument. During the operation, rats were in effective anesthetic condition with 2% pentobarbital (40 mg/kg), and the heads of rats were immobilized. Before cell injections, the skin of the heads was sterilized, and then, skulls were exposed with incisions. Through a burr hole placed 1 mm anteriorly and 3 mm right laterally to the bregma, cells in a 10-μL microsyringe were slowly injected into the white matter at a depth of 5 mm during 10 min. After 5–10 min pace times, the microsyringe was drawn, and the drilled hole was sealed. Furthermore, the wound was sutured, and animals were sent back to a specific pathogen-free laboratory animal room.

Micro-PET/CT Protocol and Data Postprocessing

The preparation and radiosynthesis of *S*-[^{18}F]CF_3-D-CYS (16), [^{18}F]FDG (18), and [^{18}F]FDOPA (19, 20) were performed as previously described. PET/CT imaging was performed by an Inveon small-animal PET/CT scanner (Siemens, Knoxville). The rats were anesthetized with 2% pentobarbital (35 mg/kg), and they were intravenously injected with different PET tracers (100 μCi/kg, 37 MBq/kg) in 100–300 μL saline via tail veins. A low-dose CT scan was started followed by a PET scan. Following our study intentions, the dynamic and/or static data were acquired for *S*-[^{18}F]CF_3-D-CYS PET imaging, and an only static scan was acquired with [^{18}F]FDG and [^{18}F]FDOPA PET imaging. The 120-min dynamic acquisition of *S*-[^{18}F]CF_3-D-CYS PET was intended to depict the uptake curve of *S*-[^{18}F]CF_3-D-CYS in tumors and determin the optimal acquisition time point of *S*-[^{18}F]CF_3-D-CYS. For static acquisition, a 15-min static PET scan was performed for [^{18}F]FDOPA at 10–30 min after injection and at 60 min after administration of [^{18}F]FDG.

Two-dimensional ordered-subsets expectation maximum was used during image reconstruction. The 120-min dynamic *S*-[^{18}F]CF_3-D-CYS PET imaging was reconstructed every 1 min with 30 frames for the first 30 min and then every 5 min with 18 frames for the last 90 min. Using the Inveon Research Workplace 4.1 software, regions of interest (ROIs) of 2-mm diameter were drawn over tumor tissues and normal brain tissues (contralateral normal cerebral tissue excluding ventricles) of certain PET/CT images. Furthermore, radioactivity uptake of tissues was presented as mean % ID/g (the average uptake value of the three different ROIs over the same area). % ID/g means a percentage of the injected dose per gram of tissue.

MRI Protocol

Conventional MRI

Before the experiment, the rats were fasted for 4 h and anesthetized with 2% pentobarbital (35 mg/kg). Furthermore, an intravenous needle was placed in the rats' tail vein for the contrast agent injection. Brain MRI was performed using a 3T MR system (Magnetom Verio, Siemens Medical Solutions, Erlangen, Germany) with eight phased-array animal coils. Transversal T_2-weighted images [repetition time (TR), 4,800 ms; echo time (TE), 116 ms; field of view (FOV), 60 mm × 60 mm; slice thickness, 1.5 mm; voxel resolution, 0.2 mm × 0.2 mm × 1.5 mm), transversal T1-weighted images (TR, 660 ms; TE, 18 ms; FOV, 60 mm × 60 mm; slice thickness, 1.5 mm; voxel resolution, 0.3 mm × 0.2 mm × 1.5 mm), and susceptibility weighted imaging (SWI) (TR, 28 ms; TE, 20 ms; FOV, 60 mm × 60 mm; slice thickness, 0.75 mm; voxel resolution, 0.2 mm × 0.2 mm × 0.8 mm) were obtained. Postcontrast sagittal 3D T_1-weighted images (TR, 1,990 ms; TE, 3.45 ms; section thickness, 0.35 mm; FOV, 90 mm × 90 mm; voxel resolution, 0.4 mm × 0.4 mm × 0.3 mm) were obtained after DCE-MRI.

DCE-MRI

T_1-VIBE was applied at two different flip angles (2 and 15°) to calculate the T_1 maps. Below were the parameters (TR, 7.07 ms; TE, 2.44 ms; slice thickness, 1.5 mm; FOV, 60 mm × 60 mm;

voxel resolution, 0.5 mm × 0.4 mm × 1.5 mm). DCE-MRI (dynamic contrast-enhanced MR perfusion) was acquired with time-resolved angiography with stochastic trajectories (TWIST) sequence; the parameters were the following: TR, 6.27 ms; TE, 2.7 ms; flip angle, 12°; slice thickness, 1.5 mm; for each measurement, 3.6 s; FOV, 60 mm × 60 mm; 75 measurements, total scan time of 276 s; voxel resolution, 0.4 mm × 0.3 mm × 1.5 mm; contrast media (0.1 mmol/kg body weight of Gd-DTPA, Magnevist, Schering, Berlin, Germany); contrast median injection rate, 1 mL/s, followed by 20 mL of 0.9% saline flush using the same injection speed. Infusion started from the fifth measurement.

All DCE-MRI data were transferred to the postprocessing workstation. The analysis was done by a commercial software tool (TISSUE 4D; Siemens Healthcare, Erlangen, Germany). A value for the arterial input function was automatically calculated using the software. TISSUE 4D was based on the two-compartment model (21), and volume transfer constant (K^{trans}) maps were automatically generated. In a line with the ROI placement in PET study, 2-mm diameter ROIs were drawn over tumor tissues and normal brain tissues.

Pathological and Immunohistochemical Analysis

The whole rat brains were obtained and put in a 4% formalin fixation overnight. Then, they were cut into continuous 3-μm slices. Several stainings were further performed, and the methods were reported previously (22–24). The HE staining was performed to validate the tumor morphology and delineate the tumor boundary. The tumor length, width, and height were measured via the HE-stained pathological specimen. The tumor growth was assumed in an ellipsoidal way (25), and the tumoral volume was calculated by the following formulas: $V = \pi/6 \times \text{length} \times \text{width} \times \text{height}$.

Immunohistochemical staining for Ki67 (monoclonal antibody, Servicebio, Wuhan, China, GB13030-2) was performed using the Envision method (22), and the Ki67 index represents the proliferative activity of glioma cells. The tumor sections were reviewed and quantified based on the percentage of positive cells in the highest density staining area; all cells with nuclear staining of any intensity were considered positive, and the Ki67 values were defined as the percentage of positive cells among the total cells counted (24).

Image Coregistration

For each model, PET images were automatically coregistered to their paired CT images because of the same anatomical position during scanning. T_2WI-MRI images of the same model were used as the reference of MRI images. Pathological images of the same model were considered as on the same level owing to the too narrow distance using the method of serial sections (3 μm), and HE images were used as the reference. Besides, images of different modalities were manually coregistered to each other among PET, MRI, and pathological images according to the anatomical structure.

Statistical Analysis

Data were reported as mean ± standard deviation of the mean. Statistical analysis was performed with GraphPad Prism 8. Paired or unpaired Student's *t* test and one-way ANOVA tests were carried out to evaluate the significant differences among two or more groups. If each of the global F was significant ($P < 0.05$), Bonferroni analysis was used to assess the difference between single groups, according to the corresponding multiplicity-adjusted *P*-values. Pearson correlation analyses were performed to assess the correlation between the values of two groups. A $P < 0.05$ was statistically considered significant.

RESULTS

The Optimal Imaging Time Point Acquisition for *S*-[^{18}F]CF_3-D-CYS PET Imaging

The representative time–activity curves (TACs, **Figure 2A**) showed relatively high tumor uptake and low normal brain uptake. *S*-[^{18}F]CF_3-D-CYS reached the maximum accumulation in the tumors at 10 min after injection and with long-term retention; then, it began to slowly decline at 30 min after injection. Until postinjection of 2 h, the uptake of *S*-[^{18}F]CF_3-D-CYS in tumors was still higher than that of the normal brain. The mean uptake ratios of the TNRs are shown in **Figure 2B**, which was consistent with the abovementioned tendency of tumor uptake.

The dynamic TNR curve revealed that the mean TNRs of *S*-[^{18}F]CF_3-D-CYS were constant from 10 to 30 min p.i., which indicated that the optimal acquisition time for static PET imaging was at 10–30 min after injections. Thus, the frames during the above time period were summed to obtain static images (**Figure 2C**) that were used for good visualization of tumors.

Assessment of the Efficiency of *S*-[^{18}F]CF_3-D-CYS PET Imaging in the Diagnosis of Gliomas in Terms of Tumor Boundary

The Highest Uptake TNRs and Early Tumor Detection

The uptake values of tumors and normal brains of C6 gliomas with the same tumor age, under the PET examinations by using three PET tracers (*S*-[^{18}F]CF_3-D-CYS, [^{18}F]FDG, and [^{18}F]FDOPA) in the same rat were shown in **Figure 3A**. And the *S*-[^{18}F]CF_3-D-CYS PET imaging demonstrated the highest mean TNRs (**Figure 3B**). Taking the 3-week C6 glioma models as an example, *S*-[^{18}F]CF_3-D-CYS was significantly accumulated in the tumor area, where T_2WI MRI showed uneven high intensity (**Figure 4A**). The mean TNRs of *S*-[^{18}F]CF_3-D-CYS PET (3.90 ± 0.25) were the highest compared with those of [^{18}F]FDG PET (1.28 ± 0.18) and [^{18}F]FDOPA PET (1.90 ± 0.21) (**Figure 3B**). Furthermore, *S*-[^{18}F]CF_3-D-CYS PET imaging could detect the tumor in the early stage, and compared with [^{18}F]FDG PET, it showed higher TNRs and more clearly depicted the tumor boundary (**Figures 3C,D**, **4B**).

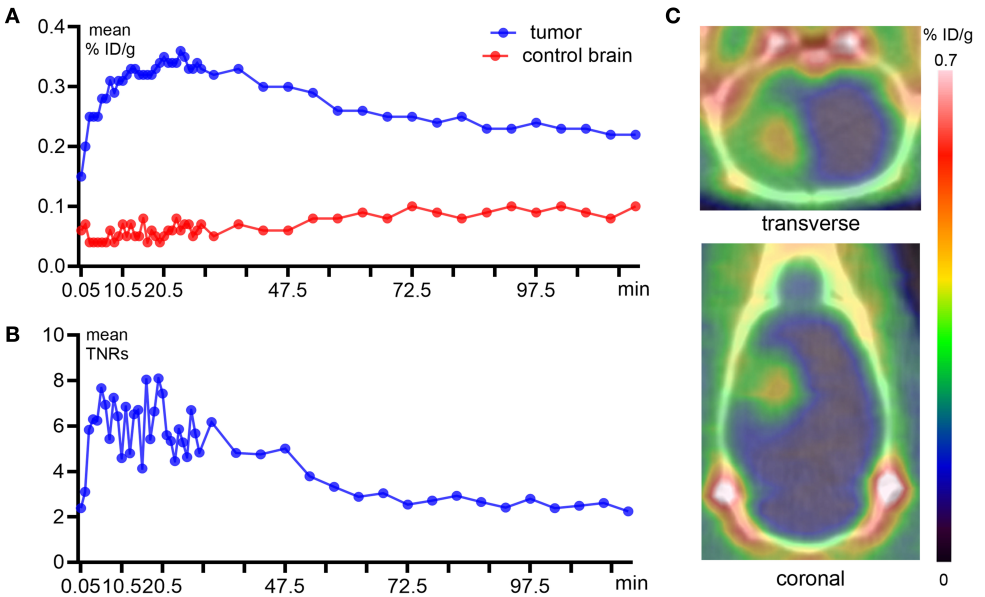

FIGURE 2 | Dynamic PET imaging with *S*-[^{18}F]CF_3-D-CYS and quantitative analysis derived from a C6 orthotopic tumor model. **(A)** Quantitative analysis of the tumor and control brain uptake during 2 h after *S*-[^{18}F]CF_3-D-CYS administration. **(B)** The time–activity curves of uptake ratios of the tumor to normal brain. **(C)** Representative static *S*-[^{18}F]CF_3-D-CYS PET imaging, which was performed at 20 min after injection, and compared with the normal brain tissue, the tumor (red arrow) had higher uptake of *S*-[^{18}F]CF_3-D-CYS (right arrows: tumors).

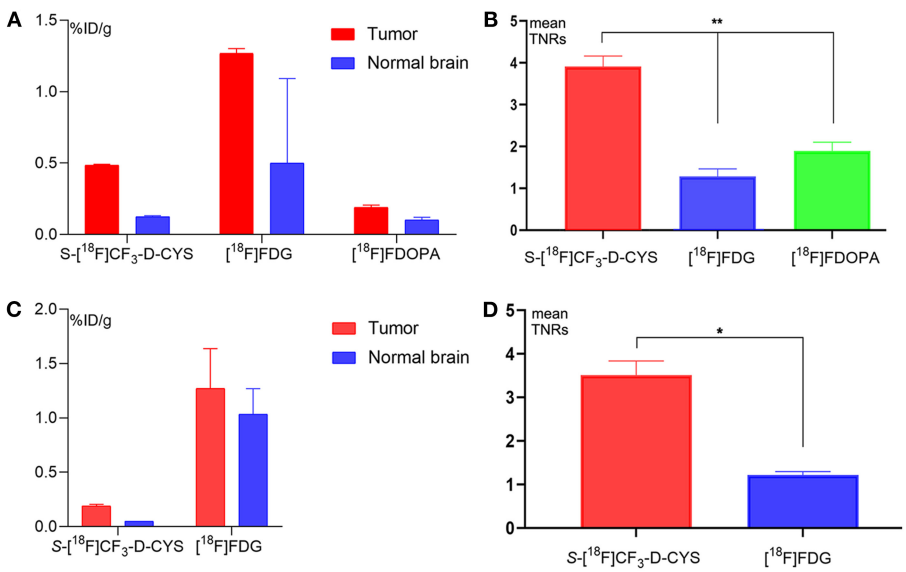

FIGURE 3 | (A,B) The uptake values of tumors and normal brains **(A)**, and the mean uptake ratios of the tumor to normal brain **(B)** for PET imaging with *S*-[^{18}F]CF_3-D-CYS, [^{18}F]FDG, and [^{18}F]FDOPA for rats bearing orthotopic C6 glioma 3 weeks after xenografts (**$P < 0.01$). **(C,D)** The uptake values of tumors and normal brains **(C)** and the mean tumor and control brain uptake **(D)** for PET imaging with *S*-[^{18}F]CF_3-D-CYS and [^{18}F]FDG for rats bearing orthotopic C6 glioma 1 week after xenografts. The mean TNRs for *S*-[^{18}F]CF_3-D-CYS PET images (3.51 ± 0.33) were nearly three times higher than those for [^{18}F]FDG PET images (1.22 ± 0.08) (*$P < 0.05$).

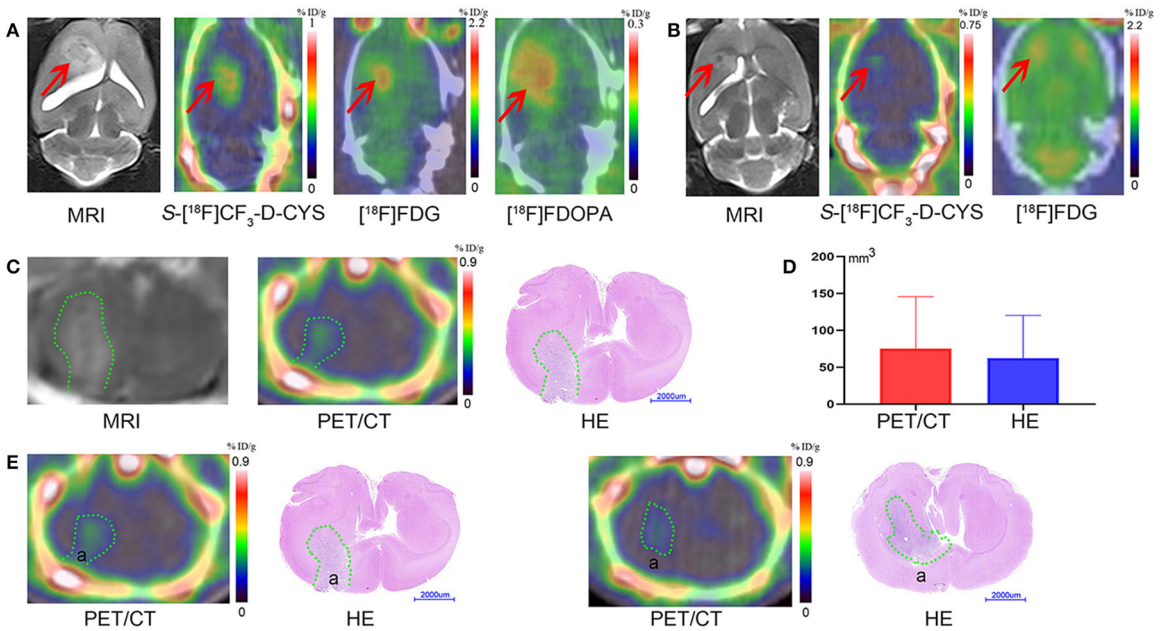

FIGURE 4 | (A) The representative coronal images of the same rat model bearing orthotopic C6 glioma 3 weeks after xenografts with MR imaging, *S*-[^{18}F]CF_3-D-CYS PET imaging, [^{18}F]FDG PET imaging, and [^{18}F]FDOPA PET imaging (from left to right) (right arrows: tumors). **(B)** The representative coronal images of the same model rat bearing orthotopic C6 glioma 1 week after xenografts with MR imaging, *S*-[^{18}F]CF_3-D-CYS PET imaging, and [^{18}F]FDG PET imaging (from left to right). Compared with MRI, the tumor with *S*-[^{18}F]CF_3-D-CYS PET imaging had a clear tumor boundary (red arrows: tumors). **(C)** Representative MRI images, *S*-[^{18}F]CF_3-D-CYS PET images, and whole-brain HE images on the parallel brain slices of the same rat model. **(D)** Comparison of the tumoral volume measured from *S*-[^{18}F]CF_3-D-CYS PET images and histopathology, showing that there was no significant difference (green curves: tumors). **(E)** Two successive slides of PET scan images and corresponding HE images. There was tumor infiltration in area a in the left images, while there was no tumor infiltration in area a in the right images.

Delineating Tumor Boundary Effectively and Close to the Pathological Tumor Volume

We selected the same section of *S*-[^{18}F]CF_3-D-CYS PET imaging, MRI, and HE-staining tumor specimen of a representative rat model as an example, which is shown in **Figure 4C**. Visually, compared with HE-staining tumor specimen, *S*-[^{18}F]CF_3-D-CYS PET imaging showed high accordance with pathology depicting this C6 glioma with irregular tumor boundary (**Figure 4C**). Besides, compared two successive slides of PET scan images and corresponding HE images (**Figure 4E**), *S*-[^{18}F]CF_3-D-CYS PET imaging could reflect changes in the tumor infiltration area shown as area in **Figure 4E**. Thus, *S*-[^{18}F]CF_3-D-CYS PET imaging could identify the irregular tumor boundary and differentiate the tumor and the normal brain tissue. Furthermore, there were no significant differences in the measured tumor volume via *S*-[^{18}F]CF_3-D-CYS PET images and histopathology ($n = 3$, $P > 0.05$; **Figure 4D**).

Assessment of the Efficiency of *S*-[^{18}F]CF_3-D-CYS PET Imaging in the Diagnosis of Gliomas in Terms of Tumor Heterogeneity

A Significant Positive Correlation of *S*-[^{18}F]CF_3-D-CYS Uptake and the Tumor Ki67 Labeling Index

As shown in **Figure 5A**, *S*-[^{18}F]CF_3-D-CYS uptake values were visually different in different regions such as areas a–e (pointed in **Figures 5A–C**) even in the same level of the C6 glioma. The mean Ki67 labeling index (34.57%) was generally higher in the PET strong-uptake area a than those (0.45%) in the PET uptake-negative area e (**Figure 5C**). Quantificationally, **Figure 5D** showed a significant positive correlation between tumor *S*-[^{18}F]CF_3-D-CYS uptake values (represented by mean TNRs) and the corresponding Ki67 labeling index ($n = 14$, $R^2 = 0.72$, $P < 0.01$), indicating that tumor *S*-[^{18}F]CF_3-D-CYS uptake values could reflect the proliferative ability of tumor cells.

Low S-[^{18}F]CF_3-D-CYS Uptake in the Tumor Bleeding Areas

To further demonstrate the ability of *S*-[^{18}F]CF_3-D-CYS PET imaging in reflecting tumor heterogeneity, we performed SWI-MRI examinations to detect the tumor bleeding. Results showed that there was internal hemorrhage for some C6 gliomas, and the bleeding was further confirmed by HE results. Comparing the tumor hemorrhagic site in SWI-MRI and *S*-[^{18}F]CF_3-D-CYS PET images, we found visually low tumor uptakes of *S*-[^{18}F]CF_3-D-CYS in the bleeding region, as shown in the **Figures 5E–I**. Moreover, compared to the corresponding [^{18}F]FDG (**Figure 5H**) and [^{18}F]FDOPA (**Figure 5I**) PET images, the visual difference in tumor uptake in the tumor bleeding area was much more appealing for the corresponding *S*-[^{18}F]CF_3-D-CYS PET images (**Figure 5G**).

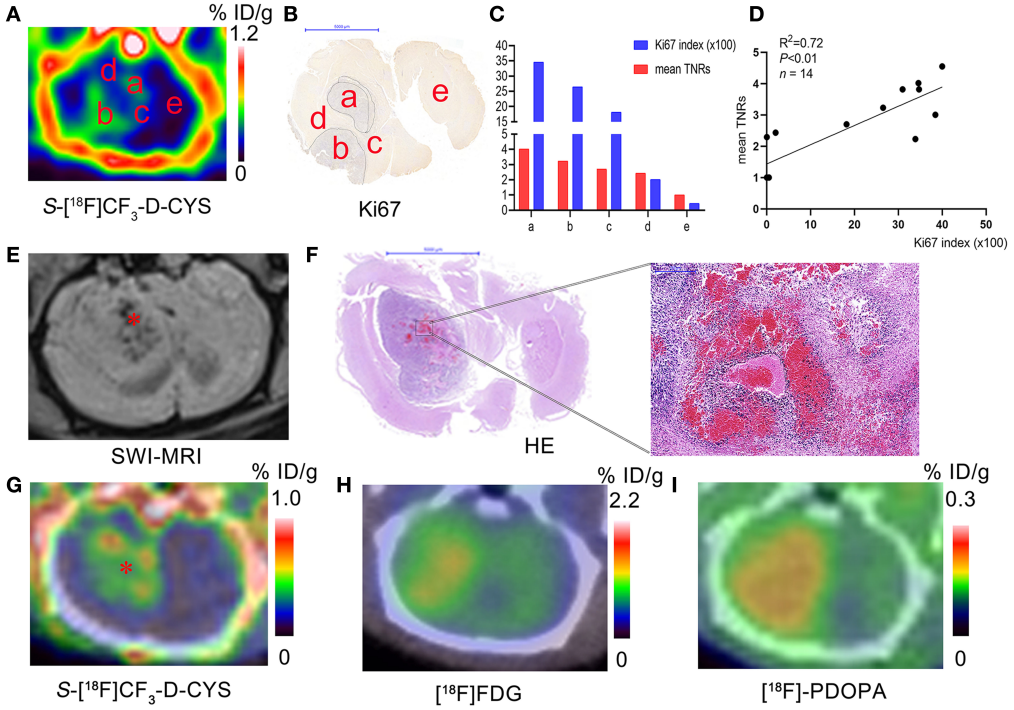

FIGURE 5 | (A–C) Representative *S*-[^{18}F]CF_3-D-CYS PET images **(A)**, the corresponding Ki67 staining image **(B)**, and the corresponding uptake values and Ki67 index for regions a–e in Panel **A (C)** (a–e in Panels **A–C**: different tissue regions; tissue regions marked by the same letters in different corresponding images are considered as the same ones). **(D)** Correlation analysis between tumor *S*-[^{18}F]CF_3-D-CYS uptake values of different regions (such as marked tissue regions a–e in the Panel **A**) in several rat models (represented by mean TNRs) and the corresponding Ki67 labeling index. **(E–I)** The representative SWI-MRI image **(E)**, HE images of the whole-brain section and the high-magnification view **(F)**, *S*-[^{18}F]CF_3-D-CYS PET image **(G)**, [^{18}F]FDG PET image **(H)**, and [^{18}F]FDOPA PET image **(I)** on the corresponding section of the same C6 glioma model (* in **E**: the tumor region with blood; * in **G**: the tumor region with low *S*-[^{18}F]CF_3-D-CYS uptake).

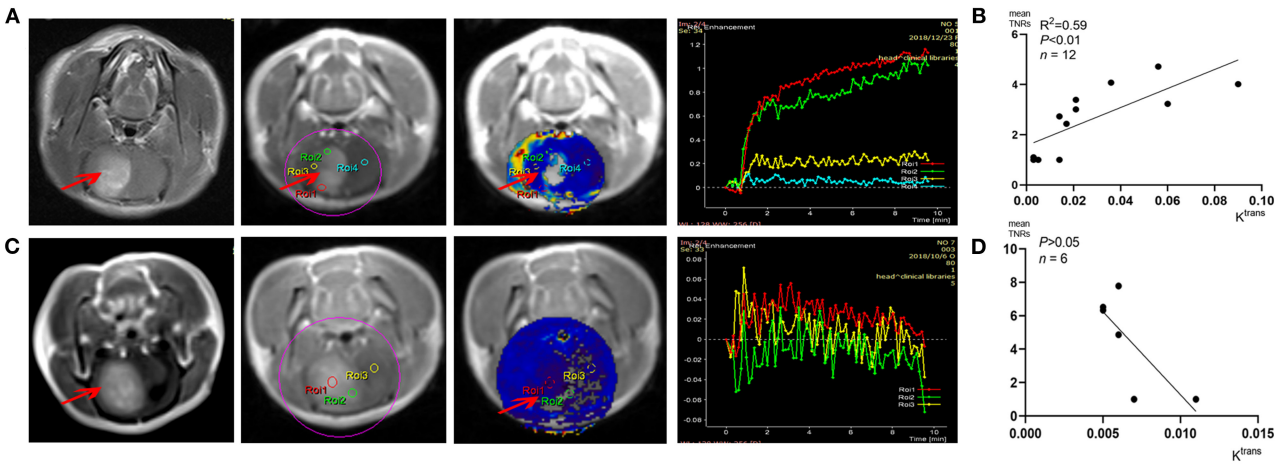

FIGURE 6 | (A,C) Representative DCE-MRI analysis results and corresponding K^{trans} maps. **(B,D)** Correlation analysis results between K^{trans} values and corresponding tumor *S*-[^{18}F]CF_3-D-CYS uptakes (represented by mean TNRs) (right arrows: tumors).

Correlation With Blood Brain Barrier and Capillary Permeability

All the tumors were vividly enhanced on T_1 enhanced imaging, which indicated that C6 glioma did disrupt the blood–brain barrier (BBB). DCE-MRI analysis and concentration–time curve results (**Figures 6A,C**) showed that K^{trans} values in the tumors (such as ROIs 1–2 in **Figure 6A**) were higher than those of the contralateral normal brain parenchyma (such as ROI 4

in **Figure 6A**), indicating that C6 glioma had higher capillary permeability than the normal brain parenchyma. **Figure 6B** shows that the positive correlation between the *S*-[^{18}F]CF_3-D-CYS uptake values and the corresponding K^{trans} values in these tumor area ($n = 12$, $R^2 = 0.59$, $P < 0.01$). However, there was an exception that there was no significant difference between the K^{trans} values of tumors and that of contralateral normal brain tissues (**Figure 6C**). Even so, the corresponding *S*-[^{18}F]CF_3-D-CYS uptakes of different ROIs in the tumor were still varied and higher than the contralateral normal parenchyma. **Figure 6D** showed that, in this kind of tumor, there was no significant correlation between *S*-[^{18}F]CF_3-D-CYS uptakes and K^{trans} values ($n = 6$, $P > 0.05$). Thus, the correlations between *S*-[^{18}F]CF_3-D-CYS uptakes and K^{trans} values were still debatable, and the tumor uptake of *S*-[^{18}F]CF_3-D-CYS was not necessary to depend on the degree of capillary permeability.

DISCUSSION

In this study, we successfully further explored and evaluated the application of a new sulfur-containing amino acid PET tracer (*S*-[^{18}F]CF_3-D-CYS) for evaluating glioma in orthotopic C6 glioma models. For *S*-[^{18}F]CF_3-D-CYS PET imaging, there was relatively high tumor uptake and low normal brain uptake. Compared with [^{18}F]FDG and [^{18}F]FDOPA PET imaging, *S*-[^{18}F]CF_3-D-CYS PET imaging had the highest TNRs, which was an advantage for tumor boundary delineation. The tumor volume in *S*-[^{18}F]CF_3-D-CYS PET imaging was close to the pathological size. Besides, we proved that *S*-[^{18}F]CF_3-D-CYS PET imaging could reflect the tumor hemorrhage and was significantly correlated with tumor cell proliferation. Furthermore, our results suggested that the uptake of *S*-[^{18}F]CF_3-D-CYS was independent of capillary permeability.

The dynamic PET scan of the glioma showed that the optimal imaging period for *S*-[^{18}F]CF_3-D-CYS PET was 10–30 min after trace injection. In detail, the TACs demonstrated that the accumulation of *S*-[^{18}F]CF_3-D-CYS in brain tumors was quick (within 10 min) and lasted for a long period (for 2 h), which makes the PET acquisition time of *S*-[^{18}F]CF_3-D-CYS flexible. Furthermore, our study showed that the uptake of *S*-[^{18}F]CF_3-D-CYS in the normal brain was relatively low, and it provided a good imaging contrast. Compared with [^{18}F]FDG and [^{18}F]FDOPA PET imaging, *S*-[^{18}F]CF_3-D-CYS PET imaging had the highest mean TNRs; it was possible to clearly define the C6 glioma boundary (26). Besides, compared with [^{18}F]FDG, our study showed that *S*-[^{18}F]CF_3-D-CYS PET imaging could detect tumors in a week after orthotopic xenograft and even could delineate the tumor contour. This was a valuable finding, which has, on the other side, proven that the *S*-[^{18}F]CF_3-D-CYS PET imaging had high sensitivity in detecting gliomas. In addition, the tumor volume measured on *S*-[^{18}F]CF_3-D-CYS PET had high accordance with the pathological findings. Thus, *S*-[^{18}F]CF_3-D-CYS PET might serve as a valuable modality for glioma boundary delineation.

It is undeniable that the accumulation of *S*-[^{18}F]CF_3-D-CYS in the tumor area was variable, in which we inferred that the uneven uptake of *S*-[^{18}F]CF_3-D-CYS might indicate or reflect the tumor heterogeneity. We verified our inference in two aspects. On the one hand, our results showed that there was a significant positive correlation between *S*-[^{18}F]CF_3-D-CYS uptakes and the Ki67 labeling index. The higher the *S*-[^{18}F]CF_3-D-CYS uptakes were, the higher the tumor cell proliferation was. These findings are consistent with previous reports that [^{11}C]-MET uptake correlated with the proliferative Ki67 index (27–29). On the other hand, we found that the tumor hemorrhage region, which was confirmed by SWI-MRI and histopathology, had a pretty low *S*-[^{18}F]CF_3-D-CYS uptake. Tumor cell proliferation rate and tumor with hemorrhage were thought to be related to tumor heterogeneity (12, 13). As a result, *S*-[^{18}F]CF_3-D-CYS is a promising candidate for evaluating glioma and reflecting tumor heterogeneity.

Interestingly, we explored whether *S*-[^{18}F]CF_3-D-CYS accumulation is dependent on BBB breakdown and capillary permeability. K^{trans} is a measure of capillary permeability obtained using DCE-MR perfusion. The negative correlation between *S*-[^{18}F]CF_3-D-CYS uptake and K^{trans} values including all cases showed that *S*-[^{18}F]CF_3-D-CYS uptake is independent on the degree of capillary permeability. However, we noticed that when the tumor has high capillary permeability, the uptake of *S*-[^{18}F]CF_3-D-CYS uptake was significantly correlated to the extent of capillary permeability, which we speculated that the increased capillary permeability might increase passive diffusion, which would help *S*-[^{18}F]CF_3-D-CYS enter and accumulate in the tumor area. Those results are in line with earlier studies reporting that AA transport into brain tumors is not dependent on, but may be intensified by, breakdown in the BBB (30, 31). Consequently, *S*-[^{18}F]CF_3-D-CYS PET imaging has another advantage over MRI in imaging tumors with intact BBB.

Going even further, the expression of some AA transporters, particularly the system L subtype LAT-1, system ASC subtype ASCT-2, and so on, is increased in malignant lesions (32, 33). In addition, our previous work (16) has identified that the cellular uptake of *S*-[^{18}F]CF_3-D-CYS in C6 cells mainly relied on the systems L (without the presence of Na+) and ASC (in the presence of Na+). Thus, we reasonably deduce that LAT-1 can transport *S*-[^{18}F]CF_3-D-CYS in the absence of Na+, and ASCT-2 is likely one of the transporters for uptake of *S*-[^{18}F]CF_3-D-CYS *in vitro*. These two transporters may play some roles *in vivo* as well. However, the transport mechanism of *S*-[^{18}F]CF_3-D-CYS is not clear yet. The final and precise conclusions with the tumor uptake mechanism of *S*-[^{18}F]CF_3-D-CYS still need to be further studied. Western blot or mass spectrometry to quantify transporter proteins needs to be further explored.

There are some comparative advantages of *S*-[^{18}F]CF_3-D-CYS over common clinical PET agents in imaging glioma. First, as D-isomers of PET enantiopure tracers, *S*-[^{18}F]CF_3-D-CYS, familiar with previous studies such as 3-[^{18}F]fluoro-a-methyl-D-tyrosine (D-[^{18}F]FAMT) and (D)-^{18}F-fluoromethyltyrosine (D-^{18}F-FMT), has some properties compared with their corresponding L-amino acids (16, 34, 35). For instance, D-isomers are characterized by fast clearance from the blood and kidney, thus low radiation burden, since D-amino acids rarely are used for the biological activity of mammals and there

is rare accumulation in normal tissues. In this study, unlike the high uptake of [^{18}F]FDG in the normal brain, there is an extremely low uptake of *S*-[^{18}F]CF_3-D-CYS in the normal brain. Therefore, it is easier to detect early tumors and more distinct to delineate tumor boundary for *S*-[^{18}F]CF_3-D-CYS PET imaging due to higher TNRs. Second, in our study, compared with [^{18}F]FDOPA, the TNRs of *S*-[^{18}F]CF_3-D-CYS are higher, which is more suitable for depicting the tumor boundaries. Moreover, unlike the physiological uptake of [^{18}F]FDOPA in striatum that mimics the tumor infiltration (6), there is no such observation for *S*-[^{18}F]CF_3-D-CYS PET imaging. For example, as is shown in **Figure 4A**, the tumor size depicted by [^{18}F]FDOPA was larger than that contoured by *S*-[^{18}F]CF_3-D-CYS. It is because the high uptake in the basal ganglia of [^{18}F]FDOPA confused the boundary contour of gliomas transplanted in the caudate nucleus. Third, compared with [^{18}F]-FET, *S*-[^{18}F]CF_3-D-CYS is more suitable for discriminating metabolically active tumors from the vessels because the [^{18}F]-FET has a longer retention time in the blood pool than *S*-[^{18}F]CF_3-D-CYS (15). Fourth, *S*-[^{18}F]CF_3-D-CYS seems to have similar potential in differentiating between tumor and inflammation compared to ^{18}F-FBPA (16, 36). However, the D-isomer of ^{18}F-FBPA was unsuitable for tumor PET probe as recently reported by Hirai et al. (37). Lastly, contrary to 3′-deoxy-3′-[^{18}F]fluorothymidine ([^{18}F]-FLT, a thymine nucleoside radiotracer not an AA, which indicates the proliferative state of cells), whose uptake is facilitated by BBB breakdown (15, 38), the uptake of *S*-[^{18}F]CF_3-D-CYS is independent of BBB breakdown, which lead a more extensive imaging range of various gliomas for *S*-[^{18}F]CF_3-D-CYS PET imaging.

However, one of the limitations of this study is the lack of autoradiographic imaging that can provide the precise comparison with histology. There could also be slow defluorination or bone intake of *S*-[^{18}F]CF_3-D-CYS, which may influence image quality. Even so, the superiority of *S*-[^{18}F]CF_3-D-CYS PET imaging in conjunction with multiparametric MRI during the long process of struggling against glioma should not be overlooked. Additional investigations are warranted in the future to improve its stability *in vivo* and optimize image effect.

In summary, our study evaluated a new ^{18}F-trifluoromethylated D-cysteine, *S*-[^{18}F]CF_3-D-CYS, as a promising brain tumor PET tracer referred from previous research. The *S*-[^{18}F]CF_3-D-CYS PET imaging exhibited high tumor uptake and clear tumor boundaries, which were the clearest compared with those that [^{18}F]FDG and [^{18}F]FDOPA PET imaging depicted in our study. The uptake of *S*-[^{18}F]CF_3-D-CYS reflected tumoral heterogeneity and was independent of the degree of capillary permeability. In conclusion, in comparison with multiparametric MRI and histopathology, the *S*-[^{18}F]CF_3-D-CYS PET provides extensive information and has an excellent effect on glioma biopsy or neurosurgical planning and tumor diagnosis.

DATA AVAILABILITY STATEMENT

The raw data supporting the conclusions of this article will be made available by the authors, without undue reservation.

ETHICS STATEMENT

This study has complied with the recommendations of the Guidance for the Care and Use of Laboratory Animals of the Ministry of Science and Technology of the People's Republic of China. Our experiments were approved by the Institutional Animal Care and Use Committee (IACUC), Sun Yat-sen University (Permit Number: SYSU-IACUC-2019-000057).

AUTHOR CONTRIBUTIONS

HM, JZ, SL, and GT: design of the study. SL and FW: synthesis of tracers. HM, JZ, and ZZ: animal experiments. DX: image scanning. DN, ZY, and GT: supervision of experiments. HM: original manuscript writing. All authors: discussion and analysis of results, critical feedback, revisions, and approval of the manuscript.

FUNDING

This study was funded in part by the National Natural Science Foundation of China (Nos. 91949121, 2001879, 81571704, 81671719, and 81901772), the Science and Technology Foundation of Guangdong Province, China (No. 2016B090920087), the Science and Technology Planning Project Foundation of Guangzhou, China (Nos. 201604020169 and 20210201040268), Nanfang Hospital Talent Introduction Foundation of Southern Medical University (No. 123456), Guangdong Basic and Applied Basic Research Foundation, China (Nos. 2020A1515011436, 2020A1515110159, and 2020A1515011399).

SUPPLEMENTARY MATERIAL

The Supplementary Material for this article can be found online at: https://www.frontiersin.org/articles/10.3389/fonc.2021.645162/full#supplementary-material

REFERENCES

1. Gerlinger M, Rowan AJ, Horswell S, Math M, James L, David E, et al. Intratumor heterogeneity and branched evolution revealed by multiregion sequencing. *N Engl J Med*. (2012) 366:883–92. doi: 10.1056/NEJMoa1113205
2. Castellano A, Cirillo S, Bello L, Riva M, Falini A. Functional MRI for surgery of gliomas. *Curr Treat Options Neurol*. (2017) 19:34. doi: 10.1007/s11940-017-0469-y
3. Brindle KM, Izquierdo-García JL, Lewis DY, Mair RJ, Wright AJ. Brain tumor imaging. *J Clin Oncol*. (2017) 35:2432–8. doi: 10.1200/JCO.2017.72.7636

4. Yang Y, He MZ, Li T, Yang X. MRI combined with PET-CT of different tracers to improve the accuracy of glioma diagnosis: a systematic review and meta-analysis. *Neurosurg Rev*. (2019) 42:185–95. doi: 10.1007/s10143-017-0906-0
5. Tsiouris S, Bougias C, Fotopoulos A. Principles and current trends in the correlative evaluation of glioma with advanced MRI techniques and PET. *Hell J Nucl Med*. (2019) 22:206–19.
6. Laverman P, Boerman OC, Corstens FH, Oyen WJ. Fluorinated amino acids for tumour imaging with positron emission tomography. *Eur J Nucl Med Mol Imaging*. (2002) 29:681–90. doi: 10.1007/s00259-001-0716-y
7. Miyagawa T, Oku T, Uehara H, Desai R, Beattie B, Tjuvajev J, et al. "Facilitated" amino acid transport is upregulated in brain tumors. *J Cereb Blood Flow Metab*. (1998) 18:500–9. doi: 10.1097/00004647-199805000-00005
8. Nawashiro H, Otani N, Shinomiya N, Fukui S, Ooigawa H, Shima K, et al. L-type amino acid transporter 1 as a potential molecular target in human astrocytic tumors. *Int J Cancer*. (2006) 119:484–92. doi: 10.1002/ijc.21866
9. D'Souza MM, Sharma R, Jaimini A, Panwar P, Saw S, Kaur P, et al. ^{11}C-MET PET/CT and advanced MRI in the evaluation of tumor recurrence in high-grade gliomas. *Clin Nucl Med*. (2014) 39:791–8. doi: 10.1097/RLU.0000000000000532
10. Lohmann P, Werner JM, Shah NJ, Fink GR, Langen KJ, Galldiks N. Combined amino acid positron emission tomography and advanced magnetic resonance imaging in glioma patients. *Cancers*. (2019) 11:153. doi: 10.3390/cancers11020153
11. Wedman J, de Bree R, van der Laan BFAM. *Visualisation of recurrent laryngeal cancer with positron emission tomography (PET): Comparison of methyl-labelled 11C-methionine (MET) and 18F-fluorodeoxyglucose* (FDG). (2008).
12. Rossi Espagnet MC, Romano A, Mancuso V, Cicone F, Napolitano A, Scaringi C, et al. Multiparametric evaluation of low grade gliomas at follow-up: comparison between diffusion and perfusion MR with (18)F-FDOPA PET. *Br J Radiol*. (2016) 89:20160476. doi: 10.1259/bjr.20160476
13. Yu J, Zheng J, Xu W, Wen J, Gao L, Tao L, et al. Accuracy of ^{18}F-FDOPA positron emission tomography and ^{18}F-FET positron emission tomography for differentiating radiation necrosis from brain tumor recurrence. *World Neurosurg*. (2018) 114:e1211–24. doi: 10.1016/j.wneu.2018.03.179
14. Juhász C, Dwivedi S, Kamson DO, Michelhaugh SK, Mittal S. Comparison of amino acid positron emission tomographic radiotracers for molecular imaging of primary and metastatic brain tumors. *Mol Imaging*. (2014) 13:7290201400015. doi: 10.2310/7290.2014.00015
15. Mansoor NM, Thust S, Militano V, Fraioli F. PET imaging in glioma: techniques and current evidence. *Nucl Med Commun*. (2018) 39:1064–80. doi: 10.1097/MNM.0000000000000914
16. Liu SY, Ma H, Zhang ZW, Lin L, Yuan G, Tang X, et al. Synthesis of enantiopure ^{18}F-trifluoromethyl cysteine as a structure-mimetic amino acid tracerfor glioma imaging. *Theranostics*. (2019) 9:1144–53. doi: 10.7150/thno.29405
17. Deng H, Tang X, Wang H, Tang G, Wen F, Shi X, et al. *S*-[^{11}C]methyl-L-cysteine: a new amino acid PET tracer for cancer imagimg. *J Nucl Med*. (2011) 52:287–93. doi: 10.2967/jnumed.110.081349
18. Toorongian SA, Mulholland GK, Jewett DM, Bachelor MA, Kilbourn MR. Routine production of 2-deoxy-2-[^{18}F]fluoro-D-glucose by direct nucleophilic exchange on a quaternary 4-aminopyridinium resin. *Int J Rad Appl Instrum B*. (1990) 17:273–9. doi: 10.1016/0883-2897(90)90052-3
19. Libert LC, Franci X, Plenevaux AR, Ooi T, Maruoka K, Luxen AJ, et al. Production at the curie level of no-carrier-added 6-^{18}F-Fluoro-L-Dopa. *J Nucl Med*. (2013) 54:1154–61. doi: 10.2967/jnumed.112.112284
20. Wen F, Zhang Z, Ma H, Zhang D, Tang G. Full automated synthesis of ^{18}F-FDOPA and preliminary PET/CT imaging. *J Isotop*. (2018) 31:276–82. doi: 10.7538/tws.2018.31.05
21. Tofts PS, Kermode AG. Blood brain barrier permeability in multiple sclerosis using labelled DTPA with PET, CT and MRI. *J Neurol Neurosurg Psychiatry*. (1989) 52:1019–20. doi: 10.1136/jnnp.52.8.1019
22. Ma H, Liu S, Xiong Y, Zhang Z, Sun A, Su S, et al. PET imaging of cardiomyocyte apoptosis in a rat myocardial infarction model. *Apoptosis*. (2018) 23:396–407. doi: 10.1007/s10495-018-1463-x
23. Aleskandarany MA, Green AR, Ashankyty I, Elmouna A, Diez-Rodriguez M, Nolan CC, et al. Impact of intratumoural heterogeneity on the assessment of Ki67 expression in breast cancer. *Breast Cancer Res Treat*. (2016) 158:287–95. doi: 10.1007/s10549-016-3893-x
24. Mason DY, Micklem K, Jones M. Double immunofluorescence labelling of routinely processed paraffin sections. *J Pathol*. (2000) 191:452–61. doi: 10.1002/1096-9896(2000)9999:9999<::AID-PATH665>3.0.CO;2-O
25. Tomayko MM, Reynolds CP. Determination of subcutaneous tumor size in athymic (nude) mice. *Cancer Chemother Pharmacol*. (1989) 24:148–54. doi: 10.1007/BF00300234
26. la Fougeʻre C, Suchorska B, Bartenstein P, Kreth FW, Tonn JC. Molecular imaging of gliomas with PET: opportunities and limitations. *Neuro Oncol*. (2011) 13:806–19. doi: 10.1093/neuonc/nor054
27. Kim S, Chung JK, Im SH, Jeong JM, Lee DS, Kim DG, et al. ^{11}C-methionine PET as a prognostic marker in patients with glioma: comparison with ^{18}F-FDG PET. *Eur J Nucl Med Mol Imaging*. (2005) 32:52–9. doi: 10.1007/s00259-004-1598-6
28. Tanaka K, Yamamoto Y, Maeda Y, Yamamoto H, Kudomi N, Kawai N, et al. Correlation of 4′-[methyl-^{11}C]-thiothymidine uptake with Ki-67 immunohistochemistry and tumor grade in patients with newly diagnosed gliomas in comparison with ^{11}C-methionine uptake. *Ann Nucl Med*. (2016) 30:89–96. doi: 10.1007/s12149-015-1035-x
29. Roodakker KR, Alhuseinalkhudhur A, Al-Jaff M, Georganaki M, Zetterling M, G, Berntsson S, et al. Region-by-region analysis of PET, MRI, and histology in en bloc-resected oligodendrogliomas reveals intra-tumoral heterogeneity. *Eur J Nucl Med Mol Imaging*. (2019) 46:569–79. doi: 10.1007/s00259-018-4107-z
30. Roelcke U, Radu EW, von Ammon K, Hausmann O, Maguire RP, Leenders KL. Alteration of blood-brain barrier in human brain tumors: comparison of [^{18}F]fluorodeoxyglucose, [^{11}C]methionine and rubidium-82 using PET. *J Neurol Sci*. (1995) 132:20–7. doi: 10.1016/0022-510X(95)00117-K
31. Chen W. Clinical applications of PET in brain tumors. *J Nucl Med*. (2007) 48:1468–81. doi: 10.2967/jnumed.106.037689
32. Karunakaran S, Ramachandran S, Coothankandaswamy V, Elangovan S, Babu E, Periyasamy-Thandavan S, et al. Protein, a highly concentrative and broad specific amino acid transporter, is a novel and effective drug target for treatment of estrogen receptor-positive breast cancer. *J Biol Chem*. (2011) 286:31830–8. doi: 10.1074/jbc.M111.229518
33. Chiotellis A, Muller A, Mu LJ, Keller C, Schibli RD, Krämer S, et al. Synthesis and biological evaluation of 18F-labeled fluoroethoxy tryptophan analogues as potential PET tumor imaging agents. *Mol Pharm*. (2014) 11:3839. doi: 10.1021/mp500312t
34. Ohshima Y, Hanaoka H, Tominaga H, Kanai Y, Kaira K, Yamaguchi A, et al. Biological evaluation of 3-[^{18}F]fluoro-α-methyl-d-tyrosine (d-[^{18}F]FAMT) as a novel amino acid tracer for positron emission tomography. *Ann Nucl Med*. (2013) 27:314–24. doi: 10.1007/s12149-013-0687-7
35. Burger IA, Zitzmann-Kolbe S, Pruim J, Friebe M, Graham K, Stephens A, et al. First clinical results of (D)-F-18-fluoromethyltyrosine (BAY 86-9596) PET/CT in patients with non small cell lung cancer and head and neck squamous cell carcinoma. *J Nucl Med*. (2014) 55:1778–85. doi: 10.2967/jnumed.114.140699
36. Watabe T, Ikeda H, Nagamori SS, Wiriyasermkul P, Tanaka Y, Naka S, et al. (18)F-FBPA as a tumor-specific probe of L-type amino acid transporter 1 (LAT1): a comparison study with (18)F-FDG and (11)C-Methionine PET. *Eur J Nucl Med Mol Imaging*. (2017) 44:321–31. doi: 10.1007/s00259-016-3487-1
37. Hirai N, Watabe T, Nagamori SS, Wiriyasermkul P, Tanaka Y, Romanov V, et al. Evaluation of D-isomer of ^{18}F-FBPA for oncology PET focusing on the differentiation of glioma and inflammation. *Asia Ocean J Nucl Med Biol*. (2020) 8:102–8. doi: 10.22038/AOJNMB.2020.47399.1321
38. Shinomiya A, Kawai N, Okada M, Miyake K, Nakamura T, Kushida Y, et al. Evaluation of 3′-deoxy-3′-[^{18}F]-fluorothymidine (^{18}F-FLT) kinetics

correlated with thymidine kinase−1 expression and cell proliferation in newly diagnosed gliomas. *Eur J Nucl Med Mol Imaging*. (2013) 40:175–85. doi: 10.1007/s00259-012-2275-9

Conflict of Interest: The authors declare that the research was conducted in the absence of any commercial or financial relationships that could be construed as a potential conflict of interest.

frontiers in Oncology

ORIGINAL RESEARCH
published: 13 May 2021
doi: 10.3389/fonc.2021.640738

Predictive Role of the Apparent Diffusion Coefficient and MRI Morphologic Features on IDH Status in Patients With Diffuse Glioma: A Retrospective Cross-Sectional Study

*Jun Zhang[1,2,3], Hong Peng[1,2], Yu-Lin Wang[2], Hua-Feng Xiao[2], Yuan-Yuan Cui[1,4], Xiang-Bing Bian[2], De-Kang Zhang[2] and Lin Ma[2]**

[1] The Medical School of Chinese People's Liberation Army (PLA) General Hospital, Beijing, China, [2] Department of Radiology, The First Medical Center, Chinese PLA General Hospital, Beijing, China, [3] Department of Radiology, The Sixth Medical Center, Chinese PLA General Hospital, Beijing, China, [4] Department of Radiology, Qingdao Special Servicemen Recuperation Center of PLA Navy, Qingdao, China

OPEN ACCESS

Edited by:
Han Zhang,
University of North Carolina at Chapel Hill, United States

Reviewed by:
Zhongxiang Ding,
Zhejiang University, China
Jun-Feng Lu,
Fudan University, China

***Correspondence:**
Lin Ma
cjr.malin@vip.163.com

Specialty section:
This article was submitted to Cancer Imaging and Image-directed Interventions, a section of the journal Frontiers in Oncology

Received: 12 December 2020
Accepted: 26 April 2021
Published: 13 May 2021

Citation:
Zhang J, Peng H, Wang Y-L, Xiao H-F, Cui Y-Y, Bian X-B, Zhang D-K and Ma L (2021) Predictive Role of the Apparent Diffusion Coefficient and MRI Morphologic Features on IDH Status in Patients With Diffuse Glioma: A Retrospective Cross-Sectional Study. Front. Oncol. 11:640738. doi: 10.3389/fonc.2021.640738

Purpose: To evaluate isocitrate dehydrogenase (IDH) status in clinically diagnosed grade II~IV glioma patients using the 2016 World Health Organization (WHO) classification based on MRI parameters.

Materials and Methods: One hundred and seventy-six patients with confirmed WHO grade II~IV glioma were retrospectively investigated as the study set, including lower-grade glioma (WHO grade II, n = 64; WHO grade III, n = 38) and glioblastoma (WHO grade IV, n = 74). The minimum apparent diffusion coefficient (ADCmin) in the tumor and the contralateral normal-appearing white matter (ADCn) and the rADC (ADCmin to ADCn ratio) were defined and calculated. Intraclass correlation coefficient (ICC) analysis was carried out to evaluate interobserver and intraobserver agreement for the ADC measurements. Interobserver agreement for the morphologic categories was evaluated by Cohen's kappa analysis. The nonparametric Kruskal-Wallis test was used to determine whether the ADC measurements and glioma subtypes were related. By univariable analysis, if the differences in a variable were significant ($P<0.05$) or an image feature had high consistency (ICC >0.8; κ >0.6), then it was chosen as a predictor variable. The performance of the area under the receiver operating characteristic curve (AUC) was evaluated using several machine learning models, including logistic regression, support vector machine, Naive Bayes and Ensemble. Five evaluation indicators were adopted to compare the models. The optimal model was developed as the final model to predict IDH status in 40 patients with glioma as the subsequent test set. DeLong analysis was used to compare significant differences in the AUCs.

Results: In the study set, six measured variables (rADC, age, enhancement, calcification, hemorrhage, and cystic change) were selected for the machine learning model. Logistic regression had better performance than other models. Two predictive models, model 1 (including all predictor variables) and model 2 (excluding calcification), correctly classified

IDH status with an AUC of 0.897 and 0.890, respectively. The test set performed equally well in prediction, indicating the effectiveness of the trained classifier. The subgroup analysis revealed that the model predicted IDH status of LGG and GBM with accuracy of 84.3% (AUC = 0.873) and 85.1% (AUC = 0.862) in the study set, and with the accuracy of 70.0% (AUC = 0.762) and 70.0% (AUC = 0.833) in the test set, respectively.

Conclusion: Through the use of machine-learning algorithms, the accurate prediction of IDH-mutant versus IDH-wildtype was achieved for adult diffuse gliomas *via* noninvasive MR imaging characteristics, including ADC values and tumor morphologic features, which are considered widely available in most clinical workstations.

Keywords: diffuse glioma, apparent diffusion coefficient, MRI, isocitrate dehydrogenase status, machine learning, prediction

INTRODUCTION

Cerebral diffuse infiltrating gliomas are the second most common type of primary central nervous system (CNS) tumor, second only to meningiomas. According to the 2016 World Health Organization (WHO) classification of CNS tumors, adult diffuse gliomas include astrocytic tumors, oligodendrogliomas, and glioblastomas (WHO grade II~IV) (1). These tumors account for approximately 22% of all CNS tumors. In the United States, more than 16,000 cases of adult diffuse glioma are reported each year, with an incidence of approximately 5.13 per 100,000 people. In addition, glioblastoma (GBM) is the most common malignant tumor in the CNS, accounting for approximately 14.6% of all CNS tumors and 48.3% of all malignant CNS tumors, with 11,833 cases reported annually within the U.S (2, 3). However, due to the heterogeneity of these neuroepithelial tumors, they have different clinical characteristics, biological behaviors, and histopathological characteristics, and substantial differences in treatment and prognosis.

Recently, the isocitrate dehydrogenase (IDH) status and other molecular subtypes have been reported as major prognostic factors and molecular diagnostic criteria for glioma tumor behavior. Thus, noninvasively detecting molecular subtypes before surgery is important for predicting the outcome and choosing the best therapy. Previous studies have shown that lower-grade glioma (LGG) IDH-wildtype and glioblastoma (GBM) have similar molecular structures and prognoses, while IDH-mutant status confers longer overall survival than IDH-wildtype status (4). In addition, compared with glioblastomas in patients with IDH-mutations (grade IV), anaplastic gliomas (grade III) in patients with wild-type IDH have a worse prognosis (5). It should be noted that IDH mutation status has been integrated into the 2016 WHO Classification of Tumors of the Central Nervous System, Revised 4th edition (1). Furthermore, it has been reported that due to different molecular subtypes, the choice of surgical resection range has different survival effects on patients with lower-grade glioma (grades II and III) (6). Based on the above research (5–7), it is necessary to predict the IDH status accurately before surgery and to guide the clinical development of appropriate tumor treatment plans.

Diffusion-weighted imaging (DWI) is a practical imaging technique that is widely employed in the clinic and is mainly used to detect the diffusion of water molecules (8). A meta-analysis showed that the quantitative measurement of the apparent diffusion coefficient (ADC) value can be used to grade gliomas with high accuracy (9). Our previous study demonstrated that the minimum ADC (ADCmin) can be used to predict the grading of neuroepithelial tumors (10). Prior studies (11, 12) have shown that the characteristics of lesions, such as location, internal structure, and enhancement pattern, are different among the genetic subtypes of glioma. In addition, machine learning has been applied in different medical fields, including medical image interpretation, prediction of disease development, and treatment response (13, 14). The advantage of machine learning is that it does not require any assumptions about the input variables and their relationships with the output; in addition, it is a fully data-driven learning method that does not rely on rules-based programming. Therefore, our study focused on the WHO 2016 classification criteria, applying machine learning methods to evaluate the value of clinically obtainable MRI features in predicting the IDH status of adult patients with diffuse grade II~IV glioma.

MATERIALS AND METHODS

Patient Cohort

This retrospective study was approved by the Institutional Ethics Committee of the Chinese PLA General Hospital, which waived the requirement for written informed consent. From August 2015 to July 2020, through the hospital's local picture archiving and communication system (PACS), two radiologists (Z.J. and P.H., with 10 and 13 years of experience, respectively), continuously collated patients with WHO grade II~IV glioma who underwent brain MRI. The original study cohort was collected from August 2015 to December 2019 as the study set, and another 40 cases from January 2020 to June 2020 were collected as the test set. The inclusion criteria included (a) a confirmed histologic diagnosis in accordance with WHO grade II-IV glioma; (b) conclusive histopathological and immunohistochemical staining results; and (c) brain MRI examinations performed within 6 months of WHO II/III and

within 5 weeks of WHO IV prior to neurosurgical treatment. The exclusion criteria included (a) an MRI scan with substandard quality, including an incomplete MRI protocol, the inability to compute the ADC map and obvious artifacts; (b) tumors other than WHO grade II~IV adult glioma; (c) incomplete or ambiguous histologic results; and d) previous treatment for glioma, such as radiotherapy, chemotherapy or immunotherapy. The flow chart of the enrolled patients (including the study set and test set) is provided in **Figure 1**.

MRI Examination

All enrolled patients underwent 3.0 T MRI. The MRI protocols included axial T2-weighted, axial or coronal T2 FLAIR, axial T1-weighted, fat-suppressed contrast-enhanced T1-weighted (including axial, coronal and sagittal) imaging, susceptibility-weighted imaging (SWI) and diffusion-weighted imaging. DWI was performed with b values of 0 s/mm^2 and 1000 s/mm^2 and was used to derive the ADC maps. Our institution is a general hospital, and although the MRI scans came from several examination rooms, they were performed with the same system (GE Healthcare, Milwaukee, USA). The MRI machines and protocols used are provided in **Supplementary Table 1**.

Histopathologic Analysis

All tumors were surgically resected, and the lesion specimens were fixed with paraffin blocks during the operation. Then, the neurologic pathology group adopted the 2016 WHO glioma classification for gross pathology and immunohistochemical staining to analyze and provide the final results.

ADC Quantification

The interobserver and intraobserver levels of agreement for ADC were assessed from the measurements made by two blinded radiologists (JZ and HP, with 10 and 13 years of experience, respectively, both with professional qualification certificates). To assess intraobserver reproducibility, the first observer performed region of interest (ROI) delineation twice within one week following the same procedure each time. At the same time, the second observer independently delineated the ROI once, and the interobserver agreement was assessed by comparing the results with the ADC outcomes extracted from the first ROI delineation made by the first observer.

Three different ROIs (30-40 mm^2) were placed into the visually perceived lowest portions inside the tumors on the ADC maps, excluding hemorrhagic, cystic, and necrotic portions and calcifications that might influence the measured results without overlapping the ROIs. Then, the minimum ADC was defined as the average value of the ROIs with the lowest ADC values, as in Maynard et al. (11) and Xing et al. (12). Subsequently, following the same method, an ROI was delineated by selecting the contralateral centrum semiovale region (8, 11), and defining the ADC value within it as ADCn. Thus, there were four ROIs per patient. Finally, the rADC

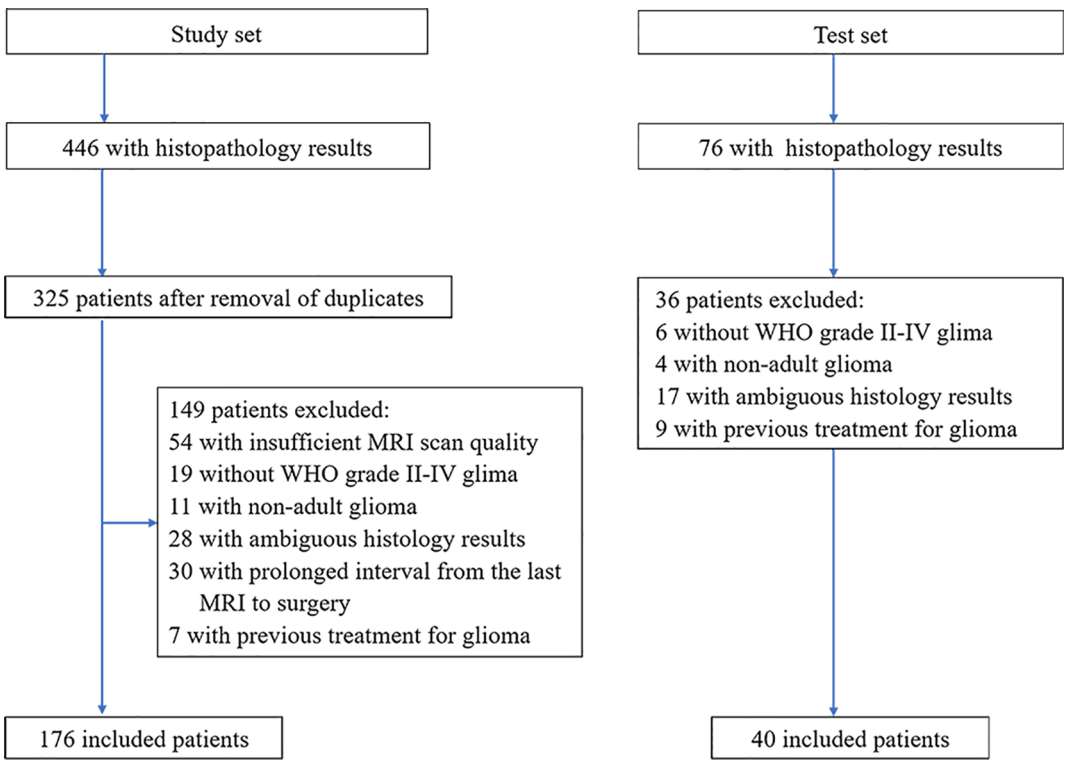

FIGURE 1 | Patient selection flowchart. ADC, apparent diffusion coefficient; WHO, World Health Organization.

(ADCmin to ADCn ratio) was calculated, resulting in three total ADC parameters (ADC_{min}, ADCn, rADC) per patient.

In the test set (n = 40), all ADC values were obtained by two certificated radiologists (Y-YC and Y-LW, with 3 and 18 years of experience, respectively) according to the method described above. Examples of ROI delineations are shown in **Figure 2**.

Morphologic Assessment

Two board-certified radiologists (JZ and HP with 10-13 years of experience) independently evaluated 176 MRI datasets in this study for 1 month while being blinded to the pathologic results.

The selection and evaluation of the tumor morphology were performed according to previous publications (11, 12). (a) Tumor location, which was specified by the center of the lesion, was divided into 4 groups: frontal lobe, other lobes (including parietal lobe, temporal lobe and occipital lobe), thalamus or brainstem, and cerebellum. (b) The maximum tumor diameter was measured by reference to the T2-weighted images, FLAIR images and contrast-enhanced T1-weighted images. (c) Contrast enhancement was categorized into 3 groups: nonenhancement, patchy enhancement, and rim enhancement. (d) Calcification and hemorrhage were observed and evaluated on T1-weighted imaging, susceptibility-weighted imaging, and CT, as available. (e) Cystic changes and central necrosis were defined as a free-liquid intensity with a nonenhanced portion. (f) T2-FLAIR mismatch signs, which previous studies considered to be specific (15, 16), were defined as tumors showing nearly homogeneous hyperintensity on T2-weighted images and relatively low intensity and peripheral hyperintensity on FLAIR sequences. **Figures 3** and **4** show examples of different morphologic characteristics of gliomas on MRI in the study set.

Statistical Analysis

Statistical analyses were performed using SPSS (version 26.0) and Python (version 3.8). Intraclass correlation coefficient analysis was used to evaluate the interobserver and intraobserver levels of agreement for ADC measurements, applying a two-way random-effects model. The interobserver agreement for morphologic categories was evaluated by Cohen's kappa analysis. For the agreement analysis, the outcomes were interpreted as follows: 0.2 or less, slight agreement; 0.21–0.40, fair agreement; 0.41–0.60, moderate agreement; 0.61–0.80, substantial agreement; and 0.81–1.00, almost perfect agreement.

The differences in ADC values among IDH subtype glioma groups were tested using nonparametric Kruskal-Wallis test. The relationship between morphologic features and glioma subtypes was analyzed using the chi-squared test. $P<0.05$ was considered to indicate a statistically significant difference.

In the univariable analysis, if the differences in a variable were significant ($P<0.05$) or an image feature had high consistency

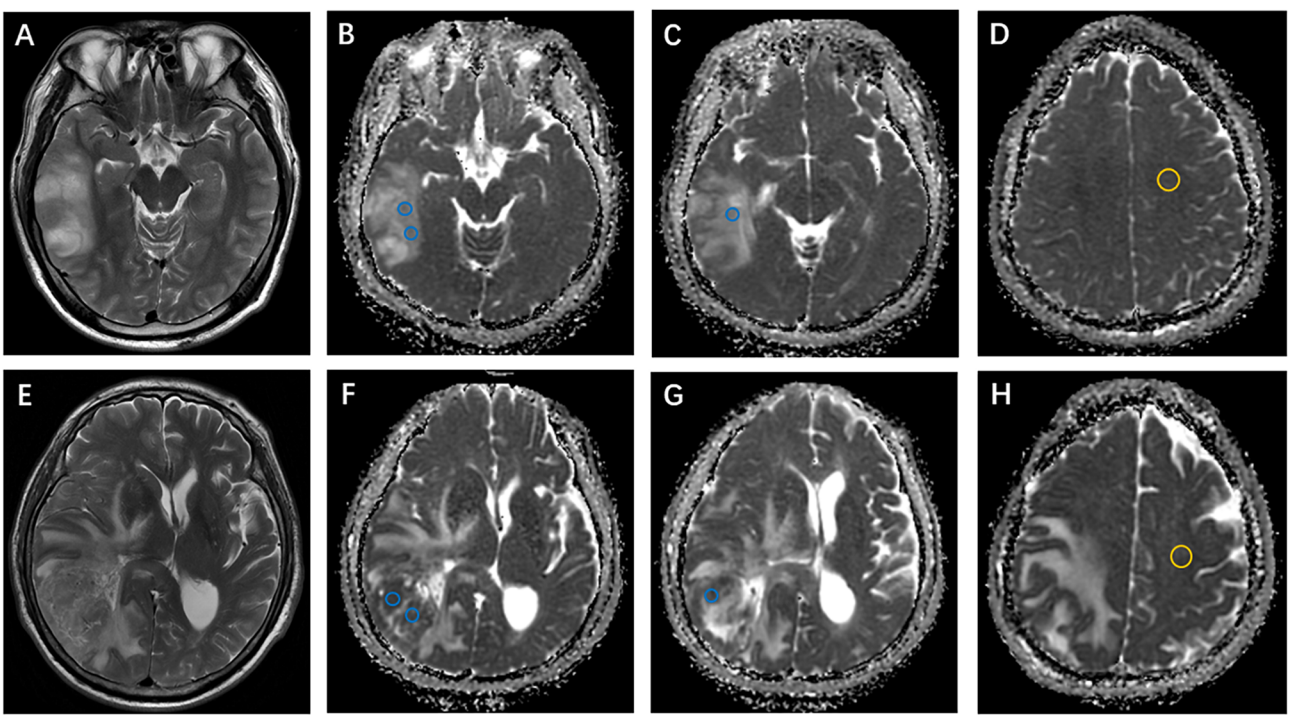

FIGURE 2 | Examples of apparent diffusion coefficient (ADC) measurements. **(A–D)** Axial T2-weighted imaging shows an isocitrate dehydrogenase (IDH)-mutant oligodendroglioma in the right temporal lobe. ADC maps show the regions of interest used to determine ADCmin (perceived lowest ADC regions, blue) and ADCn (contralateral, normal-appearing white matter, yellow). **(E–H)** Axial T2-weighted imaging of a right temporal IDH-wildtype glioblastoma. ADCmin and ADCn were calculated using the same method as above.

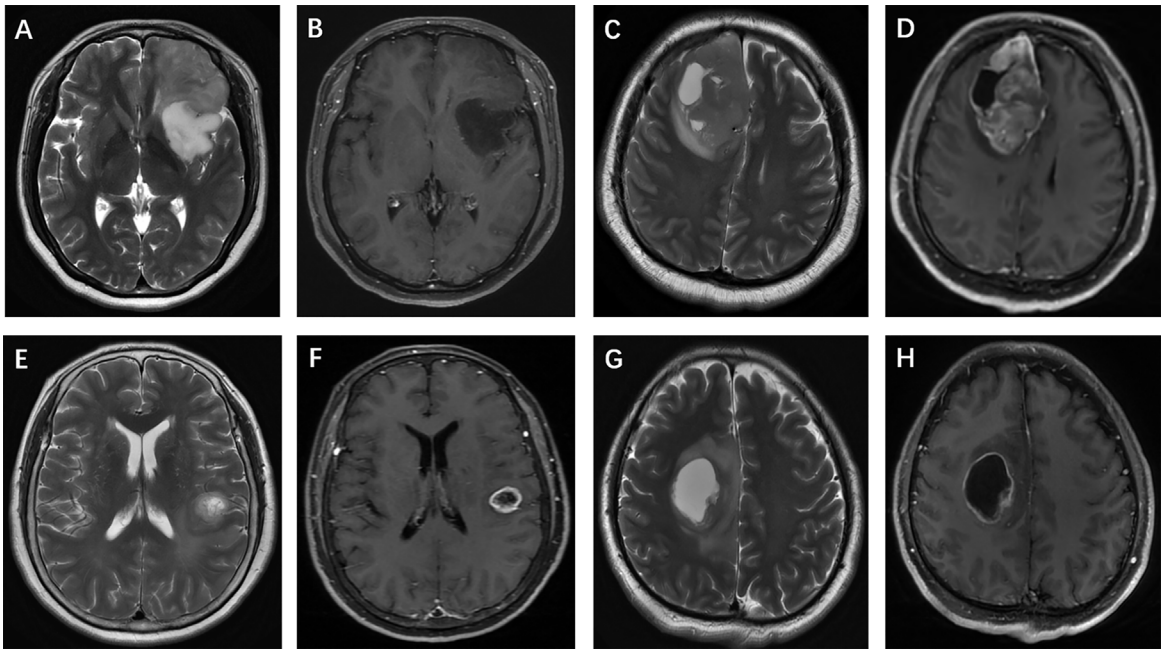

FIGURE 3 | Glioma morphologic characteristics. Enhancement pattern: **(A, B)** T2-weighted imaging shows a left frontal isocitrate dehydrogenase (IDH)-mutant oligodendroglioma without contrast agent uptake; **(C, D)** T2-weighted imaging shows a right frontal IDH-wildtype glioblastoma, and contrast-enhanced T1-weighted imaging shows patchy contrast uptake; **(E, F)** T2-weighted imaging and contrast-enhanced T1-weighted imaging show rim enhancement surrounding a central necrosis in a IDH-wildtype astrocytoma, while another patient **(G, H)** presents with a frontal IDH-mutant glioblastoma.

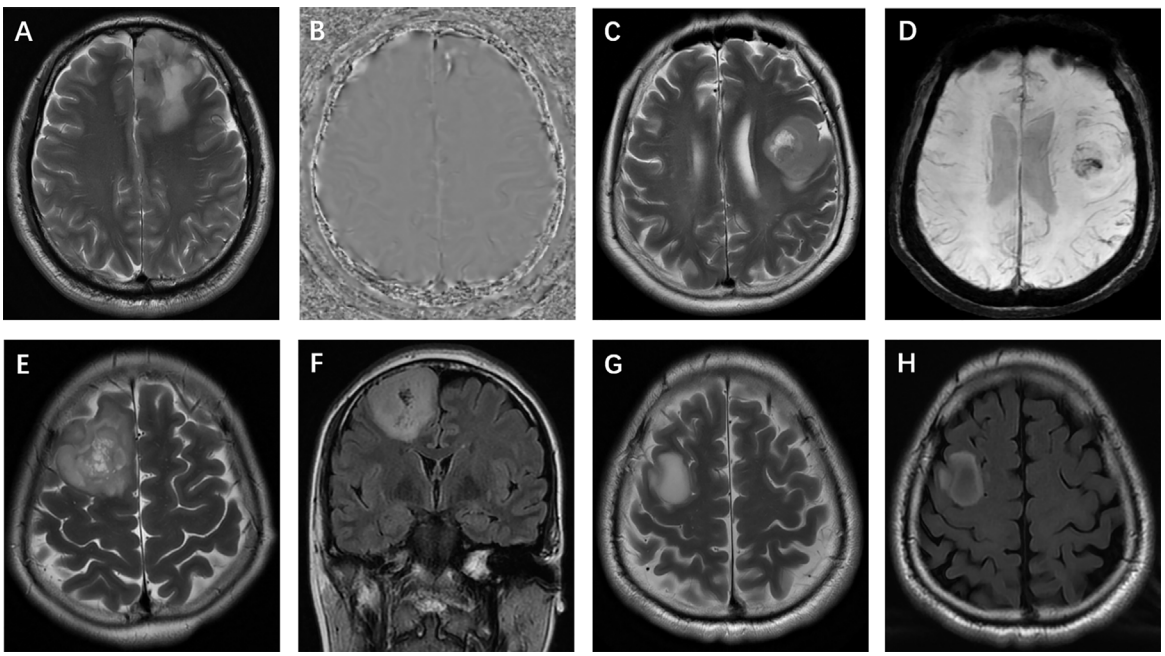

FIGURE 4 | Glioma morphologic characteristics. **(A, B)** Calcification: T2-weighted imaging and phase image on SWI show calcification in a left frontal isocitrate dehydrogenase (IDH)-mutant oligodendroglioma; **(C, D)** Hemorrhage: T2-weighted imaging and SWI show hemorrhage in a left frontal IDH-wildtype glioma; **(E, F)** Cystic change: T2-weighted and FLAIR imaging show small cysts in a mutant-IDH oligodendroglioma; **(G, H)** T2-FLAIR mismatch sign: T2-weighted and FLAIR images show a T2-FLAIR mismatch sign in a mutant-IDH diffuse astrocytoma.

(ICC >0.8; k >0.6), then it was chosen as a predictor variable for multivariable logistic regression to predict IDH subtypes of glioma.

Model Construction

For machine learning, we attempted to implement the following machine learning methods, which are currently the most popular machine learning methods used to classify glioma tumors (17–20), to develop prediction models: logistic regression, support vector machine (SVM), Naive Bayes (NB) and Ensemble (random forest + eXtreme Gradient Boosting). The logistic regression model uses the maximum likelihood method to estimate and determine the regression coefficient and accurately predict the probability of dichotomy. SVM is a supervised learning algorithm that can clearly identify high-dimensional boundaries and solve dichotomy problems (21). Ensemble algorithms include random forest and eXtreme Gradient Boosting. Random forest is an integrated algorithm that combines multiple decision trees together by voting to discriminate and classify data (22). eXtreme Gradient Boosting integrates many weak classifiers into a strong classifier, which is an optimized extreme gradient promotion to improve the predictive power (21, 23). We also attempted NB, an efficient algorithm based on the Bayesian principle that uses the knowledge of probability in statistics to classify data sets (24). The construction process for each model is provided in **Supplementary Data**.

To evaluate the predictive accuracy of these machine learning models and select the most suitable model, we calculated and compared sensitivity, specificity, accuracy, the areas under the receiver operating characteristic curve (AUC) and F1 score (25). Then, the best machine learning model was chosen as the final model to evaluate the IDH subtype probability in the test set. In clinical practice, SWI and CT, which help to observe calcification, may be unavailable in some circumstances, an alternative model (model 2) was developed in which calcification status was excluded from the multivariable logistic regression model. Subgroup analysis was also performed to validate the final model on LGG and GBM. DeLong analysis was used to compare significant differences in the AUCs (26).

RESULTS

Patients Demographic Characteristics

The flow chart of the enrolled patients (including the study and test sets) is provided in **Figure 1**. After excluding patients because of non-adult patients (age<18 y, n=11), insufficient MRI scan quality (n=54), the presence of tumors other than WHO grade II-IV glioma (n=19, including 8 WHO grade I and 11 diffuse midline gliomas), ambiguous histology results (n=28), a duration from MRI to surgery longer than 6 months in WHO II/III or 5 weeks in WHO IV (n=30), or a previous treatment for glioma (n=7). A total of 176 patients (109 male and 67 female patients; mean age, 46.5 years; age range, 21-74 years) with lower-grade glioma (n=102) and glioblastoma (n=74) were ultimately enrolled in the analysis of the study set. There was no relationship found between glioma IDH subtype and sex, but patients with the IDH-wildtype status were more likely to be older than those with the IDH-mutant status, especially in cases of GBM. An overview of patient information, morphologic features and IDH subgroups is listed in **Table 1** and **Supplemental Table 2**.

Morphologic Assessment Results

Regarding tumor location, the measured values demonstrated almost perfect interobserver agreement (κ=0.835, P<0.01). For the longest tumor diameter (<6 cm or ≥6 cm), the measurement reached almost perfect agreement (κ=0.848, P<0.01). The determination of calcification showed substantial agreement (κ=0.719, P<0.01). Determination of the presence of a cyst or necrosis reached almost perfect agreement (κ=0.862, P<0.01). For the enhancement patterns, the results demonstrated substantial agreement (κ=0.786, P<0.01). The determination of hemorrhage reached almost perfect agreement (κ=0.852,

TABLE 1 | Patient demographics and MRI morphological characteristics in the study set.

Parameter	All Gliomas	IDH Mutation	IDH Wild-Type	P value
Number of Patients	176	89	87	
Age	46.5 [35.0,54.0]	41.0 [33.0,49.0]	50.0 [40.0,59.0]	<0.001
Sex				
Female	67 (38.1)	31 (34.8)	36 (41.4)	0.460
Male	109 (61.9)	58 (65.2)	51 (58.6)	
Tumor Location				
Frontal lobe	89 (50.6)	56 (62.9)	33 (37.9)	0.010
Other lobes	74 (42.0)	29 (32.6)	45 (51.7)	
Thalamus or brainstem	9 (5.1)	3 (3.4)	6 (6.9)	
Cerebellum	4 (2.3)	1 (1.1)	3 (3.4)	
Diameter				
<6 cm	132 (75.0)	62 (69.7)	70 (80.5)	0.139
≥6 cm	44 (25.0)	27 (30.3)	17 (19.5)	
Enhancement				
Nonenhancement	63 (35.8)	53 (59.6)	10 (11.5)	<0.001
Patchy enhancement	42 (23.9)	25 (28.1)	17 (19.5)	
Ring enhancement	71 (40.3)	11 (12.4)	60 (69.0)	
Calcification				
No	152 (86.4)	68 (76.4)	84 (96.6)	<0.001
Yes	24 (13.6)	21 (23.6)	3 (3.4)	
Cystic Change				
No	73 (41.5)	48 (53.9)	25 (28.7)	0.001
Yes	103 (58.5)	41 (46.1)	62 (71.3)	
Hemorrhage				
No	91 (51.7)	63 (70.8)	28 (32.2)	<0.001
Yes	85 (48.3)	26 (29.2)	59 (67.8)	
T2 FLAIR Mismatch				
No	136 (77.3)	62 (69.7)	74 (85.1)	0.024
Yes	40 (22.7)	27 (30.3)	13 (14.9)	
WHO 2016 Grade				
Lower-grade Glioma	102 (58.0)	78 (88.7)	23 (26.4)	<0.001
Glioblastoma	74 (42.0)	10 (11.2)	64 (73.6)	

Data in parentheses are ranges, and data in brackets are interquartile ranges.
IDH, isocitrate dehydrogenase; FLAIR, fluid-attenuated inversion recovery.

P<0.01). In assessing the T2-weighted FLAIR mismatch sign, fair interobserver agreement was found (κ=0.396, P<0.01). Cohen's kappa results for the morphology categories are provided in **Supplementary Table 3**.

ADC Quantification

The interobserver and intraobserver levels of reproducibility were almost perfect for all ADC parameters (ICC=0.80-0.95), which indicated that there was no systematic difference between the observers. The rADC correctly classified IDH-mutant and IDH-wildtype in WHO grade II~IV gliomas and LGG subgroup (P<0.05), but not in GBM subgroup (P=0.126). The results are shown in **Figure 5**. Nonparametric testing (Kruskal-Wallis analysis of variance) revealed an association between ADC value and IDH status (P<0.001). The ICCs for different ADC values are provided in **Supplementary Tables 4** and **5**.

Predictor Selection (Univariable Analysis and Machine Learning Model)

The chi-squared tests revealed associations between morphological features, including enhancement, calcification, cysts, hemorrhage, cystic change and T2-FLAIR mismatch, and IDH status (P<0.05). The univariable analysis results are shown in **Table 2**.

After univariable analysis selection, combined with features with substantial agreement (k >0.6), six measured variables were selected for incorporation into the machine learning model, including rADC, age, enhancement, calcification, hemorrhage, and cystic change. In terms of the prediction accuracy of the single model, logistic regression, SVM, NB and ensemble showed similar model performance to the study set (AUC=0.866-0.897). Among them, logistic regression exhibited the largest area under the curve (AUC= 0.897) and the model achieved better performance than others. Then, we chose multivariable logistic regression as the final model. Models 1 and 2 (not including calcification) performed almost equivalently, with an AUC of 0.890 for model 2. DeLong analysis showed no statistically significant difference between the two models (P=0.361). In the lower-grade glioma and GBM, the models also achieved better performance, with the accuracy of 84.3% (AUC = 0.873) and 85.1% (AUC = 0.862), respectively. The AUCs of the different machine learning models are presented in **Figure 6**.

TABLE 2 | Crude association between IDH status and ADC value and morphologic features for the study set.

	Values	OR	P	95% CI
rADC	1.39 ± 0.39	0.05	<0.001	(0.01, 0.15)
ADCmin	1.02 ± 0.27	0.01	<0.001	(0.00, 0.07)
Age	45.30 ± 12.53	1.05	0.001	(1.02, 1.08)
Sex				
Female	67 (38.07%)	Reference		
Male	109 (61.93%)	0.76	0.372	(0.41, 1.39)
Tumor Location				
Frontal lobe	89 (50.57%)	Reference		
Other lobes	74 (42.05%)	2.63	0.003	(1.40, 4.97)
Thalamus or brainstem	9 (5.11%)	3.39	0.100	(0.80, 14.49)
Cerebellum	4 (2.27%)	5.09	0.166	(0.51, 50.97)
Diameter				
<6 cm	132 (75.00%)	Reference		
≥6 cm	44 (25.00%)	0.56	0.100	(0.28, 1.12)
Enhancement				
Nonenhancement	63 (35.80%)	Reference		
Patchy enhancement	42 (23.86%)	3.6	0.006	(1.44, 8.99)
Ring enhancement	71 (40.34%)	28.91	<0.001	(11.38,73.47)
Calcification				
No	152 (86.36%)	Reference		
Yes	24 (13.64%)	0.12	0.007	(0.03, 0.40)
Cystic Change				
No	73 (41.48%)	Reference		
Yes	103 (58.52%)	2.9	0.008	(1.56, 5.42)
Hemorrhage				
No	91 (51.70%)	Reference		
Yes	85 (48.30%)	5.11	<0.001	(2.69, 9.69)
T2-FLAIR Mismatch				
No	136 (77.27%)	Reference		
Yes	40 (22.73%)	0.4	0.017	(0.19, 0.85)

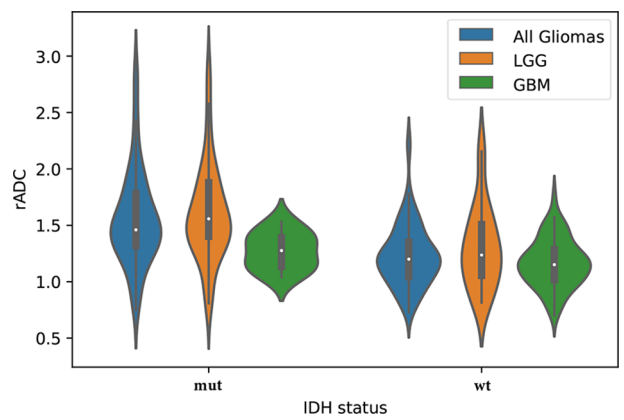

FIGURE 5 | The violin plot shows differences in the apparent diffusion coefficient (ADC) values (ADCmin to ADCn ratio, rADC) between the isocitrate dehydrogenase (IDH) statuses (mut = IDH-mutant, wt = IDH-wildtype) in the study set, including lower-grade glioma (LGG) and glioblastoma (GBM).

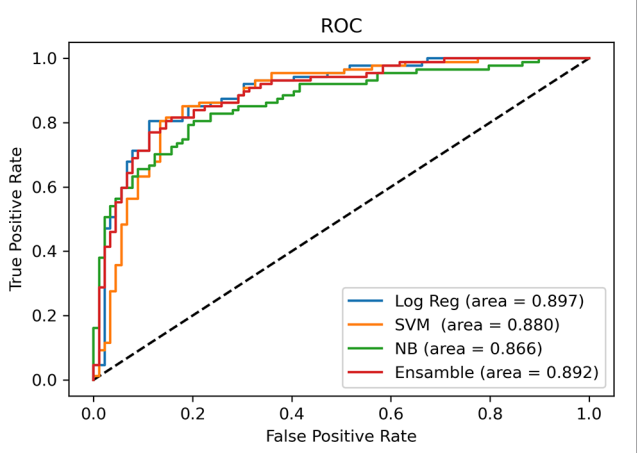

FIGURE 6 | Comparison of AUCs among machine learning models. Receiver operating characteristic curves are shown for logistic regression (Log Reg), support vector machine (SVM), Naive Bayes (NB) and Ensemble (random forest + eXtreme Gradient Boosting) in predicting the IDH status of glioma.

The comparison of machine learning models is provided in **Supplementary Table 6**. The results of models 1 and 2, LGG and GBM are shown in **Table 3** and **Figure 7**.

Test Set Results

To predict the probability of the IDH status of patients in the subsequent test set, the study set results were transcribed into Python for further calculation. From January 2020 to June 2020, 40 diagnosed glioma patients (20 with IDH-mutant and 20 with IDH-wildtype) were included in the test set according to the same inclusion criteria. Two blinded observers (Y-YC and Y-LW) replicated the ADC measurements used in the study set. The ICCs for different ADC values are provided in **Supplementary Table 4**. The AUCs of models 1 and 2, LGG and GBM in the test set are presented in **Table 3** and **Figure 7**. Model 1 correctly classified the IDH status in the test set (AUC=0.860), with sensitivity of 80% and specificity of 80%. Model 2 performed well in predicting the IDH status of glioma (AUC=0.893), demonstrating a greater specificity of 95% but a lower sensitivity of 70% than model 1. Subgroup analysis revealed that the model predicted IDH status of LGG and GBM with the accuracy of 70.0% (AUC = 0.762) and 70.0% (AUC = 0.833), respectively.

DISCUSSION

In this study, machine learning methods were developed and validated, combining rADCs with tumor morphologic characteristics to predict the IDH status of adult WHO grade II-IV gliomas. In the predictive models, the logistic regression model exhibited the greatest AUC (0.897). Two models, model 1 (including age, rADC, enhancement pattern, calcification, cystic change and hemorrhage) and model 2 (excluding calcification), were developed and correctly classified the IDH status with similar model performance for the study set (n=176, AUC=0.890-0.897) and a previously unseen test set (n = 40, AUC=0.860-0.893).

Previous studies have analyzed the association between MRI features and the IDH status of lower-grade gliomas (WHO grade II-III) and glioblastomas (WHO grade IV) [specifically, Thust et al. and Xing et al. evaluated the features of grade II/III gliomas (8, 12), while Zhang et al. identified MRI features associated with grade III and IV gliomas (7)]. To our knowledge, no previous attempts have been made to use different machine learning methods to build a suitable model combining clinical and magnetic resonance imaging features to predict the IDH molecular subtype for WHO grade II to IV gliomas. Furthermore, previous studies have used region-derived minimum ADC measurements to estimate glioma grade or molecular status (8, 11, 12, 27, 28). Not surprisingly, according to receiver operating characteristic curve analysis, the ADC value was shown to be a useful tool for detecting the IDH status in diffuse gliomas, and we found that there was a significant difference between IDH-mutant and IDH-wildtype gliomas (P<0.001). Our study revealed excellent interobserver and intra-observer reproducibility (ICC=0.80-0.95) for ROI measurements, similar to the repeatability results for ADC measurements described in other studies (8). The rADC

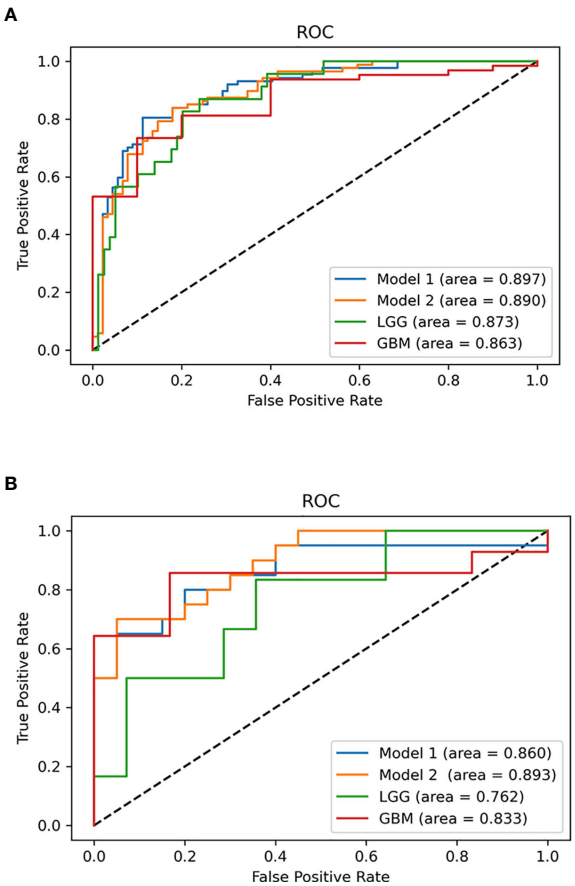

FIGURE 7 | Multivariable logistic regression analysis was used to predict isocitrate dehydrogenase (IDH) status in the study set and test set. **(A)** Receiver operating characteristic (ROC) curves of the multivariable probabilities for models 1 and 2, lower-grade glioma (LGG) and glioblastoma (GBM) in the study set. **(B)** ROC curves of the multivariable probabilities for model 1, model 2, LGG and GBM in the test set.

TABLE 3 | Multivariable logistic regression results for predicting the IDH status in the study set and the test set.

	Number	Se	Sp	PPV	NPV	YI	Accuracy	AUC
Study set								
Model 1	176	0.805	0.888	0.856	0.816	0.693	0.824	0.897
Model 2	176	0.839	0.820	0.823	0.836	0.659	0.812	0.890
LGG	102	0.870	0.759	0.783	0.854	0.629	0.843	0.873
GBM	74	0.734	0.900	0.880	0.772	0.634	0.851	0.862
Test set								
Model 1	40	0.800	0.800	0.800	0.800	0.600	0.750	0.860
Model 2	40	0.700	0.950	0.933	0.760	0.650	0.750	0.893
LGG	20	0.833	0.643	0.700	0.794	0.476	0.700	0.762
GBM	20	0.857	0.833	0.837	0.853	0.690	0.700	0.833

Se, sensitivity; Sp, specificity; PPV, positive predictive value; NPV, negative predictive value; YI, Youden Index; AUC, area under the curve; LGG, lower-grade glioma; GBM, glioblastoma.

(ADCmin to nADC ratio) was used as a fixed parameter to ensure vendor neutrality and to reduce the potential bias. When drawing the ROI, this study only included the solid part, avoiding cystic or necrotic portions and hemorrhagic areas as much as possible, which is considered feasible on most clinical workstations. This method is partially consistent with the results reported by G.Z (29) who suggested that when drawing ROIs on ADC maps, selection of the solid part is necessary and is an optimal choice for differentiating GBM from metastasis.

When testing the rADC for predicting IDH status, our study found that the ADCmin and rADC of IDH-mutant glioma were higher than those of IDH-wildtype glioma in WHO grade II~IV gliomas and LGG subgroup, but not in GBM subgroup. ADCmin has been confirmed to represent the area with the highest cellularity in heterogeneous tumors. In general, the lower the ADC value is, the denser the glioma cells, and the worse the prognosis, which is supported by several studies comparing diffusivity, histological specimens and clinical data (8, 30). Hong et al. reported that ADC was significantly lower in IDH-wildtype GBM than in IDH-mutant GBM (31). However, our study failed to find this result. One reason may be attributed to the difference in sample size, with only 10 IDH mutants in our GBM subgroup. The other reason may be due to the heterogeneity in GBM and different ROI biases. Glioblastomas have different subsets of genetic abnormalities that take part in tumorigenesis and transformation, especially IDH mutants, which may contain lower-grade tumor components (32). In our study, the lowest value of ADC was selected for analysis, which greatly avoided the measurement bias caused by measuring the whole tumor.

Although quantitative, computerized methods hold substantial promise for the noninvasive prediction of the molecular characteristics of glioma, we aimed to establish a model by combining several morphologic features that can be easily evaluated on conventional, standard MRI daily in the clinic. Considering the age and morphological characteristics of our population, consistent with previous research, younger age and forehead positions were more likely to be associated with mutation status (33, 34). Arita et al. (35) found that IDH-wildtype gliomas were mainly distributed in the parietal lobe and, to some extent, the temporal lobe but were rarely involved the frontal lobe. In our study, IDH-wildtype status was similarly associated with a greater likelihood of distribution in cerebral lobes other than the frontal lobe. Moreover, thalamic or brainstem locations and cerebellar locations showed IDH-wildtype predominance, which concurs with a study by Maynard et al. (11).

Our study showed a significant difference in postcontrast enhancement patterns between glioma subtypes in WHO grade II-IV glioma. Indeed, tumor ring-enhancement is a predictor of IDH-wildtype status, indicating a tendency for invasive behavior. While it is increasingly recognized that nonenhancement tumors also comprise a substantial proportion of grade IV gliomas (36), it should be noted that images of atypical glioblastoma might not be easily distinguished from lower-grade gliomas on routine MRI. Furthermore, the presence of hemorrhage was not related to a particular subgroup in our study. Moreover, previous studies show that the T2-FLAIR mismatch sign has high specificity in diagnosing IDH-mutant astrocytoma (16). This tendency was also shown in our research results, but it was not selected for incorporation into the model due to the fair interobserver agreement (κ=0.396).

Calcification and cystic components also significantly contributed to our predictive model in WHO grade II-IV glioma. The absence of calcification strongly correlated with the IDH-wildtype status in univariable analysis. This finding is consistent with previous studies that have extensively evaluated calcification in IDH-mutant gliomas (11). The interobserver agreement was moderate (κ=0.719, P<0.01). We hypothesize that by expanding the sample size and optimizing the examination sequence, the certainty and concordance of the observers would further increase when observing calcification. Kanazawa et al. (37) found that both calcification and cystic components could be used to predict IDH-mutant status with 1p/19q deletion in lower-grade gliomas. However, in our study, cystic components were more likely to be found in IDH-wildtype tumors than in IDH-mutant tumors. Considering that IDH-wildtype tumors are more necrotic than IDH-mutant tumors (38), we speculate that subjectivity and overlap with necrotic components limit the reproducibility of this correlation.

Several limitations of the current study should be noted. First, we did not include infantile gliomas because high-grade gliomas are a specific entity with a paradoxical clinical course that distinguishes them from their pediatric and adult counterparts (39). Second, the simplified description and measurements of the ADC values combined with DWI cannot fully reflect the complexity of cell components and structural changes; a more advanced MRI postprocessing method (for example, a method that uses semiautomatic or automatic segmentation to cover the total tumor volume) may partially overcome these limitations at the expense of more time-consuming preprocessing and postprocessing workflows. It is worth mentioning that our ADC measurements applied are available in most clinical workstations. Finally, our study is a retrospective study based on data from a single institution. The stability of the morphological features may be affected by differences in the MR parameters and protocol, the image postprocessing steps and the repeatability of ADC measurements. Therefore, the next step is to conduct a multi-center study to verify our inferences.

In conclusion, we demonstrated that the ADCmin to ADCn ratio, combined with tumor morphologic features, has high accuracy in predicting tumors with IDH-mutant status versus tumors with IDH-wildtype status in adult diffuse glioma. The combination may provide a noninvasive, significant and feasible alternative marker. Further studies in larger sample trials are needed to improve its clinical application value.

DATA AVAILABILITY STATEMENT

The original contributions presented in the study are included in the article/**Supplementary Material**. Further inquiries can be directed to the corresponding author.

ETHICS STATEMENT

The studies involving human participants were reviewed and approved by The Institutional Ethical Committee of the Chinese PLA General Hospital. Written informed consent for participation was not required for this study in accordance with the national legislation and the institutional requirements.

AUTHOR CONTRIBUTIONS

JZ and LM conceived the study design. JZ, HP, Y-YC, X-BB and D-KZ were responsible for patient recruitment and acquired clinical information. JZ, Y-LW and H-FX conducted the quality assurance of image quality. JZ and HP were responsible for statistical analysis. JZ wrote the first draft of this manuscript. Y-LW and LM reviewed the manuscript. All authors contributed to the article and approved the submitted version.

SUPPLEMENTARY MATERIAL

The Supplementary Material for this article can be found online at: https://www.frontiersin.org/articles/10.3389/fonc.2021.640738/full#supplementary-material

REFERENCES

1. Louis DN, Perry A, Reifenberger G, von Deimling A, Figarella-Branger D, Cavenee WK, et al. The 2016 World Health Organization Classification of Tumors of the Central Nervous System: A Summary. *Acta Neuropathol* (2016) 131(6):803–20. doi: 10.1007/s00401-016-1545-1
2. Mirchia K, Richardson TE. Beyond IDH-Mutation: Emerging Molecular Diagnostic and Prognostic Features in Adult Diffuse Gliomas. *Cancers (Basel)* (2020) 12(7):1817. doi: 10.3390/cancers12071817
3. Ostrom QT, Cioffi G, Gittleman H, Patil N, Waite K, Kruchko C, et al. Cbtrus Statistical Report: Primary Brain and Other Central Nervous System Tumors Diagnosed in the United States in 2012-2016. *Neuro-Oncology* (2019) 21 (Supplement_5):v1–100. doi: 10.1093/neuonc/noz150
4. Tom MC, Cahill DP, Buckner JC, Dietrich J, Parsons MW, Yu JS. Management for Different Glioma Subtypes: Are All Low-Grade Gliomas Created Equal? *Am Soc Clin Oncol Educ Book* (2019) 39:133–45. doi: 10.1200/EDBK_238353
5. Hartmann C, Hentschel B, Wick W, Capper D, Felsberg J, Simon M, et al. Patients With IDH1 Wild Type Anaplastic Astrocytomas Exhibit Worse Prognosis Than IDH1 Mutated Glioblastomas and IDH1 Mutation Status Accounts for the Unfavorable Prognostic Effect of Higher Age: Implications for Classification of Gliomas. *Acta Neuropathol* (2010) 120:707–18. doi: 10.1007/s00401-010-0781-z
6. Patel SH, Bansal AG, Young EB, Batchala PP, Patrie JT, Lopes MB, et al. Extent of Surgical Resection in Lower-Grade Gliomas: Differential Impact Based on Molecular Subtype. *AJNR Am J Neuroradiol* (2019) 40(7):1149–55. doi: 10.3174/ajnr.A6102
7. Zhang B, Chang K, Ramkissoon S, Tanguturi S, Bi WL, Reardon DA, et al. Multimodal MRI Features Predict Isocitrate Dehydrogenase Genotype in High-Grade Gliomas. *Neuro-Oncology* (2017) 19(1):109–17. doi: 10.1093/neuonc/now121
8. Thust SC, Hassanein S, Bisdas S, Rees JH, Hyare H, Maynard JA, et al. Apparent Diffusion Coefficient for Molecular Subtyping of non-Gadolinium-Enhancing WHO Grade II/III Glioma: Volumetric Segmentation Versus Two-Dimensional Region of Interest Analysis. *Eur Radiol* (2018) 28 (9):3779–88. doi: 10.1007/s00330-018-5351-0
9. Zhang L, Min Z, Tang M, Chen S, Lei X, Zhang X. The Utility of Diffusion MRI With Quantitative ADC Measurements for Differentiating High-Grade From Low-Grade Cerebral Gliomas: Evidence From a Meta-Analysis. *J Neurol Sci* (2017) 373:9–15. doi: 10.1016/j.jns.2016.12.008
10. Chen Z, Zhou P, Lv B, Liu M, Wang Y, Wang Y, et al. The Diagnostic Value of High-Frequency Power-Based Diffusion-Weighted Imaging in Prediction of Neuroepithelial Tumour Grading. *Eur Radiol* (2017) 27(12):5056–63. doi: 10.1007/s00330-017-4899-4
11. Maynard J, Okuchi S, Wastling S, Busaidi AA, Almossawi O, Mbatha W, et al. World Health Organization Grade Ii/Iii Glioma Molecular Status: Prediction by MRI Morphologic Features and Apparent Diffusion Coefficient. *Radiology* (2020) 296(1):111–21. doi: 10.1148/radiol.2020191832
12. Xing Z, Yang X, She D, Lin Y, Zhang Y, Cao D. Noninvasive Assessment of IDH Mutational Status in World Health Organization Grade II and III Astrocytomas Using DWI and DSC-PWI Combined With Conventional Mr Imaging. *Am J Neuroradiol* (2017) 38(6):1138–44. doi: 10.3174/ajnr.A5171
13. Jiang F, Jiang Y, Zhi H, Dong Y, Li H, Ma S, et al. Artificial Intelligence in Healthcare: Past, Present and Future. *Stroke Vasc Neurol* (2017) 2(4):230–43. doi: 10.1136/svn-2017-000101
14. Fralick M, Colak E, Mamdani M. Machine Learning in Medicine. *New Engl J Med* (2019) 380(26):2588–90. doi: 10.1056/NEJMc1906060
15. Patel SH, Poisson LM, Brat DJ, Zhou Y, Cooper L, Snuderl M, et al. T2-Flair Mismatch, an Imaging Biomarker for IDH and 1p/19q Status in Lower-grade Gliomas: A Tcga/Tcia Project. *Clin Cancer Res* (2017) 23(20):6078–85. doi: 10.1158/1078-0432.CCR-17-0560
16. Jain R, Johnson DR, Patel SH, Castillo M, Smits M, van den Bent MJ, et al. "Real World" Use of a Highly Reliable Imaging Sign: "T2-FLAIR Mismatch" for Identification of IDH Mutant Astrocytomas. *Neuro Oncol* (2020) 22 (7):936–43. doi: 10.1093/neuonc/noaa041
17. Sengupta A, Ramaniharan AK, Gupta RK, Agarwal S, Singh A. Glioma Grading Using a Machine-Learning Framework Based on Optimized Features Obtained From T Perfusion MRI and Volumes of Tumor Components. *J Magnet Resonance Imaging JMRI* (2019) 50(4):1295–306. doi: 10.1002/jmri.26704
18. Niu B, Liang C, Lu Y, Zhao M, Chen Q, Zhang Y, et al. Glioma Stages Prediction Based on Machine Learning Algorithm Combined With Protein-Protein Interaction Networks. *Genomics* (2020) 112(1):837–47. doi: 10.1016/j.ygeno.2019.05.024
19. Kim M, Jung SY, Park JE, Jo Y, Park SY, Nam SJ, et al. Diffusion- and Perfusion-Weighted MRI Radiomics Model may Predict Isocitrate Dehydrogenase (IDH) Mutation and Tumor Aggressiveness in Diffuse Lower Grade Glioma. *Eur Radiol* (2020) 30(4):2142–51. doi: 10.1007/s00330-019-06548-3
20. Lu CF, Hsu FT, Hsieh KL, Kao YJ, Cheng SJ, Hsu JB, et al. Machine Learning-Based Radiomics for Molecular Subtyping of Gliomas. *Clin Cancer Res* (2018) 24(18):4429–36. doi: 10.1158/1078-0432.CCR-17-3445
21. Borstelmann SM. Machine Learning Principles for Radiology Investigators. *Acad Radiol* (2020) 27(1):13–25. doi: 10.1016/j.acra.2019.07.030
22. Paul A, Mukherjee DP, Das P, Gangopadhyay A, Chintha AR, Kundu S. Improved Random Forest for Classification. *IEEE Trans Image Process* (2018) 27(8):4012–24. doi: 10.1109/TIP.2018.2834830
23. Jiang H, Zou B, Xu C, Xu J, Tang YY. Svm-Boosting Based on Markov Resampling: Theory and Algorithm. *Neural Netw* (2020) 131:276–90. doi: 10.1016/j.neunet.2020.07.036
24. Pernkopf F, Wohlmayr M, Tschiatschek S. Maximum Margin Bayesian Network Classifiers. *IEEE Trans Pattern Anal Mach Intell* (2012) 34(3):521–32. doi: 10.1109/TPAMI.2011.149
25. Handelman GS, Kok HK, Chandra RV, Razavi AH, Lee MJ, Asadi H. eDoctor: Machine Learning and the Future of Medicine. *J Intern Med* (2018) 284 (6):603–19. doi: 10.1111/joim.12822
26. DeLong ER, DeLong DM, Clarke-Pearson DL. Comparing the Areas Under Two or More Correlated Receiver Operating Characteristic Curves: A Nonparametric Approach. *Biometrics* (1988) 44(3):837–45. doi: 10.2307/2531595

27. Wang Q, Zhang J, Xu X, Chen X, Xu B. Diagnostic Performance of Apparent Diffusion Coefficient Parameters for Glioma Grading. *J Neurooncol* (2018) 139(1):61–8. doi: 10.1007/s11060-018-2841-5
28. Gihr GA, Horvath-Rizea D, Hekeler E, Ganslandt O, Henkes H, Hoffmann KT, et al. Histogram Analysis of Diffusion Weighted Imaging in Low-Grade Gliomas: In Vivo Characterization of Tumor Architecture and Corresponding Neuropathology. *Front Oncol* (2020) 10:206. doi: 10.3389/fonc.2020.00206
29. Zhang G, Chen X, Zhang S, Ruan X, Gao C, Liu Z, et al. Discrimination Between Solitary Brain Metastasis and Glioblastoma Multiforme by Using Adc-Based Texture Analysis: A Comparison of Two Different ROI Placements. *Acad Radiol* (2019) 26(11):1466–72. doi: 10.1016/j.acra.2019.01.010
30. Cuccarini V, Erbetta A, Farinotti M, Cuppini L, Ghielmetti F, Pollo B, et al. Advanced MRI may Complement Histological Diagnosis of Lower Grade Gliomas and Help in Predicting Survival. *J Neurooncol* (2016) 126(2):279–88. doi: 10.1007/s11060-015-1960-5
31. Hong EK, Choi SH, Shin DJ, Jo SW, Yoo RE, Kang KM, et al. Radiogenomics Correlation Between MR Imaging Features and Major Genetic Profiles in Glioblastoma. *Eur Radiol* (2018) 28(10):4350–61. doi: 10.1007/s00330-018-5400-8
32. Wu S MP. Same Script, Different Cast: Different Cell Origins Shape Molecular Features and Therapeutic Response in Glioblastoma. *Cancer Cell* (2020) 38 (3):311–3. doi: 10.1016/j.ccell.2020.08.012
33. Suh CH, Kim HS, Jung SC, Choi CG, Kim SJ. Imaging Prediction of Isocitrate Dehydrogenase (IDH) Mutation in Patients With Glioma: A Systemic Review and Meta-Analysis. *Eur Radiol* (2019) 29(2):745–58. doi: 10.1007/s00330-018-5608-7
34. Sonoda Y, Shibahara I, Kawaguchi T, Saito R, Kanamori M, Watanabe M, et al. Association Between Molecular Alterations and Tumor Location and MRI Characteristics in Anaplastic Gliomas. *Brain Tumor Pathol* (2015) 32 (2):99–104. doi: 10.1007/s10014-014-0211-3
35. Arita H, Kinoshita M, Kawaguchi A, Takahashi M, Narita Y, Terakawa Y, et al. Lesion Location Implemented Magnetic Resonance Imaging Radiomics for Predicting IDH and TERT Promoter Mutations in Grade II/III Gliomas. *Sci Rep-Uk* (2018) 8(1):11773. doi: 10.1038/s41598-018-30273-4
36. Lasocki A, Gaillard F. Non-Contrast-Enhancing Tumor: A New Frontier in Glioblastoma Research. *Am J Neuroradiol* (2019) 40(5):758–65. doi: 10.3174/ajnr.A6025
37. Kanazawa T, Fujiwara H, Takahashi H, Nishiyama Y, Hirose Y, Tanaka S, et al. Imaging Scoring Systems for Preoperative Molecular Diagnoses of Lower-Grade Gliomas. *Neurosurg Rev* (2019) 42(2):433–41. doi: 10.1007/s10143-018-0981-x
38. Bernabéu-Sanz Á, Fuentes-Baile M, Alenda C. Main Genetic Differences in High-Grade Gliomas may Present Different MR Imaging and MR Spectroscopy Correlates. *Eur Radiol* (2020) 31(2):749–63. doi: 10.1007/s00330-020-07138-4
39. Ceglie G, Vinci M, Carai A, Rossi S, Colafati GS, Cacchione A, et al. Infantile/Congenital High-Grade Gliomas: Molecular Features and Therapeutic Perspectives. *Diagnostics (Basel Switzerland)* (2020) 10(9):648. doi: 10.3390/diagnostics10090648

Conflict of Interest: The authors declare that the research was conducted in the absence of any commercial or financial relationships that could be construed as a potential conflict of interest.

frontiers in Oncology

ORIGINAL RESEARCH
published: 24 May 2021
doi: 10.3389/fonc.2021.646267

Exploring MRI Characteristics of Brain Diffuse Midline Gliomas With the H3 K27M Mutation Using Radiomics

*Qian Li, Fei Dong, Biao Jiang and Minming Zhang**

Department of Radiology, The Second Affiliated Hospital, Zhejiang University School of Medicine, Hangzhou, China

Objectives: To explore the magnetic resonance imaging (MRI) characteristics of brain diffuse midline gliomas with the H3 K27M mutation (DMG-M) using radiomics.

Materials and Methods: Thirty patients with diffuse midline gliomas, including 16 with the H3 K27M mutant and 14 with wild type tumors, were retrospectively included in this study. A total of 272 radiomic features were initially extracted from MR images of each tumor. Principal component analysis, univariate analysis, and three other feature selection methods, including variance thresholding, recursive feature elimination, and the elastic net, were used to analyze the radiomic features. Based on the results, related visually accessible features of the tumors were further evaluated.

Results: Patients with DMG-M were younger than those with diffuse midline gliomas with H3 K27M wild (DMG-W) (median, 25.5 and 48 years old, respectively; p=0.005). Principal component analysis showed that there were obvious overlaps in the first two principal components for both DMG-M and DMG-W tumors. The feature selection results showed that few features from T2-weighted images (T2WI) were useful for differentiating DMG-M and DMG-W tumors. Thereafter, four visually accessible features related to T2WI were further extracted and analyzed. Among these features, only cystic formation showed a significant difference between the two types of tumors (OR=7.800, 95% CI 1.476–41.214, p=0.024).

Conclusions: DMGs with and without the H3 K27M mutation shared similar MRI characteristics. T2W sequences may be valuable, and cystic formation a useful MRI biomarker, for diagnosing brain DMG-M.

Keywords: diffuse midline glioma, H3 K27M mutant, radiomics, magnetic resonance imaging, principal component analysis

OPEN ACCESS

Edited by:
Han Zhang,
University of North Carolina at Chapel Hill, United States

Reviewed by:
Shun Yao,
Brigham and Women's Hospital and Harvard Medical School, United States
Le Qi,
Hangzhou Normal University, China

***Correspondence:**
Minming Zhang
zhangminming@zju.edu.cn

Specialty section:
This article was submitted to Cancer Imaging and Image-directed Interventions, a section of the journal Frontiers in Oncology

Received: *25 December 2020*
Accepted: *26 April 2021*
Published: *24 May 2021*

Citation:
Li Q, Dong F, Jiang B and Zhang M (2021) Exploring MRI Characteristics of Brain Diffuse Midline Gliomas With the H3 K27M Mutation Using Radiomics. Front. Oncol. 11:646267. doi: 10.3389/fonc.2021.646267

INTRODUCTION

Diffuse midline gliomas with the H3 K27M mutation (diffuse midline glioma, H3 K27M-mutant) (DMG-M) is a newly defined entity in the 2016 World Health Organization (WHO) classification of central nervous system tumors (1). It describes a group of tumors with mutations in either H3F3A or HIST1H3B/C (2, 3). The term DMG-M is suggested to be only used for tumors that are diffuse,

midline gliomas with an H3 K27M mutation, and not for other tumors with the H3 K27M-mutant. A previous study showed that patients with DMG-M had a worse prognosis (with a 2-year survival rate of less than 10%) than those with a diffuse midline glioma, H3 K27M wild (DMG-W) regardless of age, tumor location, or histopathological grading (3, 4). Another advantage for identifying H3 K27M status is that it may be a potentially novel target for immunotherapy for diffuse midline glioma (DMG) (2, 5–7). However, because diffuse midline gliomas are usually located at deep anatomic sites, surgical resection or biopsy is challenging because of the substantial perioperative risks and postoperative morbidities (1). Therefore, developing a non-invasive method for diagnosing DMG-M would be highly valuable (1).

Magnetic resonance imaging (MRI) is an essential technology for the evaluation of brain tumors. Traditionally, visually accessible MRI features are often used for brain tumor evaluation. Identifying important features is often done using experience, such as reading a group of images of patients and summarizing the findings. In addition, a feature set, such as the Visually Accessible Rembrandt Images (VASARI) feature set, is sometimes applied to explore the imaging characteristics of a disease by systematically testing individual features. A previous study found that there were no differences between DMG-M and DMG-W tumors regarding visually accessible MRI features (8). However, it is unclear whether these features are sufficient to represent the characteristics of this disease.

Radiomics is a novel method for high-throughput extraction of quantitative features from a specified region of interest from images (1, 9). These features include many groups, such as shape-based, first-order and texture features. For shape-based features, radiomics not only extracts size and volume data, but also provides additional information such as degree of sphericity and surface area. First-order features provide intensity distribution information such as asymmetry (skewness) and flattening (kurtosis), and texture features provide a more in-depth analysis of the relationships between voxels (10). Analyzing these features might provide a more comprehensive method for exploring a lesion. In recent years, radiomics has been widely used for the classification of phenotypes and genotypes, as well as to predict disease progression (11).

We believe that the analysis of radiomic features may be highly useful for exploring the imaging characteristics of DMG-M and may further guide us in finding useful visually accessible features of this type of tumor. Thus, the aim of this study was to explore the MRI characteristics of brain DMG-M using radiomics.

MATERIALS AND METHODS

Patients

This study was approved by the Local Ethics Committee of our hospital, and the requirement for patient informed consent was waived due to the retrospective character of the study. Thirty patients with diffuse midline gliomas with pathologically confirmed H3 K27M status by immunohistochemistry from January 2017 to October 2020 were retrospectively collected in this study. For all patients, the preoperative Karnofsky Performance Score (KPS) was evaluated when they were admitted to the hospital. The overall survival (OS) time was measured from the time of diagnosis to death or to the last follow-up (censored) (12).

MRI Protocol

MRI was performed with 1.5T Sonata, Aera, Avanto scanner (Siemens Medical Solutions), 3.0T Discovery 750, Signa HDxt scanner (GE Healthcare) and uMR 790 scanner (United Imaging Healthcare). Axial T1-weighted images (T1WI), T2-weighted images (T2WI) and contrast enhanced T1-weighted images (CeT1WI) were acquired with the following parameters: T1WI and CeT1WI (repetition time (TR), 400–2096.3 ms, and echo time (TE), 6.9–26.5 ms), T2WI (TR, 2,800–4,730 ms, and TE, 83–116 ms), and all the images were acquired with a section thickness of 6 mm. Pre-contrast Gadodiamide (Omniscan, GE Healthcare) was injected through a peripheral venous catheter at a dose that was standardized based on patient body weight (0.2 ml/kg body weight, up to a maximum of 20 ml).

Image Preprocessing and Segmentation

To reduce discrepancies caused by different MR image acquisition conditions, a series of image preprocessing steps were performed. First, the T1W and CeT1W images were co-registered to the corresponding T2W images using a rigid transformation (13). Denoising was then performed for all images. To compensate for intensity non-uniformities due to variations in the magnetic field, an N4 bias field correction was performed (14, 15). The hybrid white-stripe method was then used for signal intensity normalization (16). Finally, the images were resampled to 3 mm × 3 mm × 3 mm voxels using a sitkBSpline interpolator. Preprocessing was performed using the ITK-SNAP software (http://www.itksnap.org), Cancer Imaging Phenomics Toolkit (17, 18), and Pyradiomics (http://www.radiomics.io/pyradiomics.html).

Manual segmentation of the tumor for all cases was performed by a radiologist (F.D., with 10 years of experience) on T2WI, T1WI, and CeT1WI in a sequential manner one slice at a time. The segmentation for all cases was then repeated by another radiologist (Q.L., with 7 years of experience). To identify tumor boundary, the tumors were defined as regions with high signal intensity on T2WI but with less than that of cerebrospinal fluid, and with corresponding T1WI hypointensity (**Figure 1**).

Feature Extraction

Radiomic features were extracted using Pyradiomics from axial T1WI, T2WI, and CeT1WI. Seven groups of features were extracted, including shape features (n = 14), first-order features (n=18), gray level co-occurrence matrix (GLCM) features (n=22), gray-level run length matrix (GLRLM) features (n = 16), gray-level size zone matrix (GLSZM) features (n=16), gray level dependence matrix (GLDM) features (n = 14). The extracted features were consistent with the Imaging Biomarker Standardization Initiative (IBSI) (19).

The visually accessible features were selectively extracted based on the results of the analysis of radiomic features. We selected visually accessible features from a comprehensive

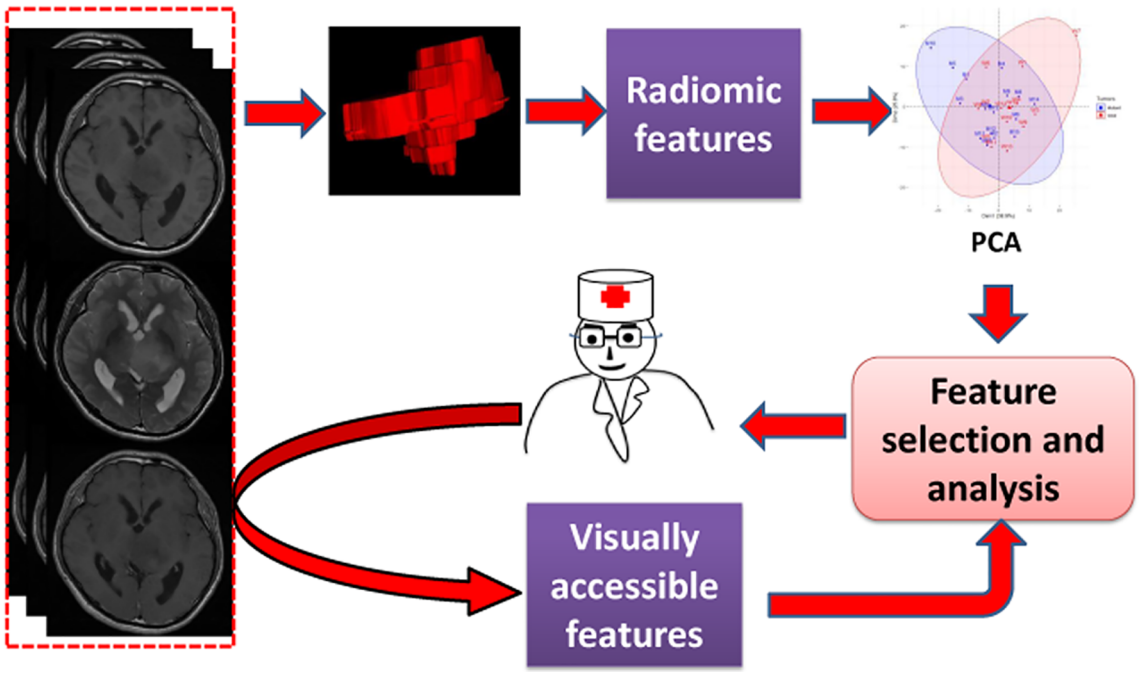

FIGURE 1 | The workflow of this study.

feature set, known as the Visually Accessible Rembrandt Images (VASARI) (https://wiki.cancerimagingarchive.net/display/Public/VASARI+Research+Project), which was specially designed to describe the MR features of human gliomas.

Reproducibility Evaluation of Features

For radiomic features, intraclass correlation coefficient (ICC) values were calculated to evaluate reproducibility. Features with an ICC value ≥0.90 (13, 20) were retained in this study. For visually accessible features (if they were used), inter-reader agreement was evaluated by calculating the κ values; κ values > 0.81, 0.61 to 0.80, and < 0.60 reflected excellent, good, and poor agreement, respectively (21).

Exploring MRI Characteristics

To explore the overall characteristics of the tumors, principal component analysis (PCA) of radiomic features was performed. PCA is a type of unsupervised exploratory method, and its main purpose is to transform correlated metric variables into principal components (PCs) that still contain most of the information from the original variables. It is an efficient method for preliminary analysis to determine the number of factors (22). Because we wanted to determine whether differences in imaging characteristics of overall, shape and in each sequence existed between the two kinds of tumors, PCA was implemented in five datasets, including the retained radiomic features (all features) and shape features as well as first-order and texture features in T1WI (T1WI features), T2WI (T2WI features), and CeT1WI (CeT1WI features). The first two or more components were selected, ensuring that at least 60% of the total variance was explained.

Univariate analysis (Student's t-test or Mann–Whitney U test, as appropriate) was used to explore features with significant differences between DMG-M and DMG-W tumors. A correlation analysis between the significant features was also performed. The number of pairwise correlations of features with |rho| ≥0.90 was regarded as highly correlated (23).

To further explore the MRI features, three feature selection methods were used to select the radiomic features with significant differences between DMG-M and DMG-W tumors. Feature selection methods included variance thresholding, recursive feature elimination, and the elastic net. These methods employ the filter, wrapper, and embedded feature selection methods, respectively. The variance thresholding method first calculates the variance of each feature and then removes features with a variance lower than the threshold. The recursive feature elimination method ranks all of the features from high to low *via* a model, and removes redundant unrelated features (24). The elastic net method is regarded as a combination of the ridge and LASSO (least absolute shrinkage and selection operator) regression methods. It performs better than LASSO in selecting features with multicollinearity (25, 26). In this study, a variance threshold of 0.8 was used for the variance threshold method (27), a support vector machine-based algorithm was used for the recursive feature elimination method (24), and the parameters lambda and alpha (0 to 1, steps of 0.1) were selected using 10-fold cross-validation *via* the minimum-plus-one standard error criterion for the elastic net method (28).

Visually accessible features (if they were used) were evaluated by Fisher's exact test or Fisher-Freeman-Halton test to explore the differences between DMG-M and DMG-W tumors.

Statistical Analyses

The demographic characteristics between patients with DGM-M and those with DGM-W tumors were compared using Pearson chi-square test, Fisher's exact test, Student's t-test, or the Mann–Whitney U test, as appropriate. The Kaplan-Meier method was used to estimate OS, and the log-rank method was used to compare survival differences between DGM-M and DGM-W patients. Survival analysis was conducted using Cox regression for variate analysis. All statistical tests were two-sided with statistical significance set at $p < 0.05$. Fisher's exact test or Fisher-Freeman-Halton test was performed using SPSS19.0. Feature selection with variance thresholding method was implemented by Python (Python 3.6.3, https://www.python.org/). The other data analysis was performed with R software (R 3.6.3, http://www.Rproject.org). The main packages used were: "irr", "FactoMineR", "factoextra", "caret", "e1071", "glmnet", "doParallel", "dplyr", "corrplot", "psy", "survival", "survminer", "qqman".

RESULTS

Clinical Characteristics and Follow-up

A total of 30 patients (18 men and 12 women) were included in the study. Their ages ranged from 8 to 75 years. DMG-M tumors were found in 16 patients (10 men and 6 women), and DMG-W tumors were found in 14 patients (8 men and 6 women). The median time from symptom onset to MR scanning was one month (range, 0.17–36 months). Among the 30 patients, two died due to operative complications, and one was lost to follow-up. The other 27 patients had a median follow-up time of 7 months (range, 1–44 months) and were included in the survival analysis. Demographic and clinical data are presented in **Table 1**.

Extracted Features

A total of 272 radiomic features were initially extracted, including 14 shape features and 86 first-order and texture features for each MR sequence (**Supplemental Data 1**). Thirteen shape features and 196 first-order and texture features (55 from T1WI, 72 from T2WI, and 69 from CeT1WI) showing ICC values ≥0.90 were retained (n = 209).

TABLE 1 | Results of the analysis of basic demographic and clinical data.

		DMG-M	DMG-W	p value
Gender	Male	10	6	0.702*
	Female	6	6	
Age, median (range)		25.5 (8–58)	48 (18–75)	0.005#
Location	Thalamus	10	7	0.713*
	Brain stem	6	7	
KPS	≤80	7	9	0.722*
	>80	5	9	
OS, median (months)		22	20	0.400&

DMG-M, diffuse midline gliomas, H3 K27M Mutation; DMG-W, diffuse midline gliomas, H3 K27M wild type. Fisher's exact test (*); Mann–Whitney U test (#); log-rank test (&).

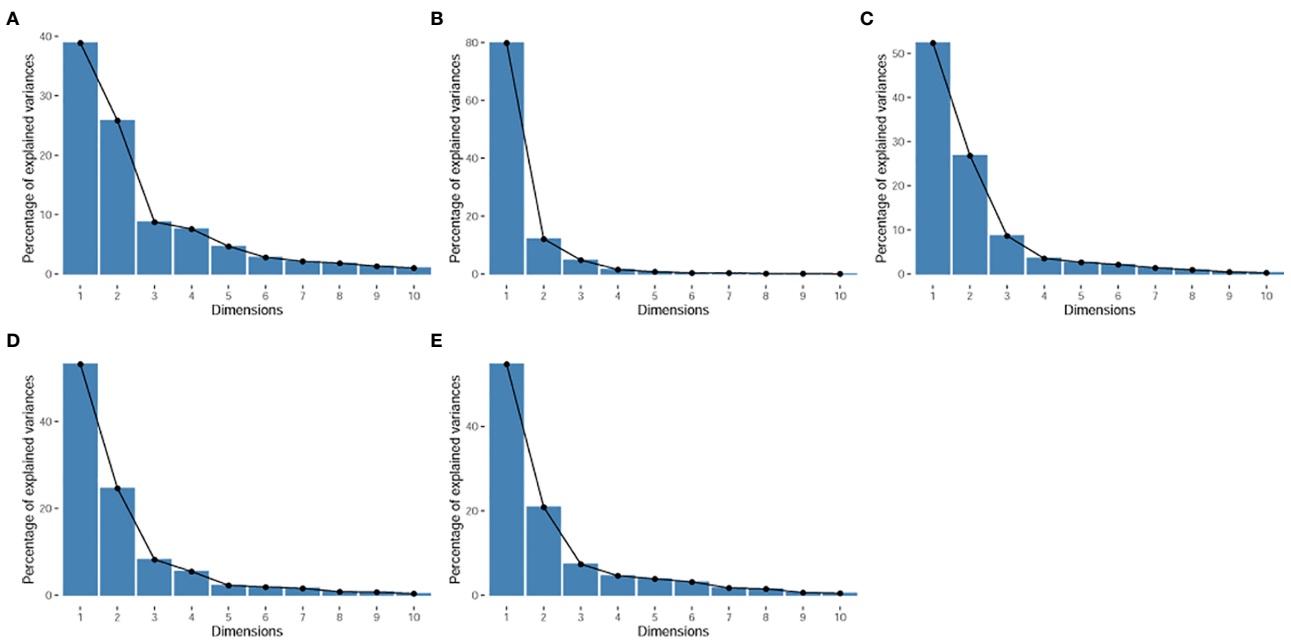

FIGURE 2 | Scree plot. It displays the percentage of explained variances against the number of principal components. **(A)**, for all radiomic features. **(B)**, for shape features. **(C)**, for T1WI features. **(D)**, for T2WI features. **(E)**, for CeT1WI features.

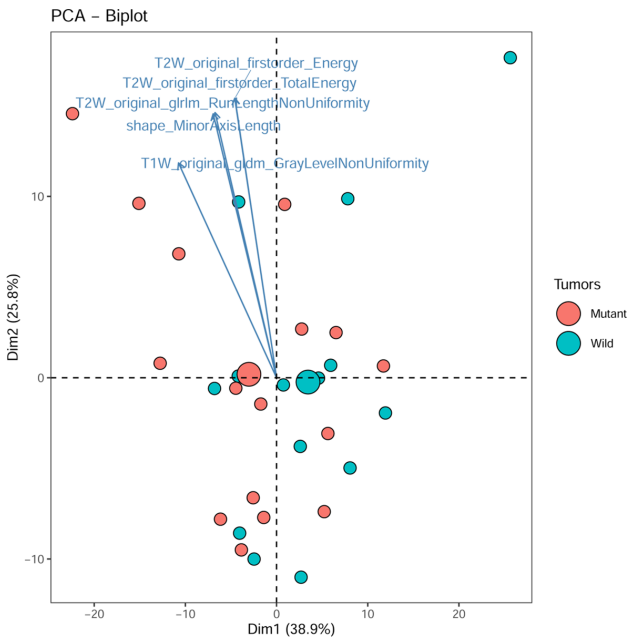

FIGURE 3 | PCA biplot. It shows the contribution of top 5 radiomic features and all individuals to the first two principal components. Mutant, diffuse midline gliomas with the H3 K27M Mutation; Wild, diffuse midline gliomas with the H3 K27M wild.

Exploring Imaging Characteristics

The principal component analysis showed that for all features, shape, T1WI, T2WI, and CeT1WI features, the first principal component explained 38.9% to 79.9% of the total variance. The first two principal components explained 64.7% to 92.0% of the total variance, which explained most of the information of the features. Among the top 5 features that contribution to the first two principal components, three of them derived from T2WI. In addition, two cases (cases M10 and W7) were distinct from the others in the principal component, and both tumors were located in the thalamus (**Figures 2**–**4**).

Univariate analysis showed that there were 18 features with significant differences between DGM-M and DGM-W tumors (**Figure 5**). Only five features left after discarding the highly correlated features (**Figure 6**), and 60% (three of five) of these features were texture features from T2WI.

Although the features selected by the three methods were not identical, all of them were texture features from T2WI (**Table 2**). Therefore, visually accessible features related to T2WI in the VASARI feature set were selected and further analyzed (**Figure 7**).

The extracted visually accessible features included cystic formation, necrosis, hemorrhage, and the T1/T2 ratio. A cystic formation was identified as a region that was well defined and usually rounded, showing a low signal on T1WI and high signal on T2WI (higher than the solid part of the tumor and close to cerebrospinal fluid leakage signal intensity), with very thin,

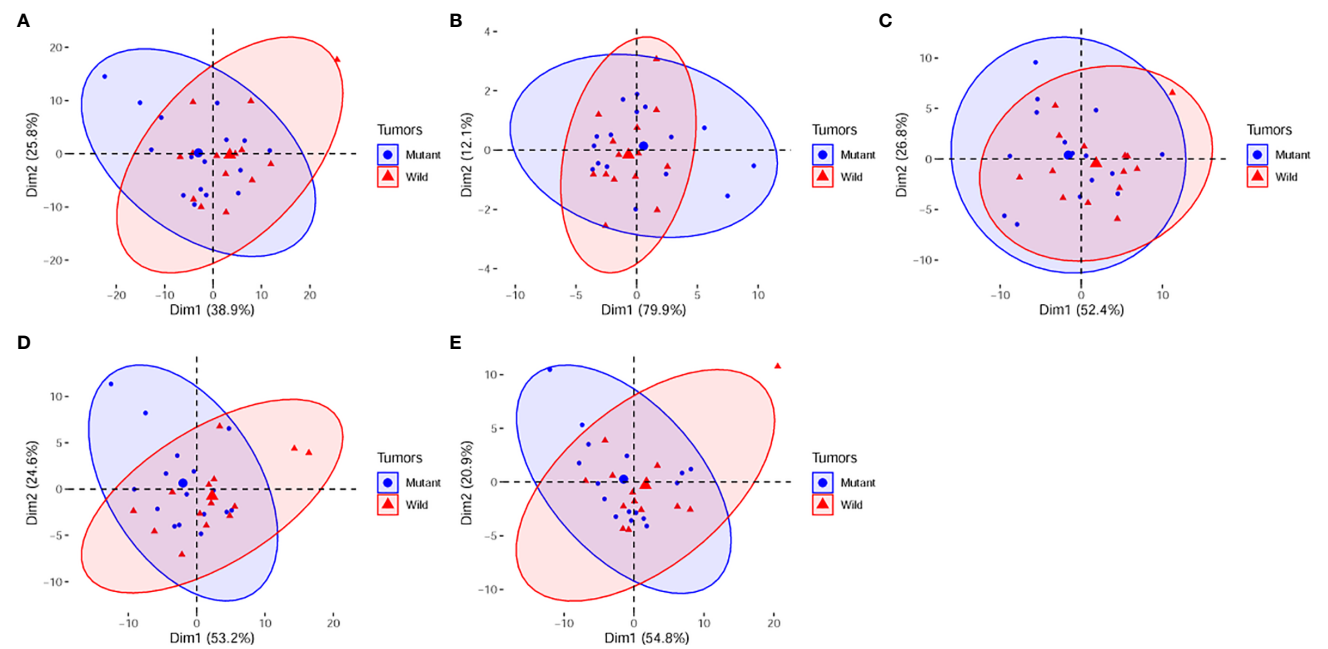

FIGURE 4 | PCA score plots of **(A)**, all radiomic features; **(B)**, shape features. **(C)**, T1WI features. **(D)**, T2WI features. **(E)**, CeT1WI features. PC1, first principal component; PC2, second principal component; Mutant, diffuse midline gliomas with the H3 K27M Mutation; Wild, diffuse midline gliomas with the H3 K27M wild. PCA, principal component analysis; PC, principal component.

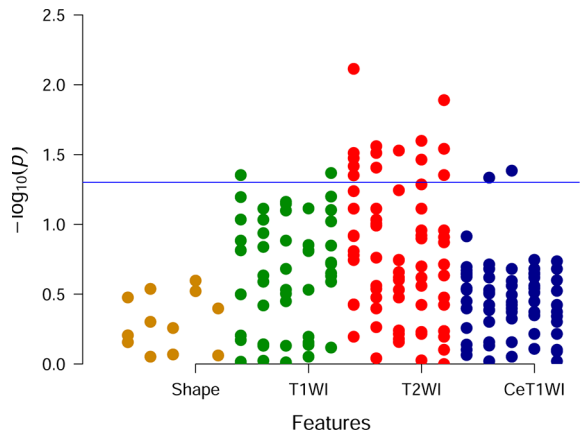

FIGURE 5 | Manhattan plot. Each point is corresponding to a feature and the blue line represents the level of p value equal to 0.05.

regular, and smooth walls. Necrosis was identified in regions within the tumor that had an irregular border, showing a low signal on T1WI, high signal on T2WI. Hemorrhages were defined as foci with a low signal on T2WI or a high signal on T1WI. The T1/T2 ratio was defined as the abnormality size ratio on pre-contrast T1WI and T2WI. The rules for evaluating the features were as follows: (a) cyst formation, 1 = no, 2 = yes; (b) necrosis, 1 = none (0%), 2 = <5%, 3 = 6–33%, 4 = 34–67%, 5 = 68–95% 6 = >95%, 7 = all (100%), 8 = indeterminate; (c) hemorrhage, 1 = no, 2 = yes; (d) T1/T2 ratio, 1 = T1 and T2 approximately the same (T1≈T2), 2 = T1 less than T2 (T1<T2), 3 = T1 far less than T2 (T1<<T2). (https://wiki.cancerimagingarchive.net/display/Public/VASARI+Research+Project).

TABLE 2 | Features selection results.

Methods	Features
Variance threshold	T2W_original_glcm_Contrast
	T2W_original_gldm_LargeDependenceEmphasis
Recursive feature elimination	T2W_original_glcm_Contrast
	T2W_original_glszm_LargeAreaLowGrayLevelEmphasis
	T2W_original_glcm_DifferenceEntropy
Elastic net	T2W_original_gldm_SmallDependenceEmphasis

The inter-reader agreement on visual accessible feature evaluation by the two radiologists was excellent [κ range, (0.84, 0.90)].

Among the visually accessible features, cyst formation showed a significant difference between DGM-M and DGM-W tumors (OR = 7.800, 95% CI 1.476-41.214; p=0.024). There were no significant differences between DGM-M and DGM-W tumors for necrosis (p = 0.191, data in groups 5 and 6 were merged for the limited cases), hemorrhage (p = 0.657), and the T1/T2 ratio (p = 0.689).

Correlation Between MR Features and Clinical Data

There were no significant differences in symptoms from onset to MR scanning between the two groups with and without cyst formation (p=0.358).

Cox analysis showed that DGM-M type tumor (HR=1.787, p=0.422), older age (HR=1.015, p = 0.540), cystic formation

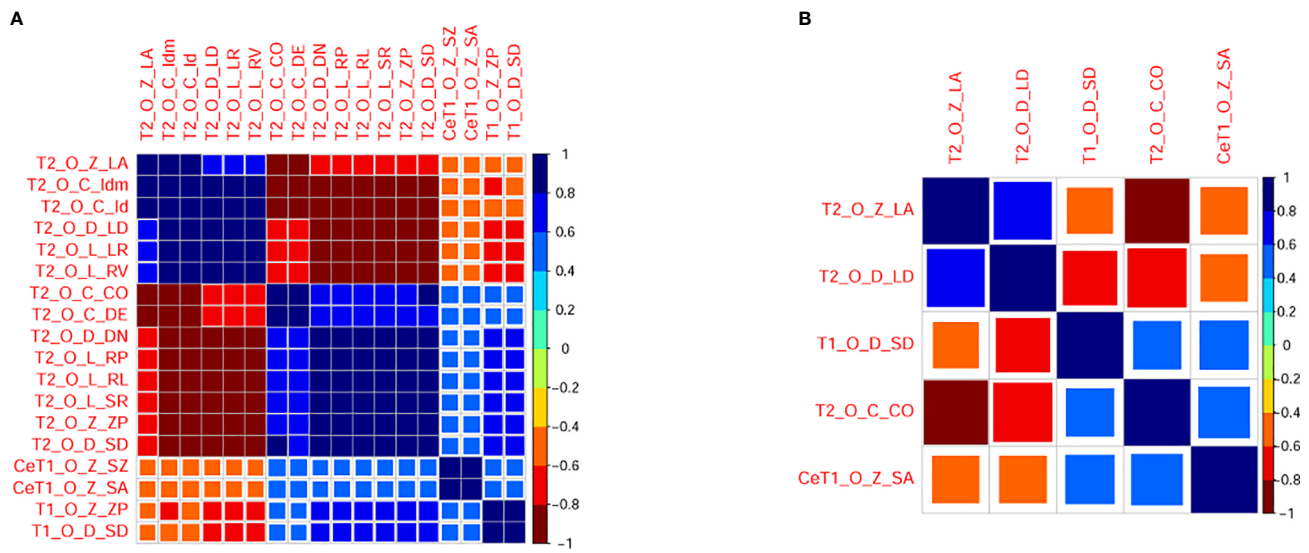

FIGURE 6 | Correlogram illustrating correlations between radiomic features before **(A)** and after **(B)** eliminating redundancy. The larger the square and the darker the color is, the higher the correlation between two features. T1, T1 weighted imaging; T2, T2 weighted imaging, CeT1, contrast enhanced T1 weighted imaging, O, original; Z, GLSZM; D, GLDM; C, GLCM; L, GLRLM; ZP, ZonePercentage; SD, Small Dependence Emphasis; CO, Contrast; DE, Difference Entropy; LR, Long Run Emphasis; RL, Run Length Non Uniformity Normalized; RP, Run Percentage; RV, Run Variance; SR, ShortRunEmphasis; LA, Large Area Low Gray Level Emphasis; DN, Dependence Non Uniformity Normalized; LD, Large Dependence Emphasis; SZ, Size Zone Non Uniformity Normalized; SA, Small Area Emphasis.

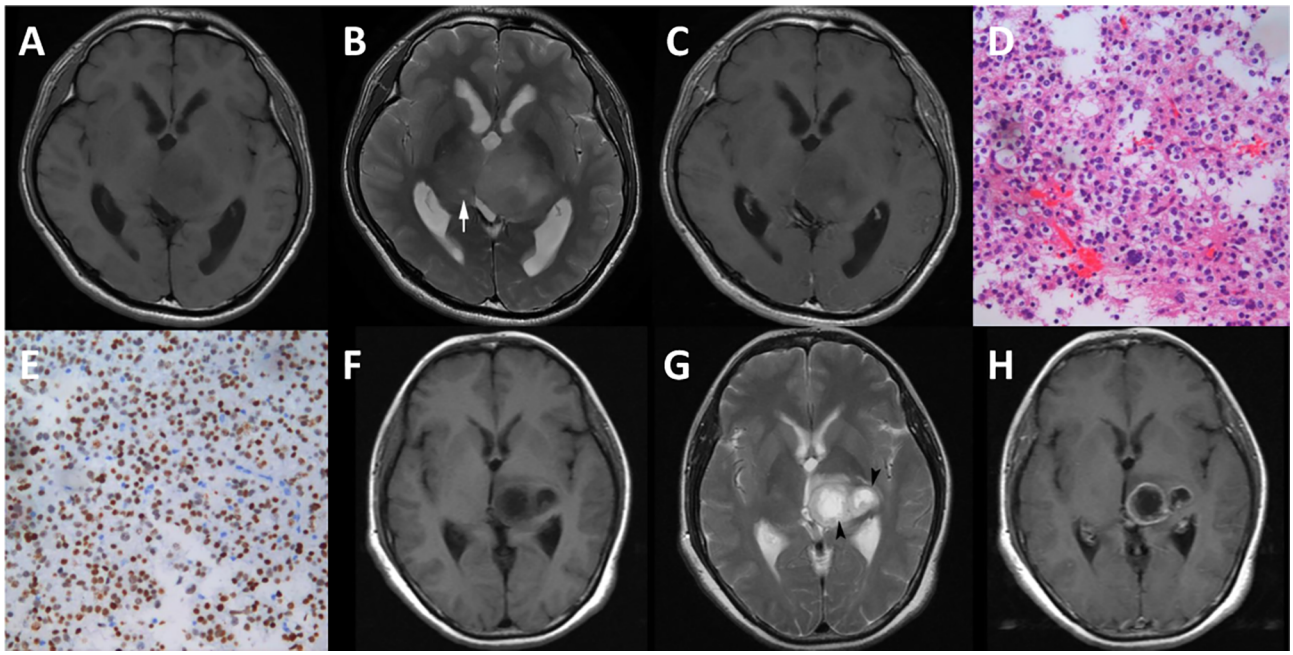

FIGURE 7 | Cases of diffuse midline gliomas. **(A–E)**, a case of diffuse midline gliomas with the H3 K27M mutation. **(F–H)**, a case of diffuse midline gliomas with the H3 K27M wild. **(A, F)**, T1 weighted imaging. **(B, G)**, T2 weighted imaging. **(C, H)**, contrast enhanced T1 weighted imaging. **(D)**, hematoxylin-eosin staining (×20). **(E)**, immunohistological staining (×20) shows H3 K27M positive. cyst formation (white arrow), necrosis (black arrow head).

(HR=1.292, p=0.740), larger value of T2W_original_glszm_LargeAreaLowGrayLevelEmphasis (HR=58.848, p=0.277), T2W_original_gldm_LargeDependenceEmphasis (HR=1.181, p=0.105) tended to have a poor OS, while males (HR=0.342, p= 0.168), larger value of T1W_original_gldm_SmallDependenceEmphasis (HR=0.141, 0.685), T2W_original_glcm_Contrast (HR=0.980, p= 0.294) and CeT1W_original_glszm_SmallAreaEmphasis (HR=0.256, p= 0.840) tended to have a good outcome. However, none of these variables were significantly associated with OS.

DISCUSSION

Identifying DMG-M is critical for treatment decision making, prognosis evaluation. In this study, we explored the MRI characteristics of DMG-Ms using radiomics. Our results showed that although it shared similar characteristics with DMG-W tumors, cyst formation might be a useful MRI characteristic of DMG-M.

Using radiomic analysis, we found that there was an obvious overlap of main principal components in all radiomic features, shape features, and T1WI, T2WI, and CeT1WI features for DMG-M and DMG-W tumors. This indicated that the imaging characteristics of the two types of tumors were similar, and that it may be challenging to differentiate between them.

A previous study used 13 visually accessible features such as size, contrast enhancement pattern, edema, and infiltrative patterns, and found that there was no significant difference in imaging characteristics between DMG-M and DMG-W tumors (8). In fact, even using functional MRI techniques, the authors found no differences in ADC histogram parameters between DGM-M and DGM-W tumors (29). These findings support our PCA results. Therefore, the radiomics-based PCA method may be highly beneficial for initially exploring the overview of imaging characteristics of diseases.

Interestingly, some thalamic DMG tumors showed distinct principal components, indicating that DMG tumors in different locations may have different characteristics, and thus further investigations on DMG tumors according to specific locations may be valuable.

The feature selection results in our study showed that only a few texture features from T2WI were useful for differentiating DMG-M and DMG-W tumors. Similarly, a previous study showed that a gradient boosting classifier, which was built using radiomic features from T2W fluid-attenuated inversion recovery images (FLAIR) was highly efficient in predicting DMG-M (2). However, the specific features selected in our study were different from those of the previous study. Algorithmic differences for feature selection in the two studies may have contributed to these differences. Another reason for differences in feature selection may be attributed to differences between T2WI and FLAIR. Because the range of gliomas may be mismatched on T2WI and FLAIR images, especially for high-grade gliomas (30), the radiomic features derived from the two sequences may be different. It has been reported that DMG-M is a distinct subtype of isocitrate dehydrogenase (IDH) wild-type

glioma (31), and that the co-deletion of IDH and 1p/19q are related to T2-FLAIR mismatch (30, 32, 33). Accordingly, we speculate that stratification analysis according to molecular status (such as the presence of an IDH mutant) or T2-FLAIR mismatch may be useful for distinguishing DMG-M and DMG-W tumors, and this therefore warrants further investigation.

We found that among the four visually accessible features, only cyst formation presented significant differences between DMG-M and DMG-W tumors. This was not the first time for cyst formation to be scrutinized. In a previous study, cyst formation was the only feature selected among 13 radiomic and 11 visually accessible features for the identification of high-risk atypical meningiomas (34). Another previous study (8) showed that although there was no significant difference in the cystic component or necrosis between DMG-M and DMG-W tumors, there was a higher ratio of cystic components or necrosis of DMG-M (62.5%) compared to DMG-M (33.3%). Cyst formation is a common feature of gliomas, which may be caused by leakage or secretion of fluid in certain low-grade gliomas (35). Although the mechanism of cyst formation is unclear for diffuse midline gliomas, cyst formation may lead to heterogeneity of the tumor (30). However, our study showed that there was no significant difference in symptom time between the two groups of patients with and without cyst formation, yet cystic formation was not significantly associated with overall survival. This suggests that cyst formation may act as a diagnostic biomarker that is not related to disease course.

This study explored the MR imaging characteristics of DMG-M and found a visually accessible feature that might be useful for identifying this type of tumor. The analysis of a large number of radiomic features using the PCA method and multiple feature selection method provided an overview of the characteristics of the tumor, and may guide us in the selection of special visually accessible features. It may narrow the range of visually accessible features and improved the efficiency of feature selection.

Our study has some limitations. First, the number of subjects included in this study was small, and the ratio of diffuse midline gliomas with the H3 K27M mutation type and those that were wild type might not be representative of the general population. Second, the MR scanning parameters were not the same. Although we performed several preprocessing steps for the images, there might still exist some potential effects on radiomic features. Third, only the original radiomic features and four visually accessible features were used in this study, and more features of the tumor could be explored in the future. Fourth, the follow-up time was short, and our study showed that there was no significant difference in OS between DMG-M and DMG-W tumors. Although previous work has also reported similar results (31), further validation of our results with a large patient cohort is needed.

In conclusion, by using radiomics, our study showed that DMG-M and DMG-W tumors share similar characteristics; however, T2WI and cyst formation may provide useful MR sequences and imaging biomarkers, respectively, for identifying DMG-M tumors.

DATA AVAILABILITY STATEMENT

The raw data supporting the conclusions of this article will be made available by the authors, without undue reservation.

ETHICS STATEMENT

The studies involving human participants were reviewed and approved by the ethics committee of the Second Affiliated Hospital of Zhejiang University. Written informed consent from the participants' legal guardian/next of kin was not required to participate in this study in accordance with the national legislation and the institutional requirements.

AUTHOR CONTRIBUTIONS

Concept and design: BJ and MZ. Data acquisition: QL and FD. Data analysis and interpretation: QL and FD. Manuscript drafting: FD. Manuscript editing and revising: QL and MZ. Statistical analysis: FD. Administrative and technical support: BJ and MZ. Supervision: MZ. All authors contributed to the article and approved the submitted version.

SUPPLEMENTARY MATERIAL

The Supplementary Material for this article can be found online at: https://www.frontiersin.org/articles/10.3389/fonc.2021.646267/full#supplementary-material

REFERENCES

1. Huang RY, Guenette JP. Non-Invasive Diagnosis of H3 K27M Mutant Midline Glioma. *Neuro Oncol* (2020) 22(3):309–10. doi: 10.1093/neuonc/noz240
2. Su X, Chen N, Sun H, Liu Y, Yang X, Wang W, et al. Automated Machine Learning Based on Radiomics Features Predicts H3 K27M Mutation in Midline Gliomas of the Brain. *Neuro Oncol* (2020) 22(3):393–401. doi: 10.1093/neuonc/noz184
3. Louis DN, Giannini C, Capper D, Paulus W, Figarella-Branger D, Lopes MB, et al. cIMPACT-NOW Update 2: Diagnostic Clarifications for Diffuse Midline Glioma, H3 K27M-Mutant and Diffuse Astrocytoma/Anaplastic Astrocytoma, IDH-Mutant. *Acta Neuropathol* (2018) 135(4):639–42. doi: 10.1007/s00401-018-1826-y
4. Qiu T, Chanchotisatien A, Qin Z, Wu J, Du Z, Zhang X, et al. Imaging Characteristics of Adult H3 K27M-Mutant Gliomas. *J Neurosurg* (2019), 1–9. doi: 10.3171/2019.9.JNS191920
5. Karremann M, Gielen GH, Hoffmann M, Wiese M, Colditz N, Warmuth-Metz M, et al. Diffuse High-Grade Gliomas With H3 K27M Mutations Carry a Dismal Prognosis Independent of Tumor Location. *Neuro Oncol* (2018) 20 (1):123–31. doi: 10.1093/neuonc/nox149
6. Kleinschmidt-DeMasters BK, Mulcahy Levy JM. H3 K27M-mutant Gliomas in Adults vs. Children Share Similar Histological Features and Adverse Prognosis. *Clin Neuropathol* (2018) 37(2018):53–63. doi: 10.5414/NP301085

7. Ryall S, Krishnatry R, Arnoldo A, Buczkowicz P, Mistry M, Siddaway R, et al. Targeted Detection of Genetic Alterations Reveal the Prognostic Impact of H3K27M and MAPK Pathway Aberrations in Paediatric Thalamic Glioma. *Acta Neuropathol Commun* (2016) 4(1):93. doi: 10.1186/s40478-016-0353-0
8. Aboian MS, Solomon DA, Felton E, Mabray MC, Villanueva-Meyer JE, Mueller S, et al. Imaging Characteristics of Pediatric Diffuse Midline Gliomas With Histone H3 K27M Mutation. *AJNR Am J Neuroradiol* (2017) 38(4):795–800. doi: 10.3174/ajnr.A5076
9. Gillies RJ, Kinahan PE, Hricak H. Radiomics: Images are More Than Pictures, They Are Data. *Radiology* (2016) 278(2):563–77. doi: 10.1148/radiol.2015151169
10. Gardin I, Gregoire V, Gibon D, Kirisli H, Pasquier D, Thariat J, et al. Radiomics: Principles and Radiotherapy Applications. *Crit Rev Oncol Hematol* (2019) 138:44–50. doi: 10.1016/j.critrevonc.2019.03.015
11. Nougaret S, Tardieu M, Vargas HA, Reinhold C, Vande Perre S, Bonanno N, et al. Ovarian Cancer: An Update on Imaging in the Era of Radiomics. *Diagn Interv Imaging* (2019) 100(10):647–55. doi: 10.1016/j.diii.2018.11.007
12. Zeng Q, Dong F, Shi F, Ling C, Jiang B, Zhang J. Apparent Diffusion Coefficient Maps Obtained From High B Value Diffusion-Weighted Imaging in the Preoperative Evaluation of Gliomas at 3T: Comparison With Standard B Value Diffusion-Weighted Imaging. *Eur Radiol* (2017) 27 (12):5309–15. doi: 10.1007/s00330-017-4910-0
13. Dong F, Li Q, Jiang B, Zhu X, Zeng Q, Huang P, et al. Differentiation of Supratentorial Single Brain Metastasis and Glioblastoma by Using Peri-Enhancing Oedema Region-Derived Radiomic Features and Multiple Classifiers. *Eur Radiol* (2020) 30(5):3015–22. doi: 10.1007/s00330-019-06460-w
14. Bologna M, Corino V, Calareso G, Tenconi C, Alfieri S, Iacovelli NA, et al. Baseline MRI-Radiomics can Predict Overall Survival in Non-Endemic Ebv-Related Nasopharyngeal Carcinoma Patients. *Cancers (Basel)* (2020) 12(10). doi: 10.3390/cancers12102958
15. Wang J, Zheng X, Zhang J, Xue H, Wang L, Jing R, et al. An MRI-based Radiomics Signature as a Pretreatment Noninvasive Predictor of Overall Survival and Chemotherapeutic Benefits in Lower-Grade Gliomas. *Eur Radiol* (2021) 31(4):1785–94. doi: 10.1007/s00330-020-07581-3
16. Kim M, Jung SY, Park JE, Jo Y, Park SY, Nam SJ, et al. Diffusion- and Perfusion-Weighted MRI Radiomics Model may Predict Isocitrate Dehydrogenase (IDH) Mutation and Tumor Aggressiveness in Diffuse Lower Grade Glioma. *Eur Radiol* (2020) 30(4):2142–51. doi: 10.1007/s00330-019-06548-3
17. Davatzikos C, Rathore S, Bakas S, Pati S, Bergman M, Kalarot R, et al. Cancer Imaging Phenomics Toolkit: Quantitative Imaging Analytics for Precision Diagnostics and Predictive Modeling of Clinical Outcome. *J Med Imaging (Bellingham)* (2018) 5(1):11018. doi: 10.1117/1.JMI.5.1.011018
18. Pati S, Singh A, Rathore S, Gastounioti A, Bergman M, Ngo P, et al. The Cancer Imaging Phenomics Toolkit (Captk): Technical Overview. *Brainlesion* (2020) 11993:380–94. doi: 10.1007/978-3-030-46643-5_38
19. Zwanenburg A, Vallieres M, Abdalah MA, Aerts H, Andrearczyk V, Apte A, et al. The Image Biomarker Standardization Initiative: Standardized Quantitative Radiomics for High-Throughput Image-Based Phenotyping. *Radiology* (2020) 295(2):328–38. doi: 10.1148/radiol.2020191145
20. Yuan M, Zhang YD, Pu XH, Zhong Y, Li H, Wu JF, et al. Comparison of a Radiomic Biomarker With Volumetric Analysis for Decoding Tumour Phenotypes of Lung Adenocarcinoma With Different Disease-Specific Survival. *Eur Radiol* (2017) 27(11):4857–65. doi: 10.1007/s00330-017-4855-3
21. Xie H, Ma S, Wang X, Zhang X. Noncontrast Computer Tomography-Based Radiomics Model for Predicting Intracerebral Hemorrhage Expansion: Preliminary Findings and Comparison With Conventional Radiological Model. *Eur Radiol* (2020) 30(1):87–98. doi: 10.1007/s00330-019-06378-3
22. Kim D, Kim SK. Comparing Patterns of Component Loadings: Principal Component Analysis (PCA) Versus Independent Component Analysis (ICA) in Analyzing Multivariate non-Normal Data. *Behav Res Methods* (2012) 44 (4):1239–43. doi: 10.3758/s13428-012-0193-1
23. Oikonomou EK, Williams MC, Kotanidis CP, Desai MY, Marwan M, Antonopoulos AS, et al. A Novel Machine Learning-Derived Radiotranscriptomic Signature of Perivascular Fat Improves Cardiac Risk Prediction Using Coronary CT Angiography. *Eur Heart J* (2019) 40(43):3529–43. doi: 10.1093/eurheartj/ehz592
24. Liu Z, Li M, Zuo C, Yang Z, Yang X, Ren S, et al. Radiomics Model of Dual-Time 2-[(18)F]FDG PET/CT Imaging to Distinguish Between Pancreatic Ductal Adenocarcinoma and Autoimmune Pancreatitis. *Eur Radiol* (2021). doi: 10.1007/s00330-021-07778-0
25. Ho IMK, Cheong KY, Weldon A. Predicting Student Satisfaction of Emergency Remote Learning in Higher Education During COVID-19 Using Machine Learning Techniques. *PloS One* (2021) 16(4):e0249423. doi: 10.1371/journal.pone.0249423
26. Yoo JE. Timss 2011 Student and Teacher Predictors for Mathematics Achievement Explored and Identified Via Elastic Net. *Front Psychol* (2018) 9:317. doi: 10.3389/fpsyg.2018.00317
27. Wu W, Ye J, Wang Q, Luo J, Xu S. Ct-Based Radiomics Signature for the Preoperative Discrimination Between Head and Neck Squamous Cell Carcinoma Grades. *Front Oncol* (2019) 9:821. doi: 10.3389/fonc.2019.00821
28. Fang S, Fan Z, Sun Z, Li Y, Liu X, Liang Y, et al. Radiomics Features Predict Telomerase Reverse Transcriptase Promoter Mutations in World Health Organization Grade II Gliomas Via a Machine-Learning Approach. *Front Oncol* (2020) 10:606741. doi: 10.3389/fonc.2020.606741
29. Aboian MS, Tong E, Solomon DA, Kline C, Gautam A, Vardapetyan A, et al. Diffusion Characteristics of Pediatric Diffuse Midline Gliomas With Histone H3-K27m Mutation Using Apparent Diffusion Coefficient Histogram Analysis. *AJNR Am J Neuroradiol* (2019) 40(11):1804–10. doi: 10.3174/ajnr.A6302
30. Throckmorton P, Graber JJ. T2-FLAIR Mismatch in Isocitrate Dehydrogenase Mutant Astrocytomas: Variability and Evolution. *Neurology* (2020) 95(11): e1582–e9. doi: 10.1212/WNL.0000000000010324
31. Meyronet D, Esteban-Mader M, Bonnet C, Joly MO, Uro-Coste E, Amiel-Benouaich A, et al. Characteristics of H3 K27M-Mutant Gliomas in Adults. *Neuro Oncol* (2017) 19(8):1127–34. doi: 10.1093/neuonc/now274
32. Kapsalaki EZ, Brotis AG, Tsikrika A, Tzerefos C, Paschalis T, Dardiotis E, et al. The Role of the T2-FLAIR Mismatch Sign as an Imaging Marker of IDH Status in a Mixed Population of Low- and High-Grade Gliomas. *Brain Sci* (2020) 10(11). doi: 10.3390/brainsci10110874
33. Broen MPG, Smits M, Wijnenga MMJ, Dubbink HJ, Anten M, Schijns O, et al. The T2-FLAIR Mismatch Sign as an Imaging Marker for non-Enhancing IDH-mutant, 1p/19q-Intact Lower-Grade Glioma: A Validation Study. *Neuro Oncol* (2018) 20(10):1393–9. doi: 10.1093/neuonc/noy048
34. Kalasauskas D, Kronfeld A, Renovanz M, Kurz E, Leukel P, Krenzlin H, et al. Identification of High-Risk Atypical Meningiomas According to Semantic and Radiomic Features. *Cancers (Basel)* (2020) 12(10). doi: 10.3390/cancers12102942
35. Smirniotopoulos JG, Murphy FM, Rushing EJ, Rees JH, Schroeder JW. Patterns of Contrast Enhancement in the Brain and Meninges. *Radiographics* (2007) 27(2):525–51. doi: 10.1148/rg.272065155

Conflict of Interest: The authors declare that the research was conducted in the absence of any commercial or financial relationships that could be construed as a potential conflict of interest.

frontiers in Oncology

ORIGINAL RESEARCH
published: 31 May 2021
doi: 10.3389/fonc.2021.663451

Multiparametric MRI Features Predict the SYP Gene Expression in Low-Grade Glioma Patients: A Machine Learning-Based Radiomics Analysis

Zheng Xiao[1], Shun Yao[2,3], Zong-ming Wang[2], Di-min Zhu[2], Ya-nan Bie[4], Shi-zhong Zhang[1]* and Wen-li Chen[2]**

[1] Department of Neurosurgery, Zhujiang Hospital, Southern Medical University, Guangzhou, China, [2] Center for Pituitary Tumor Surgery, Department of Neurosurgery, The First Affiliated Hospital of Sun Yat-sen University, Guangzhou, China, [3] Center for Skull Base Surgery, Department of Neurosurgery, Brigham and Women's Hospital, Harvard Medical School, Boston, MA, United States, [4] School of Life Sciences and Biopharmaceutics, Guangdong Pharmaceutical University, Guangzhou, China

Purpose: Synaptophysin (SYP) gene expression levels correlate with the survival rate of glioma patients. This study aimed to explore the feasibility of applying a multiparametric magnetic resonance imaging (MRI) radiomics model composed of a convolutional neural network to predict the SYP gene expression in patients with glioma.

Method: Using the TCGA database, we examined 614 patients diagnosed with glioma. First, the relationship between the SYP gene expression level and outcome of survival rate was investigated using partial correlation analysis. Then, 7266 patches were extracted from each of the 108 low-grade glioma patients who had available multiparametric MRI scans, which included preoperative T1-weighted images (T1WI), T2-weighted images (T2WI), and contrast-enhanced T1WI images in the TCIA database. Finally, a radiomics features-based model was built using a convolutional neural network (ConvNet), which can perform autonomous learning classification using a ROC curve, accuracy, recall rate, sensitivity, and specificity as evaluation indicators.

Results: The expression level of SYP decreased with the increase in the tumor grade. With regard to grade II, grade III, and general patients, those with higher SYP expression levels had better survival rates. However, the SYP expression level did not show any significant association with the outcome in Level IV patients.

Conclusion: Our multiparametric MRI radiomics model constructed using ConvNet showed good performance in predicting the SYP gene expression level and prognosis in low-grade glioma patients.

Keywords: synaptophysin (SYP), MRI radiomics model, convolutional neural network, glioma, machine learning

OPEN ACCESS

Edited by:
Han Zhang,
University of North Carolina at Chapel Hill, United States

Reviewed by:
Tejpal Gupta,
Tata Memorial Hospital, India
Huaiqiang Sun,
Sichuan University, China
Ye Wu,
University of North Carolina at Chapel Hill, United States

****Correspondence:***
Wen-li Chen
chenwenli@mail.sysu.edu.cn
Shi-zhong Zhang
shizhong_zh@163.com
Ya-nan Bie
bieyanan0624@outlook.com

Specialty section:
This article was submitted to Cancer Imaging and Image-directed Interventions, a section of the journal Frontiers in Oncology

Received: *02 February 2021*
Accepted: *06 May 2021*
Published: *31 May 2021*

Citation:
Xiao Z, Yao S, Wang Z-m, Zhu D-m, Bie Y-n, Zhang S-z and Chen W-l (2021) Multiparametric MRI Features Predict the SYP Gene Expression in Low-Grade Glioma Patients: A Machine Learning-Based Radiomics Analysis. Front. Oncol. 11:663451. doi: 10.3389/fonc.2021.663451

INTRODUCTION

In 2016, the World Health Organization (WHO) updated the tumor classification in the central nervous system and precisely introduced several molecular biomarkers that were integrated into the diagnostic criteria of glioma along with conventional histopathological diagnosis, aiding the advancement of precise diagnosis in glioma (1, 2). Likewise, under the guidance of molecular typing, the precise treatment of glioma has also been considerably expanded (3). Given these significant molecular markers, detecting them early and quickly has become extremely crucial.

Synaptophysin, the most commonly expressed neural marker, exists widely in a variety of lesions of primary central nervous system neoplasms, from gliomas to the lowest differentiated primitive neuroectodermal tumors (4, 5). The higher the degree of dedifferentiation of the tumor, the higher is the malignant degree. Therefore, as the most common neural marker, it is worth exploring whether the expressive level of synaptophysin is related to the malignant degree of gliomas and the survival prognosis of patients (6, 7).

In recent years, with the dramatic expansion of medical image analysis technology, radiomics has become a promising technique to bridge the gap between universal images and histopathological or molecular signatures (8). From medical images, a large number of high-throughput imaging features, including the extraction of tumor characteristics, can be used to quickly obtain heterogeneous information about tumors in a non-invasive manner (9, 10). The radiomics model established using machine learning has a high predictive potential and has been widely used for the precise prediction of various molecular types of glioma (11–13).

In this study, we used a convolutional neural network (ConvNet) to build a radiomics model based on multiparametric magnetic resonance imaging (MRI) to predict SYP expression levels in patients with low-grade glioma. The model is aimed at facilitating the implementation of molecular diagnosis in the early preoperative stage and the individualized treatment for patients with glioma.

MATERIALS AND METHODS

Data Acquisition and Annotation

The imaging data and corresponding TCGA sequencing data of 124 patients with low-grade gliomas (WHOII, WHOIII) were downloaded from the TCIA. As the patients' private information was de-identified by the TCGA/TCIA organization and their information was made available for download by the public, we did not have to apply for the approval of the Institutional Review Board or the health organizations following the Health Insurance Portability and Accountability Act.

The image were acquired using a 3.0-T MRI (Achieva, Philips). The T1WI(TR, 2000 ms; TE, 10 ms; FOV, 240 mm; slice thickness, 5 mm; and matrix size, 256 × 256), T2WI(TR, 3000 ms; TE, 80 ms; FOV, 240 mm; slice thickness, 5 mm; and matrix size, 256 × 256), and T1WI-enhanced (TR, 6.3 ms; TE, 3.1 ms) cross-sectional images of the tumor were imported into the 3D slicer analysis software in the Nifti format (14). Two neurosurgeons with over 10 years of working experience manually outlined the region of interest (ROI) along the tumor contour under double-blind conditions. The ROI included tumor parenchyma, necrosis, and cystic area, as well as surrounding edema. After finishing the outlining, the neurosurgeons analyzed the accuracy of the ROI and adjusted it after negotiating for the parts in dispute.

Images were re-sampled by the PyRadiomics toolkit (Version2.1.0, https://github.com/Radiomics/pyradiomics) to guarantee a 1.0 mm pixels interval among images on 3 anatomical directions, eliminating inconsistent spatial resolutions' interference caused by the use of different models of MRI machine. Meanwhile, z-score normalization was applied to normalize the T1, T2, and T1E images, thereby obtaining the standard normal distribution of image intensity.

The transcriptome expression data of 614 gliomas were collected and downloaded online (http://cancergenome.nih.gov), ranging from WHO grade II to grade IV (150 GBM and 464 LGG samples). Information on age, sex, diagnosis, WHO grade, molecular data, and the patient prognosis was also collected. Patients were selected and grouped according to their median SYP expression (15, 16).

Model Establishment and Performance Evaluation

Considering the shortcomings of traditional machine learning techniques, such as insufficient performance in classifying brain tumors, high complexity of manual feature extraction, and network degradation of conventional deep learning in deep-going networks, an automatic model of classifying brain tumors based on the ResNet50 network is proposed in this paper. First, the weight parameters of the model are obtained by training the source data, and then the performance of the model is tested using the test set.

In deep learning, the main problems associated with network depth are gradient vanishing and gradient exploding. The traditional solution is to initialize and regularize the data, which deepens the depth and addresses the problem of the gradient but leads to the degradation of network performance. ResNet50 is a residual learning framework based on the existing deep network of training, which is easy to optimize and has the advantage of a small computational burden. Residuals are designed to address the problems of degradation and gradient, as a result of which the performance of the network improves. There are 49 convolutional layers and 1 fully connected layer in ResNet 50. Among them, the ID Block x2 in the second to the fifth stages represents two residual

Abbreviations: SYP, Synaptophysin; LGG, low grade glioma; MRI, Magnetic resonance imaging; TCGA, The Cancer Genome Atlas; TCIA, The Cancer Imaging Archive; ROC, Receiver Operating Characteristic; PRC, precision recall curve; ROI, region of interest; GBM, Glioblastoma multiform; ConvNet/CNN, convolutional neural network; MGMT,O-6-methylguanine-DNA methyltransferase; IDH, Isocitrate dehydrogenase; TR, Repetition time; TE, Echo time; FOV, Field of view.

blocks that do not change the dimension, and the Conv Block represents the residual block with the dimension. Each residual Block contains three convolutional layers; therefore, there are 49 convolutional layers in total, that is, $1 + 3 \times (3 + 4 + 6 + 3) = 49$ (**Figure 1**). The structure is as follows:

The size of the input data of the ResNet50 neural network is $224 \times 224 \times 3$. After the image passes through the continuous convolution operation of the residual blocks, the channels of the pixel matrix of the image become deeper and deeper. Subsequently, after passing through the Flatten layer, the size of the image pixel matrix is changed to 2048. Finally, it is input into the fully connected layer, and the corresponding category probability is output through the SoftMax layer. The ResNet50 structure contains cross-layer connections, which pass the input across layers through shortcuts, and then adds the output after convolution to fully train the underlying network. As a result, the accuracy is significantly improved with the increase in depth (**Figure 2**). The structure of the residual block of the ResNet is as follows:

The shortcut connection, as seen in the figure above, has a function equivalent to performing equivalent mapping directly. However, this operation does not add any additional parameters, nor does it lead to computational complexity. Therefore, the model is reduced to a shallow network to a certain extent. To avoid this, the identical mapping function $H(x) = x$ must be learned, but directly fitting such a function is challenging. Let us suppose that the output of the residual network is $H(x)$ and the output after the convolution operation is $F(x)$, $H(x) = F(x) + x$. For $F(x) = (\omega 3\delta(\omega 2\delta(\omega 1x)))$, where ω refers to the convolution operation and δ represents the activation function. Therefore, if $F(x) = 0$, the aforementioned

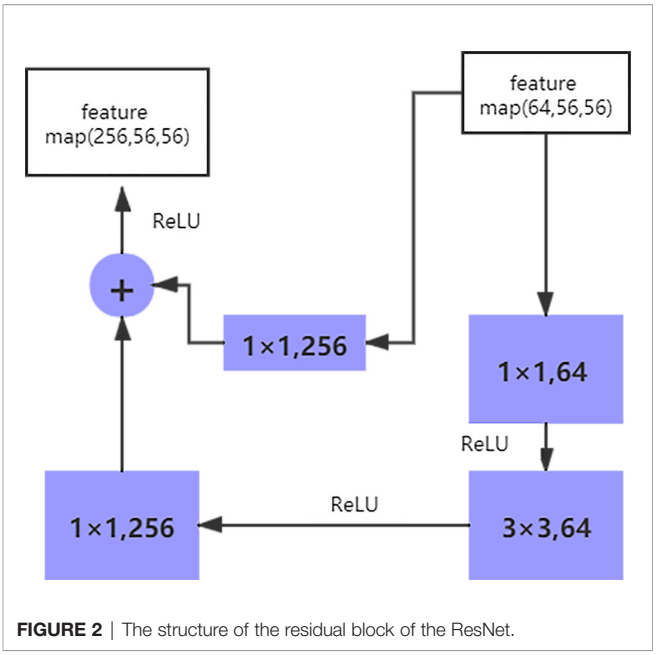

FIGURE 2 | The structure of the residual block of the ResNet.

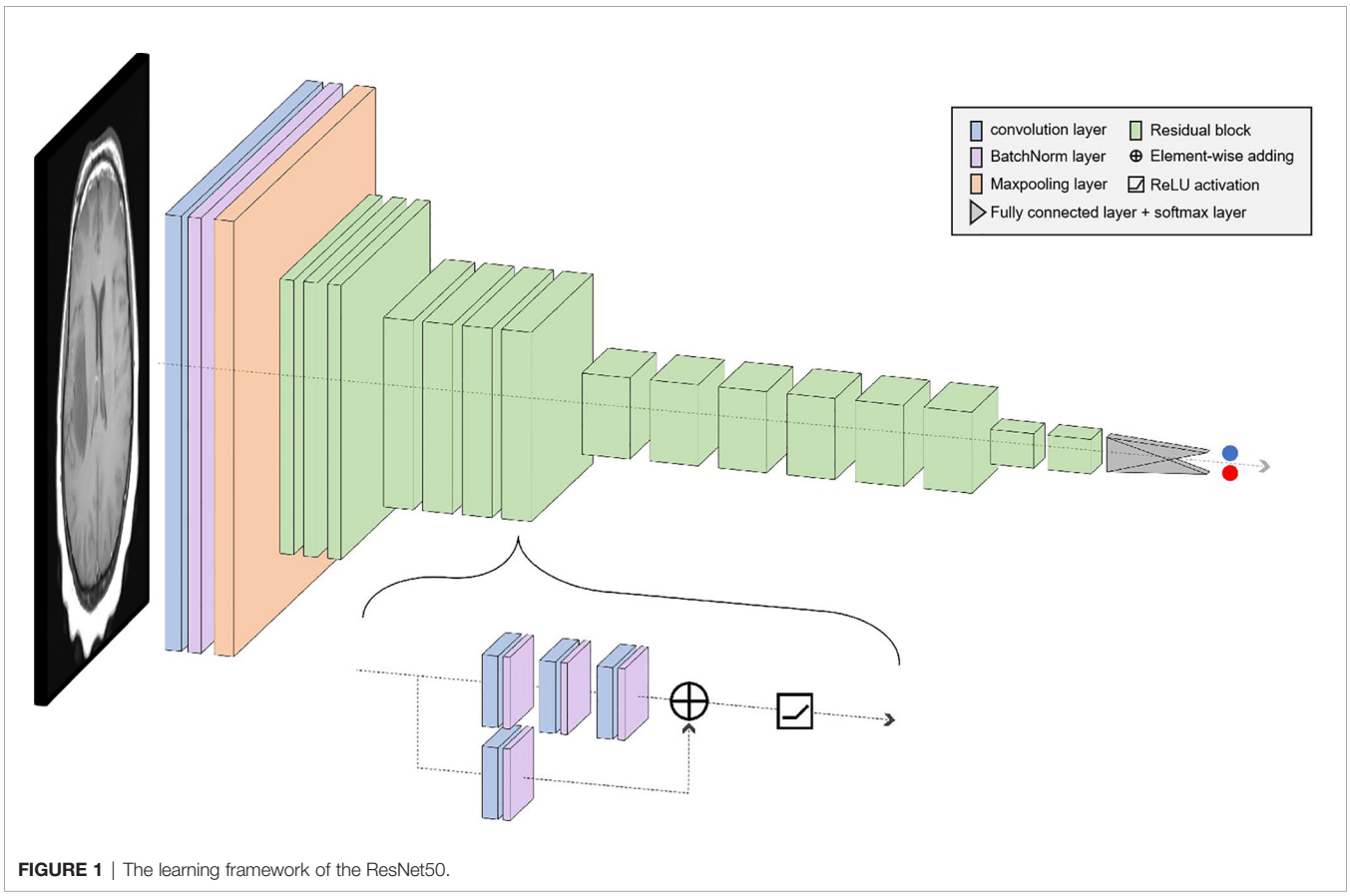

FIGURE 1 | The learning framework of the ResNet50.

identical mapping function H(x) = x can be easily obtained, and the problem that needs to be addressed is learning an easily fitted residual function F(x) = H(x) - x.

Model Development

Pytorch framework was used for model development. In the implementation of our model, an open-source repository is used (available at https://pytorch.org/). During training, we use ADAM as the optimizer, which is initialized with the learning rate of 1e-4. In the analyses of the results, we use the CAM technique implemented in an open-source repository (https://github.com/yizt/Grad-CAM.pytorch). The data were divided into a training set and a test set in a ratio of 8:2. ResNet50 was used as the classifier, and the original images were directly inputted into the network to achieve end-to-end prediction. While training the model, we divided the data set into five parts (No.1–No.5) and trained five models at the same time. No. 1 was considered as the test set for the first model, and the others were considered as the training set; No. 2 was considered as the test set for the second model, and the others were considered as the training set, and the rest were done in the same manner. In the evaluation phase, we recorded the performance of the model on the classification task of high and low expression of SYP. Taking high expression of SYP as a positive event, we obtained TP, TN, FP, and FN based on the confusion matrix and the following indicators were calculated. Sensitivity = TP/(TP + FN), Specificity = TN/(FP + TN), Positive predictive value = TP/(TP + FP), Negative predictive value = TN/(TN + FN), Accuracy = (TN + TP) /(TN + FP + FN +TP).

Statistical Analyses

JMP 10.0 software (SAS Institute Inc., Cary, NC, USA) was used to conduct the statistical analyses. Comparison between groups was conducted using the chi-square test, Fisher's exact test, or binomial distribution test for categorical variables, while the independent t-test for continuous variables. The Kaplan–Meier estimate and Cox proportional-hazards regression model were used for the survival analysis. The P value less than 0.05 is deemed as statistically significant.

RESULTS

Clinical Significance of SYP

After analyzing the sequencing data of 614 cases from TCGA, we found the expression level of SYP in the glioma to be correlated with the tumor grade and the survival rate of the patient, and that the expression level of SYP decreased with an increase in tumor grade (**Figure 3A**). In glioma patients, particularly in grade II and grade III patients, the higher the expression level of SYP, the better was the survival rate of the patient (**Figures 3B–D**). In grade IV patients, the expression level of SYP was not associated with the survival rate (**Figure 3E**). It is suggested that SYP can be a molecular index to judge the tumor grade and predict prognosis, especially for low-grade gliomas.

Molecular Markers and SYP

At the same time, we verified the expression levels and status of well-known molecular markers including MGMT promoter methylation, IDH1 mutant, and co-deletion of 1p19q in low-grade glioma patients (WHOII, WHOIII) between high and low expression of SYP (**Supplementary Figures S1A–C**). A total of 288 patients had co-deletion of 1p19q, and the expression level of SYP was 11.7 ± 0.068; 169 patients had no co-deletion of 1p19q and the expression level of SYP was 10.93 ± 0.0886, $p < 0.0001$. It prompted that the expression level of SYP in the patients with common deletion of 1p19q was higher (**Supplementary Figure S1C**). Among the patients of the WHOII level, 160 patients had MGMT promoter methylation, and the expression level of SYP was 11.82 ± 0.0915; 31 patients had no MGMT promoter methylation, and the expression level of SYP was 11.48 ± 0.2512, $p = 0.15$. There was no significant difference between the two. It was shown that the expression level of SYP was higher in patients with MGMT promoter methylation. Among the patients of the WHOIII level, 195 patients had MGMT promoter methylation, and the expression level of SYP was 11.32 ± 0.0659; 49 patients had no MGMT promoter methylation, and the expression level of SYP was 10.68 ± 0.2058, $p = 0.006$. Among patients with WHOIII gliomas, it was shown that the expression level of SYP was higher in patients with MGMT promoter methylation (**Supplementary Figure S1A**). Among the patients of the WHOII level, the IDH genes of 19 patients were of the wild type and the expression level of SYP was 11.91 ± 0.399; the IDH genes of 198 patients were mutant and the expression level of SYP was 11.67 ± 0.082, $p = 0.46$. There was no significant difference between the two. Among the patients of the WHOIII level, the IDH genes of 67 patients were of the wild type and the expression level of SYP was 10.47 ± 0.169; the IDH genes of 177 patients were mutant and the expression level of SYP was 11.46 ± 0.715, $P< 0.0001$. It was shown that the expression level of SYP was higher in patients with mutant IDH genes (**Supplementary Figure S1B**). In order to make clear the influence of related genes on prognosis, we performed a regression analysis of a single factor and multi-factors (**Figure 4**) (**Supplementary Figures S1D, E**).

Analysis of Predictive Results of a Neural Network Model

Based on the good predictive performance of the SYP gene in low-grade gliomas, preoperative MRI data of 124 patients with WHO grades II and III were downloaded from the TCGA database. Among them, 4 patients who lacked sequencing results and 12 patients who lacked complete T1, T2, and T1 enhanced phase sequences were excluded. A total of 108 patients were selected and grouped according to their the previous median SYP expression. There were 48 cases with high SYP expression and 60 cases with low SYP expression. There was no significant difference in sex and age between the group with high expression of SYP and the group with low expression of SYP.

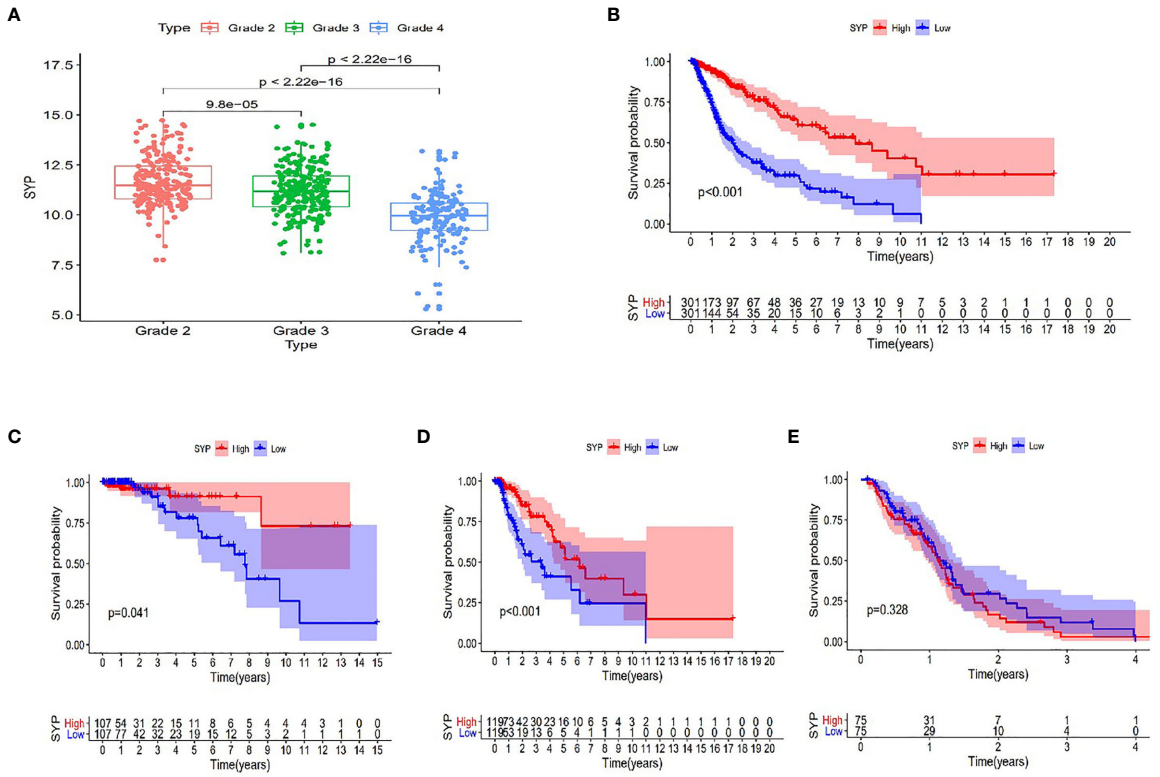

FIGURE 3 | Expression of SYP genes in different grades of gliomas and their relationship with the survival rate of patients. **(A)** Expression level of SYP genes is significantly correlated with the grade of gliomas. **(B–E)** In terms of patients with grade II, III and the overall, the higher the level of SYP expression, the higher the survival rate of patients, while in terms of patients with grade IV, the level of SYP expression is not related to prognosis.

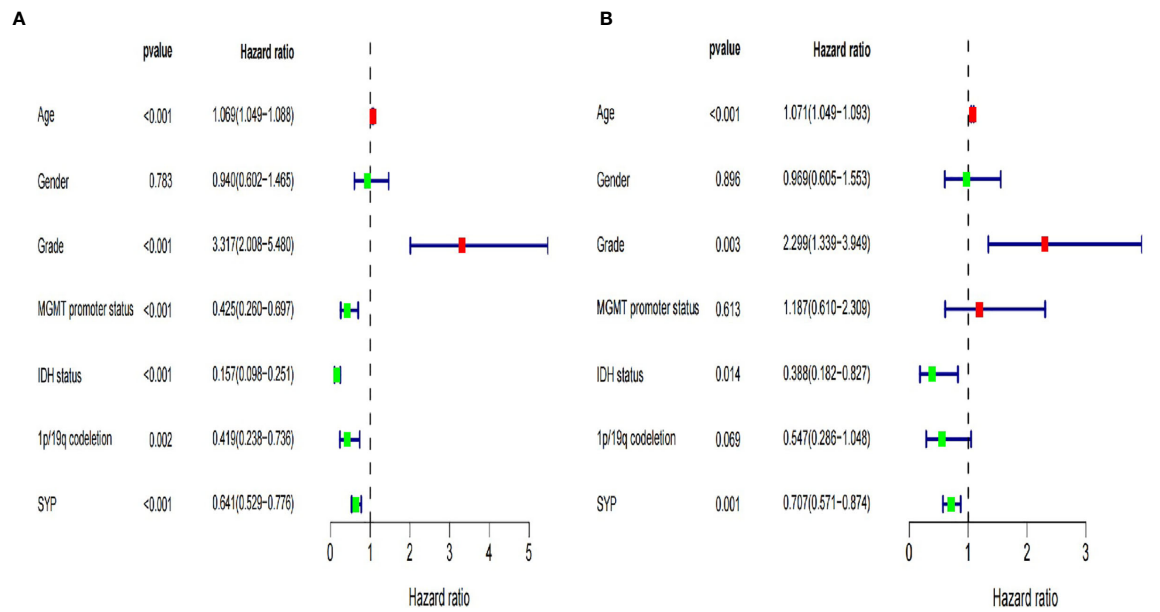

FIGURE 4 | Forest map of clinical characters in univariate **(A)** and multivariate analysis **(B)**. The coordinate of the blue diamond represents the odds ratio. Univariate and multivariate Cox regression analysis were performed. Subgroup with a value of $p < 0.05$ was considered statistically significant.

MRI images were classified according to median SPY values. Those greater than the median were considered positive, and those lower than the median as negative. After picking out the images with tumor regions and classifying them by cross-section, 3822 positive patches and 3444 negative patches were obtained (**Figure 5**). The model trained 250 rounds in total. The ROC curve, accuracy, positive predictive value, negative predictive value, sensitivity, and specificity were used as evaluation indexes. For the prediction model in the test group, the ROC curve area = 0.98 (**Figure 6A**), accuracy = 0.93, sensitivity = 90.34%, specificity = 95.44%, positive predictive value = 95.62%, and negative predictive value = 89.96% (**Figure 6B**).

DISCUSSION

Glioma, a type of malignant tumor originating from neuroglial cells, is one of the most common primary intracranial tumors (17). Grade II and III gliomas are regarded as low-grade gliomas that are well-differentiated, slow-growing, and biologically less invasive (18). However, they usually show significantly different clinical manifestations, recurrence rates, and prognosis (19). According to previous studies, patient age (>40 years), tumor resection, and tumor histology classification are important predictors of poor prognosis in low-grade gliomas (20–23). Nevertheless, Daniel J Brat used the TCGA database to divide

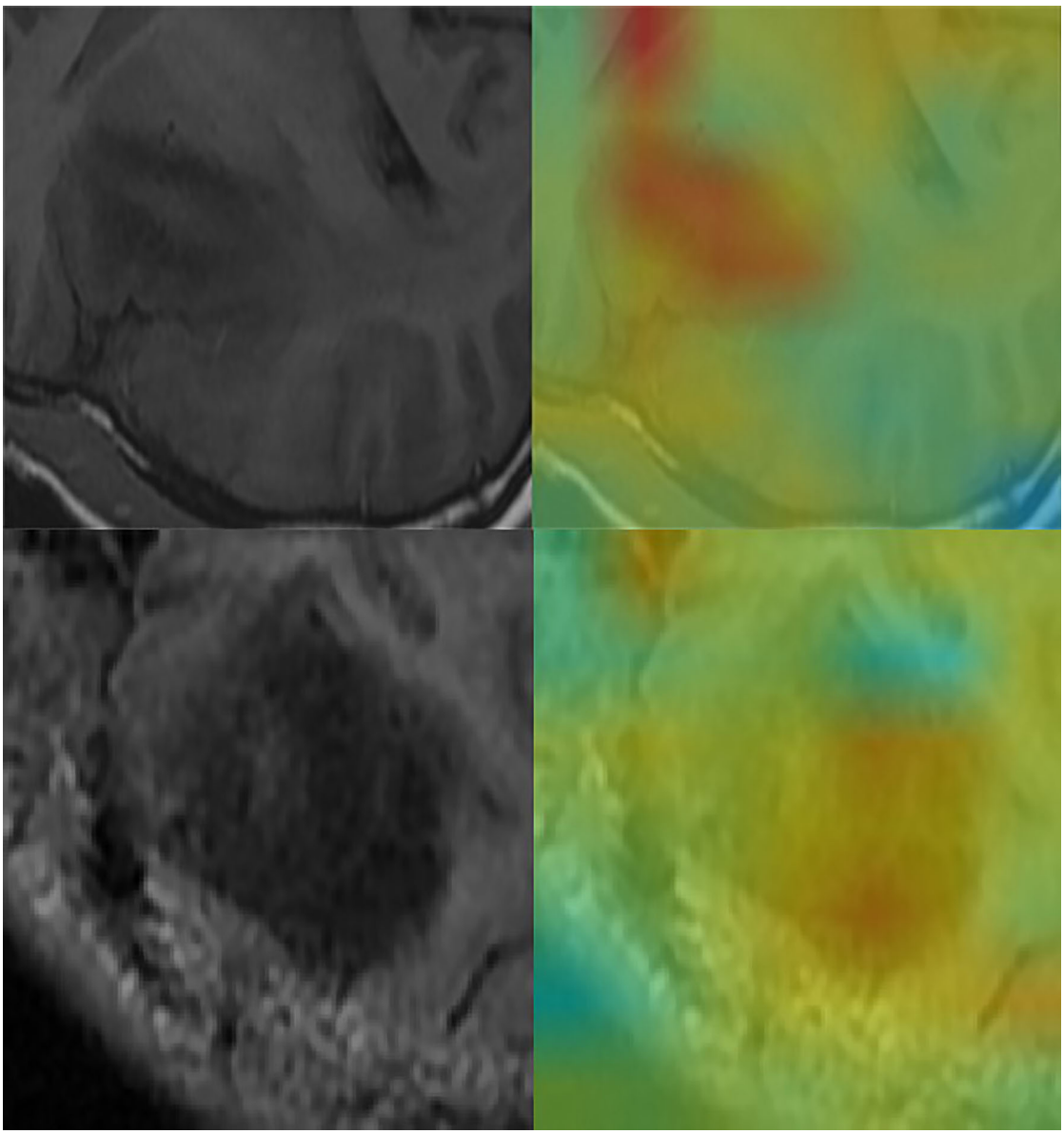

FIGURE 5 | Convolutional neural network for the extraction of image features. Through the automatic extraction of image features by class activation mapping (CAM), the areas marked red in the image are the ones with high activation response to the visualized image.

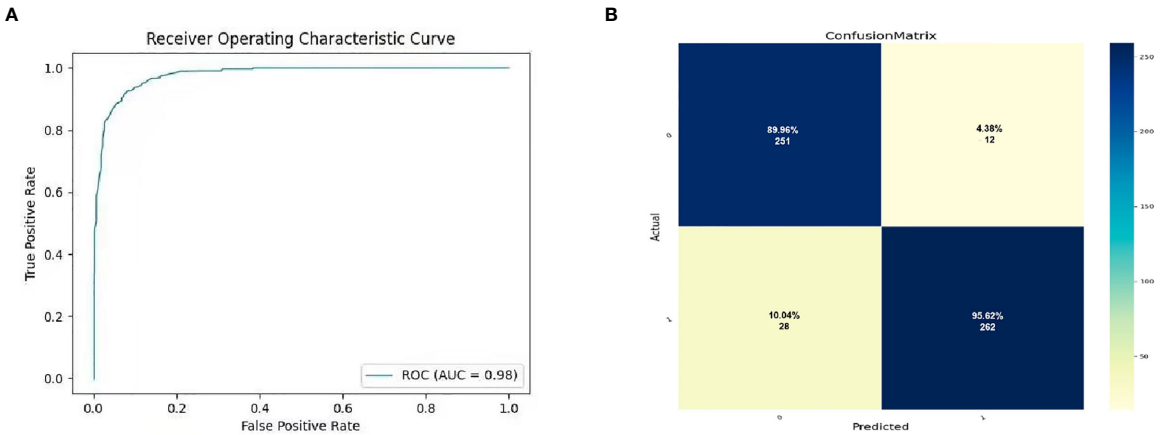

FIGURE 6 | The prediction potential of convolutional neural network for the expression level of SYP genes. **(A)** Evaluation of radiomics model constructed by convolutional neural network through ROC. **(B)** Confusion matrix of the radiomics model. The upper left is true negative, the lower left is false negative, the upper right is false positive, and the lower right is true positive.

LGGs into three categories based on isocitrate dehydrogenase mutation and 1p/19q gene deletion state in 2015 (2), including neuroglioma with IDH mutation and 1p/19q gene deletion, neuroglioma with IDH mutation, and without 1p/19q gene deletion, and neuroglioma with wild-type IDH. Furthermore, it was found that the new classification scheme could be more precise in reflecting the biological characteristics of LGGs, instructing patient treatment, and predicting prognostic status than the traditional classification (24); therefore, the significance of molecular biomarkers has attracted widespread attention (1).

In accordance with clinical work, synaptophysin (SYP) can be used as a predictor of disease progression and clinical prognosis of gliomas, especially low-grade gliomas (7). Unlike the malignant progression of glioblastoma, there is a great heterogeneity in the prognosis of patients with low-grade gliomas, ranging from one or two years to more than ten years. Therefore, it is highly significant to make a personalized and accurate prediction of the prognosis of patients with low-grade gliomas. The expression results of SYP, which is a common index for the pathological diagnosis of glioma, are easy to obtain. Further, it is simple, rapid, and highly effective for evaluation of prognosis of patients.

However, traditional CT and MR imaging techniques cannot be applied to the molecular diagnosis of gliomas, and the rise of imaging technology makes the connection between machine learning and molecular diagnosis possible (25). This study adds ConvNet technology to the traditional machine learning method. Consequently, the considerable improvement in image processing enables automated feature extraction, filters characteristics free from manual design, and avoids subjective results, eventually acquiring a better predictive performance. This is the core advantage of model building suggested in this study.

There are some limitations to this study. First, the input images are only tomographic MRI, which might enhance the predictive performance of the study's model further in case of segmentation in the coronal plane, sagittal plane, or other multilevel reconstruction of images. Second, the study includes relatively few cases, so the inclusion of more data to further enhance the accuracy and universality of the ConvNet model is suggested.

In conclusion, the ConvNet model built in this study is able to discern the expression level of glioma SYP impartially and effectively. In consideration of a better predictive result, the ConvNet model is groundbreaking in the development of a multi-parameter model to help enhance the individualized diagnosis and treatment of gliomas.

DATA AVAILABILITY STATEMENT

Publicly available datasets were analyzed in this study. This data can be found here: TCIA(https://www.cancerimagingarchive.net/) TCGA(http://cancergenome.nih.gov) The model is stored in the Baidu network disk: https://pan.baidu.com/s/1AmXjAQb5Oyt_9LGQiUNbTw Password.99yc.

ETHICS STATEMENT

Ethical approval was not provided for this study on human participants because the imaging data and TCGA sequencing data were downloaded from the TCIA and the TCGA. As the patients' private information were de-identified by the TCGA/TCIA organization and their information was made available for download by public, we did not have to apply for the approval of the Institutional Review Board or the health organizations following the Health Insurance Portability and Accountability Act. Written informed consent from the participants' legal guardian/next of kin was not required to participate in this

study in accordance with the national legislation and the institutional requirements.

AUTHOR CONTRIBUTIONS

Conceived and designed the experiments: ZX and W-lC. Analyzed the data: Z-mW, D-mZ, and Y-nB. Wrote the paper: ZX and Y-nB. Edited and revised the manuscript: Y-nB, S-zZ, and W-lC. Improve the model: SY. All authors contributed to the article and approved the submitted version.

FUNDING

This work was supported by Guangdong Medical Research Foundation (A2018245), Natural Science Foundation of Guangdong province (2018A0303130333), Medical Scientific Research Foundation of Guangdong Province, China (A2020449), Chinese Postdoctoral Science Foundation (2019M663271) and Guangdong Enterprise Science and Technology Commissioner Project (GDKTP2020041900).

ACKNOWLEDGEMENT

We are grateful to all participants for their contribution.

SUPPLEMENTARY MATERIAL

The Supplementary Material for this article can be found online at: https://www.frontiersin.org/articles/10.3389/fonc.2021.663451/full#supplementary-material

REFERENCES

1. Ryall S, Zapotocky M, Fukuoka K, Nobre L, Guerreiro Stucklin A, Bennett J, et al. Integrated Molecular and Clinical Analysis of 1,000 Pediatric Low-Grade Gliomas. *Cancer Cell* (2020) 37:569–83. doi: 10.1016/j.ccell.2020.03.011
2. Brat DJ, Verhaak RG, Aldape KD, Yung WK, Salama SR, Cooper LA, et al. Comprehensive, Integrative Genomic Analysis of Diffuse Lower-Grade Gliomas. *N Engl J Med* (2015) 372:2481–98. doi: 10.1056/NEJMoa1402121
3. Weller M, van den Bent M, Tonn J, Stupp R, Preusser M, Cohen-Jonathan-Moyal E, et al. European Association for Neuro-Oncology (EANO) Guideline on the Diagnosis and Treatment of Adult Astrocytic and Oligodendroglial Gliomas. *Lancet Oncol* (2017) 18:e315–29. doi: 10.1016/S1470-2045(17)30194-8
4. Rusu P, Shao C, Neuerburg A, Acikgöz A, Wu Y, Zou P, et al. GPD1 Specifically Marks Dormant Glioma Stem Cells With a Distinct Metabolic Profile. *Cell Stem Cell* (2019) 25:241–57. doi: 10.1016/j.stem.2019.06.004
5. Hill R, Kuijper S, Lindsey J, Petrie K, Schwalbe E, Barker K, et al. Combined MYC and P53 Defects Emerge at Medulloblastoma Relapse and Define Rapidly Progressive, Therapeutically Targetable Disease. *Cancer Cell* (2015) 27:72–84. doi: 10.1016/j.ccell.2014.11.002
6. Pietsch T, Schmidt R, Remke M, Korshunov A, Hovestadt V, Jones DT, et al. Prognostic Significance of Clinical, Histopathological, and Molecular Characteristics of Medulloblastomas in the Prospective HIT2000 Multicenter Clinical Trial Cohort. *Acta Neuropathol* (2014) 128:137–49. doi: 10.1007/s00401-014-1276-0
7. Rodriguez F, Perry A, Rosenblum M, Krawitz S, Cohen K, Lin D, et al. Disseminated Oligodendroglial-Like Leptomeningeal Tumor of Childhood: A Distinctive Clinicopathologic Entity. *Acta Neuropathol* (2012) 124:627–41. doi: 10.1007/s00401-012-1037-x
8. Lambin P, Leijenaar R, Deist T, Peerlings J, de Jong E, van Timmeren J, et al. Radiomics: The Bridge Between Medical Imaging and Personalized Medicine. *Nat Rev Clin Oncol* (2017) 14:749–62. doi: 10.1038/nrclinonc.2017.141
9. Verburg N, Koopman T, Yaqub M, Hoekstra O, Lammertsma A, Barkhof F, et al. Improved Detection of Diffuse Glioma Infiltration With Imaging Combinations: A Diagnostic Accuracy Study. *Neuro Oncol* (2020) 22:412–22. doi: 10.1093/neuonc/noz180
10. Molinaro A, Hervey-Jumper S, Morshed R, Young J, Han S, Chunduru P, et al. Association of Maximal Extent of Resection of Contrast-Enhanced and Non-Contrast-Enhanced Tumor With Survival Within Molecular Subgroups of Patients With Newly Diagnosed Glioblastoma. *JAMA Oncol* (2020) 6:495–503. doi: 10.1001/jamaoncol.2019.6143
11. Caudell J, Torres-Roca J, Gillies R, Enderling H, Kim S, Rishi A, et al. The Future of Personalised Radiotherapy for Head and Neck Cancer. *Lancet Oncol* (2017) 18:e266–73. doi: 10.1016/S1470-2045(17)30252-8
12. Binder Z, Thorne A, Bakas S, Wileyto E, Bilello M, Akbari H, et al. Epidermal Growth Factor Receptor Extracellular Domain Mutations in Glioblastoma Present Opportunities for Clinical Imaging and Therapeutic Development. *Cancer Cell* (2018) 34:163–77. doi: 10.1016/j.ccell.2018.06.006
13. Maros M, Capper D, Jones D, Hovestadt V, von Deimling A, Pfister SM, et al. Machine Learning Workflows to Estimate Class Probabilities for Precision Cancer Diagnostics on DNA Methylation Microarray Data. *Nat Protoc* (2020) 15:479–512. doi: 10.1038/s41596-019-0251-6
14. Norton I, Essayed W, Zhang F, Pujol S, Yarmarkovich A, Golby AJ, et al. SlicerDMRI: Open Source Diffusion MRI Software for Brain Cancer Research. *Cancer Res* (2017) 77:e101–3. doi: 10.1158/0008-5472.CAN-17-0332
15. Liu Q, Cheng R, Kong X, Wang Z, Fang Y, Wang J. Molecular and Clinical Characterization of PD-1 in Breast Cancer Using Large-Scale Transcriptome Data. *Front Immunol* (2020) 11:558757. doi: 10.3389/fimmu.2020.558757
16. Hu J, Yu A, Othmane B, Qiu D, Li H, Li C, et al. Siglec15 Shapes a non-Inflamed Tumor Microenvironment and Predicts the Molecular Subtype in Bladder Cancer. *Theranostics* (2021) 11:3089–108. doi: 10.7150/thno.53649
17. Molinaro A, Taylor J, Wiencke J, Wrensch M. Genetic and Molecular Epidemiology of Adult Diffuse Glioma. *Nat Rev Neurol* (2019) 15:405–17. doi: 10.1038/s41582-019-0220-2
18. Fangusaro J, Witt O, Hernaiz Driever P, Bag A, de Blank P, Kadom N, et al. Response Assessment in Paediatric Low-Grade Glioma: Recommendations From the Response Assessment in Pediatric Neuro-Oncology (RAPNO) Working Group. *Lancet Oncol* (2020) 21:e305–16. doi: 10.1016/S1470-2045(20)30064-4
19. Wen P, Reardon D. Neuro-Oncology in 2015: Progress in Glioma Diagnosis, Classification and Treatment. *Nat Rev Neurol* (2016) 12:69–70. doi: 10.1038/nrneurol.2015.242
20. van den Bent M, Smits M, Kros J, Chang S. Diffuse Infiltrating Oligodendroglioma and Astrocytoma. *J Clin Oncol* (2017) 35:2394–401. doi: 10.1200/JCO.2017.72.6737
21. Sturm D, Pfister S, Jones D. Pediatric Gliomas: Current Concepts on Diagnosis, Biology, and Clinical Management. *J Clin Oncol* (2017) 35:2370–7. doi: 10.1200/JCO.2017.73.0242
22. Buckner J, Giannini C, Eckel-Passow J, Lachance D, Parney I, Laack N, et al. Management of Diffuse Low-Grade Gliomas in Adults - Use of Molecular Diagnostics. *Nat Rev Neurol* (2017) 13:340–51. doi: 10.1038/nrneurol.2017.54
23. Qi S, Yu L, Li H, Ou Y, Qiu X, Ding Y, et al. Isocitrate Dehydrogenase Mutation Is Associated With Tumor Location and Magnetic Resonance Imaging Characteristics in Astrocytic Neoplasms. *Oncol Lett* (2014) 7(6):1895–02. doi: 10.3892/ol.2014.2013
24. Barthel F, Johnson K, Varn F, Moskalik A, Tanner G, Kocakavuk E, et al. Longitudinal Molecular Trajectories of Diffuse Glioma in Adults. *Nature* (2019) 576:112–20. doi: 10.1038/s41586-019-1775-1

25. Zachariah M, Oliveira-Costa J, Carter B, Stott S, Nahed B. Blood-Based Biomarkers for the Diagnosis and Monitoring of Gliomas. *Neuro Oncol* (2018) 20:1155–61. doi: 10.1093/neuonc/noy074

Conflict of Interest: The authors declare that the research was conducted in the absence of any commercial or financial relationships that could be construed as a potential conflict of interest.

frontiers in Oncology

ORIGINAL RESEARCH
published: 25 June 2021
doi: 10.3389/fonc.2021.679331

A Comparative Retrospective Study of Immunotherapy RANO *Versus* Standard RANO Criteria in Glioblastoma Patients Receiving Immune Checkpoint Inhibitor Therapy

Xin Chen[1,2†], Mary Jane Lim-Fat[3†], Lei Qin[4,5], Angie Li[1,6], Annie Bryant[4], Camden P. Bay[1], Lu Gao[1,7], Nityanand Miskin[1,5], Zaiyi Liu[8], J. Bryan Iorgulescu[9], Xiaoyin Xu[1,5], David A. Reardon[10,11] and Geoffrey S. Young[1,4,5]*

[1] Department of Radiology, Brigham and Women's Hospital, Boston, MA, United States, [2] Department of Radiology, Guangzhou First People's Hospital, The Second Affiliated Hospital of South China University of Technology, Guangzhou, China, [3] Division of Neurology, Department of Medicine, Sunnybrook Health Sciences Center, University of Toronto, Toronto, ON, Canada, [4] Department of Imaging, Dana-Farber Cancer Institute, Boston, MA, United States, [5] Department of Radiology, Harvard Medical School, Boston, MA, United States, [6] Department of Family Medicine, University of California, Riverside School of Medicine, Riverside, CA, United States, [7] Department of Neurosurgery, Peking Union Medical College Hospital, Chinese Academy of Medical Sciences and Peking Union Medical College, Beijing, China, [8] Department of Radiology, Guangdong Provincial People's Hospital, Guangdong Academy of Medical Sciences, Guangzhou, China, [9] Department of Pathology, Brigham and Women's Hospital, Boston, MA, United States, [10] Center for Neuro-Oncology, Dana-Farber Cancer Institute, Boston, MA, United States, [11] Department of Medicine, Harvard Medical School, Boston, MA, United States

Objectives: Real-time assessment of treatment response in glioblastoma (GBM) patients on immune checkpoint blockade (ICB) remains challenging because inflammatory effects of therapy may mimic progressive disease, and the temporal evolution of these inflammatory findings is poorly understood. We compare GBM patient response during ICB as assessed with the Immunotherapy Response Assessment in Neuro-Oncology (iRANO) and the standard Response Assessment in Neuro-Oncology (RANO) radiological criteria.

Methods: 49 GBM patients (seven newly diagnosed and 42 recurrent) treated with ICBs at a single institution were identified. Tumor burden was quantified on serial MR scans according to RANO criteria during ICB. Radiographic response assessment by iRANO and RANO were compared.

Results: 82% (40/49) of patients received anti–PD-1, 16% (8/49) received anti-PD-L1, and 2% (1/49) received anti-PD-1 and anti-CTLA4 treatment. Change in tumor burden and best overall response ranged from –100 to +557% (median: +48%). 12% (6/49) of patients were classified as concordant non-progressors by both RANO and iRANO (best response: one CR, one PR, and four SD). Another12% (6/49) had discordant assessments: 15% (6/41) of RANO grade progressive disease (PD) patients had iRANO grade of progressive disease unconfirmed (PDU). The final classification of these

OPEN ACCESS

Edited by:
Cornelia Brendle, Tübingen University Hospital, Germany

Reviewed by:
Natarajan Raghunand, Moffitt Cancer Center, United States
Miles C. Andrews, Monash University, Australia

***Correspondence:**
Geoffrey S. Young
gsyoung@bwh.harvard.edu

†These authors have contributed equally to this work and share first authorship

Specialty section:
This article was submitted to Cancer Imaging and Image-directed Interventions, a section of the journal Frontiers in Oncology

Received: *11 March 2021*
Accepted: *08 June 2021*
Published: *25 June 2021*

Citation:
Chen X, Lim-Fat MJ, Qin L, Li A, Bryant A, Bay CP, Gao L, Miskin N, Liu Z, Iorgulescu JB, Xu X, Reardon DA and Young GS (2021) A Comparative Retrospective Study of Immunotherapy RANO Versus Standard RANO Criteria in Glioblastoma Patients Receiving Immune Checkpoint Inhibitor Therapy. Front. Oncol. 11:679331. doi: 10.3389/fonc.2021.679331

discordant patients was pseudoprogression (PsP) in three of six, PD in two of six, and PDU in one of six who went off study before the iRANO assessment of PDU. iRANO delayed diagnosis of PD by 42 and 93 days in the two PD patients. 76% (37/49) patients were classified as concordant PD by both RANO and iRANO. 12% (6/49) of all patients were classified as PsP, starting at a median of 12 weeks (range, 4–30 weeks) after ICB initiation.

Conclusions: Standard RANO and iRANO have high concordance for assessing PD in patients within 6 months of ICB initiation. iRANO was beneficial in 6% (3/49) cases later proven to be PsP, but delayed confirmation of PD by <3 months in 4% (2/49). PsP occurred in 12% of patients, starting at up to 7 months after initiation of ICB. Further study to define the utility of modified RANO compared with iRANO in ICB GBM patients is needed.

Keywords: glioblastoma, immunotherapy, magnetic resonance imaging, disease progression, pseudoprogression, response assessment in neuro-oncology criteria, immunotherapy response assessment for neuro-oncology

INTRODUCTION

Patients with glioblastoma (GBM), the most common primary malignant brain tumor in adults, face a poor prognosis, limited effective treatment options, and early clinical deterioration (1). Despite recent advances, current standard treatment with maximal surgical resection, and temozolomide chemoradiation yields a median overall survival (OS) of roughly 15 to 16 months in patients with newly diagnosed GBM (2, 3), and no salvage therapy has been proven to prolong OS. A number of immune-based strategies are being investigated in GBM, including immune checkpoint blockade (ICB), neoantigen vaccines, oncolytic viruses, and chimeric antigen receptor T cell therapy (4).

Over the past decade, immune checkpoint inhibitors targeting cytotoxic T lymphocyte-4 (CTLA-4; ipilimumab), programmed cell death protein 1 (PD-1; pembrolizumab, nivolumab, and cemiplimab), and programmed cell death ligand1 (PD-L1; durvalumab, atezolizumab, and avelumab) have obtained approval from the US Food and Drug Administration and become part of the standard of care for melanoma, non-small cell lung cancer, and other solid tumors based on impressive responses and prolonged OS in a minority of patients, some with very advanced disease (5–11). While ICB has produced promising responses in animal models of GBM (12), phase 3 human trials in both newly diagnosed GBM (CheckMate-498; press release, Bristol Myers Squibb, May 9, 2019, and Checkmate-548; press release, Bristol Myers Squibb, 12/23/2020) and recurrent GBM (CheckMate-143) (13) have failed to prolong OS. However, neoadjuvant use of both pembrolizumab (14) and nivolumab (15) has shown immunomodulatory effects, and neoadjuvant pembrolizumab appeared to have an OS benefit in a randomized multi-institutional cohort of 35 patients with recurrent GBM (14). Reports that the subpopulation of long-term responders to PD-1 ICB have tumors enriched in certain MAPK pathway alterations raises hope that ICB may prove effective in this or other targeted subpopulations, indicating the need research to discover biomarkers for identification of potential long-term responders before or early after ICB initiation (16). Biomarkers derived from clinical GBM patient MRI obtained soon after ICB initiation that are capable of differentiating patients likely to respond from patients unlikely to respond would be especially beneficial. In neuro-oncology, MRI assessment of GBM by the Response Assessment in Neuro-Oncology (RANO) criteria has been used in clinical trials since its inception in 2010 (17). RANO categorizes patients as having radiographic progressive disease (PD) when the tumor burden either (1) increases more than 25% when compared to MRI at baseline (defined as pre-therapy or best imaging response timepoint), or (2) when new lesions appear. However, in about 20% to 30% of patients treated with standard chemoradiation, treatment-related "pseudoprogression" (PsP) confounds this assessment by producing enhancement, edema, mass effect, and symptomatic worsening that subsequently resolve (18, 19). PsP is also observed following ICB, but the true rate and timing have not been clearly defined.

Because this early worsening of abnormality on MRI can lead to premature termination of therapy in potential responders and/or misinterpretation of clinical trial data, the revised immunotherapy RANO (iRANO) criteria were created in 2015 (20). iRANO differs from RANO in that per iRANO radiographic PD cannot be confirmed when the progressive imaging changes initially appear less than 6 months after starting immunotherapy. By iRANO such patients are classified as PD only after sustained worsening on MRI for three consecutive months. Although iRANO is designed to address ICB-related PsP, no published data exist that directly compare iRANO to RANO in ICB patients. Because that definition of response and progression is crucial when studying

Abbreviations: GBM, glioblastoma; OS, overall survival; ICB, immune checkpoint blockade; CTLA-4, cytotoxic T-lymphocyte-associated protein 4; PD-1, programmed death receptor 1; PD-L1, programmed death-ligand 1; NSCLC, non-small cell lung cancer; RANO, response assessment in neuro-oncology; PD, progressive disease; iRANO, immunotherapy RANO; CR, complete response; PR, partial response; BOR, best overall response; SD, stable disease; PDU, progressive disease unconfirmed; PsP, pseudoprogression; PFS, progression free survival.

the effectiveness of novel immunotherapies, validation of iRANO is needed. We report direct comparison of RANO and iRANO assessments of ICB response and describe the patterns of response in a retrospective cohort of 49 GBM patients treated with ICB.

MATERIALS AND METHODS

Patients

The institutional review board at our institution approved this retrospective analysis of patient records with a waiver of informed consent. Medical record data including MRI from 49 patients with GBM (seven newly diagnosed and 42 recurrent) treated in clinical trials of anti–PD-1 blockade with nivolumab (Bristol-Myers Squibb, Princeton, NJ, USA) or pembrolizumab (Merck, Kenilworth, NJ, USA), or anti-PD-L1 blockade with durvalumab (AstraZeneca Inc, NJ, USA) was retrieved. Patients with newly diagnosed GBM received standard treatment (maximal surgical resection, radiotherapy, and concomitant/adjuvant temozolomide) with biweekly nivolumab or pembrolizumab. One patient received dual checkpoint inhibition with ipilimumab and nivolumab alongside adjuvant temozolomide (ipilimumab once every 4 weeks for four courses and nivolumab every 2 weeks). Recurrent GBM patients received pembrolizumab every 3 weeks or nivolumab every 2 weeks, or durvalumab every 2 weeks, with or without bevacizumab. Patients were treated until disease progression, unacceptable toxicity, or voluntary withdrawal. MRI tumor assessment was performed every 8 weeks. As specified by RANO, a maximum of five target lesions were assessed per patient. All patients had baseline MRI prior to the initiation of ICB therapy and at least one follow-up MRI during ICB therapy.

MRI Acquisition

MR images were acquired on 1.5 or 3T scanners (Siemens Erlangen, Germany and GE Healthcare, Waukesha, WI) using standard institutional protocols including axial FLAIR T2 and axial spin echo pre- and post-contrast T1-weighted images. The parameters in detail for MRI scans were as following: axial FLAIR T2WI, TR 8000-12ms; TE 550/81 to 135 ms; TI 2000 to 2650 ms; 3- to 5-mm slice thickness; gap 0 to 1 mm; matrix 256 to 384 × 244–288; axial spin echo pre- and post-contrast T1WI, TR 400 to 706ms; TE 2.5 to 17 ms; slice thickness 3 to 5 mm; gap 0 to 1 mm; matrix 256 to 384 × 192 to 244.

Tumor Response Assessment According to iRANO and RANO

Imaging determinants of progression were assessed following published iRANO (20) and RANO (17) criteria. Clinical performance status was incorporated in our grading of PD. Data regarding steroid use were not available in all cases and so was not incorporated in the analysis. Per RANO, on baseline and all follow-up scans, the cross-product burden of abnormal enhancement was calculated as the sum of the products of the two largest perpendicular diameters of enhancing lesions on contrast-enhanced T1WI, and lesions with largest perpendicular diameter <10 mm and lesions visible on only one axial section were regarded as non-measurable excluded from analysis. Non-enhancing tumor and edema were not assessed.

Patients were classified as experiencing complete response (CR), partial response (PR), stable disease (SD), progressive disease (PD), and progressive disease unconfirmed (PDU) at each time point, according to RANO and iRANO. For patients meeting criteria for complete response (CR; i.e., complete disappearance of abnormal enhancement and no increase in non-enhancing abnormality on FLAIR T2WI) or partial response (PR; i.e., >50% decrease in cross-product enhancing tumor burden and no increase in non-enhancing abnormality on FLAIR T2WI), best overall response (BOR) was defined as the minimum enhancing lesion burden by the cross-product method during the trial. For patients meeting criteria for stable disease (SD; i.e., (<50% decrease and <25% increase in cross product tumor burden and no increase in non-enhancing abnormality on FLAIR T2WI) (17), the smallest cross-product was considered BOR only if abnormal enhancement remained stable on ICB 6 months from start of ICB.

iRANO criteria for SD, PR, and CR were the same as RANO, but PD criteria differ. Under iRANO, radiographic PD (i.e., >25% increase in burden of abnormal enhancement by cross product method or increase in FLAIR T2WI abnormality), identified within 6 months of starting ICB, was classified as unconfirmed progressive disease (PDU) until follow-up MRI 3 months after detection of PDU confirmed sustained progression on post-contrast and/or FLAIR T2WI (20). In addition, under RANO detection of a new measurable enhancing lesion constitutes PD by definition. Under iRANO, patients with a new enhancing measurable lesion were allowed to continue study therapy pending confirmation of progression on follow-up imaging. Finally, according to iRANO, patients who underwent resection or biopsy during the trial because of imaging evidence of worsening edema and enhancement were classified as PD if histopathologic assessment revealed a predominance of active viable tumor; alternatively, they were classified as SD if the specimen revealed predominantly necrosis, inflammation, and/or other treatment-related effects.

For RANO/iRANO, patients who required an increased dose of corticosteroids (usually dexamethasone) could not be defined as having achieved a response, while those who decreased dexamethasone prior to MRI and had progressive imaging changes should be deemed as non-evaluable. This component was, however, not included in our grading scheme.

For the purposes of this study, we defined pseudoprogression (PsP) as ≥25% increase in enhancing lesion cross-product compared with the smallest measurement since pretreatment baseline, when the enhancing lesion burden decreased on follow-up MRI or tissue pathology demonstrated predominantly necrosis, inflammation, and/or other treatment-related effect. PsP occurring <12 weeks after start of ICB was considered "early" PsP and PsP occurring >12 weeks after start of ICB was considered "late" PsP.

The authors were blinded to clinical assessment of progression or response. Percent agreement between iRANO and RANO for progression versus non-progression and 95% confidence intervals for agreement were calculated. Progression-free survival (PFS) was calculated from date of ICB initiation to

date of progression or death by any cause, or if no progression was observed, from ICB initiation to the censored date. OS was calculated from start of initial therapy to death from any cause, or for patients still alive at the time of analysis, to the censored date. The last date of study follow-up was February 6, 2019.

Statistical Analysis

Patients were classified into three groups based on difference between RANO and iRANO response assessment: group 1 (concordant non-progressors) includes patients with BOR of SD, PR, or CR by both RANO and iRANO; group 2 (discordant) includes patients with BOR of PD by RANO but PDU, SD, PR, or CR by iRANO; and group 3 (concordant progressors), patients with BOR of PD by both RANO and iRANO. Kaplan-Meier curves were plotted for the three groups, and pairwise log-rank tests were used to compare OS between the three groups. Individuals were right censored at the end of follow-up or if they voluntarily withdrew from the study; right censoring was considered non-informative. Testing was two-tailed, and a p-value < 0.05 was considered statistically significant. No correction was made to account for multiple hypothesis testing. Statistical analysis was conducted using R version 3.3.

RESULTS

Patient Demographics and Treatment Characteristics

Median age at GBM diagnosis was 61 years (range, 26–81) (**Table 1**). 82% (40/49) of the patients received anti-PD-1 (nivolumab or pembrolizumab monotherapy), 16% (8/49) received anti–PD-L1 (durvalumab), and 4% (1/49) received dual ICB (nivolumab and ipilimumab). 82% (40/49) received ICB for recurrent GBM and 14% (7/49) as upfront therapy in newly diagnosed GBM. The Kaplan-Meier estimated median OS was 12.3 months (range, 3.1–43.8 months). Median time on therapy was 17.7 weeks (range, 2–208 weeks). Median follow-up time was 38 weeks (range, 13.4–187.7 weeks). One patient voluntarily withdrew from the study and was lost to follow-up. One patient was still receiving nivolumab therapy at the time of censoring.

Response Assessment by RANO and iRANO

Forty-four of 49 patients had at least one measurable enhancing lesion on pretreatment baseline MRI. In these 44 patients, the change in enhancing lesion burden at BOR, compared to baseline ranged from −100% to +557% (median: +48%) (**Figure 1**). The percentage agreement between iRANO and RANO for PD status was 88% (95% confidence interval [CI], 79% to 97%) (**Table 2**).

12% (6/49) patients were stratified into group 1 (concordant non-progressors by both RANO and iRANO criteria); one CR, one PR, and four SD. Three of six patients in group 1 (one CR, one PR, one SD) received ICB upfront and the other three of six (three SD) received ICB for recurrence. 43% (3/7) of the upfront patients were in group 1, compared with 7% (3/42) of the recurrence patients.

12% (6/49) patients overall were stratified into group 2 (discrepant classification between RANO and iRANO), representing 15% (6/41) of the PD patients (**Tables 3A**, **B**). All six of these patients had PDU based on increasing burden of enhancing abnormality on MRI within 6 months ICB initiation.

TABLE 1 | Patient demographics and clinical characteristics.

Characteristics	Variable (%)	All patients (n=49)	Group 1 Non-PD both criteria (n=6)	Group 2 PD per RANO, non-PD per iRANO (n=6)	Group 3 PD by both criteria (n=37)
Sex	Male	32 (65)	3 (50)	1 (17)	28 (76)
	Female	17 (35)	3 (50)	5 (83)	9 (24)
Age (years)	Median (range)	61 (26–81)	49 (41–68)	61 (57–69)	66 (26–81)
Type of tumor	New GBM	7 (14)	3 (50)	0 (0)	4 (11)
	Recurrent	42 (97)	3 (50)	6 (100)	33 (89)
Treatment	Nivolumab	10 (20)	3 (50)	3 (50)	4 (11)
	Pembrolizumab	30 (61)	3 (50)	2 (33)	25 (68)
	Durvalumab	8 (16)	0 (0)	1 (17)	7 (19)
	Nivolumab + Ipilimumab	1 (2)	0 (0)	0 (0)	1 (3)
IDH status	Wildtype	42 (86)	6 (100)	5 (83)	31 (84)
	Mutant	4 (8)	0 (0)	0 (0)	4 (11)
	Unknown	3 (6)	0 (0)	1 (17)	2 (5)
MGMT promoter	Methylated	15 (31)	3 (50)	1 (17)	12 (32)
	Unmethylated	16 (33)	3 (50)	1 (17)	11 (30)
	Partially methylated	7 (14)	0 (0)	1 (17)	6 (16)
	Unknown	11 (22)	0 (0)	3 (50)	8 (22)
Concurrent Bevacizumab Number of infusions	Yes	20 (41)	3 (50)	0 (0)	17 (46)
	No	29 (59)	3 (50)	6 (100)	20 (54)
	Median (range)	6 (2–76)	32 (8–76)	6.5 (2–18)	5.0 (2–32)

PD, progressive disease; RANO, Response Assessment in Neuro-Oncology; iRANO, Immunotherapy Response Assessment in Neuro-Oncology.

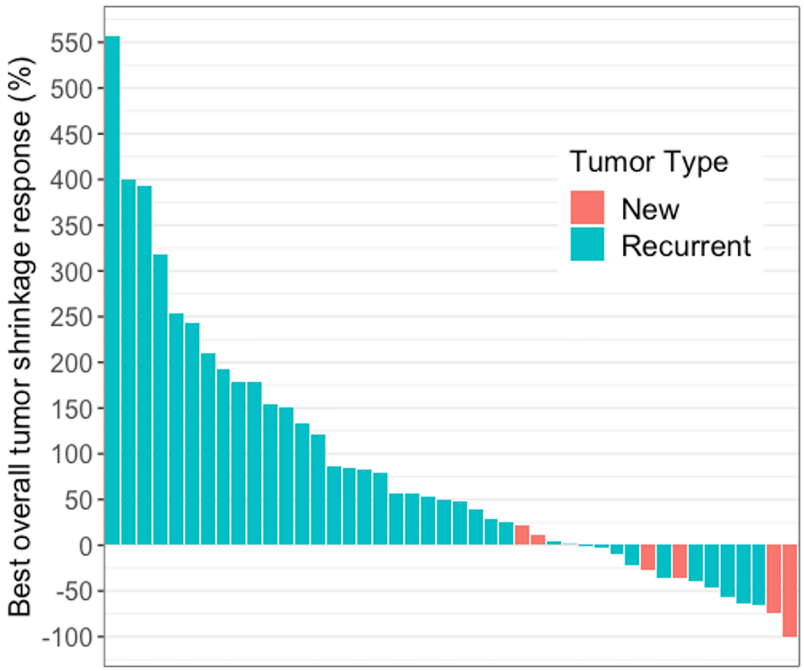

FIGURE 1 | Waterfall plot showing best overall tumor shrinkage in the form of percentage change in enhancing lesion size compared to baseline in 44 of 49 patients with glioblastoma receiving immune checkpoint blockade. These 44 patients had measurable disease at baseline and the change in enhancing lesion burden at BOR, compared to baseline ranged from −100% to +557% (median: +48%).

All six received ICB for recurrent GBM and none received concurrent bevacizumab with ICB. Half (3/6) were ultimately confirmed to have had PsP, two by pathology and one by later decrease in enhancement on MRI. PD was later confirmed in two of the other three patients by iRANO, at 42 and 93 days, respectively, after PD classification by RANO. The remaining one patient with PDU by iRANO was taken off trial after 3 months, and no follow-up scan obtained. 76% (37/49) of the patients were classified into group 3 (concordant PD by both RANO and iRANO).

TABLE 2 | Confusion matrix of PD status by iRANO and RANO (n = 49).

		RANO		
		PD	**Non-PD**	
iRANO	PD	37	0	37
	Non-PD	6	6	12
		43	6	49

PD, progressive disease; RANO, Response Assessment in Neuro-Oncology; iRANO, Immunotherapy Response Assessment in Neuro-Oncology.

PsP During Immunotherapy

12% (6/49) met the criteria for PsP (two receiving up-front ICB and four ICB for recurrence; **Table 4**). Median time from ICB initiation to initial detection of PsP was 12 weeks (range, 4–30 weeks). Three of six received nivolumab, one of six received nivolumab and ipilimumab, and two of six received pembrolizumab. MRI of patient 11 (nivolumab and ipilimumab) demonstrated a 27% increase in enhancing lesion burden at first MRI (week 6), 13% decrease on next follow-up MRI (week 12), additional 36% decrease on the next MRI (week 17), after which, the burden of enhancing abnormality remained stable for two additional months until ICB was discontinued due to declining performance status (**Figure 2**). MRI

TABLE 3A | Group 2 representing six patients with recurrent GBM with discordant PD date by RANO *vs* iRANO (PD by RANO and PDU by iRANO.

Patients	PsP	PD by RANO (trial day)	Date of confirmed PD or PsP (trial day)	Additional days on trial until confirmation of PD/PsP
4	Yes	29	92 (PsP: pathology)	63
7	No	70	112 (PD: pathology)	42
11	Yes	44	86 (PsP: imaging)	42
13	No	66	NA90 (no follow up scan)	NA
38	No	134	227 (PD: pathology)	93
46	Yes	68	150 (PsP: pathology)	82

Pathology denotes disease diagnosed by pathology specimen which revealed predominantly necrosis, inflammation, and/or other treatment-related effects.
PsP, pseudoprogression; NA, not available.

of patient 6 (nivolumab) revealed 31% increase in enhancing lesion burden at 30 weeks from the start of ICB, and no change at 38 weeks after which histopathology confirmed predominant treatment effect. MRI of the other four PsP patients (pembrolizumab or nivolumab) demonstrated progressive increase in enhancing lesion burden leading to re-resection at 4 to 30 weeks with pathology showing extensive treatment-related effects.

New Lesions During Immunotherapy

16% (8/49) of the patients (one up-front ACB and seven ICB for recurrence) developed one to three new lesions per patient during ICB (**Table 5**). In four of eight, none of the enhancing lesions were large enough to be measurable.

Survival Outcomes

OS was significantly longer in the concordant non-progression group 1 (median, 24.3 months; 95% CI, 12.3 to not estimable) compared with discordant group 2 (median, 12.8 months; 95% CI, 8.2 to not estimable; $p < 0.05$) and concordant progression group 3 (median, 8.1; 95% CI, 6.5–14.5; $p = 0.01$) (**Figure 3**). There was no difference in OS between group 2 and group 3 ($p = 0.7$). Median PFS as assessed by RANO was 2.7 months (1.9–3.8 months) and median PFS by iRANO was 3.7 months (2.9–5.6 months).

The median OS in the newly diagnosed GBM patients treated with up-front ICB was 24.3 months (95% CI, 15.4 to not estimable) compared with 8.2 months (95% CI, 6.9–14.1 months) in patients treated with ICB for recurrent GBM. Using the RANO criteria, median PFS was 8.9 months (95% CI, 6.5 to NA) in newly diagnosed GBM compared to 1.9 months (95% CI, 1.9 to 2.8 months) in recurrent GBM. Using the iRANO criteria, the median PFS was 8.9 months (95% CI, 6.5 to NA) in the up-front ICB group compared with 3.3 months (95% CI, 2.8–4.7; $p = 0.003$) in ICB for recurrence. Patients experiencing PsP did not differ in OS (median, 14.6 months; 95% CI, 8.1 to NA) compared with the other patients (median, 8.9 months; 95% CI, 6.9–15.3; $p = 1.0$).

DISCUSSION

In order to simulate typical prospective clinical application of MRI response criteria, our retrospective analysis of MRI in 49 GBM patients receiving ICB compared response assessment by iRANO criteria with the standard RANO criteria. The wide range of observed changes in enhancing lesion burden (−100% to +556.6%) (**Figure 1**) was consistent with known heterogeneous patient response to PD-1 or PD-L1 ICB among GBM and other cancer patients (21–23). We found a high concordance between RANO and iRANO. Concordant non-progression was determined in 12% (6/49) of the patients, and progression in 76% (37/49) by both criteria, for a substantial percentage agreement of 88%. Non-progressors by either RANO or iRANO had better survival than patients who were classified

TABLE 3B | Group 2 representing six patients with recurrent GBM with discordant PD date by RANO *vs* iRANO (PD by RANO and PDU by iRANO.

Patient		Day 30	Day 60	Day 90	Day 120	Day 150	Day 180	Day 210	Day 240
4	RANO	PD							
	iRANO	PDU	PDU	PDU	PsP				
7	RANO	–	–	PD					
	iRANO	–	–	PDU	PD				
11	RANO	–	PD						
	iRANO	–	PDU	PsP					
13	RANO	–	–	PD					
	iRANO	–	–	PDU					
38	RANO	–	SD	SD	SD	PD			
	iRANO	–	SD	SD	SD	PDU	PDU	–	PD
46	RANO	–	–	PD					
	iRANO	–	–	PDU	PDU	PsP			

Scan dates were rounded to the nearest following month.
PD, progressive disease; PDU, PD unconfirmed; PsP, pseudoprogression; "-", no scan.

TABLE 4 | Pseudoprogression characteristics in 6/49 glioblastoma patients.

Patient	Type	Treatment	Time to PsP (weeks)	OS/time spent on trial (weeks)	Confirmed
4	recurrent	N	4	23/12	Pathology
6	new	N	30	70/66	Pathology
9	new	N	23	104/59	Pathology
11	recurrent	N+I	6	73/27	Follow-up
43	recurrent	P	6	35/19	Pathology
46	recurrent	P	10	55/41	Pathology

Pathology denotes disease diagnosed by pathology specimen which revealed predominantly necrosis, inflammation, and/or other treatment-related effects. Follow-up denotes confirmed by stable disease of follow-up imaging.
N, nivolumab; I, ipilimumab; P, pembrolizumab; PsP, pseudoprogression; OS, overall survival.

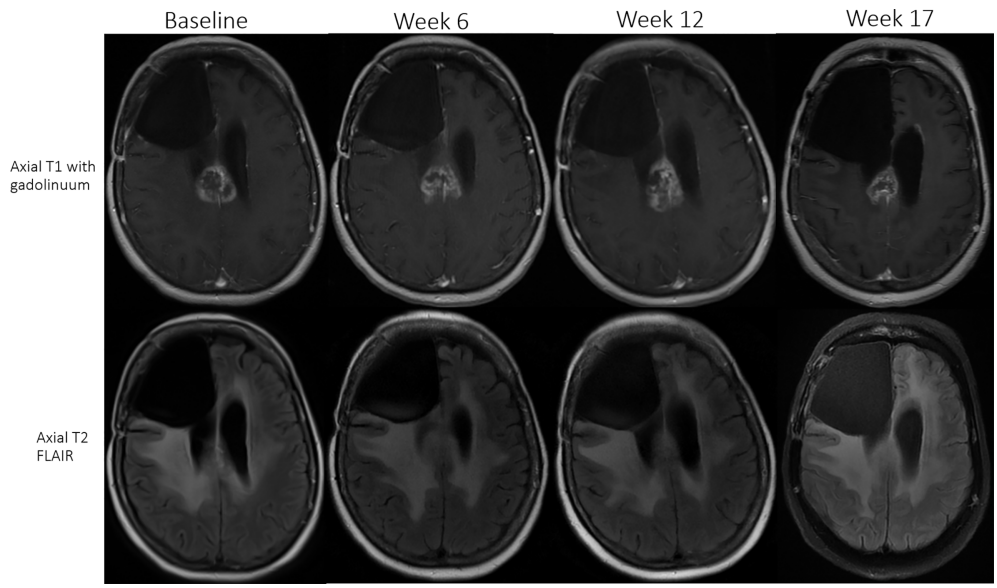

FIGURE 2 | Patient 11 (received nivolumab and ipilimumab) had an initial 27% increase in enhancing lesion burden at first MRI (week 6), 13% decrease at the next follow-up MRI (week 12), and subsequently a 36% decrease (week 17) in size of the enhancing lesion. The patient remained stable on ICB for two additional months until treatment was discontinued due to declining performance status in the setting of a stable MRI scan.

as PD by both criteria and better survival than patients with discordant grading by RANO and iRANO. This indicates that a subset of GBM patients have sustained response to ICB, which confers a survival advantage. In our cohort, the median PFS was 2.7 months using standard RANO and 3.7 months using iRANO, but a subgroup of long-term responders also had PFS of 24.4 months (patient 5), 26.1 months (patient 45), 35.6 months (patient 1), and 37.5 months (patient 10). We did not design our study to account for expected differences in survival between newly diagnosed and recurrent GBM and only a small subset of our cohort received up-front ICB for newly diagnosed GBM. Nevertheless, two interesting patterns suggest the possibility that up-front ICB patients may derive more benefit from ICB compared with patients receiving ICB for recurrence. We did not design our study to account for expected differences in survival between newly diagnosed and recurrent GBM and only a small subset of our cohort received up-front ICB for newly diagnosed GBM. Nevertheless, the significantly longer PFS and OS and higher rate of concordant non-progression in the newly diagnosed group (50% in group 1 compared to 0% in group 2 and 12% in group 3) deserves additional study in larger up-front cohorts to assess whether up-front ICB may be more effective than ICB at recurrence."

MRI assessment by iRANO differs from standard RANO principally in that PD is only confirmed by iRANO when (1) the increasing enhanced tumor burden on MRI first appears at or later than 6 months after immunotherapy initiation, or (2) enhancing lesion burden continues to increase on follow-up MRI > 3 months after initial detection. This is based on studies in other solid tumors demonstrating that increasing enhancing lesion burden stabilized or improved within 3 months in patients who were ultimately found to derive benefit from ICB (24, 25).

In two of 49 patients subsequently confirmed to have PD by pathology, MRI within the first 6 months demonstrated

TABLE 5 | Characteristics of new lesions during immunotherapy.

Patient	type	treatment	Time (weeks)	# of lesion(s)	iRANO	Confirmed results	OS (weeks)
9	new	N	55	1 non-measurable	PD	PD	104
13	R	D	9	1 measurable	PDU	PDU	23
16	R	D	24	1 measurable	PDU	PDU	61
18	R	D	11	3 non-measurable	PD	PD	24
21	R	P+B	25	1 non-measurable	SD	PD	77
24	R	P+B	10	1 non-measurable	SD	PD	27
28	R	P+B	14	2 non- and 1 measurable	PD	PD	16
41	R	P+B	2	1 measurable	PDU	PD	13

Time was measured from initial i—ICB to appearance of new lesion.
new, newly diagnosed GBM; R, recurrent GBM; N, nivolumab; D, durvalumab; P, pembrolizumab; B, bevacizumab; SD, stable disease; PD, progressive disease; PDU, PD unconfirmed; OS, overall survival.

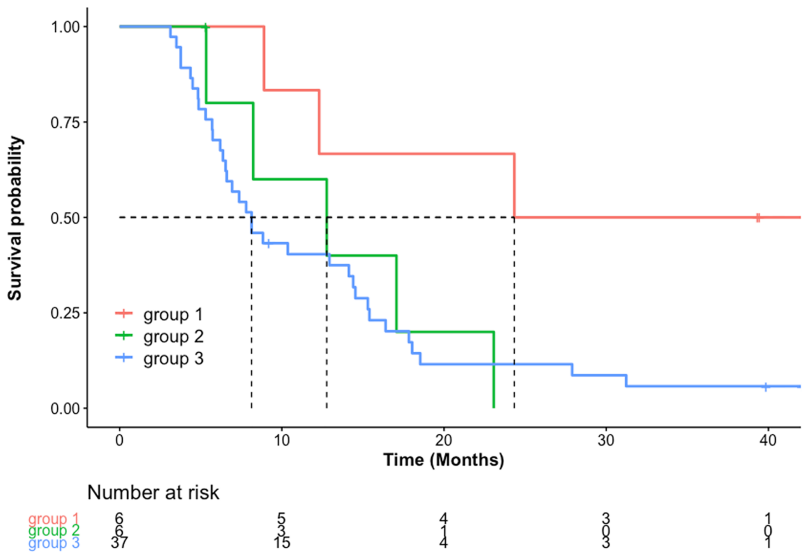

FIGURE 3 | OS in months [Kaplan-Meier estimated median and 95% confidence interval (CI), months] was significantly longer in group 1 [24.3 (12.3-not estimable)] compared to group 2 [12.8 (8.2 to not estimable)] (p=0.05) and group 3 [8.1 (6.5–14.5) (p=0.01)]. There was no significant difference in median OS between group 2 and group 3 (p=0.7).

increasing enhancement, which was classified as PD by RANO but PDU by iRANO. The differences in the criteria and/or lack of follow-up imaging 3 months following the initial MRI with increasing enhancement led to delay in confirmation of progression and extension of time on trial by 42 and 93 days, respectively, after initial PD determination by RANO. It is unclear whether earlier identification and withdrawal from the clinical trial would have provided any clinical benefit, because no effective salvage therapy exists for GBM recurrence. On the other hand, the use of iRANO allowed maintenance of ICB in 3 of 49 patients who were later found to have PsP, extending their progression-free time on trial for 42 to 82 days. These patients may have benefited from use of iRANO. However, it is worth noting that there was no difference in overall survival in patients in group 2 or group 3, and that in this context, using iRANO, while more precise, may not reflect any difference in underlying tumor biology. If in the future, more effective therapies are developed for patients with recurrent disease, the significance of differences between iRANO and RANO may require re-analysis because the relative delay in assignment of PD by iRANO could have the unintended effect of delaying transition to effective salvage therapy.

The incidence of PsP was 12% in our cohort, which is lower than previously reported rates of PsP in GBM after temozolomide chemoradiation (18, 19). This may in part be due to the fact that most patients in our cohort had recurrent GBM (42/49, 86%), a group in which true progression is more common than PsP. Indeed, 28.5% (2/7) of the patients with newly diagnosed GBM and 9.5% (4/42) of the patients with recurrent GBM in our cohort experienced PsP. PsP was noted initially between 4 and 10 weeks after ICB initiation in patients with the ICB for recurrence group, and 23 to 30 weeks in the up-front ICB group. This is consistent with a published analysis of ICB in a multi-institutional cohort of 152 GBM patients reporting that immunotherapy-related inflammation is less common than progressive disease within 6 months of ICB initiation (26). These data suggest that inflammatory PsP in immunotherapy may present differently in newly diagnosed compared with recurrent ICB; the optimal ideal timeframe and monitoring strategy may differ between these groups. The OS in patients with PsP was not significantly different from those without PsP. This finding was consistent with that of the previously cited data presented at ASCO 2020, which showed no difference in post-progression OS between patients with and without prior immune-related inflammation (26). These data raise the possibility that the potential clinical benefit of ICB may be partially masked by the morbidity of ICB-induced PsP, and emphasizes the importance of ongoing efforts to modulate the inflammatory effects of immunotherapy.

Of the 16% (8/49) of the patients who developed new lesions in our cohort, two of eight initially met iRANO criteria for SD. Six of eight were eventually confirmed to have PD on follow-up MRI, but one of two patients with PDU by iRANO survived longer than 1 year after PDU, in spite of discontinuation of immunotherapy based on RANO criteria at the time of new lesion appearance. It is unclear if this patient or several other patients in which ICB was discontinued based on RANO criteria would have had benefited from additional ICB if iRANO criteria had been used instead, but this suggests the hypothesis that iRANO may make an important difference to a small number of patients. The role of iRANO remains to be further elucidated in the context of the anticipated rise of more effective immunotherapeutic strategies both in the upfront and recurrent setting.

Limitations of our study inherent to its retrospective design include the heterogeneous population of newly diagnosed and

recurrent GBM patients, different combinations of prior tumor-directed therapies, and lack of sufficient follow-up scans to confirm progression in some patients. A larger population of patients will be needed to identify imaging or other prognostic factors predictive of ICB response. In addition, while both standard RANO and iRANO include information on corticosteroid use, we did not include this. This weakness leads to possible under-estimation of the theoretical accuracy of the criteria but accurately reproduces clinical MRI practice in which reliable steroid dosing data are rarely available at time of image interpretation. Further, availability of steroid dose information would not have changed MRI assessment of PD by either RANO or iRANO, and most clinical trials do not allow for continuation of ICB after significant increase in corticosteroid dose because of evidence that steroid use may abolish the benefit of ICB. Lastly, we did not include the modified RANO (mRANO) criteria in this study. mRANO was developed to take into account PsP and adopts a strategy of intermediate rigor between RANO and iRANO by requiring confirmation of PD on a subsequent scan at the next scheduled time point, after which, if there is further increase in tumor size, PD is backdated to the preliminary PD scan (27). In addition, if stable disease or partial response is seen on the subsequent follow up scan, mRANO grades the response as PsP. In short mRANO represents a more recent rational adaptation of RANO that may improve performance, but the ideal timing of the follow-up confirmatory scan after preliminary PD remains to be defined in future studies.

In conclusion, MRI assessment of anti-PD-1 and anti-PD-L1 ICB of GBM in our retrospective cohort suggests a high concordance of RANO and iRANO. iRANO may provide important benefit by identifying PsP, seen in 12% of our cohort. Use of iRANO delayed identification of PD in two of 49 cases prolonging time on trial for these patients compared with RANO. The utility of these criteria may need to be assessed if immunotherapies are developed, which are more effective in a subgroup or all GBM patients, or if imaging or genomic markers can be identified that predict higher probability of PsP, early progression, and/or substantial ICB benefit in a subgroup of patients. This retrospective study cannot determine whether these patients would have benefited clinically from use of RANO or conversely if several other patients discontinued from ICB based on RANO would have benefited from use of iRANO leading to continuation of ICB. Recent mRANO criteria may be better adapted for patients on ICB, allowing for identification of PsP while also allowing for early confirmation of PD, although the timeframe for follow up scans remains unclear. Imaging markers predictive of GBM patient subgroups with high probability of PsP, early progression, and/or substantial benefit from ICB deserve further study in larger cohorts with combined imaging, clinical, and genomic datasets.

DATA AVAILABILITY STATEMENT

The raw data supporting the conclusions of this article will be made available by the authors, without undue reservation.

ETHICS STATEMENT

The studies involving human participants were reviewed and approved by Institutional Review Board of Brigham and Women's Hospital. The patients/participants provided their written informed consent to participate in this study. Written informed consent was obtained from the individual(s) for the publication of any potentially identifiable images or data included in this article.

AUTHOR CONTRIBUTIONS

XC, ML-F, LQ, GY, and DR participated in the conception and study design, data acquisition and review of the images and measurements, statistical analysis and interpretation of data, drafting and revising the manuscript. AL, AB, LG, and NM participated in the data acquisition and review of the images and measurements. CB participated in the statistical analysis and revising the manuscript. ZL, XX and JI participated in the interpretation data and revising the manuscript. All authors contributed to the article and approved the submitted version.

FUNDING

This study was supported with US National Institutes of Health (NIH R01LM012434) [XX-Salary, GY-Salary], the National Key R&D Program of China (2017YFC1309100) [ZL-Salary], the National Science Fund for Distinguished Young Scholars (81925023) [ZL-Salary], the National Natural Scientific Foundation of China (81601469 [XC-Salary], 82072090 [XC-Salary], 81771912 [ZL-Salary]), Guangzhou Science and Technology Project of Health (20191A011002) [XC-Salary], China Scholarship Council funding (201808440033 [XC-Salary], 201706210406 [LG-Salary]), the National Cancer Institute (K12CA090354) [BI-Salary] and the Conquer Cancer Foundation/Sontag Foundation [BI-Salary].

ACKNOWLEDGMENTS

Provision of research software license from Siemens Healthineers MRA BWH-2017-MR-27-00- Young_C00224002 to GY.

REFERENCES

1. Wen PY, Weller M, Lee EQ, Alexander BM, Barnholtz-Sloan JS, Barthel FP, et al. Glioblastoma in Adults: A Society for Neuro-Oncology (SNO) and European Society of Neuro-Oncology (EANO) Consensus Review on Current Management and Future Directions. *Neuro Oncol* (2020) 22:1073–113. doi: 10.1093/neuonc/noaa106
2. Stupp R, Mason WP, van den Bent MJ, Weller M, Fisher B, Taphoorn MJ, et al. Radiotherapy Plus Concomitant and Adjuvant Temozolomide for Glioblastoma. *N Engl J Med* (2005) 352:987–96. doi: 10.1056/NEJMoa043330

3. Stupp R, Taillibert S, Kanner A, Read W, Steinberg D, Lhermitte B, et al. Effect of Tumor-Treating Fields Plus Maintenance Temozolomide vs Maintenance Temozolomide Alone on Survival in Patients With Glioblastoma: A Randomized Clinical Trial. *JAMA* (2017) 318:2306–16. doi: 10.1001/jama.2017.18718
4. Lim M, Xia Y, Bettegowda C, Weller M. Current State of Immunotherapy for Glioblastoma. *Nat Rev Clin Oncol* (2018) 15:422–42. doi: 10.1038/s41571-018-0003-5
5. Hodi FS, O'Day SJ, McDermott DF, Weber RW, Sosman JA, Haanen JB, et al. Improved Survival With Ipilimumab in Patients With Metastatic Melanoma. *N Engl J Med* (2010) 363:711–23. doi: 10.1056/NEJMoa1003466
6. Robert C, Ribas A, Wolchok JD, Hodi FS, Hamid O, Kefford R, et al. Anti-Programmed-Death-Receptor-1 Treatment With Pembrolizumab in Ipilimumab-Refractory Advanced Melanoma: A Randomised Dose-Comparison Cohort of a Phase 1 Trial. *Lancet* (2014) 384:1109–17. doi: 10.1016/s0140-6736(14)60958-2
7. Robert C, Long GV, Brady B, Dutriaux C, Maio M, Mortier L, et al. Nivolumab in Previously Untreated Melanoma Without BRAF Mutation. *N Engl J Med* (2015) 372:320–30. doi: 10.1056/NEJMoa1412082
8. Reck M, Rodríguez-Abreu D, Robinson AG, Hui R, Csőszi T, Fülöp A, et al. Pembrolizumab Versus Chemotherapy for PD-L1-Positive Non-Small-Cell Lung Cancer. *N Engl J Med* (2016) 375:1823–33. doi: 10.1056/NEJMoa1606774
9. Gandhi L, Rodríguez-Abreu D, Gadgeel S, Esteban E, Felip E, De Angelis F, et al. Pembrolizumab Plus Chemotherapy in Metastatic Non-Small-Cell Lung Cancer. *N Engl J Med* (2018) 378:2078–92. doi: 10.1056/NEJMoa1801005
10. Mok TSK, Wu YL, Kudaba I, Kowalski DM, Cho BC, Turna HZ, et al. Pembrolizumab Versus Chemotherapy for Previously Untreated, PD-L1-expressing, Locally Advanced or Metastatic Non-Small-Cell Lung Cancer (KEYNOTE-042): A Randomised, Open-Label, Controlled, Phase 3 Trial. *Lancet* (2019) 393:1819–30. doi: 10.1016/s0140-6736(18)32409-7
11. Sharma P, Siefker-Radtke A, de Braud F, Basso U, Calvo E, Bono P, et al. Nivolumab Alone and With Ipilimumab in Previously Treated Metastatic Urothelial Carcinoma: CheckMate 032 Nivolumab 1 Mg/Kg Plus Ipilimumab 3 Mg/Kg Expansion Cohort Results. *J Clin Oncol* (2019) 37:1608–16. doi: 10.1200/jco.19.00538
12. Reardon DA, Gokhale PC, Klein SR, Ligon KL, Rodig SJ, Ramkissoon SH, et al. Glioblastoma Eradication Following Immune Checkpoint Blockade in an Orthotopic, Immunocompetent Model. *Cancer Immunol Res* (2016) 4:124–35. doi: 10.1158/2326-6066.cir-15-0151
13. Reardon DA, Brandes AA, Omuro A, Mulholland P, Lim M, Wick A, et al. Effect of Nivolumab vs Bevacizumab in Patients With Recurrent Glioblastoma: The CheckMate 143 Phase 3 Randomized Clinical Trial. *JAMA Oncol* (2020) 6:1003–10. doi: 10.1001/jamaoncol.2020.1024
14. Cloughesy TF, Mochizuki AY, Orpilla JR, Hugo W, Lee AH, Davidson TB, et al. Neoadjuvant anti-PD-1 Immunotherapy Promotes a Survival Benefit With Intratumoral and Systemic Immune Responses in Recurrent Glioblastoma. *Nat Med* (2019) 25:477–86. doi: 10.1038/s41591-018-0337-7
15. Schalper KA, Rodriguez-Ruiz ME, Diez-Valle R, López-Janeiro A, Porciuncula A, Idoate MA, et al. Neoadjuvant Nivolumab Modifies the Tumor Immune Microenvironment in Resectable Glioblastoma. *Nat Med* (2019) 25:470–6. doi: 10.1038/s41591-018-0339-5
16. Zhao J, Chen AX, Gartrell RD, Silverman AM, Aparicio L, Chu T, et al. Immune and Genomic Correlates of Response to Anti-PD-1 Immunotherapy in Glioblastoma. *Nat Med* (2019) 25:462–9. doi: 10.1038/s41591-019-0349-y
17. Wen PY, Macdonald DR, Reardon DA, Cloughesy TF, Sorensen AG, Galanis E, et al. Updated Response Assessment Criteria for High-Grade Gliomas: Response Assessment in Neuro-Oncology Working Group. *J Clin Oncol* (2010) 28:1963–72. doi: 10.1200/jco.2009.26.3541
18. Balaña C, Capellades J, Pineda E, Estival A, Puig J, Domenech S, et al. Pseudoprogression as an Adverse Event of Glioblastoma Therapy. *Cancer Med* (2017) 6:2858–66. doi: 10.1002/cam4.1242
19. Brandes AA, Franceschi E, Tosoni A, Blatt V, Pession A, Tallini G, et al. MGMT Promoter Methylation Status can Predict the Incidence and Outcome of Pseudoprogression After Concomitant Radiochemotherapy in Newly Diagnosed Glioblastoma Patients. *J Clin Oncol* (2008) 26:2192–7. doi: 10.1200/jco.2007.14.8163
20. Okada H, Weller M, Huang R, Finocchiaro G, Gilbert MR, Wick W, et al. Immunotherapy Response Assessment in Neuro-Oncology: A Report of the RANO Working Group. *Lancet Oncol* (2015) 16:e534–e42. doi: 10.1016/S1470-2045(15)00088-1
21. Hodi FS, Hwu WJ, Kefford R, Weber JS, Daud A, Hamid O, et al. Evaluation of Immune-Related Response Criteria and RECIST v1.1 in Patients With Advanced Melanoma Treated With Pembrolizumab. *J Clin Oncol* (2016) 34:1510–7. doi: 10.1200/JCO.2015.64.0391
22. Nishino M, Ramaiya NH, Chambers ES, Adeni AE, Hatabu H, Janne PA, et al. Immune-Related Response Assessment During PD-1 Inhibitor Therapy in Advanced Non-Small-Cell Lung Cancer Patients. *J Immunother Cancer* (2016) 4:84. doi: 10.1186/s40425-016-0193-2
23. Pignon JC, Jegede OA, Shukla SA, Braun DA, Horak CE, Wind-Rotolo M, et al. irRECIST for the Evaluation of Candidate Biomarkers of Response to Nivolumab in Metastatic Clear Cell Renal Cell Carcinoma: Analysis of a Phase Ii Prospective Clinical Trial. *Clin Cancer Res* (2019) 25:2174–84. doi: 10.1158/1078-0432.ccr-18-3206
24. Brahmer JR, Tykodi SS, Chow LQ, Hwu WJ, Topalian SL, Hwu P, et al. Safety and Activity of anti-PD-L1 Antibody in Patients With Advanced Cancer. *N Engl J Med* (2012) 366:2455–65. doi: 10.1056/NEJMoa1200694
25. Hamid O, Robert C, Daud A, Hodi FS, Hwu WJ, Kefford R, et al. Safety and Tumor Responses With Lambrolizumab (anti-PD-1) in Melanoma. *N Engl J Med* (2013) 369:134–44. doi: 10.1056/NEJMoa1305133
26. Ellingson BM, Huang R-k, Villanueva-Meyer J, Lim-Fat MJ, George E, Iorgulescu B, et al. Estimated Clinical Efficacy and Radiographic Response Characteristics of PD1 Inhibition in Newly Diagnosed and Recurrent Glioblastoma in Clinical Practice: A Report From the Irano Working Group. *J Clin Oncol* (2020) 38:2521. doi: 10.1200/JCO.2020.38.15_suppl.2521
27. Ellingson BM, Wen PY, Cloughesy TF. Modified Criteria for Radiographic Response Assessment in Glioblastoma Clinical Trials. *Neurotherapeutics* (2017) 14:307–20. doi: 10.1007/s13311-016-0507-6

Conflict of Interest: The authors declare that the research was conducted in the absence of any commercial or financial relationships that could be construed as a potential conflict of interest.

Advantages of publishing in Frontiers

OPEN ACCESS
Articles are free to read for greatest visibility and readership

FAST PUBLICATION
Around 90 days from submission to decision

HIGH QUALITY PEER-REVIEW
Rigorous, collaborative, and constructive peer-review

TRANSPARENT PEER-REVIEW
Editors and reviewers acknowledged by name on published articles

Frontiers
Avenue du Tribunal-Fédéral 34
1005 Lausanne | Switzerland

Visit us: www.frontiersin.org
Contact us: frontiersin.org/about/contact

REPRODUCIBILITY OF RESEARCH
Support open data and methods to enhance research reproducibility

DIGITAL PUBLISHING
Articles designed for optimal readership across devices

FOLLOW US
@frontiersin

IMPACT METRICS
Advanced article metrics track visibility across digital media

EXTENSIVE PROMOTION
Marketing and promotion of impactful research

LOOP RESEARCH NETWORK
Our network increases your article's readership